STRUCTURAL, METABOLIC AND PHYSIOLOGIC MR IMAGING TO STUDY GLIOBLASTOMAS

EDITED BY: Sanjeev Chawla, Manoj Kumar and Ravi Prakash Reddy Nanga
PUBLISHED IN: Frontiers in Neurology and Frontiers in Oncology

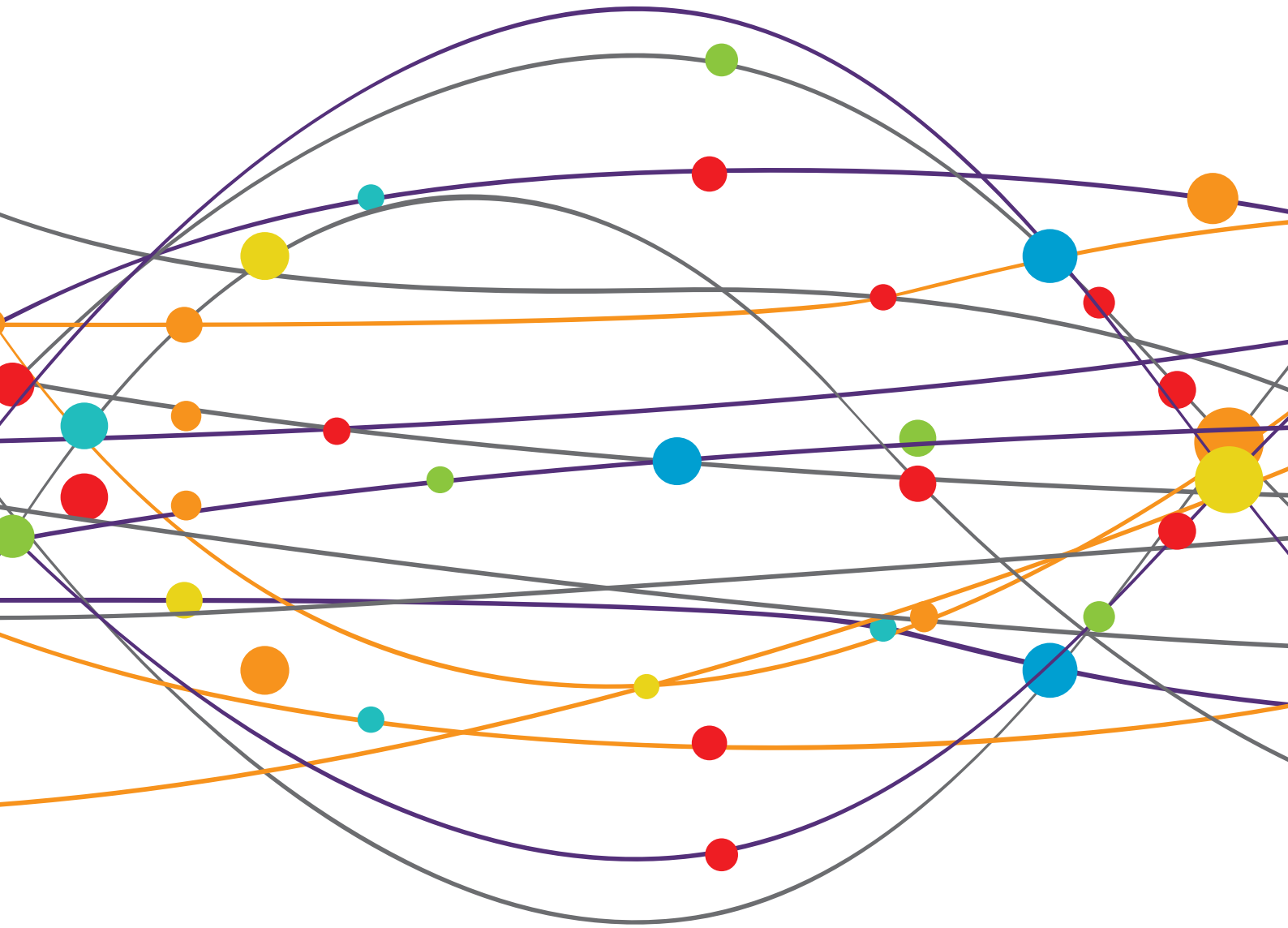

frontiers Research Topics

ISSN 1664-8714
ISBN 978-2-88974-968-3
DOI 10.3389/978-2-88974-968-3

About Frontiers

Frontiers is more than just an open-access publisher of scholarly articles: it is a pioneering approach to the world of academia, radically improving the way scholarly research is managed. The grand vision of Frontiers is a world where all people have an equal opportunity to seek, share and generate knowledge. Frontiers provides immediate and permanent online open access to all its publications, but this alone is not enough to realize our grand goals.

Frontiers Journal Series

The Frontiers Journal Series is a multi-tier and interdisciplinary set of open-access, online journals, promising a paradigm shift from the current review, selection and dissemination processes in academic publishing. All Frontiers journals are driven by researchers for researchers; therefore, they constitute a service to the scholarly community. At the same time, the Frontiers Journal Series operates on a revolutionary invention, the tiered publishing system, initially addressing specific communities of scholars, and gradually climbing up to broader public understanding, thus serving the interests of the lay society, too.

Dedication to Quality

Each Frontiers article is a landmark of the highest quality, thanks to genuinely collaborative interactions between authors and review editors, who include some of the world's best academicians. Research must be certified by peers before entering a stream of knowledge that may eventually reach the public - and shape society; therefore, Frontiers only applies the most rigorous and unbiased reviews.
Frontiers revolutionizes research publishing by freely delivering the most outstanding research, evaluated with no bias from both the academic and social point of view. By applying the most advanced information technologies, Frontiers is catapulting scholarly publishing into a new generation.

What are Frontiers Research Topics?

Frontiers Research Topics are very popular trademarks of the Frontiers Journals Series: they are collections of at least ten articles, all centered on a particular subject. With their unique mix of varied contributions from Original Research to Review Articles, Frontiers Research Topics unify the most influential researchers, the latest key findings and historical advances in a hot research area! Find out more on how to host your own Frontiers Research Topic or contribute to one as an author by contacting the Frontiers Editorial Office: frontiersin.org/about/contact

STRUCTURAL, METABOLIC AND PHYSIOLOGIC MR IMAGING TO STUDY GLIOBLASTOMAS

Topic Editors:
Sanjeev Chawla, University of Pennsylvania, United States
Manoj Kumar, National Institute of Mental Health and Neurosciences (NIMHANS), India
Ravi Prakash Reddy Nanga, University of Pennsylvania, United States

Citation: Chawla, S., Kumar, M., Nanga, R. P. R., eds. (2022). Structural, Metabolic and Physiologic MR Imaging to Study Glioblastomas. Lausanne: Frontiers Media SA. doi: 10.3389/978-2-88974-968-3

Table of Contents

frontiers in Neurology

EDITORIAL
published: 30 March 2022
doi: 10.3389/fneur.2022.887027

Editorial: Structural, Metabolic, and Physiologic MR Imaging to Study Glioblastomas

Manoj Kumar[1]*, *Ravi Prakash Reddy Nanga*[2] *and Sanjeev Chawla*[2]*

[1] Department of Neuroimaging and Intervention Radiology, National Institute of Mental Health and Neurosciences, Bangalore, India, [2] Department of Radiology, Perelman School of Medicine at the University of Pennsylvania, Philadelphia, PA, United States

Keywords: glioblastoma, radiomics, metabolic MR imaging, physiologic MR imaging, brain tumor

Editorial on the Research Topic

Structural, Metabolic, and Physiologic MR Imaging to Study Glioblastomas

Glioblastoma (GBM) is the most common and fatal primary malignant brain neoplasm in adults (1). The current standard of care treatment for GBM comprises maximal safe surgical resection followed by concurrent chemoradiation therapy (CCRT) and maintenance chemotherapy with temozolomide. Despite aggressive multimodal treatment the prognosis has remained poor (2). Recently, novel therapeutic approaches such as immunotherapy (3) and electric field therapy (4) have been introduced. Currently, several clinical trials are in progress to evaluate the safety profile and therapeutic efficacy of these new frontiers in fight against this devastating and life-threatening disease.

In the field of neuro-oncology, diagnosis and treatment response evaluation remain highly dependent on neuroimaging methods. While conventional magnetic resonance (MR) imaging sequences provide valuable information about the anatomic details and blood-brain-barrier (BBB) integrity, they lack specificity in characterizing gliomas as these neoplasms are highly heterogeneous both in spatial and temporal dimensions. Continuous developments in metabolic and physiologic MR imaging techniques have provided new insights into understanding underlying tumor biology and tumor microenvironment (5–9). Taken together, these techniques have been utilized to make the correct diagnosis, prognosis, evaluation of treatment response to both established and novel therapeutic regimens, and identification of new molecular targets for fostering the discovery of new treatments. Additionally, an emerging field of "*radiomics*" has the potential to change the ways in which advanced MR imaging techniques can be utilized more efficiently (10). This Research Topic was launched to collect high-quality manuscripts to advance our knowledge on clinical utilities, existing challenges, and limitations of using metabolic and physiologic MR imaging techniques in characterizing GBMs. A total of twelve manuscripts (nine original research and three review articles) were finally accepted for publication under this Research Topic.

ORIGINAL RESEARCH ARTICLES

The leakage of the contrast agent into the extravascular extracellular space (EES) during the dynamic susceptibility contrast (DSC)-perfusion MRI affects the signals produced in two

OPEN ACCESS

Edited and reviewed by:
Jan Kassubek,
University of Ulm, Germany

***Correspondence:**
Manoj Kumar
vermanojk@gmail.com
Sanjeev Chawla
sanjeev.chawla@pennmedicine.upenn.edu

Specialty section:
This article was submitted to Applied Neuroimaging, a section of the journal Frontiers in Neurology

Received: *01 March 2022*
Accepted: *08 March 2022*
Published: *30 March 2022*

Citation:
Kumar M, Nanga RPR and Chawla S (2022) Editorial: Structural, Metabolic, and Physiologic MR Imaging to Study Glioblastomas. Front. Neurol. 13:887027. doi: 10.3389/fneur.2022.887027

competing ways. Contrast agent shortens T_1 values of tissue water within the EES, thereby increasing MR signal results in an underestimation of cerebral blood volume (CBV). Conversely, T_2^*-effects caused by changes in susceptibility differences between EES and intravascular compartments reduce the MR signal, which does not recover to baseline during the DSC scan. This effect causes an overestimation of CBV. When the contrast agent extravasation is especially fast (as in malignant gliomas), CBV can be calculated as a negative estimate because the signal increase caused by T_1 effects is greater than the signal reduction due to T_2^* effects. To address this problem of contrast leakage in gliomas, Arzanforoosh et al. investigated the effect of two known leakage correction algorithms on CBV measurements. The leakage correction algorithms were based on unidirectional contrast agent transport from the intravascular to EES and bidirectional contrast agent transport between these two compartments. The investigators reported that in enhancing gliomas (situations when the BBB is generally disrupted), applying either of these two leakage correction methods decreased CBV measurements.

While exploring the potential associations between molecular features and patterns of contrast enhancement in GBMs, Yang et al. identified endothelial cell-enriched genes from transcriptome data from the GBM patients. The investigators demonstrated that contrast enhancement was associated with distinct vascular molecular imprints which is characterized by up-regulation of proinflammatory genes and de-regulation of BBB-related genes in endothelial cells. Moreover, high contrast enhancement was associated with poor patient prognosis and survival outcomes. Furthermore, enhancing volume/complete tumor volume ratio was significantly higher in the mesenchymal subtype of GBMs.

Huang et al. have suggested that neuroplasticity in patients with insular glioma might play a crucial role in preserving the neurological functions and subsequently improving the post-resection prognosis. The authors correlated gene expression profiles of isocitrate dehydrogenase (IDH), telomerase reverse transcriptase (TERT), and 1p19q codeletions with MRI volumetric data. The authors observed that IDH mutation status was the only genotype that was found to be associated with significant structural compensation in patients with insular glioma. These authors suggested that such findings may help in predicting neurocognitive and functional outcomes in patients with insular glioma undergoing surgical resection.

Adult supratentorial extra ventricular ependymoma (STEE) are rare neoplasms often misdiagnosed as high-grade gliomas (HGG) due to their similar characteristics on conventional neuroimaging. Safai et al. developed a machine learning-based diagnostic model by using quantitative radiomic signatures from multi-model MRI data for distinguishing adult STEE from HGG. The investigators reported that texture-based radiomic features from T_2-FLAIR images were vital in discriminating STEE from GBM. On the other hand, first-order features from T_2-weighted images and apparent diffusion coefficient (ADC) maps were consistently ranked higher in differentiating multiple tumor groups.

Against the backdrop of growing concern over patients' radiation exposure from undergoing 2-deoxy-2-[fluorine-18]fluoro-D-glucose (^{18}F-FDG)-positron emission tomography (PET) and other inherent shortcomings associated with this technique, Mangalore et al. explored whether high "b" value diffusion-weighted imaging (DWI) and ^{18}FDG-PET can provide similar or complementary information in detecting malignant brain lesions. The investigators obtained comparable sensitivity and specificity for DWI and ^{18}FDG-PET derived parameters and concluded that DWI could act as a surrogate for ^{18}FDG-PET in the diagnosis of brain tumors.

Despite the clinical importance, the accurate distinction between GBMs and solitary metastasis often remains challenging as these entities exhibit similar features on conventional neuroimaging. To address this issue, Zhang et al. designed a clinical trial and developed an integrated radiomics model by incorporating DWI-derived ADC and ^{18}FDG-PET derived standardized uptake value (SUV). This integrated model provided significantly better diagnostic performance than the utilization of any single imaging parameter alone.

Using multivariate logistic regression analyses, Wong et al. developed a mathematical model by incorporating multiple clinical features and imaging factors (DWI-derived ADC, contrast-enhancement size, whole-tumor size) in predicting malignant transformation of low-grade gliomas. This model had an accuracy of 84% from the training group and 85% from the validation group.

In a seminal study, Cui et al. investigated the prognostic significance of metabolic alterations from the postoperative peritumoral edematous zone (PEZ) in GBMs. Authors proposed that an elevated choline/N-acetyl aspartate ratio in PEZ can be considered as an independent risk factor for predicting early tumor recurrence. Moreover, this metabolic abnormality was also associated with poor prognosis and adverse clinical outcomes in patients with GBM.

By leveraging the utility of unique brain functional connectivity information obtained from resting-state functional MRI combined with machine learning algorithms, Lamichhane et al. classified GBM patients into short-term and long-term survival groups with high sensitivity and specificity (*precision prognostics*).

REVIEW ARTICLES

Determining the utility of interval imaging (i.e., imaging at pre-planned time-points to assess tumor status) in brain tumor management remains crucial in neuro-oncology. An expert panel comprising of professionals from data science, health economics, trial management of adult brain tumors, and patient representatives extensively reviewed the current evidence on the use of interval imaging to monitor brain tumors, and summarized their findings in a review article. The investigators concluded that evidence for the value of regular interval imaging is currently lacking. At the same time, the authors indicated that ongoing collaborative efforts might provide some evidence to optimize monitoring imaging biomarkers for the standard of care brain tumor management (Booth et al.).

A review article by Kumar et al. comprehensively showcased the clinical potentials of emerging metabolic imaging techniques such as 3D-echoplanar spectroscopic imaging, 2D-correlation spectroscopy, and chemical exchange saturation transfer imaging

in several neuro-oncologic applications. The authors also provided a detailed head-to-head comparison of these three metabolic techniques.

In another review article, Gonçalves et al. provided an overview on the potential utilities of advanced MR imaging techniques for studying pediatric GBMs.

Altogether, the studies published in this special issue have highlighted the importance of using advanced MR imaging and PET imaging techniques in redefining and reshaping our understanding of GBMs. Collectively, these techniques provide crucial information about the tumor microstructure, microvasculature, and metabolism, thus offering opportunities for optimizing clinical care of glioma patients. "*Radiomics*" is a relatively young and evolving field, and has a tremendous potential to provide meaningful biological understandings of imaging features for further improvement in the clinical outcomes and quality of life of these patients. However, the widespread translation of advanced imaging and radiomics methods into the routine clinical workflow has been slow due to some technical challenges. We believe that standardization as well as harmonization of data acquisition and post-processing procedures will strengthen the clinical applications and advance progress toward developing and validating new imaging biomarkers in the field of neuro-oncology.

AUTHOR CONTRIBUTIONS

All authors listed have made a substantial, direct, and intellectual contribution to the work and approved it for publication.

REFERENCES

1. Ostrom QT, Patil N, Cioffi G, Waite K, Kruchko C, Barnholtz-Sloan JS. CBTRUS statistical report: primary brain and other central nervous system tumors diagnosed in the United States in 2013-2017. *Neuro Oncol.* (2020) 22:iv1–iv96. doi: 10.1093/neuonc/noaa200
2. Rossignol J, Srinageshwar B, Dunbar GL. Current therapeutic strategies for glioblastoma. *Brain Sci.* (2019) 10:15. doi: 10.3390/brainsci10010015
3. Buerki RA, Chheda ZS, Okada H. Immunotherapy of primary brain tumors: facts and hopes. *Clin Cancer Res.* (2018) 24:5198–205. doi: 10.1158/1078-0432.CCR-17-2769
4. Wong ET, Lok E, Swanson KD. Alternating electric fields therapy for malignant gliomas: from bench observation to clinical reality. *Prog Neurol Surg.* (2018) 32:180–95. doi: 10.1159/000469690
5. Chawla S, Bukhari S, Afridi OM, Wang S, Yadav SK, Akbari H, et al. Metabolic and physiologic MR imaging in distinguishing true progression from pseudo-progression in patients with glioblastoma. *NMR Biomed.* (2022) 2:e4719. doi: 10.1002/nbm.4719
6. Chawla S, Wang S, Kim S, Sheriff S, Lee P, Rengan R, et al. Radiation injury to the normal brain measured by 3D-Echo-planar spectroscopic imaging and diffusion tensor imaging: initial experience: assessment of radiation injury to normal brain. *J Neuroimaging.* (2015) 25:97–104. doi: 10.1111/jon.12070
7. Chawla S, Shehu V, Gupta PK, Nath K, Poptani H. Physiological imaging methods for evaluating response to immunotherapies in glioblastomas. *Int J Mol Sci.* (2021) 22:3867. doi: 10.3390/ijms22083867
8. Chawla S, Wang S, Mohan S, Nasrallah M, Verma G, Brem S, et al. Differentiation of brain infection from necrotic glioblastoma using combined analysis of diffusion and perfusion MRI. *J Magn Reson Imaging.* (2019) 49:184–194. doi: 10.1002/jmri.26053
9. Neal A, Moffat BA, Stein JM, Nanga RPR, Desmond P, Shinohara RT, et al. Glutamate weighted imaging contrast in gliomas with 7 Tesla magnetic resonance imaging. *NeuroImage Clin.* (2019) 22:101694. doi: 10.1016/j.nicl.2019.101694
10. Chaddad A, Kucharczyk MJ, Daniel P, Sabri S, Jean-Claude BJ, Niazi T, et al. Radiomics in Glioblastoma: current status and challenges facing clinical implementation. *Front Oncol.* (2019) 9:374. doi: 10.3389/fonc.2019.00374

Conflict of Interest: The authors declare that the research was conducted in the absence of any commercial or financial relationships that could be construed as a potential conflict of interest.

frontiers in Neurology

ORIGINAL RESEARCH
published: 04 December 2020
doi: 10.3389/fneur.2020.592155

Higher Cho/NAA Ratio in Postoperative Peritumoral Edema Zone Is Associated With Earlier Recurrence of Glioblastoma

Yong Cui[1,2], *Wei Zeng*[3], *Haihui Jiang*[1,2], *Xiaohui Ren*[1,2], *Song Lin*[1,2], *Yanzhu Fan*[1,2], *Yapeng Liu*[1,2] *and Jizong Zhao*[1,2]*

[1] Department of Neurosurgery, Beijing Tiantan Hospital, Capital Medical University, Beijing, China, [2] National Clinical Research Center for Neurological Diseases, Center of Brain Tumor, Beijing Institute for Brain Disorders and Beijing Key Laboratory of Brain Tumor, Beijing, China, [3] Department of Neurosurgery, Beijing Electric Power Hospital, Beijing, China

Objective: To explore the prognostic significance of metabolic parameters in postoperative peritumoral edema zone (PEZ) of patients with glioblastoma (GBM) based on proton magnetic resonance spectroscopy (MRS).

Methods: The postoperative MRS data of 67 patients with GBM from Beijing Tiantan Hospital were retrospectively reviewed. Metabolite ratios including Cho/NAA, Cho/Cr, and NAA/Cr in both postoperative PEZ and contralateral normal brain region were recorded. Log-rank analysis and Cox regression model were used to identify parameters correlated with progression-free survival (PFS) and overall survival (OS).

Results: Compared with the contralateral normal brain region, postoperative PEZ showed a lower ratio of NAA/Cr (1.20 ± 0.42 vs. 1.81 ± 0.48, $P < 0.001$), and higher ratios of Cho/Cr and Cho/NAA (1.36 ± 0.44 vs. 1.02 ± 0.27, $P < 0.001$ and 1.32 ± 0.59 vs. 0.57 ± 0.14, $P < 0.001$). Both the ratios of Cho/NAA and NAA/Cr were identified as prognostic factors in univariate analysis ($P < 0.05$), while only Cho/NAA ≥ 1.31 was further confirmed as an independent risk factor for early recurrence in the Cox regression model ($P < 0.01$). According to the factors of MGMT promoter unmethylation, without radiotherapy and Cho/NAA ≥ 1.31, a prognostic scoring scale for GBM was established, which could divide patients into low-risk, moderate-risk, and high-risk groups. There was a significant difference of survival rate between the three groups ($P < 0.001$).

Conclusions: Higher Cho/NAA ratio in the postoperative PEZ of GBM predicts earlier recurrence and is associated with poor prognosis. The prognostic scoring scale based on clinical, molecular and metabolic parameters of patients with GBM can help doctors to make more precise prediction of survival time and to adjust therapeutic regimens.

Keywords: glioblastoma, magnetic resonance spectroscopy, choline abnormality, peritumoral edema zone, recurrence, survival

OPEN ACCESS

Edited by:
Manoj Kumar, National Institute of Mental Health and Neurosciences (NIMHANS), India

Reviewed by:
Pradeep Kumar Gupta, University of Pennsylvania, United States
Sanjeev Chawla, University of Pennsylvania, United States

***Correspondence:**
Jizong Zhao
zhaojz205@163.com

Specialty section:
This article was submitted to Neuro-Oncology and Neurosurgical Oncology, a section of the journal Frontiers in Neurology

Received: *06 August 2020*
Accepted: *17 November 2020*
Published: *04 December 2020*

Citation:
Cui Y, Zeng W, Jiang H, Ren X, Lin S, Fan Y, Liu Y and Zhao J (2020) Higher Cho/NAA Ratio in Postoperative Peritumoral Edema Zone Is Associated With Earlier Recurrence of Glioblastoma. Front. Neurol. 11:592155. doi: 10.3389/fneur.2020.592155

INTRODUCTION

Glioblastoma (GBM) is the most common primary malignant tumor of central nervous system (1). It is charactered by rapid proliferation, strong invasion to normal tissue, and dismal prognosis (2). Surgical resection plays a vital role in the treatment protocol of patients with GBM (3, 4). And the resection degree has been proved to be closely correlated with patient's clinical outcome (4). Although the gross-total resection (GTR) evaluated from contrast-enhanced T1 weighted imaging can be achieved in nowadays (5, 6), the residual T2 or fluid attenuated inversion recovery (FLAIR) abnormal signal region surrounding the surgical cavity is frequently found in routine clinical practice (7, 8). The components of this region are quite complicated and studies committed to addressing this issue are relatively rare (9). It may be a combined consequence of surgical injury, tumor cells invasion, or even demyelination, etc., which cannot be differentiated normally by routine magnetic resonance imaging (MRI) (10–13).

1H magnetic resonance spectroscopy (1H-MRS) is widely used to non-invasively detect the biochemical index and metabolic changes of intracranial lesions, which plays a vital role in making precise diagnosis and predicting the prognosis of patients (14, 15). 1H-MRS can reinforce the diagnostic confidence in the following three situations in which conventional MRI may be of limited significance: (1) the distinction of neoplastic and non-neoplastic intracranial lesions (16, 17); (2) the differentiation between tumor recurrence and radiation necrosis (18); (3) the role in biopsy guidance and radiotherapy planning (19, 20).

Therefore, in this study, the residual T2/FLAIR abnormal signal region surrounding the surgical cavity was defined as postoperative peritumoral edema zone (PEZ), which was the major cause of tumor recurrence of GBM. Our primary objective was to compare the metabolic parameters between postoperative PEZ and contralateral region, and further explore the clinical significance of these properties in predicting tumor recurrence.

MATERIALS AND METHODS

Patients Cohort

A total number of 67 patients with diagnosis of GBM were surgically treated in the Neurosurgery department IV of Beijing Tiantan Hospital from January 2014 to August 2015. All patients underwent routine and enhanced MRI and MRS within 48–72 h after operation. Volumetric calculation of tumor has been fully described in a prior study (3). The extent of resection (EOR) was evaluated by two experienced neuro-radiologists who were blinded to clinical information of patients, according to the following equation: (preoperative tumor volume – postoperative tumor volume) / preoperative tumor volume. The EOR for each patient was classified as either GTR (>99%), near-total resection (NTR) (95–99%), or subtotal resection (STR) (80–95%). All pathological slides were morphologically examined and graded according to the World Health Organization (WHO) Classification of Tumors of the Central Nervous System (21, 22). Once pathological diagnosis was confirmed, all the patients were recommended to receive standard Stupp protocol (23). Briefly, radiotherapy divided into 30 daily fractions of 2 Gy each was delivered to patients within 1 month after operation. Concomitant chemotherapy consisted of temozolomide (TMZ) at a dose of 75 mg/m^2/d was given during the whole procedure of radiotherapy. After a 4-weeks break, patients would receive six cycles of adjuvant TMZ at a dose of 150–200 mg/m^2/d for 5 days in every 28 days. Unfortunately, seven patients, in this study, quit the continued treatment after operation for personal reason.

Acquisition of MRI Data

All MRI data acquisition was performed on a 3.0 Tesla scanner (Siemens Magnetom Trio Tim, Germany) (**Figure 1**). The routine sequences included T1-weighted imaging, T2-weighted imaging, and contrast-enhanced imaging. The specific scanning protocol of axial/sagittal T1Flair was field of view (FOV) 240 × 240 mm^2, matrix 256 × 256, slice thickness 5 mm, spacing 1 mm, time of repetition (TR) 1,500 ms, time of echo (TE) 13 ms, echo train length (ETL) 5, average 1, and scan time of 1 min and 23 s. The specific scanning protocol of Axial T2Flair was FOV 240 × 240 mm^2, matrix 256 × 180, slice thickness 5 mm, spacing 1 mm, TR 8,000 ms, TE 13 ms, time of inversion (TI) 2,500 ms, ETL 17, average 1, and scan time of 1 min and 48 s. 1H-MRS data was acquired using a 3D MRS sequence with point-resolved spectroscopy (PRESS). Acquisition parameters were as follows: TE 135 ms, TR 1,700 ms, FOV 160 × 160 mm^2, slice thickness 15 mm, voxel sizes 10 × 10 × 15 mm^3, average 3, and scan time of 6 min and 53 s. Spectral bandwidth was 2,000 Hz and number of points was 1,024 points. The postoperative PEZ was defined as target region and the contralateral mirror area of target region was served as reference, avoiding bone, subcutaneous fat, hemorrhage, and infarction. Six voxels per case were placed in the target region in order to cover as much of the image abnormality as possible. For cases with residual tumor, at least one voxel was placed on the enhanced region. The relative amounts (area under the curve) of the signals from N-acetyl-aspartate (NAA), choline (Cho), and creatine (Cr) in the target and reference voxels were measured. The MRS detection mentioned above was performed by two independent neuro-radiologists who were blinded to the outcomes of patients. The mean ratios of Cho/NAA, Cho/Cr, NAA/Cr of 12 voxels from two neuro-radiologists was calculated for each patient.

Follow-Up

Patients were followed up using MRI scans with an interval of 3 months after operation, or 1 month if necessary. Multimodal MR including perfusion, diffusion and MRS was used to rule out radiation necrosis and pseudoprogression. All the patients enrolled in this study would be followed until death. Progression-free survival (PFS) was defined as the time period from the date of operation to date of tumor recurrence or last follow-up. Overall survival (OS) was defined as the time period from the date of operation to the date of death or last follow-up. At the time of data analysis, the median follow-up of this cohort was 44.0 (range: 3.0–58.0) months, and there were 59 (88.1%) patients progressed and 47 (70.1%) patients died.

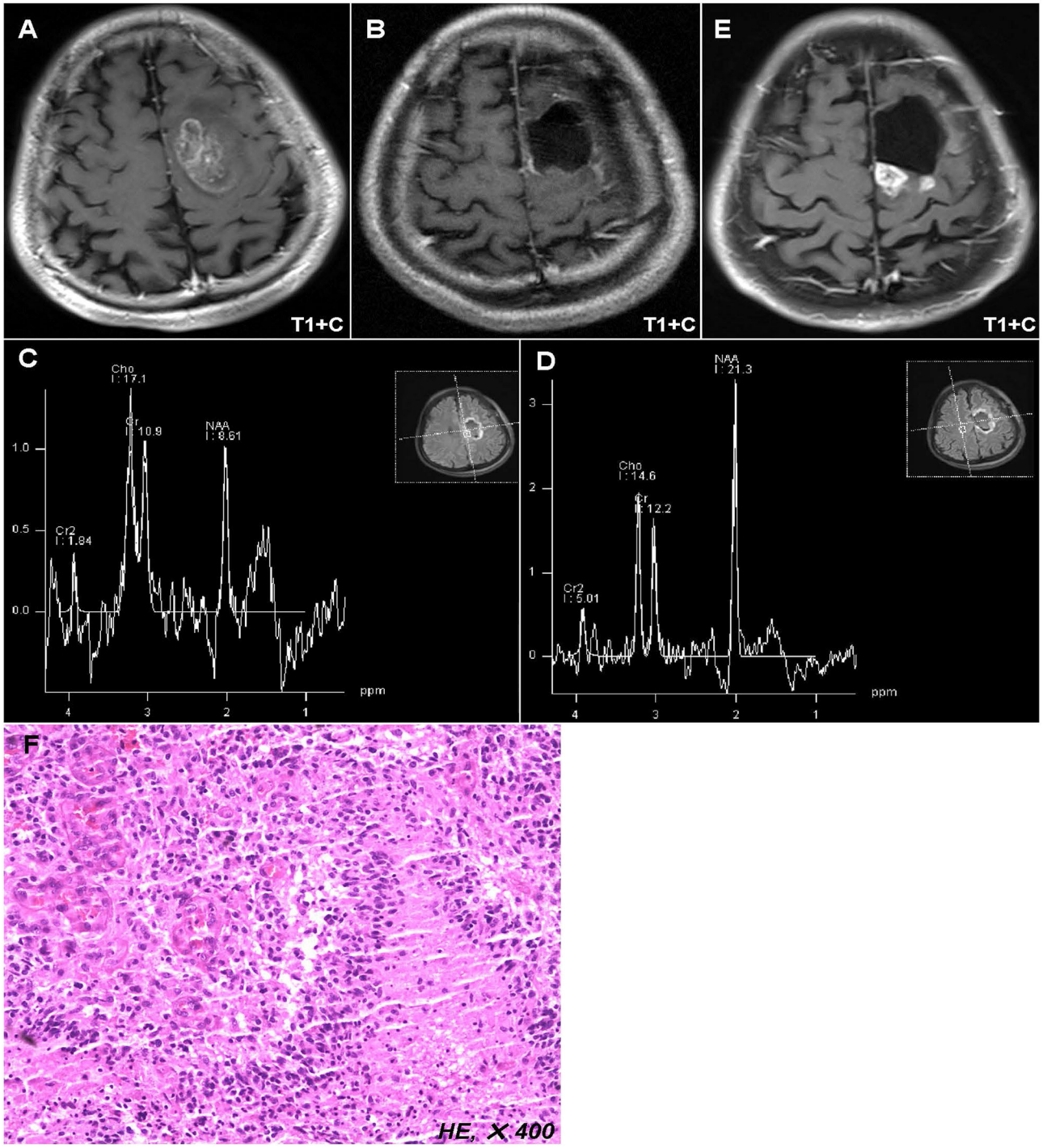

FIGURE 1 | Representative case of this study. Preoperative MR images showed a lesion located in the left anterior central gyrus and supplementary motor area **(A)**. Postoperative MR images displayed that the tumor has been totally removed **(B)**, while the postoperative peritumoral zone showed a higher ratio of Cho/NAA (>1.31) than that in the contralateral region **(C,D)**. Twelve months after operation, the MR images showed a new enhanced lesion in the peritumoral zone **(E)**, which was further confirmed as tumor recurrence by biopsy **(F)**.

Statistical Analysis

Summary of data are presented as the mean ± *SD* for parametric variables and percentage for categorical variables. For the comparison of the metabolic ratios between target and reference regions, paired *t*-test was performed. Receiver operating characteristic (ROC) curves were constructed and

TABLE 1 | Baseline characteristics for all patients with GBM.

Characteristics	No. of patients (%)
Age (years)	
Mean ± *SD*	47.1 ± 11.6
Gender	
Male	41 (61.2)
Female	26 (38.8)
Tumor location	
1 lobe	23 (34.3)
2 lobes	28 (41.8)
3 lobes	12 (17.9)
4 lobes	4 (6.0)
Tumor size (cm)	
Mean ± *SD*	5.1 ± 1.5
KPS score	
Median (range)	80 (30–90)
Extent of resection	
GTR	49 (73.1)
NTR	13 (19.4)
STR	5 (7.5)
Chemotherapy	
Yes	60 (89.6)
Radiotherapy	
Yes	60 (89.6)
1p/19q codeletion	
Yes	0 (0.0)
IDH mutation	
Yes	6 (9.0)
MGMT methylation	
Yes	35 (52.2)

SD, standard deviation; KPS, Karnofsky performance scale; GTR, gross-total resection; NTR, near-total resection; STR, subtotal resection; IDH, isocitrate dehydrogenase; MGMT, O^6-methylguanine-DNA-methyltransferase.

were used to determine the area under the curve (AUC) and the optimal cutoff of metabolic ratios in predicting recurrence. Survival as a function of time was plotted using the Kaplan-Meier method, and the Log-rank analysis was used to compare Kaplan-Meier plots. Multivariate proportional hazard regression analysis was used to identify factors associated with PFS and OS. In this analysis, all variables associated with survival in univariate analysis ($P < 0.05$) were included in a step-wise multivariate proportional hazard regression model. All data were analyzed with SPSS software package version 22.0, IBM Corporation, Armonk, NY, USA. Probability values were obtained using 2-sided tests, with statistical significance defined as $P < 0.05$.

RESULTS

Overall Characteristics of Study Population

The baseline characteristics of the 67 patients with supratentorial GBM were summarized in **Table 1**. There were 41 (61.2%) male and 26 (38.8%) female patients with a mean age of 47.1 ± 11.6 years). Of the 67 patients, 23 (34.3%) with tumor located in one lobe, 28 (41.8%) in two lobes, 12 (17.9%) in three lobes, and 4 (6.0%) in four lobes. GTR was achieved in 49 (73.1%) patients, NTR in 13 (19.4%) patients, and STR in 5 (7.5%) patients. Chromosome 1p/19q was intact in all detected cases and only 6 (9.0%) patients harbored isocitrate dehydrogenase (IDH) mutation. Thirty-five (52.2%) patients were identified with O^6-methylguanine-DNA-methyltransferase (MGMT) promoter methylation.

Comparisons of Metabolic Parameters Between PEZ and Contralateral Brain Region

The mean ratios of Cho/NAA, Cho/Cr, and NAA/Cr in the postoperative PEZ (target region) were 1.32 ± 0.59, 1.36 ± 0.44, and 1.20 ± 0.42, respectively; while the mean ratios of Cho/NAA, Cho/Cr and NAA/Cr in the contralateral brain region (reference region) were 0.57 ± 0.14, 1.02 ± 0.27, and 1.81 ± 0.48, respectively (**Supplementary Table 1**). Compared with the reference region, ratios of Cho/NAA and Cho/Cr in the target region were remarkably increased, but the ratio of NAA/Cr was significantly decreased ($P < 0.001$, **Figure 2**).

Values of Metabolic Parameters in Predicting Tumor Recurrence

We used ROC curves to determine the optimal cutoff ratios of Cho/NAA, Cho/Cr, and NAA/Cr in predicting tumor recurrence. As the median PFS of our cohort was 10.0 months, 10-months recurrence was selected to serve as the observation point. According to the results of ROC analyses, the cutoff ratio of Cho/NAA was 1.31 with an AUC of 0.731 (95% confidence interval [CI]: 0.607–0.856, $P = 0.001$). The sensitivity and specificity were 82.4 and 66.7% for recurrence, respectively. The cutoff ratio of Cho/Cr was 1.43 with an AUC of 0.542 (95% CI: 0.402–0.683, $P = 0.551$). The sensitivity and specificity were 73.5 and 45.5% for recurrence, respectively. The cutoff ratio of NAA/Cr was 1.10 with an AUC of 0.754 (95% CI: 0.635–0.872, $P < 0.001$). The sensitivity and specificity were 76.5 and 69.7% for recurrence, respectively (**Figure 3**).

Univariate and Multivariate Survival Analysis

Univariate analysis showed that EOR, radiotherapy, chemotherapy, MGMT promoter methylation, and ratios of Cho/NAA and NAA/Cr were correlated with PFS and OS ($P < 0.05$) (**Table 2**). All these factors correlated with PFS and OS were further enrolled in Cox multivariate analysis. In the Cox proportional hazards regression model, radiotherapy, MGMT promoter methylation and Cho/NAA ratio were confirmed as independent factors associated with both PFS (hazard ratio [HR] = 0.417, 95% CI: 0.174–0.996, $P = 0.049$; HR = 0.401, 95% CI: 0.233–0.690, $P = 0.001$; HR = 2.959, 95% CI: 1.706–5.132, $P < 0.001$, respectively) and OS (HR = 0.083, 95% CI: 0.030–0.230, $P < 0.001$; HR = 0.290, 95% CI: 0.156–0.539, $P < 0.001$; HR = 2.755, 95% CI: 1.512–5.020, $P = 0.001$, respectively) (**Table 2**).

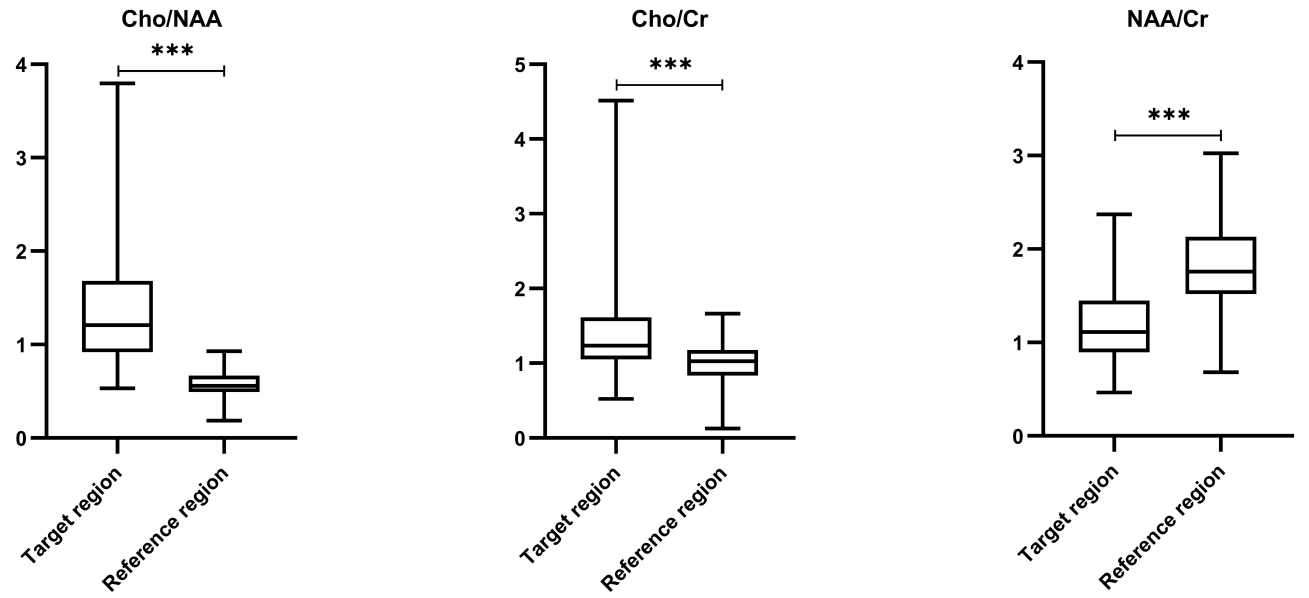

FIGURE 2 | Comparisons of metabolic ratios between target and reference regions by paired *t*-test. Comparing with reference region, ratios of Cho/NAA (0.57 ± 0.14 vs. 1.32 ± 0.59) and Cho/Cr (1.02 ± 0.27 vs. 1.36 ± 0.44) in the target region were remarkably increased, but the ratio of NAA/Cr (1.81 ± 0.48 vs. 1.20 ± 0.42) was significantly decreased ($P < 0.001$). *** $p < 0.001$.

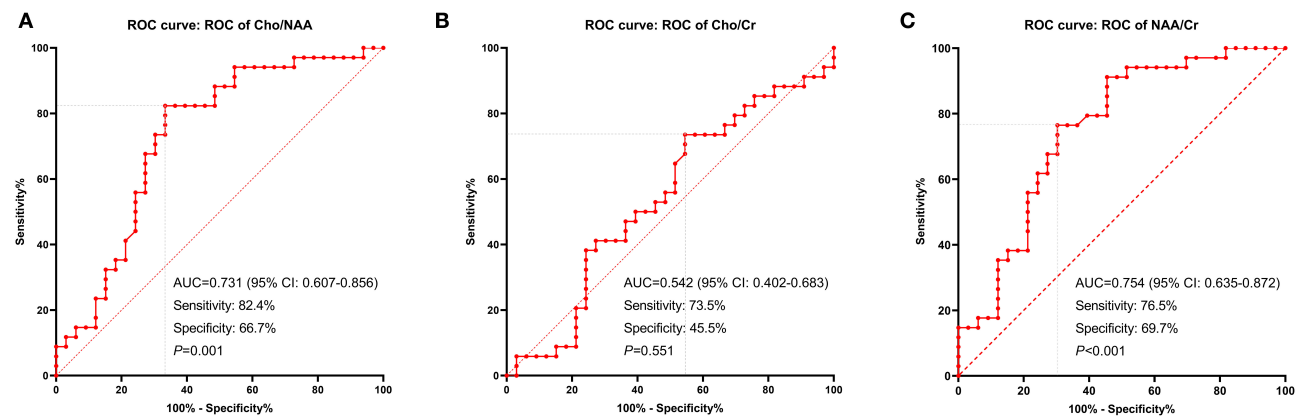

FIGURE 3 | ROC curves displaying the metabolic ratios: Cho/NAA **(A)**, Cho/Cr **(B)**, and NAA/Cr **(C)** in recurrence prediction. The cutoff ratio of Cho/NAA was 1.31 with an area under the curve (AUC) of 0.731 ($P = 0.001$). The cutoff ratio of Cho/Cr was 1.43 with an AUC of 0.542 ($P = 0.551$). The cutoff ratio of NAA/Cr was 1.10 with an AUC of 0.754 ($P < 0.001$).

A Proposed Prognostic Scoring Scale for GBM

According to the independent prognostic factors identified by the multivariate Cox proportional hazards regression model, a prognostic scoring scale was thereby proposed. Briefly, one point was assigned for each of the prognostic risk factors (MGMT promoter unmethylation, without radiotherapy, and Cho/NAA $\geq$ 1.31). Accordingly, the patients would get a score ranging from 0 to 3 points. Then patients with a score of 0, 1, and equal or more than 2, could be respectively divided into low-risk, moderate-risk, and high-risk subgroups. The median PFS for patients in low-risk, moderate-risk and high-risk groups was 18.0, 11.0, and 5.5 months, respectively, which conferred a significant difference according to the log-rank analysis ($P < 0.001$) (**Figure 4A**). Meanwhile, a similar survival tendency was also observed in terms of OS among the three subgroups ($P < 0.001$) (**Figure 4B**).

Illustrative Case

A 42-years-old male who complained of right limb weakness for 2 months was admitted in our hospital with radiological diagnosis of high-grade glioma. Neurological examination found that the muscle strength of right limbs was grade IV. Radiological result showed a round-like lesion with contrast enhancement in the left anterior central gyrus and supplementary motor

TABLE 2 | Univariate and multivariate survival analysis in all patients.

Variables	Univariate analysis		*P*-value	Multivariate analysis		*P*-value
	HR	95% CI		HR	95% CI	
Factors associated with PFS						
Age (≥50/<50 years)	0.923	0.544–1.567	0.767			
Gender (male/female)	1.142	0.673–1.938	0.623			
Tumor size (≥4/<4 cm)	1.765	0.929–3.352	0.082			
KPS score (≥70/<70)	0.792	0.387–1.621	0.524			
Tumor location (≥3/<3 lobes)	1.604	0.887–2.898	0.118			
EOR (GTR/No-GTR)	0.464	0.263–0.821	**0.008**			
Radiotherapy (yes/no)	0.326	0.141–0.755	**0.009**	0.417	0.174–0.996	**0.049**
Chemotherapy (yes/no)	0.325	0.142–0.747	**0.008**			
MGMT methylation (yes/no)	0.474	0.280–0.802	**0.005**	0.401	0.233–0.690	**0.001**
IDH mutation (yes/no)	0.925	0.368–2.328	0.869			
Cho/NAA (≥1.31/<1.31)	2.674	1.578–4.529	**<0.001**	2.959	1.706–5.132	**<0.001**
Cho/Cr (≥1.43/<1.43)	1.503	0.884–2.554	0.132			
NAA/Cr (≥1.10/<1.10)	0.379	0.224–0.641	**<0.001**			
Factors associated with OS						
Age (≥50/<50 years)	0.964	0.533–1.742	0.903			
Gender (male/female)	1.041	0.577–1.877	0.894			
Tumor size (≥6/<6 cm)	2.045	0.951–4.401	0.067			
KPS score (≥70/<70)	0.919	0.390–2.169	0.847			
Tumor location (≥3/<3 lobes)	1.731	0.923–3.247	0.087			
EOR (GTR/No-GTR)	0.482	0.258–0.900	**0.022**			
Radiotherapy (yes/no)	0.075	0.027–0.206	**<0.001**	0.083	0.030–0.230	**<0.001**
Chemotherapy (yes/no)	0.249	0.109–0.571	**0.001**			
MGMT methylation (yes/no)	0.311	0.169–0.572	**<0.001**	0.290	0.156–0.539	**<0.001**
IDH mutation (yes/no)	0.510	0.158–1.645	0.260			
Cho/NAA (≥1.31/<1.31)	2.502	1.396–4.486	**0.002**	2.755	1.512–5.020	**0.001**
Cho/Cr (≥1.43/<1.43)	1.243	0.689–2.243	0.469			
NAA/Cr (≥1.10/<1.10)	0.412	0.228–0.746	**0.003**			

HR, hazard ratio; CI, confidence interval; KPS, Karnofsky performance scale; EOR, extent of resection; GTR, gross-total resection; MGMT, O6-methylguanine-DNA-methyltransferase; IDH, isocitrate dehydrogenase PFS, progression-free survival; OS, overall survival; NAA, N-acetyl-aspartate; Cho, choline; Cr, creatine.
Bold value represents $p < 0.05$.

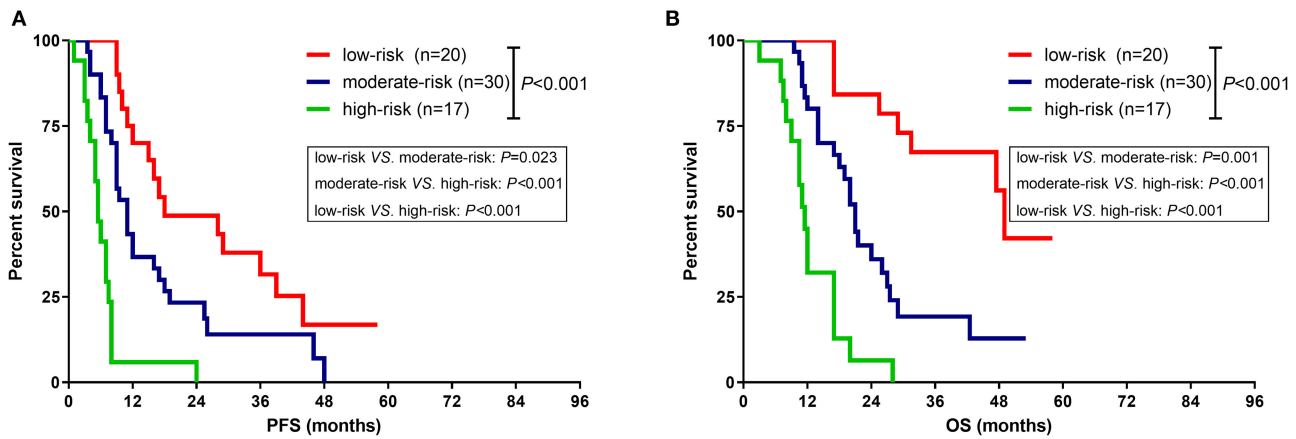

FIGURE 4 | Comparison of survival rate between different subgroups based on the prognostic scoring scale. **(A)** The median PFS for patients in low-risk, moderate-risk and high-risk groups was 18.0, 11.0, and 5.5 months, respectively, which imparted a significant difference ($P < 0.001$). **(B)** The median OS for patients in low-risk, moderate-risk and high-risk groups was 49.0, 21.0, and 11.5 months, respectively, which imparted a significant difference ($P < 0.001$).

area (**Figure 1A**). The patient underwent surgical resection in our hospital. Postoperative MR implied the enhanced tumor was totally removed (**Figure 1B**), while the peritumoral zone with abnormal T2/FLAIR signal showed a higher ratio of Cho/NAA (>1.31) than that in the contralateral region (**Figures 1C,D**). After operation, the patient received concurrent chemoradiotherapy and six cycles adjuvant chemotherapy. Twelve months post of operation, the patient was hospitalized again in our department because of seizures. The MR images showed a new enhanced lesion in the peritumoral zone where initially conferred a higher ratio of Cho/NAA (**Figure 1E**). To rule out radiation necrosis and pseudoprogression, stereotactic biopsy was performed. And final result confirmed the tumor recurrence (**Figure 1F**).

DISCUSSION

GBM, unlike the circumscribed glioma, commonly spreads along the axonal, vascular or subarachnoid space (24). The infiltrated extent of GBM is traditionally refer to the central region on contrast-enhanced T1-weighted images which includes both enhancement and necrosis. However, this central region, to a certain degree, is smaller than the truly infiltrated extent of tumor (25, 26). In contrast, the abnormal region with hyper intensity signal on T2/FLAIR image which reflects a combined consequence of tumor and edema, is larger than the truly infiltrated extent of tumor (27, 28). It's well-established that peritumoral edema is frequently presented in malignant glioma, metastases, and meningioma (29–31). The degree and range of peritumoral edema is correlated with tumor malignancy, and can be used to predict the prognosis of patients (32). Therefore, the peritumoral edema zone (PEZ) is worthy to make further exploration and research.

Given the PEZ was infiltrated with tumor cells which has been validated by histopathological examination, several studies tried to explore the clinical implication of extensively resecting PEZ (3, 33). Li et al., in 2016, conducted a study based on a larger single-center series of GBM patients in order to disclose the association between EOR and prognosis and found that additional resection of PEZ could prolong the survival of patients with GBM (33). Meanwhile, our previous study showed that patients with proliferation-dominant and/or IDH-mutant high-grade astrocytoma could benefit from extensive resection of the FLAIR abnormality region (3). However, current assessment of EOR of patients with GBM is mainly dependent on contrast-enhanced T1-weighted images. Patients who achieved complete removal of the contrast-enhanced region can be defined as gross-total resection. It indicates that the PEZ which is considered as the major origin of tumor recurrence has been remained during operation. How to monitor the change of tumor burden in PEZ is of great significance.

MRS is an imaging technique which can non-invasively detect the metabolism and biochemical changes of tissue. It has been used to differentiate tumor from edema in the PEZ of intracranial malignancies (34, 35). In this study, we systematically analyzed the metabolic changes in postoperative PEZ of patients with GBM. To our knowledge, it's the first study that devoted to disclosing the relationship between metabolic parameters in postoperative PEZ and tumor recurrence. The most important finding was that higher Cho/NAA ratio in postoperative PEZ was associated with early recurrence and the prognostic implication of Cho/NAA has been further confirmed in multivariate analysis. Theoretically, a higher ratio of Cho/NAA implies a more destruction of neuron and a stronger activity of tumor cells (36). This is the reason for higher Cho/NAA ratio in postoperative PEZ harboring poor prognosis. Cordova and colleagues maintained that Cho/NAA could not only identify regions at high risk for contrast-enhancing recurrence, but also show a significant association with PFS in the cohort of GBM patients (37). Tarnawski et al. (38) prospectively analyzed the postoperative tumor bed of 51 patients with malignant gliomas using MRS and found that the ratios of Cho/Cr, Cho/NAA, and myo-inosytol/Cr in PEZ were remarkably increased, but the ratio of NAA/Cr was significantly decreased, which was consistent with our results. They also reported that Lac/NAA > 2 was a strong independent prognostic risk factor (38). In 2015, Tolia et al. explored the prognostic value of MRS metabolites in postoperative irradiated high-grade gliomas and found that Cho/Cr $\geq$ 2 was associated with earlier recurrence (39). All these results support the hypothesis that substantial tumor cells do exist in PEZ and spectroscopy can provide accurate tumor metabolism information for physicians to better control gliomas.

The second valuable and interesting finding in our study was that patients could be divided into low-risk, moderate-risk, and high-risk subgroups with distinct survival time according to a scoring scale based on the prognostic parameters of radiotherapy, MGMT promoter, and ratio of Cho/NAA. This prognostic scoring scale could lead to an incremental increase in the strength of survival prediction. Li et al. built a survival tree based on older age, larger contrast enhancement, higher ratios of Cho/Cr, Cho/NAA, and lactate/lipid, and lower ratio of Cr/NAA in order to better predict survival (40). But the operation of this survival tree was complicated which limited the use of it in clinical practice. Similarly, TCGA Glioma Phenotype Research Group established a model based on clinical, imaging, and genetic variables which showed the highest accuracy in predicting survival (41). However, the AUC of this predicting model was only 0.679 ± 0.068, which implied a low stability and reliability. In 2019, Gandia-Gonzalez et al. proposed an OS prediction model based on the metabolic markers for patients with glioma, which could do help to make more precise therapeutic decisions (42). Unfortunately, molecular biomarkers have not been included in the model. Therefore, our presented model seems to be relatively stable, easy to use, and more practical.

This study has limitations common to other retrospectively designed studies. First, the sample size is relatively small. However, even given the small sample size, the analytical methods are robust enough to describe the significance of metabolic parameters in predicting tumor recurrence. Second, some patients still fail to reach endpoint event. In the future, we will continue this study until all patients died in order to recheck our results and conclusions. Moreover, several important molecular biomarkers, such as telomerase reverse

transcriptase (TERT), phosphate and tension homology deleted on chromosome ten (PTEN), etc., have not been included in our prognostic scoring scale. In spite of these limitations, our study reported some interesting and important findings which might help to extend the application of MRS in the assessment of early recurrence and prognosis prediction of patients with GBM.

CONCLUSIONS

The ratio of Cho/NAA $\geq$ 1.31 in postoperative PEZ predicts earlier recurrence and is associated with poor prognosis. The prognostic scoring scale based on clinical, molecular and metabolic parameters of patients with GBM can contribute to making more precise prediction of survival time and adjusting therapeutic regimens timely.

DATA AVAILABILITY STATEMENT

All data supporting the conclusions of this article are available on request from any qualified investigator.

ETHICS STATEMENT

The studies involving human participants were reviewed and approved by Institutional review board of Capital Medical University. The patients/participants provided their written informed consent to participate in this study.

AUTHOR CONTRIBUTIONS

YC, WZ, and XR: acquisition of data. YC, WZ, and HJ: analysis and interpretation of data and drafting the article. YC, HJ, and XR: statistical analysis. SL and YC: funding acquisition. YC and JZ: conception and design. JZ: study supervision. All authors contributed to the article and approved the submitted version.

FUNDING

This work was supported by the National Natural Science Foundation of China (81771309) and the Capital's Funds for Health Improvement and Research (2020-2-1075).

ACKNOWLEDGMENTS

The authors would like to thank Dr. Gehong Dong, and Dr. Guang Li, Department of Pathology, Beijing Tiantan Hospital, Capital Medical University, for pathology diagnosis. We also appreciate Dr. Hongyan Chen and Prof. Xuzhu Chen, Department of Neuroradiology, Beijing Tiantan Hospital, Capital Medical University, for the evaluation of EOR and metabolic ratios.

SUPPLEMENTARY MATERIAL

The Supplementary Material for this article can be found online at: https://www.frontiersin.org/articles/10.3389/fneur.2020.592155/full#supplementary-material

REFERENCES

1. Ostrom QT, Cioffi G, Gittleman H, Patil N, Waite K, Kruchko C, et al. CBTRUS statistical report: primary brain and other central nervous system tumors diagnosed in the United States in 2012–2016. *Neuro Oncol.* (2019) 21(Suppl.5):v1. doi: 10.1093/neuonc/noz150
2. Alexander BM, Cloughesy TF. Adult glioblastoma. *J Clin Oncol.* (2017) 35:2402–9. doi: 10.1200/JCO.2017.73.0119
3. Jiang H, Cui Y, Liu X, Ren X, Li M, Lin S. Proliferation-dominant high-grade astrocytoma: survival benefit associated with extensive resection of FLAIR abnormality region. *J Neurosurg.* (2019) 132:998–1005. doi: 10.3171/2018.12.JNS182775
4. Brown TJ, Brennan MC, Li M, Church EW, Brandmeir NJ, Rakszawski KL, et al. Association of the extent of resection with survival in glioblastoma: a systematic review and meta-analysis. *JAMA Oncol.* (2016) 2:1460–9. doi: 10.1001/jamaoncol.2016.1373
5. Suero Molina E, Wolfer J, Ewelt C, Ehrhardt A, Brokinkel B, Stummer W. Dual-labeling with 5-aminolevulinic acid and fluorescein for fluorescence-guided resection of high-grade gliomas: technical note. *J Neurosurg.* (2018) 128:399–405. doi: 10.3171/2016.11.JNS161072
6. D'Amico RS, Kennedy BC, Bruce JN. Neurosurgical oncology: advances in operative technologies and adjuncts. *J Neurooncol.* (2014) 119:451–63. doi: 10.1007/s11060-014-1493-3
7. Yano H, Nakayama N, Ohe N, Miwa K, Shinoda J, Iwama T. Pathological analysis of the surgical margins of resected glioblastomas excised using photodynamic visualization with both 5-aminolevulinic acid and fluorescein sodium. *J Neurooncol.* (2017) 133:389–97. doi: 10.1007/s11060-017-2445-5
8. Elson A, Bovi J, Siker M, Schultz C, Paulson E. Evaluation of absolute and normalized apparent diffusion coefficient (ADC) values within the post-operative T2/FLAIR volume as adverse prognostic indicators in glioblastoma. *J Neurooncol.* (2015) 122:549–58. doi: 10.1007/s11060-015-1743-z
9. Yan JL, Li C, Boonzaier NR, Fountain DM, Larkin TJ, Matys T, et al. Multimodal MRI characteristics of the glioblastoma infiltration beyond contrast enhancement. *Ther Adv Neurol Disord.* (2019) 12:1756286419844664. doi: 10.1177/1756286419844664
10. Lama G, Mangiola A, Anile C, Sabatino G, de Bonis P, Lauriola L, et al. Activated ERK1/2 expression in glioblastoma multiforme and in peritumor tissue. *Int J Oncol.* (2007) 30:1333–42. doi: 10.3892/ijo.30.6.1333
11. Mangiola A, Lama G, Giannitelli C, de Bonis P, Anile C, Lauriola L, et al. Stem cell marker nestin and c-Jun NH2-terminal kinases in tumor and peritumor areas of glioblastoma multiforme: possible prognostic implications. *Clin Cancer Res.* (2007) 13:6970–7. doi: 10.1158/1078-0432.CCR-07-1229
12. Jensen TR, Schmainda KM. Computer-aided detection of brain tumor invasion using multiparametric MRI. *J Magn Reson Imaging.* (2009) 30:481–9. doi: 10.1002/jmri.21878
13. Sica G, Lama G, Anile C, Geloso MC, La Torre G, de Bonis P, et al. Assessment of angiogenesis by CD105 and nestin expression in peritumor tissue of glioblastoma. *Int J Oncol.* (2011) 38:41–9. doi: 10.3892/ijo_00000822
14. Nelson SJ, Kadambi AK, Park I, Li Y, Crane J, Olson M, et al. Association of early changes in 1H MRSI parameters with survival for patients with newly diagnosed glioblastoma receiving a multimodality treatment regimen. *Neuro Oncol.* (2017) 19:430–9. doi: 10.1093/neuonc/now159
15. Fellows GA, Wright AJ, Sibtain NA, Rich P, Opstad KS, McIntyre DJ, et al. Combined use of neuroradiology and 1H-MR spectroscopy may provide an intervention limiting diagnosis of glioblastoma multiforme. *J Magn Reson Imaging.* (2010) 32:1038–44. doi: 10.1002/jmri.22350
16. Butzen J, Prost R, Chetty V, Donahue K, Neppl R, Bowen W, et al. Discrimination between neoplastic and nonneoplastic brain lesions by use

of proton MR spectroscopy: the limits of accuracy with a logistic regression model. *AJNR Am J Neuroradiol.* (2000) 21:1213–9.
17. Wijnen JP, Idema AJS, Stawicki M, Lagemaat MW, Wesseling P, Wright AJ, et al. Quantitative short echo time 1H MRSI of the peripheral edematous region of human brain tumors in the differentiation between glioblastoma, metastasis, and meningioma. *J Magn Reson Imaging.* (2012) 36:1072–82. doi: 10.1002/jmri.23737
18. Zhang H, Ma L, Wang Q, Zheng X, Wu C, Xu BN. Role of magnetic resonance spectroscopy for the differentiation of recurrent glioma from radiation necrosis: a systematic review and meta-analysis. *Eur J Radiol.* (2014) 83:2181–9. doi: 10.1016/j.ejrad.2014.09.018
19. Dowling C, Bollen AW, Noworolski SM, McDermott MW, Barbaro NM, Day MR, et al. Preoperative proton MR spectroscopic imaging of brain tumors: correlation with histopathologic analysis of resection specimens. *AJNR Am J Neuroradiol.* (2001) 22:604–12.
20. Pirzkall A, McKnight TR, Graves EE, Carol MP, Sneed PK, Wara WW, et al. MR-spectroscopy guided target delineation for high-grade gliomas. *Int J Radiat Oncol Biol Phys.* (2001) 50:915–28. doi: 10.1016/S0360-3016(01)01548-6
21. Louis DN, Ohgaki H, Wiestler OD, Cavenee WK, Burger PC, Jouvet A, et al. The 2007 WHO classification of tumours of the central nervous system. *Acta Neuropathol.* (2007) 114:97–109. doi: 10.1007/s00401-007-0243-4
22. Louis DN, Perry A, Reifenberger G, von Deimling A, Figarella-Branger D, Cavenee WK, et al. The 2016 World health organization classification of tumors of the central nervous system: a summary. *Acta Neuropathologica.* (2016) 131:803–20. doi: 10.1007/s00401-016-1545-1
23. Stupp R, Mason WP, van den Bent MJ, Weller M, Fisher B, Taphoorn MJB, et al. Radiotherapy plus concomitant and adjuvant temozolomide for glioblastoma. *New Engl J Med.* (2005) 352:987–96. doi: 10.1056/NEJMoa043330
24. Laws ER, Shaffrey ME. The inherent invasiveness of cerebral gliomas: Implications for clinical management. *Int J Dev Neurosci.* (1999) 17:413–20. doi: 10.1016/S0736-5748(99)00013-1
25. Kalpathy-Cranner J, Gerstner ER, Emblen KE, Andronesi OC, Rosen B. Advanced magnetic resonance imaging of the physical processes in human glioblastoma. *Cancer Res.* (2014) 74:4622–37. doi: 10.1158/0008-5472.CAN-14-0383
26. Kelly PJ, Daumas-Duport C, Kispert DB, Kall BA, Scheithauer BW, Illig JJ. Imaging-based stereotaxic serial biopsies in untreated intracranial glial neoplasms. *J Neurosurg.* (1987) 66:865–74. doi: 10.3171/jns.1987.66.6.0865
27. Badie B, Schartner JM, Hagar AR, Prabakaran S, Peebles TR, Bartley B, et al. Microglia cyclooxygenase-2 activity in experimental gliomas: possible role in cerebral edema formation. *Clin Cancer Res.* (2003) 9:872–7.
28. Blystad I, Warntjes JBM, Smedby O, Lundberg P, Larsson EM, Tisell A. Quantitative MRI for analysis of peritumoral edema in malignant gliomas. *PLoS ONE.* (2017) 12:e0177135. doi: 10.1371/journal.pone.0177135
29. Wang W, Da R, Wang MD, Wang T, Qi L, Jiang HT, et al. Expression of brain-specific angiogenesis inhibitor 1 is inversely correlated with pathological grade, angiogenesis and peritumoral brain edema in human astrocytomas. *Oncol Lett.* (2013) 5:1513–8. doi: 10.3892/ol.2013.1250
30. Tsao MN, Khuntia D, Mehta MP. Brain metastases: what's new with an old problem? *Curr Opin Support Pa.* (2012) 6:85–90. doi: 10.1097/SPC.0b013e32834de714
31. Nassehi D, Dyrbye H, Andresen M, Thomsen C, Juhler M, Laursen H, et al. Vascular endothelial growth factor A protein level and gene expression in intracranial meningiomas with brain edema. *Apmis.* (2011) 119:831–43. doi: 10.1111/j.1600-0463.2011.02764.x
32. Wu CX, Lin GS, Lin ZX, Zhang JD, Chen L, Liu SY, et al. Peritumoral edema on magnetic resonance imaging predicts a poor clinical outcome in malignant glioma. *Oncol Lett.* (2015) 10:2769–76. doi: 10.3892/ol.2015.3639
33. Li YM, Suki D, Hess K, Sawaya R. The influence of maximum safe resection of glioblastoma on survival in 1229 patients: can we do better than gross-total resection? *J Neurosurg.* (2016) 124:977–88. doi: 10.3171/2015.5.JNS142087
34. Law M, Cha S, Knopp EA, Johnson G, Arnett J, Litt AW. High-grade gliomas and solitary metastases: differentiation by using perfusion and proton spectroscopic MR imaging. *Radiology.* (2002) 222:715–21. doi: 10.1148/radiol.2223010558
35. Kuznetsov YE, Caramanos Z, Antel SB, Preul MC, Leblanc R, Villemure JG, et al. Proton magnetic resonance spectroscopic imaging can predict length of survival in patients with supratentorial gliomas. *Neurosurgery.* (2003) 53:565–74. doi: 10.1227/01.NEU.0000079331.21178.8E
36. Guo J, Yao CJ, Chen H, Zhuang DX, Tang WJ, Ren G, et al. The relationship between Cho/NAA and glioma metabolism: implementation for margin delineation of cerebral gliomas. *Acta Neurochir.* (2012) 154:1361–70. doi: 10.1007/s00701-012-1418-x
37. Cordova JS, Shu H-KG, Liang Z, Gurbani SS, Cooper LAD, Holder CA, et al. Whole-brain spectroscopic MRI biomarkers identify infiltrating margins in glioblastoma patients. *Neuro-oncology.* (2016) 18:1180–9. doi: 10.1093/neuonc/now036
38. Tarnawski R, Sokol M, Pieniazek P, Maciejewski B, Walecki J, Miszczyk L, et al. 1H-MRS *in vivo* predicts the early treatment outcome of postoperative radiotherapy for malignant gliomas. *Int J Radiat Oncol Biol Phys.* (2002) 52:1271–6. doi: 10.1016/S0360-3016(01)02769-9
39. Tolia M, Verganelakis D, Tsoukalas N, Kyrgias G, Papathanasiou M, Mosa E, et al. Prognostic value of MRS metabolites in postoperative irradiated high grade gliomas. *BioMed Res Int.* (2015) 2015:341042. doi: 10.1155/2015/341042
40. Li X, Jin H, Lu Y, Oh J, Chang S, Nelson SJ. Identification of MRI and 1H MRSI parameters that may predict survival for patients with malignant gliomas. *NMR Biomed.* (2004) 17:10–20. doi: 10.1002/nbm.858
41. Nicolasjilwan M, Hu Y, Yan CH, Meerzaman D, Holder CA, Gutman D, et al. Addition of MR imaging features and genetic biomarkers strengthens glioblastoma survival prediction in TCGA patients. *J Neuroradiol.* (2015) 42:212–21. doi: 10.1016/j.neurad.2014.02.006
42. Gandia-Gonzalez ML, Cerdan S, Barrios L, Lopez-Larrubia P, Feijoo PG, Palpan A, et al. Assessment of overall survival in glioma patients as predicted by metabolomic criteria. *Front Oncol.* (2019) 9:328. doi: 10.3389/fonc.2019.00328

Conflict of Interest: The authors declare that the research was conducted in the absence of any commercial or financial relationships that could be construed as a potential conflict of interest.

frontiers in Oncology

REVIEW
published: 09 February 2021
doi: 10.3389/fonc.2021.620070

A Position Statement on the Utility of Interval Imaging in Standard of Care Brain Tumour Management: Defining the Evidence Gap and Opportunities for Future Research

Thomas C. Booth[1,2†], Gerard Thompson[3†], Helen Bulbeck[4], Florien Boele[5,6], Craig Buckley[7], Jorge Cardoso[1], Liane Dos Santos Canas[1], David Jenkinson[8], Keyoumars Ashkan[9], Jack Kreindler[10], Nicky Huskens[11], Aysha Luis[1,12], Catherine McBain[13], Samantha J. Mills[14], Marc Modat[1], Nick Morley[15], Caroline Murphy[16], Sebastian Ourselin[1], Mark Pennington[17], James Powell[18], David Summers[19], Adam D. Waldman[3], Colin Watts[20,21], Matthew Williams[22], Robin Grant[3‡] and Michael D. Jenkinson[23,24‡] on behalf of the National Cancer Research Institute Brain Tumour Group*

[1] School of Biomedical Engineering & Imaging Sciences, King's College London, London, United Kingdom, [2] Department of Neuroradiology, King's College Hospital NHS Foundation Trust, London, United Kingdom, [3] Centre for Clinical Brain Sciences, University of Edinburgh, Edinburgh, United Kingdom, [4] Brainstrust, Cowes, United Kingdom, [5] Leeds Institute of Medical Research at St James's, St James's University Hospital, Leeds, United Kingdom, [6] Faculty of Medicine and Health, Leeds Institute of Health Sciences, University of Leeds, Leeds, United Kingdom, [7] Siemens Healthineers, Frimley, United Kingdom, [8] The Brain Tumour Charity, Fleet, United Kingdom, [9] Department of Neurosurgery, King's College Hospital NHS Foundation Trust, London, United Kingdom, [10] ACT for Cancer, London, United Kingdom, [11] The Tessa Jowell Brain Cancer Mission, London, United Kingdom, [12] Lysholm Department of Neuroradiology, National Hospital for Neurology and Neurosurgery, London, United Kingdom, [13] Department of Oncology, Christie Hospital NHS Foundation Trust, Manchester, United Kingdom, [14] Department of Neuroradiology, The Walton Centre NHS Foundation Trust, Liverpool, United Kingdom, [15] Department of Radiology, Wales Research and Diagnostic PET Imaging Centre, Cardiff University School of Medicine, Cardiff, United Kingdom, [16] King's College Trials Unit, King's College London, London, United Kingdom, [17] King's Health Economics, King's College London, London, United Kingdom, [18] Department of Oncology, Velindre Cancer Centre, Cardiff, United Kingdom, [19] Department of Neuroradiology, Western General Hospital, Edinburgh, United Kingdom, [20] Birmingham Brain Cancer Program, University of Birmingham, Birmingham, United Kingdom, [21] University Hospitals Birmingham NHS Foundation Trust, Birmingham, United Kingdom, [22] Department of Neuro-oncology, Imperial College Healthcare NHS Trust, London, United Kingdom, [23] Institute of Translational Medicine, University of Liverpool, Liverpool, United Kingdom, [24] Department of Neurosurgery, The Walton Centre NHS Foundation Trust, Liverpool, United Kingdom

OPEN ACCESS

Edited by:
Jose R. Pineda,
University of the Basque Country, Spain

Reviewed by:
Margarida Julià-Sapé,
Centre for Biomedical Network Research (CIBER), Spain
Alfredo Vellido,
Universitat Politecnica de Catalunya, Spain
Andrea Salmaggi,
ASST Lecco, Italy

***Correspondence:**
Thomas C. Booth
tombooth@doctors.org.uk

†These authors share first authorship

‡These authors share last authorship

Specialty section:
This article was submitted to Neuro-Oncology and Neurosurgical Oncology, a section of the journal Frontiers in Oncology

Received: 21 October 2020
Accepted: 06 January 2021
Published: 09 February 2021

Citation:
Booth TC, Thompson G, Bulbeck H, Boele F, Buckley C, Cardoso J, Dos Santos Canas L, Jenkinson D, Ashkan K, Kreindler J, Huskens N, Luis A, McBain C, Mills SJ, Modat M, Morley N, Murphy C, Ourselin S, Pennington M, Powell J, Summers D, Waldman AD, Watts C, Williams M, Grant R and Jenkinson MD (2021) A Position Statement on the Utility of Interval Imaging in Standard of Care Brain Tumour Management: Defining the Evidence Gap and Opportunities for Future Research. Front. Oncol. 11:620070. doi: 10.3389/fonc.2021.620070

Objective: To summarise current evidence for the utility of interval imaging in monitoring disease in adult brain tumours, and to develop a position for future evidence gathering while incorporating the application of data science and health economics.

Methods: Experts in 'interval imaging' (imaging at pre-planned time-points to assess tumour status); data science; health economics, trial management of adult brain tumours, and patient representatives convened in London, UK. The current evidence on the use of interval imaging for monitoring brain tumours was reviewed. To improve the evidence that interval imaging has a role in disease management, we discussed specific themes of data science, health economics, statistical considerations, patient and carer perspectives, and

multi-centre study design. Suggestions for future studies aimed at filling knowledge gaps were discussed.

Results: Meningioma and glioma were identified as priorities for interval imaging utility analysis. The "monitoring biomarkers" most commonly used in adult brain tumour patients were standard structural MRI features. Interval imaging was commonly scheduled to provide reported imaging prior to planned, regular clinic visits. There is limited evidence relating interval imaging in the absence of clinical deterioration to management change that alters morbidity, mortality, quality of life, or resource use. Progression-free survival is confounded as an outcome measure when using structural MRI in glioma. Uncertainty from imaging causes distress for some patients and their caregivers, while for others it provides an important indicator of disease activity. Any study design that changes imaging regimens should consider the potential for influencing current or planned therapeutic trials, ensure that opportunity costs are measured, and capture indirect benefits and added value.

Conclusion: Evidence for the value, and therefore utility, of regular interval imaging is currently lacking. Ongoing collaborative efforts will improve trial design and generate the evidence to optimise monitoring imaging biomarkers in standard of care brain tumour management.

Keywords: glioblastoma, high grade glioma, glioma, meningioma, interval imaging, magnetic resonance imaging, utility, monitoring biomarker

INTRODUCTION

Over the last decade the treatment landscape for adult brain tumours has changed incrementally for some tumour types, such as metastases, where there have been improvements in systemic therapy and brain radiotherapy (1). For other tumour types there has been little change. The management of glioblastoma remains largely based on maximum safe resection and radiotherapy with concomitant and adjuvant temozolomide chemotherapy (2). Evidence from randomised controlled trials [level 1 (3)] underpins clinical treatments of adult brain tumours. In contrast, there is little evidence (< level 3) to support the current imaging practices used to monitor disease progression or response to treatment (4, 5). Therefore, the clinical utility [the relevance and usefulness of an intervention in patient care using all sources of evidence (6)] of interval imaging (imaging at pre-planned time-points to assess tumour status, as compared with scanning for reasons of clinical deterioration) is largely unknown.

"Interval imaging" was first introduced into neuro-oncology in 1977 by Victor Levin, shortly after the introduction of computed tomography (CT) (7). In 1981 the World Health Organisation (WHO) convened two expert meetings on the "Standardization of Reporting Results of Cancer Treatment". The recommendations were widely adopted to ensure consistency of timing between centres and became the basis of subsequent iterations of high-grade glioma treatment monitoring and result reporting (8). These evolved with the development of MRI. In 1990, Macdonald also recommended assessing factors affecting imaging appearance such as corticosteroid use (9) which subsequently formed the basis of the AVAglio trial response criteria (10) and the 2010 response assessment in neuro-oncology (RANO) trial guidelines (11). There is a demonstrable historical lineage following the advent of CT for how enhancing tumour size, following exogenous contrast administration, has been incorporated into current clinical and trial practice. The expert committees were informed by observational studies, supported by a biologically plausible assumption that the images from each time-point, or the rate of change in a series of imaging investigations, are reliable "monitoring biomarkers" (12) reflecting tumour behaviour. The assumption is that changes in tumour size identify progression of disease, potentially before it becomes clinically apparent, resulting in a lead time improvement for therapeutic intervention. Indeed, there may be benefits in changing management before the development of irreversible disability or before the extent of tumour precludes intervention. Some justification for enhancement as a disease proxy has been inferred from data showing that enhancing tumour size and extent of resection are "prognostic biomarkers" (12) at both first presentation and recurrence (13–15). However, there is no evidence that earlier diagnosis influences prognosis pre- or post-operatively, and individual enhancing tumour growth trajectories vary between individuals with the same histological tumour type.

Deriving an evidence base surrounding current imaging practices is important for several reasons. There is a lack of biological specificity for contrast enhancement, particularly in the context of treatment effects and pseudophenomena, which can confound imaging assessment. There is also variability in clinical adoption of interval imaging practice across UK and

European neuro-oncology centres which is unlikely to be in the best interests of patients or healthcare systems (16, 17). It is also noteworthy that the widely reported observation that increasing enhancement tracks growth of most brain tumour types, has extended the use of contrast-enhancing tumour size as a biomarker beyond high-grade glioma. The impetus to derive an evidence-base is driven by researchers (4, 5, 16), but more importantly patients and carers (**Box 1**) (18). This in part relates to factors such as understanding the anxiety surrounding the imaging event and awaiting the results – so-called "scanxiety" (19). Furthermore, determining the health economics related to interval imaging is equally important. These include understanding the direct costs of subsequent investigations (for example, 'advanced imaging' requiring additional sequences and processing time, or earlier interval imaging than usual), additional hospital appointments that may follow uncertain tumour changes, continuation of futile therapies, as well as indirect and opportunity costs.

The purpose of this position statement is to summarise the current evidence base for the utility of interval imaging in brain tumours and to propose potential studies for future evidence gathering incorporating the disciplines of data science and health economics.

MATERIALS AND METHODS

Clinicians, scientists, and patient advocates and representatives with expertise in interval imaging, data science, health economics or trial management of adult brain tumours, convened in London, UK, in April 2019 in conjunction with a National Cancer Research Institute (NCRI) Brain Tumour group workshop. Available evidence for interval imaging pathways for different tumour types was discussed in the context of research recommendations of previous publications, including the UK's National Institute for Health and Care Excellence (NICE) brain tumour guidelines NG99 (**Supplementary Table 1**) and a systematic review of glioma imaging (4, 5, 16). Specifically, we sought to assess value in the context of morbidity, mortality, quality of life and resource use (together these outcomes give the additional outcome measure of cost effectiveness). Clinical utility incorporates all these outcome measures as well as considering the interests and goals of stakeholders (6). In addition, the results of a UK national clinical practice survey on the use of internal imaging in glioblastoma management were reviewed. Opportunities to generate evidence were explored in the context of specific study designs, with a focus on the utility and limitations of applying each design to a specific scenario. We outlined the advantages and disadvantages of each design based on current evidence and expert opinion. The discussion was compiled into a manuscript and circulated to NCRI Brain Tumour Group members and invited experts in attendance as well as those unable to attend. Edits and feedback were incorporated until all authors were in agreement with the content, and a position statement was produced around potential approaches to studying interval imaging in glioma and meningioma.

RESULTS

Targeting of Interval Imaging Studies

Following explicit agreement that there was an evidence gap, and that the JLA priority (**Box 1**) should be addressed, an initial question was to determine which brain tumour types should be included in the position statement. Whilst central nervous system (CNS) tumours comprise a range of diverse histological and molecular entities (20), meningioma and gliomas are the two commonest accounting for 36% and 28% of tumours, respectively. These were selected as the focus for interval imaging studies. Although brain metastases are more common overall, because of the rapidly evolving treatment paradigms according to primary cancer site (stereotactic radiosurgery, chemotherapy, immunotherapy) (1), the reliance on disease response assessment in the body to systemic treatments, and the fact that this can even vary between different intracranial lesions in the same individual (1), it was agreed that metastases were beyond the scope of the workshop (21–23). It was acknowledged that high-grade (WHO III-IV) and lower-grade (WHO II) infiltrating gliomas should be treated separately. Individual imaging biomarker techniques beyond standard structural clinical MRI have been reviewed extensively elsewhere (24, 25) and the uptake of these "advanced" MRI and positron emission tomography (PET) techniques is limited

BOX 1 | A National Institute for Health Research (NIHR) James Lind Alliance (JLA) Priority.

The National Institute for Health Research (NIHR) James Lind Alliance (JLA) brings patients, carers and clinicians together in Priority Setting Partnerships stating that "addressing uncertainties about the effects of a treatment should become accepted as a routine part of clinical practice" and that "patients, carers and clinicians should work together to agree which, among those uncertainties, matter most and deserve priority attention".

In 2015, the group met to establish the ten highest clinical priority uncertainties in neuro-oncology in the UK. Number two is: "what is the effect on prognosis of interval scanning to detect tumour recurrence compared with scanning on symptomatic recurrence in people with a brain tumour?" Patients expect imaging will give an accurate account of the effect of treatment and either reassure or initiate a change in the treatment plan. If there is uncertainty regarding progression, that leads to anxiety until the next scan or specialist MR imaging. In addition, if there is minor imaging progression only, there may be the clinical dilemma as to whether to change management if there are further options, even though the patient has had no clinical deterioration and it is not known whether earlier pre-symptomatic intervention improves survival.

This might be interpreted as:

"For me, a patient, does earlier scanning to detect asymptomatic progression improve my quality of life and survival, or does it not make any difference, or make it worse?"

And:

"Would I, as a doctor, improve the quality of life and survival of my patients if I monitored them more proactively and detected progression before it became symptomatic or does it not make any difference or make it worse?"

and highly heterogeneous, even in specialist neuro-oncology centres across Europe (17). The focus at the workshop was therefore on determining the value of the structural MRI interval imaging pathway and methods to interrogate this, although the potential role of additional imaging techniques remains relevant. Improving the diagnostic performance of structural or "advanced" imaging biomarkers is a further means to rationalise imaging timepoints by reducing repeat imaging while there is ongoing uncertainty. Key points regarding study design types are summarised in **Table 1**.

Interval Imaging Overview

Neuro-oncology multi-disciplinary team meetings (MDTs, referred to as "Tumor Boards" in North America) consider longitudinal patient management, with serial imaging follow-up having a central role. Meningioma and glioma imaging follow up schedules from UK's National Institute for Health and Care Excellence (NICE) brain tumour guidelines NG99 are shown in **Supplementary Tables 2** and **3** (4). In the broadest sense, interval imaging is typically performed in order to determine whether a tumour is growing, which may initiate or change treatment. A planned imaging schedule provides clinicians with a framework to track an aspect of tumour biology just before clinical review and allows easier administrative timetabling for the imaging department, MDT planning, and the patient diary planning, but cannot determine what the symptoms will be at the point of imaging. The radiologist only has information of symptoms at the time of request, which may limit interpretation. This allows decisions to be made on commencing, continuing, or discontinuing treatment and provides insight into whether treatment has caused a meaningful alteration in tumour biology. Standard structural MRI is routinely used for this purpose. In some centres, "advanced" MRI techniques (e.g. dynamic-susceptibility contrast enhanced, DSC, imaging or 1H-magnetic resonance spectroscopy MRS) or PET (targeting glucose or amino acid uptake) helps problem solving in instances when structural imaging is indeterminate (16, 17). As an alternative to a planned imaging schedule, imaging can also be triggered by a change in symptomatology or clinician concern, regardless of any scheduled follow-up interval. While triggered imaging is more difficult to organise at short notice, the strategy benefits from addressing patient concerns regarding the cause of new symptoms and providing the radiologist with contemporaneous clinical information at the time of imaging. In most centres the strategy for interval imaging is a combination of both a planned schedule and triggered imaging (16). Clinical and other non-imaging biomarkers of disease progression, whether as triggers for imaging or additional treatment response biomarkers, have the potential to be incorporated into the patient pathway and would benefit from further research (**Supplementary Information 1**).

The emergence of novel therapies, such as immunotherapy have created challenges for follow-up imaging of glioma in clinical trials, with pseudophenomena occurring in up to 5% of patients leading to the development of modified response assessment approaches such as iRANO (26). The central modification is that the moratorium on progressive disease is extended to cover the first 6 months of treatment. Stopping routine interval imaging for 6 months is, however, not recommended given the potential for the side effects of these therapies. Immunotherapy is not currently recommended as a second-line treatment option in most countries outside of research trials.

Interval Imaging and Confounds

Although MRI is a safe and effective technique, structural imaging can lead to false positive, false negative, and indeterminate results, particularly relating to post-treatment related pseudophenomena in glioma. In glioblastoma, pseudoprogression is an early post-treatment related effect typically occurring within 6 month of finishing concomitant temozolomide and radiotherapy whereas pseudoresponse typically occurs after anti-angiogenic agents such as bevacuzimab have been administered. False positive progression and false negative treatment response are manifest as an increase or decrease in MRI contrast enhancing volume respectively. Confounding of treatment response commonly occurs with the use of current standard interval imaging conventions in therapeutic and novel imaging glioma trials due to the impact of such pseudophenomena (27). Delayed treatment effects such as increased enhancement due to radiation necrosis can similarly cause false positive progression. Other examples of non-specificity include post-operative peritumoral parenchymal enhancement following operative "tissue handling"; or following operative infarction. Confounding is particularly relevant if progression-free survival is used as an outcome measure which is fundamentally based on, and therefore affected by, the timing of routine interval imaging. In part to mitigate this, objective criteria such as RANO require a threshold of enhancing size change (a 25% increase or 50% decrease in the product of perpendicular dimensions) and an indication of clinical status, corticosteroid dose, and other possible confounds of deterioration such as unrelated health issues; and for true positive progression there is a requirement for sustained size change beyond one time point. It is noteworthy that overall survival is also confounded by differences in treatment at progression. Management typically consists of second-line chemotherapy including the combination of procarbazine, lomustine and vincristine (PCV) (28–30), TMZ re-challenge (31, 32) or supportive care. Not only is management heterogenous, but pseudophenomona will confound this management choice. Furthermore, such detail to understand these co-variates are rarely included in studies (33).

The Patient and Carer Experience of Interval Imaging

Patients undergoing MRI often experience anxiety prior to and during scanning (34). Up to 37% of patients undergoing MRI experience moderate to high levels of anxiety related to the procedure itself (35–37). When the patient is aware they have a brain tumour that is being assessed for response or progression, anxiety is likely to be more frequent and magnified. Such "scanxiety" is a recognised consequence of interval imaging in cancer (19). Incorporating phenomena such as "scanxiety" into neuro-oncological studies requires patient-reported outcome

TABLE 1 | Different study designs to interrogate interval imaging.

Design	Time direction	Tumour and Comment	Objectives and Comment	Advantages	Disadvantages
Audit (single centre)	Retrospective	HGG Meningioma LGG	• understand MDTM decision making (not morbidity and mortality) • understand if there is standardised MRI interval imaging protocol or not; if so protocol details	• fast way to estimate factors influencing MDTM decision making • can inform more complex studies • some modelling of health economic outcomes plausible in meningioma/ LGG who undergo imaging over many years	• level 3 evidence (confounded data capture) • high likelihood that modelling of health economic outcomes may fail
Audit (multicentre)	Retrospective	HGG Meningioma LGG	• understand MDTM decision making (not morbidity and mortality) • modelling of health economic outcomes; requires some data to predict what would have happened in the absence of the change in management (counterfactual outcomes). • understand if there is standardised MRI interval imaging protocol or not; if so protocol details	• larger numbers: more statistical inference • more representative sample • fast way to estimate factors influencing MDTM decision making • modelling of health economic outcomes plausible in meningioma/ LGG who undergo imaging over many years • can inform more complex studies	• level 3 evidence (confounded data capture) • time consuming preparing data collection • effort could be going into level 1 or 2 evidence • robustness in the modelling of health economic outcomes dependent on quality of data used to extrapolate counterfactual outcomes
Observational (single centre)	Prospective	HGG Meningioma LGG	• test decision making at MDTM (not morbidity and mortality) • No need to examine those imaging timepoints clearly changing management if audit shows this already • understand if there is standardised MRI interval imaging protocol or not; if so protocol details	• level 2 evidence • accurately understand all factors influencing MDTM decision making • potential to capture data on multiple timepoints throughout pathway	• time consuming collecting prospective data • maybe challenging for a health economic assessment given a lack of comparator data may limit the scope of economic evaluation
Observational (multicentre) (additional points relating to cancer registries shown in bold)	Prospective	HGG Meningioma LGG	• test decision making at MDTM (not morbidity and mortality) • no need to examine those imaging time points clearly changing management if audit shows this already • understand if there is standardised MRI interval imaging protocol or not; if so protocol details **• cancer registries may allow high level interval imaging comparisons**	• level 2 evidence • accurately understand all factors influencing MDTM decision making • potential to capture data on multiple timepoints throughout pathway • more representative sample • possibly RADIANT (UK) perform study **• quality assured available resource** **• with large datasets, interval imaging comparisons, accounting for health service organization variation, may provide useful information**	• time consuming preparing data collection • time consuming collecting prospective data **• data may not be detailed enough & incomparable**
RCT (multicentre)	Prospective	HGG Meningioma & LGG challenging given long follow up	• compare: symptomatic imaging vs. regular interval imaging • non-inferiority study	• level 1 evidence to assess morbidity, mortality • analysis of quality of life & resource use outcomes using trial data and extrapolation with a decision model • Answers JLA question	• recruitment challenging both for patients & PI ("no equipoise"). This may be explored by feasibility study. • time consuming preparing data collection • time consuming collecting data • expensive
RCT (multicentre)	Prospective	HGG	• compare: EPMRI vs. No EPMRI • non-inferiority study	• level 1 evidence to assess morbidity, mortality • analysis of quality of life & resource use outcomes using trial data and extrapolation with a decision model	• recruitment challenging both for patients & PI ("no equipoise"). This may be explored by feasibility study. • time consuming preparing data collection • time consuming collecting data • expensive
RCT (multicentre)	Prospective	HGG Meningioma & LGG challenging	• compare: joint decision between patient and clinician for imaging vs. regular interval imaging • non-inferiority study	• level 1 evidence to assess morbidity, mortality • analysis of quality of life & resource use outcomes using trial data and extrapolation with a decision model	• recruitment challenging both for patients & PI ("no equipoise"). This may be explored by feasibility study. • time consuming preparing data

(Continued)

TABLE 1 | Continued

Design	Time direction	Tumour and Comment	Objectives and Comment	Advantages	Disadvantages
		given long follow up			collection • time consuming collecting data • expensive
RCT (multicentre)	Prospective	HGG Meningioma & LGG challenging given long follow up	• compare: imaging vs. no imaging at a timepoint informed by prior studies • non-inferiority study	• level 1 evidence to assess morbidity, mortality • analysis of quality of life & resource use outcomes using trial data and extrapolation with a decision model	• recruitment challenging both for patients & PI ("no equipoise"). This may be explored by feasibility study. • time consuming preparing data collection • time consuming collecting data expensive
RCT (multicentre)	Prospective	HGG Meningioma & LGG challenging given long follow up	• compare: imaging vs no imaging at multiple (or all) timepoints • non-inferiority study	• level 1 evidence • to assess morbidity, mortality analysis of quality of life & resource use outcomes using trial data and extrapolation with a decision model • Analysis of multiple points of current pathway	• recruitment challenging both for patients & PI ("no equipoise"). This may be explored by feasibility study. • potential ethical concerns • complex • very large numbers required as multiple decision points • time consuming preparing data collection • time consuming collecting data expensive
RCT (multicentre)	Prospective	HGG Meningioma & LGG challenging given long follow up	• compare: imaging at multiple short interval timepoints (e.g. at 1 month) vs routine interval imaging (e.g. at 3 months) • non-inferiority study	• level 1 evidence • to assess morbidity, mortality • analysis of quality of life & resource use outcomes using trial data and extrapolation with a decision model • Optimal way to understand points of progression	• compliance • challenging both for patients & PI. This may be explored by feasibility study. • difficult to justify increased scans if no clear step towards a change in management after scans. • time consuming preparing data collection • time consuming collecting data very expensive
in silico (single centre)	Retrospective	HGG Meningioma LGG	• discover high value imaging time points • understand influence of co-variates	• some discovery prediction • some modelling opportunities • some limited ability to inform RCTs of best imaging point to analyse • some ability to look at different levels of granularity including radiomics • some assessment of morbidity, mortality • may support some model based economic evaluation • small possibility of finding ways to improve survival	• lower level evidence (level not quantifiable) • (confounded data capture) • modelling limited with small numbers
in silico (multicentre)	Retrospective	HGG Meningioma LGG	• discover high value imaging time points • understand influence of co-variates	• larger numbers: more discovery prediction • more representative sample • modelling opportunities ability to look at different levels of granularity including radiomics • inform RCTs of best imaging point to analyse • leverage additional trial data e.g. EORTC or intellance AbbVie (2 month follow up) or Paradigm (3 month follow up) or CODAGLIO trial data • more accurate modelling of morbidity, mortality,	• lower level evidence (level not quantifiable) (confounded data capture) • time consuming preparing data collection

(Continued)

TABLE 1 | Continued

Design	Time direction	Tumour and Comment	Objectives and Comment	Advantages	Disadvantages
				• may support some model based economic evaluation • possibility of finding ways to improve survival	
in silico (single centre)	Prospective	HGG Meningioma & LGG challenging given long follow up	• discover high value imaging time points • understand influence of co-variates	• Moderately higher level evidence (level not quantifiable) • some discovery prediction • some modelling opportunities inform RCTs of best imaging point to analyse • ability to look at different levels of granularity including radiomics • potential to add MR fingerprinting • moderately more accurate modelling of morbidity, mortality, quality of life, resource use, co-variates • small possibility of finding ways to improve survival	• modelling limited with very small numbers • time consuming collecting data • if adding additional experiments e.g. MR fingerprinting, trial more complex
in silico (multicentre) Non-federated (additional federated points shown in bold)	Prospective	HGG Meningioma & LGG challenging given long follow up	• discover high value imaging time points • understand influence of co-variates	• Higher level evidence (level not quantifiable) • larger numbers: more discovery prediction • more representative sample • modelling opportunities • inform RCTs of best imaging point to analyse • ability to look at different levels of granularity including radiomics • potential to add MR fingerprinting • leverage Health Data Research UK BRAIN MATRIX, BRIAN • more accurate modelling of morbidity, mortality, quality of life, resource use co-variates • possibility of finding ways to improve survival **• overcome concerns regarding de-identification** **• constant iteration of models**	• time consuming preparing data collection • time consuming collecting data expensive • if adding additional experiments e.g. MR fingerprinting, trial more complex **• federated learning is still at the research stage: time consuming to develop and resolve challenges**

(PRO) measures which are well defined and reliable and therefore can generate high-quality evidence (38).

Uncertainty is defined as an individual's "lack of ability to determine the meaning of illness-related events" (39). In patients with primary brain tumours this has a direct impact on all negative mood states (tension, depression, anger, fatigue, and confusion) measured using the Profile of Mood States-Short Form (POMS-SF)) (40). These negative mood states impact on symptom severity, with higher levels of uncertainty associated with worse negative mood states and symptom severity. Due of the high likelihood of disease progression or recurrence in glioma, negative mood states may be exacerbated when patients who have symptoms are awaiting MRI results. Interventions designed to reduce uncertainty may help lessen patients' perception of symptom severity, which may subsequently result in better treatment outcomes and quality of life. One solution might be "one-stop" clinics in neuro-oncology, but this can be logistically challenging due to managing scanner capacity and radiologist availability for providing direct access reporting. Another approach to reduce uncertainty might be to provide re-assurance that the disease is better or to give a clear management plan for treatment at the point when the imaging results are conveyed to them. Conversely, any new uncertainty or uncertainty that persists following imaging, such as the consideration of pseudophenomena, might reinforce or perpetuate negative mood states. In the typically slower progressing lower grade glioma and meningioma, where there is less impact of pseudophenomena and delayed treatment effects, it is unclear how the relatively long imaging intervals influence uncertainty.

There are several sources of low-level evidence (level 4) indicating that patient and carer anxiety related to perceived unnecessary MRI scans or inaccurate or indeterminate imaging findings in primary brain tumours is a concern. This was a motivating factor behind the James Lind Alliance Priority Setting Partnership priority to establish the value and benefit of neuro-oncological interval scanning (18). Study design into interval imaging would benefit from including

patient-reported outcomes (PRO) so that "uncertainty reduction" can be measured.

Interval Imaging Practices With a Focus on Glioblastoma

There is no robust evidence (< level 3) to support the value or lack of value for the imaging practices currently used to monitor disease or to determine the response of any treatment given in adult brain tumours (4). There is also a lack of evidence around the utility of early post-operative MRI (EPMRI; within 72 h) on adult brain tumour patients after surgical resection of glioblastoma (16, 41–43). Interval imaging conventions are based predominantly on expert opinion and have been primarily motivated by efforts to standardise outcomes for comparing therapeutic trials (9, 11). For EPMRI, it is also noted that indirect contributors to value, such as improving surgical practice (5, 44), are challenging to measure, particularly at the start of a complex treatment pathway. Any study design into interval imaging value must consider current or planned therapeutic trials where outcomes are based on interval imaging regimens. Similarly, there should be awareness that current imaging conventions and the reliance of regulatory approval pathways on them [e.g. FDA endorsing RANO-based treatment outcomes (45)] might impede the development of innovative imaging solutions and other biomarkers designed to rationalise or optimise the imaging pathway.

An understanding of current practice is critical to subsequent study design. A recent UK-wide national clinical practice survey on the use of interval imaging in glioblastoma management (GIN CUP study) showed considerable variation between centres (16). Similarly, the timing and interval length between MRI examinations in the period following completion of adjuvant chemotherapy, shows considerable inter-institutional variation. It is also noted that current UK, European, and international guidelines (4, 46–49) show variation and lack of consensus on the frequency and timing of neuroimaging during the post treatment follow-up period, likely as a result of the lack of objective evidence base and different resourcing between jurisdictions.

In summary, there is considerable variation in interval imaging practice between centres during the glioblastoma post treatment follow-up period which should be considered in the study design of interval imaging value. Neuroimaging is believed to be crucial in making subsequent plausible management decisions once treatment is initiated, however there is a paucity of evidence for this assertion at all timepoints. Additional evidence, therefore, needs to be obtained to determine whether imaging protocols used in current routine clinical practice, and the type of neuroimaging performed at each component of the pathway, result in a measurable and impactful change in management (as opposed to the perception of a change or impact). Determining whether there is a change in outcome and value (morbidity, mortality, quality of life or resource use) is key.

Health Economics of Interval Imaging

Economic evaluation addresses issues of efficiency and cost effectiveness: are the resources required to provide the intervention, in this case MRI scans, justified by the health benefits? If the MRI scan offers no health benefit, then the intervention is not considered cost effective, with robust economic evaluation required to determine under which circumstances cost-effectiveness is achieved. Whilst retrospective analyses may determine to some extent whether there has been a change in management, prospective studies are needed to quantify the benefit in the context of confounds.

To determine cost effectiveness, an estimate of the impact of imaging on overall resource use is required as well as an estimate of the impact of imaging on survival and quality of life. Consideration of resource data collection is important in the design of future studies. Prospective collection of quality of life data can support a within-trial analysis of quality adjusted life-years (QALYs: a measure of the impact of the intervention on health-related quality of life and survival). To inform QALYs, quality of life is typically measured using generic quality of life instruments, of which the most commonly used are the EuroQol EQ-5D (50), the SF-6D (51) (based on the Rand SF-36 questionnaire) and the health utilities index (52). The EQ-5D is the most commonly used measure, and reports health status as the level of functioning in five domains. The five level (5L) instrument differentiates 3,125 response combinations each of which has an associated tariff ranging from 1 for full health, through 0 for dead, to negative scores for a small number of health states considered worse than dead. Measurement might be performed at baseline and 3 monthly intervals during the imaging period, in a similar fashion to interval imaging. More extensive questionnaires such as the European Co-operative Oncology Group Quality of Life Questionnaire Core 30 (EORTC QLQ C30) (53) may provide a more targeted capture of quality of life and may prove to be suitable instruments. Further work is required to determine more detailed evidence surrounding patients' views on quality of life in relation to interval imaging cost effectiveness. Other sources of information to capture outcomes such as mortality or resource use can come from case report forms (CRF) within a trial or from clinical registers, e.g. the Surveillance, Epidemiology and End Results database in the US (SEER) (54) and the National Cancer Registration and Analysis Service (NCRAS) in the UK (55). Administrative databases may also provide useful data on diagnosis, treatments and survival (56). The literature also provides estimates of the cost of care for relevant events that may not be observed during a trial such as the cost of end-of-life-care (EOLC) (57).

Trial follow-up is frequently insufficient to capture the full implications of monitoring and treatment on patient costs and outcomes. A decision model is commonly used to extrapolate costs and outcomes beyond trial follow-up, often over the remaining lifetime of the patient cohort. The most commonly used is the Markov model, which captures patient trajectories as a sequence of health states representing progression of the disease (58). Estimation of lifetime costs and outcomes of different monitoring and treatment strategies allows quantification of the difference in costs and outcomes across strategies. The ratio of incremental costs to incremental

outcomes, known as the incremental cost-effectiveness ratio (ICER), reports the efficiency of more effective strategies in terms of the cost per unit improvement in outcome. These data typically influence recommendations from national health technology agencies on the use of new technology and care pathways, although the application of an explicit upper limit or threshold with regard to cost-effectiveness is limited to the UK, Australia and Canada (59).

Deriving evidence to determine the cost effectiveness of interval imaging requires consideration of the impact of imaging on downstream costs and outcomes. Downstream costs for surgical treatments such as craniotomy or licensed chemotherapy drugs can greatly outweigh the costs of the imaging. Hence quantifying small changes in treatments arising from imaging is important. Therefore, any design or modelling to optimise interval imaging cost effectiveness in routine clinical practice should incorporate changes in the costs of any subsequent alteration in treatment i.e. related and opportunity costs. For example, the model should incorporate changes in the costs of continuing expensive and ineffective therapies which themselves may be associated with adverse effects; changes to surgical procedures which themselves may be associated with reduced or prolonged hospital stays; and changes to the costs of rehabilitation if the clinical impacts of progression of underlying disease are altered.

The conclusions of any health economic design framework described above are most applicable to integrated healthcare systems such as the UK. In these healthcare systems, imaging was historically considered relatively costly, and most agencies endorse rationing which can limit use. However, other reimbursement models in other healthcare systems can incentivise additional investigation, as reflected by the wide discrepancy in MRI use between countries (60).

Beyond providers, there are individual financial implications for imaging. For example, 54% of carers of US patients with high-grade gliomas out of active treatment had costs of $271 per month with transportation to hospitals amongst the greatest out of pocket costs (61). These personal costs may be lower in healthcare systems such as the UK where hospitals and charities provide additional support, but evidence suggests they remain substantial (62). Health economic modelling would benefit from incorporating such individual costs and regional/international variations.

More evidence to determine the cost effectiveness of interval imaging incorporating the patient, carer, and healthcare system is required. Careful study design using standard tools should achieve this. Evidence on cost-effectiveness will improve care pathways in all systems, and is central to the efficient use of resources in centrally funded healthcare systems.

Data Science *In Silico* Interval Imaging Studies

In silico studies are those performed on a computer or *via* computer simulation. Sophisticated algorithms or simulations can advance scientific understanding, although the inferences drawn must recognise the limitations introduced by the simplified or reductive framework. The results of these simulations can be tested in existing trials or serve as a guide for future trials. Machine learning applications may move beyond inferential statistical approaches to attempt to extract more accurate predictions from complex datasets. Such approaches for imaging monitoring biomarkers in neuro-oncology are at an early stage of development in terms of clinical validation and applied techniques are not yet ready to be incorporated into the clinic (63, 64). A recent systematic review using PRISMA-DTA and QUADAS-2 methodology, showed that the small numbers of patients included in machine learning studies, the high risk of bias and concerns of applicability in the study designs, and the low level of evidence given that the monitoring biomarker studies are retrospective, suggest that limited conclusions can be drawn from the data (33).

Studies may take advantage of enhanced computational approaches to build data-rich neuro-oncology monitoring biomarker models, although more involved or computationally expensive approaches such as those used in deep learning, may not *de facto* outperform more traditional machine learning techniques, for example multivariate logistic regression (63). It is also notable that studies applying machine learning to build neuro-oncology monitoring biomarker models have yet to show overall advantage over those using traditional statistical methods in terms of analytical validation and diagnostic performance (63, 65, 66). Such statistical methodology is wide ranging and includes generalised estimating equations and mixed models (67) but for clarity, we note that there is a continuum between the two fields, a pertinent example being non-parametric orthogonal transformations for dimensionality reduction.

We note several barriers in translating machine learning which the neuro-oncology community must appreciate for *in silico* study design: (1) the clinical context may not be represented with a decreased ability to perform holistic evaluations of patients, with loss of valuable and irreducible aspects of the human experience such as psychological, relational, social, and organizational issues (68); (2) accuracy-driven performance metrics have led to more opaque models (69) although advances in interpretability and explainability may mitigate this somewhat (70); (3) binding the empirical data to categorical interpretation misses an intrinsic ambiguity in the observed phenomena (71) which might negatively affect performance (68); (4) overreliance on the capabilities of automation can lead to the related phenomenon of deskilling (72). Furthermore, there are several technical limitations that make many algorithms unreliable: domain adaptation is still in its infancy and further solutions are required to help algorithms extrapolate well to new hospitals. Uncertainty estimation is still underdeveloped, and necessary to know when algorithms are out-of-distribution or when the accuracy might be poor. Robustness to data issues, such as artefacts, is very much needed but also at its infancy. Lastly, the presence of multiple pathologies (for example, tumours and stroke) can also confound algorithms as these cases are rare and often unlabelled.

Nonetheless, we emphasise that machine learning models have key advantages: whilst three decades ago it was noted that

they require less formal statistical training given developments in software (73, 74), more recently there has also been a transformative reduction in the requisite programming expertise for researchers which has been enabled by open source software standardised implementations (75–77); have the ability to detect implicitly any complex non-linear relationship between independent and dependent variables (73, 78); and have the ability to detect all possible interactions between predictor variables (69). Indeed, new approaches have proven to bring new perspectives and insights to the diagnosis of neuro-oncology pathologies, such as glioma (79, 80). In particular, some of these models are currently used as diagnostic biomarkers (12) for prediction of tumour grading and genomics from imaging as well as automating diagnosis from histopathology; furthermore prognostic biomarkers can provide insights into survival (80).

Advances in brain tumour database curation will facilitate integration of imaging data with demographic, clinical, and molecular marker data into large databases [in the UK, for example, these include Health Data Research UK, the Tessa Jowell BRAIN MATRIX (81) or BRIAN – the Brain tumouR Information and Analysis Network (82)]. The capture of large volumes of data and the inclusion of a wider spectrum of imaging phenotypes, typically results in improved diagnostic performance during machine learning or statistical tasks; the relative improvement of deep learning model performance is particularly marked (83–85). Note that for deep learning, the dependency on very large datasets can be reduced by data augmentation and transfer learning; the latter, where an already developed model for a task is reused as the starting point or a model on a second task, is especially advantageous for medical tasks since these pre-trained models not only obviate the need for very large datasets but are less computationally expensive (70, 79, 80). Once established, incoming data from each of these larger scale live repositories will facilitate ongoing refinement and assessment of impacts. Examples of machine learning tools that have been used with large datasets in neuro-oncology, as well as generic approaches to multi-centre machine learning which might overcome privacy issues, are contained in the **Supplementary Information 2**.

Initiatives and consensus statements have provided recommended frameworks (86–89) for standardising imaging biomarker discovery, analytical validation, and clinical validation (12), which can help to improve the robustness of study design of machine learning applied to neuro-oncology. It is clear that for such an approach large, well-annotated datasets, and therefore, multi-disciplinary and multi-centre collaborations are mandated (63), and this will require a collaborative approach to reach meaningful dataset size and quality.

Interval Imaging Study Design and Statistical Considerations

The overarching purpose of any study design would be to determine the value of interval imaging and to maximise this value where possible. Ideally, studies would provide robust evidence (≤ level 3) for morbidity, mortality, quality of life and resource use (together these outcomes give the additional outcome measure of cost effectiveness) of three tumour groups (meningiomas, lower grade gliomas, and high-grade gliomas) undergoing interval imaging. Further Patient and Public Involvement (PPI) work is underway to refine measurable metrics although a primary outcome of mortality and secondary outcomes of quality of life e.g. the EUROQOL EQ 5D–5L or EORTC QLQ C30 score, may be sensible. Outcomes are confounded by treatment type and motivate thorough co-variate collection. Progression-free survival is especially confounded as described above and must be considered carefully as an outcome measure in glioma study design. This is a major driver for the consideration of adopting "advanced imaging" in more robustly defining a progression event through imaging.

Given these, it is likely that different approaches are required to construct an evidence framework surrounding interval imaging (**Table 1**); building the framework is likely to be stepwise (90), using less robust evidence (< level 3) initially as well as determining baseline quality of life and resource use outcomes. Whilst the trial giving the highest level of evidence would be a randomised controlled trial (RCT), and likely a non-inferiority design, knowing which aspects of the pathway to randomise will require additional supportive intermediate evidence from preliminary studies. For example, data can be acquired using audit or observational studies to determine whether there is a change in management or not. If management is changed, an RCT may be able to address whether there is additional value from the change in management in terms of morbidity, mortality, quality of life and resource use. However, there may be challenges for recruitment of patients into an RCT, predominantly influenced by tumour type. For example, in a high-grade glioma RCT with reduced imaging in one arm, some participants and recruiters may oppose reduced imaging in a tumour where changes in disease can be rapid. It is plausible that there would be less concern for lower grade gliomas or meningioma interval imaging studies.

In silico studies using statistical or machine learning approaches might provide an alternative to inform which aspects of the pathway should be randomised in an RCT (91, 92). Alternatively, such techniques might be used to approximate outcomes themselves, however, as with an RCT, a large number of centres would be required to provide sufficient data, particularly if PROs and health economic measures are also incorporated. It is noteworthy that within existing provision and clinical trials, there will be natural jitter and missed time points in the follow-up of patients. With large datasets this might provide an opportunity using appropriate modelling techniques to assess the impacts of these natural timing differences and missing data points. Despite the potential of *in silico* studies, a disadvantage is that they do not produce level 1 evidence nor is it clear how the most complex modelling studies equate with traditional levels of evidence (3).

Whilst the focus of study design relates to the structural MRI interval imaging pathway and by default the "when" of imaging, the "how" and "what else" remain important avenues for research (5). It is conceivable that the interrogation of

biomarkers such as MRI radiomic features, advanced MRI or PET studies can be added as secondary objectives. It is acknowledged that these are not routinely used nor widely available modalities, and in the case of PET in particular, have a distinct risk and cost effectiveness profile compared to structural MRI. We note other expert consortia are looking specifically into advanced imaging and processing techniques to develop international recommendations and guidelines on their application as monitoring biomarkers (93, 94).

Regardless of the approach to achieve accurate, complete, and transparent reporting of studies contributing to the evidence of interval imaging in standard of care brain tumour management, we strongly recommend following reporting guidelines from the EQUATOR Network (95), available for example in prospective biomarker studies (96, 97), RCTs (98) or economic evaluations (99).

DISCUSSION

Determining the value, and therefore the utility, of interval imaging in brain tumour management remains a key priority in neuro-oncology. Meningioma and glioma were identified as priorities for interval imaging utility analysis. Any study design that changes imaging regimens should consider the potential for influencing current or planned therapeutic trials; ensure opportunity costs are measured; and that indirect contributions to value are identified and assessed.

Whilst it was agreed that an RCT would provide level 1 evidence, no consensus was reached on specific trial design, reflecting the immense challenge faced in addressing this evidence gap. While development of level 1 evidence is the desired goal, given that current practice is predominantly based on expert opinion (level 5) there is a role for establishing "intermediate level" evidence that might support a future RCT. The outcomes of any study must include overall survival, quality of life and resource use. The panel agreed that this "intermediate level" evidence was unlikely to be obtained solely through descriptive and inferential statistics of existing datasets and would benefit from modelling and advanced statistical and machine learning approaches, and that larger, aggregate datasets would be required involving multicentre collaborations. Overall, no consensus was reached as to the specific studies which should be undertaken, but types of study have been described here for consideration along with their strengths and limitations.

This position statement aims to provide a framework for developing the evidence base for the value of interval imaging in primary brain tumours and, thereafter, practice recommendations. The panel welcomes any collaborative approach from groups interested in aggregating data and contributing to study design. Ongoing collaborative efforts will improve trial design and generate the evidence to optimise monitoring imaging biomarkers in standard of care brain tumour management.

AUTHOR CONTRIBUTIONS

FB, TB HB, CB, JC, LD, RG, MJ, CMc, SM, NM, CMu, MP, JP, DS, GT and MW contributed conception and design of the study. TB wrote the first draft of the manuscript. FB, TB, HB, JC, RG, MJ, SM, NM, MP, JP, DS, GT, AW and MW wrote sections of the manuscript. DJ, KA, JK, NH, AL, SO, AW and CW: Not in attendance at incubator day; provided subsequent input. All authors contributed to the article and approved the submitted version.

FUNDING

This Interval Imaging Incubator Day meeting was facilitated and funded by *brainstrust* – the brain cancer people. No participants were remunerated for their contribution. National Cancer Research Institute (NCRI) separately provided travel and accommodation for those panel members who had travelled for either the main brain tumour group meeting or the glioma subgroup. This work was supported by the Wellcome/EPSRC Centre for Medical Engineering [WT 203148/Z/16/Z].

ACKNOWLEDGMENTS

Jonathon Buwanabala and Stephen J. Price also attended the incubator day.

SUPPLEMENTARY MATERIAL

The Supplementary Material for this article can be found online at: https://www.frontiersin.org/articles/10.3389/fonc.2021.620070/full#supplementary-material

REFERENCES

1. Anvold ND, Lee EQ, Mehta MP, Margolin K, Alexander BM, Lin NU, et al. Updates in the management of brain metastases. *Neuro Oncol* (2016) 18:1043–65. doi: 10.1093/neuonc/now127
2. Stupp R, Mason WP, van den Bent MJ, Weller M, Fisher B, Taphoorn MJB, et al. Radiotherapy plus concomitant and adjuvant temozolomide for glioblastoma. *N Engl J Med* (2005) 352:987–96. doi: 10.1056/NEJMoa043330
3. Howick J, Chalmer I, Glasziou P, Greenhalgh T, Heneghan C, Liberati A, et al. *Oxford Centre for Evidence-Based Medicine The Oxford 2011 levels of evidence*. Oxford (2016). Available at: http://www.cebm.net/index.aspx?o1/45653 (Accessed 1 August, 2018).
4. The National Institute for Health and Care Excellence. *Guideline NG99*. Available at: https://www.nice.org.uk/guidance/ng99 (Accessed 1 March 2019).
5. Thompson G, Lawrie TA, Kernohan A, Jenkinson MD. Interval brain imaging for adults with cerebral glioma. *Cochrane Database System Rev* (2019) 10. doi: 10.1002/14651858.CD013137
6. Lesko LJ, Zineh I, Huang S-M. What is clinical utility and why should we care. *Clin Pharm Ther* (2010) 88:729–33. doi: 10.1038/clpt.2010.229

7. Levin VA Crafts DC, Norman DM, Hoffer PB, Spire JP, Wilson CB. Criteria for evaluating patients undergoing chemotherapy for malignant brain tumors. *J Neurosurg* (1977) 47:329–35. doi: 10.3171/jns.1977.47.3.0329
8. Miller AB, Hoogstraten B, Staquest M, Winkler A. Reporting results of cancer treatment. *Cancer* (1981) 47:207–14. doi: 10.1002/1097-0142(19810101)47:1<207::AID-CNCR2820470134>3.0.CO;2-6
9. Macdonald DR, Cascino TL, Schold SC, Cairncross JG. Response criteria for phase II studies of supratentorial malignant glioma. *J Clin Oncol* (1990) 8:1277–80. doi: 10.1200/JCO.1990.8.7.1277
10. Chinot OL, de La Motte R, Moore N. AVAglio: Phase 3 trial of bevacizumab plus temozolomide and radiotherapy in newly diagnosed glioblastoma multiforme. *Adv Ther* (2011) 28:334–40. doi: 10.1007/s12325-011-0007-3
11. Wen PY, MacDonald DR, Reardon DA, Cloughesy TF, Sorensen AG, Galanis E, et al. Updated Response Assessment Criteria for High-Grade Gliomas: Response Assessment in Neuro-Oncology Working Group. *J Clin Oncol* (2010) 28:1963–72. doi: 10.1200/JCO.2009.26.3541
12. FDA-NIH Biomarker Working Group. In: *BEST (biomarkers, EndpointS, and other tools) resource. 1st edn*. Silver Spring, MD: Food and Drug Administration (US), co-published by Bethesda, MD: National Institutes of Health (US) (2016). Available at: https://pubmed.ncbi.nlm.nih.gov/27010052/; https://www.ncbi.nlm.nih.gov/books/NBK326791
13. Ellingson BM, Harris RJ, Woodworth DC, Leu K, Zaw O, Mason WP, et al. Baseline pretreatment contrast enhancing tumor volume including central necrosis is a prognostic factor in recurrent glioblastoma: evidence from single- and multicenter trials. *Neuro Oncol* (2017) 19:89–98. doi: 10.1093/neuonc/now187
14. Lacroix M, Abi-Said D, Fourney DR, Gokaslan ZL, Shi W, DeMonte F, et al. A multivariate analysis of 416 patients with glioblastoma multiforme: prognosis, extent of resection, and survival. *J Neurosurg* (2001) 95:190–8. doi: 10.3171/jns.2001.95.2.0190
15. Sanai N, Polley M-Y, McDermott MW, Parsa AT, Berger MS. An extent of resection threshold for newly diagnosed glioblastomas. *J Neurosurg* (2011) 115:3–8. doi: 10.3171/2011.2.JNS10998
16. Booth TC, Luis A, Brazil L, Thompson G, Daniel RA Shuaib H, et al. Glioblastoma post-operative Imaging in Neuro-oncology: Current UK practice (GIN CUP study). *Eur Radiol* (2020). doi: 10.1007/s00330-020-07387-3
17. Thust S, Heiland S, Falini AR, Jäger H, Waldman AC, Sundgren P, et al. Glioma imaging in Europe: a survey of 220 centres and recommendations for best clinical practice. *Eur Radiol* (2018) 28:3306–17. doi: 10.1007/s00330-018-5314-5
18. The James Lind Alliance Priority Setting Partnerships. Available at: http://www.jla.nihr.ac.uk/priority-setting-partnerships/neuro-oncology/ (Accessed 1 August 2018).
19. Baumi JM, Troxel A, Epperson CN, Cohen RB, Schmitz K, Stricker C, et al. Scan-associated distress in lung cancer: Quantifying the impact of "scanxiety". *Lung Cancer* (2016) 100:110–3. doi: 10.1016/j.lungcan.2016.08.002
20. Gondi V, Pugh SL, Tome WA, Caine C, Corn B, Kanner A, et al. Preservation of memory with conformal avoidance of the hippocampal neural stem-cell compartment during whole-brain radiotherapy for brain metastases (RTOG 0933): a phase II multi-institutional trial. *J Clin Oncol* (2014) 32:3810–6. doi: 10.1200/JCO.2014.57.2909
21. Louis DN, Perry A, Reifenberger G, von Deimling A, Figarella-Branger D, Cavenee WK, et al. The 2016 World Health organization classification of tumors of the central nervous system: a summary. *Acta Neuropathol* (2016) 131:803–20. doi: 10.1007/s00401-016-1545-1
22. Yamamoto M, Serizawa T, Shuto T, Akabane A, Higuchi Y, Kawagishi J, et al. Stereotactic radiosurgery for patients with multiple brain metastases (JLGK0901): a multi-institutional prospective observational study. *Lancet Oncol* (2014) 15:387–95. doi: 10.1016/S1470-2045(14)70221-9
23. Liu Y, Alexander BM, Chen Y-H, Horvath MC, Aizer AA, Claus EB, et al. Salvage whole brain radiotherapy or stereotactic radiosurgery after initial stereotactic radiosurgery for 1-4 brain metastases. *J Neurooncol* (2015) 124:429–37. doi: 10.1007/s11060-015-1855-5
24. Waldman AD, Jackson A, Price SJ, Clark CA, Booth TC, Auer DP, et al. Quantitative imaging biomarkers in neuro-oncology. *Nat Rev Clin Oncol* (2009) 6:445–54. doi: 10.1038/nrclinonc.2009.92
25. Dhermain FG, Hau P, Lanfermann H, Jacobs AH, van den Bent MJ. Advanced MRI and PET imaging for assessment of treatment response in patients with gliomas. *Lancet Neurol* (2010) 9:906–20. doi: 10.1016/S1474-4422(10)70181-2
26. Okada H, Weller M, Huang R, Finocchiaro G, Gilbert MR, Wick W, et al. Immunotherapy response assessment in neuro-oncology: a report of the RANO working group. *Lancet Oncol* (2015) 16(15):e534–42. doi: 10.1016/s1470-2045(15)00088-1
27. Buwanabala J, Mirchandani A, Booth TC. (2019). The (mis)use of imaging criteria in the assessment of glioblastoma treatment response. In: *Proceedings of the 57th American Society of Neuroradiology*, Boston, USA. Oak Brook, 2019 May 18-23. p. 1.
28. Weller M, van den Bent M, Tonn JC, Stupp R, Preusser M, Cohen-Jonathan-Moyal E, et al. European Association for Neuro-Oncology (EANO) guideline on the diagnosis and treatment of adult astrocytic and oligodendroglial gliomas. *Lancet Oncol* (2017) 18(6):e315–29. doi: 10.1016/S1470-2045(17)30194-8
29. Weller M, Cloughesy T, Perry JR. Wick W Standards of care for treatment of recurrent glioblastoma–are we there yet? *Neuro Oncol* (2013) 15(1):4–27. doi: 10.1093/neuonc/nos273
30. Parasramka S, Talari G, Rosenfeld M, Guo J, Villano JL. Procarbazine, lomustine and vincristine for recurrent high-grade glioma. *Cochrane Database Syst Rev* (2017) 7:CD011773. doi: 10.1002/14651858.CD011773.pub2
31. Perry JR, Bélanger K, Mason WP, Fulton D, Kavan P, Easaw J, et al. Phase II trial of continuous dose-intense temozolomide in recurrent malignant glioma: RESCUE study. *J Clin Oncol* (2010) 28(12):2051–7. doi: 10.1200/JCO.2009.26.5520
32. Weller M, Tabatabai G, Kästner B, Felsberg J, Steinbach JP, Wick A, et al. MGMT promoter methylation is a strong prognostic biomarker for benefit from dose- intensified temozolomide rechallenge in progressive glioblastoma: the DIRECTOR trial. *Clin Cancer Res* (2015) 21(9):2057–64. doi: 10.1158/1078-0432.CCR-14-2737
33. Booth TC, Akpinar B, Roman A, Shuaib H, Luis A, Chelliah A, et al. Machine learning and glioblastoma: treatment response monitoring biomarkers in 2021. In: A Crimi, editor. *MLCN/RNO-AI 2020, LNCS*. Switzerland AG: Springer Nature (2020). p. 12449.
34. Tugwell JR, Goulden N, Mullins P. Alleviating anxiety in patients prior to MRI: A pilot single-centre single-blinded randomised controlled trial to compare video demonstration or telephone conversation with a radiographer versus routine intervention. *Radiography* (2018) 24:122–1329. doi: 10.1016/j.radi.2017.10.001
35. van Minde D, Klaming L, Weda H. Pinpointing moments of high anxiety during an MRI examination. *Int J Behav Med* (2014) 21:487–95. doi: 10.1007/s12529-013-9339-5
36. Törnqvist E, Månsson Å, Larsson E-M, Hallström I. Impact of extended written information on patient anxiety and image motion artifacts during magnetic resonance imaging. *Acta Radiologica* (2006) 47:474–80. doi: 10.1080/02841850600690355
37. Eshed I, Althoff CE, Hamm B, Hermann KA. Claustrophobia and premature termination of magnetic resonance imaging examinations. *J Magn Reson Imaging* (2007) 26:401–4. doi: 10.1002/jmri.21012
38. Dirven L, Armstrong TS, Blakeley JO, Brown PD, Grant R, Jalali R, et al. Working Plan for the Use of Patient-Reported Outcome Measures in Adults With Brain Tumours: A Response Assessment in Neuro-Oncology (RANO) Initiative. *Lancet Oncol* (2018) 19:173–80. doi: 10.1016/S1470-2045(18)30004-4
39. Mishel MH. Uncertainty in illness. *Image J Nurs Sch* (1988) 20:225–32. doi: 10.1111/j.1547-5069.1988.tb00082.x
40. Lin L, Chiang H-S, Acquaye AA, Vera-Bolanos E, Gilbert MR, Armstrong TS. Uncertainty, mood states, and symptom distress in patients with primary brain tumors. *Cancer* (2013) 119:2796–806. doi: 10.1002/cncr.28121
41. Bette S, Gempt K, Huber T, Boeckh-Behrens T, Ringel F, Meyer B, et al. Patterns and Time Dependence of Unspecific Enhancement in Postoperative Magnetic Resonance Imaging After Glioblastoma Resection. *World Neurosurg* (2016) 90:440–7. doi: 10.1016/j.wneu.2016.03.031
42. Lescher S, Schniewindt S, Jurcoane CA, Senft C, Hattingen E. Time window for postoperative reactive enhancement after resection of brain tumors: less than 72 hours. *Neurosurg Focus* (2014) 37:E3. doi: 10.3171/2014.9.FOCUS14479
43. Kläsner B, Buchmann N, Gempt J, Ringel F, Lapa C, Krause BJ. Early 18F] FET-PET in Gliomas after Surgical Resection: Comparison with MRI and

Histopathology. *PLoS One* (2015) 10:e0141153. doi: 10.1371/journal.pone.0141153
44. Mrowczynski OD, Zammar S, Bourcier AJ, Langan ST, Liao J, Specht C, et al. Utility of Early Post-operative MRI after Glioblastoma Resection: Implications on Patient Survival. *World Neurosurg* (2018) 120:e1171–4. doi: 10.1016/j.wneu.2018.09.027
45. Wen PY, Cloughesy TF, Ellingson BM, Reardon DA, Fine HA, Abrey L, et al. Report of the Jumpstarting Brain Tumor Drug Development Coalition and FDA clinical trials neuroimaging endpoint workshop (January 30, 2014, Bethesda MD). *Neuro-Oncology* (2014) 16:vii36–47. doi: 10.1093/neuonc/nou226
46. Sanghera P, Rampling R, Haylock B, Jefferies S, McBain C, Rees JH, et al. The concepts, diagnosis and management of early imaging changes after therapy for glioblastomas. *Clin Oncol (R Coll Radiol)* (2012) 24:216–27. doi: 10.1016/j.clon.2011.06.004
47. Stupp R, Brada M, van den Bent MJ, Tonn J-C, Pentheroudakis G. High-grade glioma: ESMO Clinical Practice Guidelines for diagnosis, treatment and follow-up. *Ann Oncol* (2014) 25:iii93–iii101. doi: 10.1093/annonc/mdu050
48. Weller M, van den Bent MJ, Tonn J-C, Stupp R, Preusser M, Cohen-Jonathan-Moyal E, et al. European Association for Neuro-Oncology (EANO) guideline on the diagnosis and treatment of adult astrocytic and oligodendroglial gliomas. *Lancet Oncol* (2017) 18:e315–29. doi: 10.1016/S1470-2045(17)30194-8
49. National Cancer Comprehensive Network Foundation. *NCCN guidelines for treatment of cancer by site. Central Nervous System Cancers* (2019). Available at: http://www.nccn.org/professionals/physician_gls/f_guidelines.asp#cns (Accessed 1 September 2019).
50. EuroQol Research Foundation. *EQ-5D* (2017). Available at: https://euroqol.org/eq-5d-instruments/eq-5d-5l-about/ (Accessed 1 February 2017).
51. Brazier J, Roberts J, Deverill M. The estimation of a preference-based measure of health from the SF-36. *J Health economics* (2002) 21(2):271–92. doi: 10.1016/S0167-6296(01)00130-8
52. Feeny D, Furlong W, Torrance GW, Goldsmith CH, Zhu Z, DePauw S, et al. Multiattribute and single-attribute utility functions for the health utilities index mark 3 system. *Med Care* (2002) 40(2):113–28. doi: 10.1097/00005650-200202000-00006
53. EORTC Quality of Life Group. (2019). Available at: https://qol.eortc.org (Accessed 4 November 2019).
54. Hayat MJ, Howlader N, Reichman ME, Edwards BK. Cancer statistics, trends, and multiple primary cancer analyses from the Surveillance, Epidemiology, and End Results (SEER) Program. *Oncologist* (2007) 12(1):20–37. doi: 10.1634/theoncologist.12-1-20
55. The National Cancer Registration and Analysis Service. (2019). Available at: http://www.ncin.org.uk/publications/data_briefings/astrocytic_brain_tumours_survival_rates_in_england (Accessed 4 November 2019).
56. Mazzali C, Duca P. Use of administrative data in healthcare research. *Internal Emergency medicine* (2015) 10(4):517–24. doi: 10.1007/s11739-015-1213-9
57. Engelhardt JB, McClive-Reed KP, Toseland RW, Smith TL, Larson DG, Tobin DR. Effects of a program for coordinated care of advanced illness on patients, surrogates, and healthcare costs: a randomized trial. *Am J Manag Care* (2006) 12:93–100.
58. York Health Economics Consortium. (2016). Available at: https://yhec.co.uk/glossary/markov-model/ (Accessed 4 November 2019).
59. Thokala P, Ochalek J, Leech AA, Tong T. Cost-effectiveness thresholds: the past, the present and the future. *Pharmacoeconomics* (2018) 36(5):509–22. doi: 10.1007/s40273-017-0606-1
60. Papanicolas I, Woskie LR, Jha AK. Health Care Spending in the United States and Other High-Income Countries. *JAMA* (2018) 319:1024–39. doi: 10.1001/jama.2018.1150
61. Raizer JJ, Fitzner KA, Jacobs DI, Bennet CL, Liebling DB, Luu TH. Economics of Malignant Gliomas: A Critical Review. *J Oncol Pract* (2015) 11:e59–65. doi: 10.1200/JOP.2012.000560
62. Finney A, Davies S, Hayes D, Collard S. *Cancer's hidden price tag: revealing the costs behind the illness* (2013). Available at: https://www.macmillan.org.uk/_images/Cancers-Hidden-Price-Tag-report-England_tcm9-270862.pdf (Accessed 4 October 2020).
63. Booth TC, Williams M, Luis A, Cardoso J, Keyoumars A, Shuaib H. Machine learning and glioma imaging biomarkers. *Clin Radiol* (2019) 75:20–32. doi: 10.1016/j.crad.2019.07.001
64. Booth TC. An Update on Machine Learning in Neuro-oncology Diagnostics. In: A Crimi, editor. *LNCS*, vol. 11383 . BrainLes: Springer Nature Switzerland AG (2019). p. 1–8.
65. Hansen MR, Pan E, Wilson A, McCreary M, Wang Y, Stanley T, et al. Post-gadolinium 3-dimensional spatial, surface, and structural characteristics of glioblastomas differentiate pseudoprogression from true tumor progression. *J Neurooncol* (2018) 139:731–8. doi: 10.1007/s11060-018-2920-7
66. Ceschin R, Kurlan BF, Abberbock SR, Ellingson BM, Okada H, Jakacki RI, et al. Parametric response mapping of apparent diffusion coefficient (ADC) as an imaging biomarker to distinguish pseudoprogression from true tumor progression in peptide-based vaccine therapy for pediatric diffuse instrinsic pontine glioma. *AJNR Am J Neuroradiol* (2015) 36:2170–6. doi: 10.3174/ajnr.A4428
67. Williamson JM, Datta S, Satten GA. Marginal analyses of clustered data when cluster size is informative. *Biometrics* (2003) 59(1):36–42. doi: 10.1111/1541-0420.00005
68. Cabitza F, Rasoini R, Genisi GF. Unintended consequences of machine learning in medicine. *JAMA* (2017) 318(6):517–8. doi: 10.1001/jama.2017.7797
69. Tu J. Advantages and disadvantages of using artificial neural networks versus logistic regression for predicting medical outcomes. *J Clin Epidemiol* (1996) 49:1225–31. doi: 10.1016/S0895-4356(96)00002-9
70. Reyes M, Meier R, Pereira S, Silva CA, Dahlweid F-M, von Tengg-Kobligk, et al. On the Interpretability of Artificial Intelligence in Radiology: Challenges and Opportunities. *Radiol Artif Intell* (2020) 2(3):e190043. doi: 10.1148/ryai.2020190043
71. Dharmarajan K, Strait KM, Tinetti ME, Lagu T, Lindenauer PK, Lynn J, et al. Treatment for multiple acute cardiopulmonary conditions in older adults hospitalized with pneumonia, chronic obstructive pulmonary disease, or heart failure. *J Am Geriatr Soc* (2016) 64(8):1574– 1582. doi: 10.1111/jgs.14303
72. Hoff T. Deskilling and adaptation among primary care physicians using two work innovations. *Health Care Manage Rev* (2011) 36(4):338–48. doi: 10.1097/HMR.0b013e31821826a1
73. White H. Learning in artificial neural networks: A statistical perspective. *Neural Comput* (1989) 1:425–64. doi: 10.1162/neco.1989.1.4.425
74. Astion ML, Wilding P. The application of back-propagation neural networks to problems in pathology and laboratory medicine. *Arch Pathol Lab Med* (1992) 116:995–1001.
75. Medical Open Network for AI (MONAI). Available at: https://monai.io/ (Accessed 30 Dec 2020).
76. Ratib O, Rosset A, Heuberger J. Open source software and social networks: disruptive alternatives for medical imaging. *Eur J Radiol* (2011) 78(2):259–65. doi: 10.1016/j.ejrad.2010.05.004
77. Caban JJ, Joshi A, Nagy P. Rapid development of medical imaging tools with open-source libraries. *J Digit Imaging* (2007) 20(Suppl 1):83–93. doi: 10.1007/s10278-007-9062-3
78. Hinton GE. How neural networks learn from experience. *Sci Am* (1992) 267:145–51. doi: 10.1038/scientificamerican0992-144
79. Rudie JD, Rauschecker AM, Bryan RN, Davatzikos C, Mohan S. Emerging Applications of Artificial Intelligence in Neuro-Oncology. *Radiology* (2019) 290(3):607–18. doi: 10.1148/radiol.2018181928
80. Sotoudeh H, Shafaat O, Bernstock JD, Brooks MD, Elsayed GA, Chen JA, et al. Artificial Intelligence in the Management of Glioma: Era of Personalized Medicine. *Front Oncol* (2019) 9:768. doi: 10.3389/fonc.2019.00768
81. Jowell T. *BRAIN MATRIX* (2020). Available at: https://www.birmingham.ac.uk/research/activity/mds/trials/crctu/trials/brain-matrix/index.aspx (Accessed 2 May 2020).
82. BRIAN The Brain Tumour Charity. (2020). Available at: https://www.askbrian.org.uk (Accessed 2 May 2020).
83. Hestness J, Narang S, Ardalani N, Diamos G, Jun H, Kianinejad H, et al. *Deep Learning Scaling is Predictable, Empirically* (2017). (Accessed 4 December, 2019).
84. Sun C, Shrivastava A, Singh S, Gupta A. *Revisiting unreasonable effectiveness of data in deep learning era* (2017). (Accessed 4 December, 2019).
85. Lei S, Zhang H, Wang K, Su Z. How training data affect the accuracy & robustness of neural networks for image classification. In: *Proceedings of the 2019 International Conference on Learning Representations (ICLR-2019)*. New Orleans, USA (2019).

86. Zwanenburg A, Leger S, Vallières M. Image biomarker standardisation initiative (2019). Available at: https://arXiv.preprint.arXiv:1612.07003 (Accessed 1 November, 2019).
87. O'Connor JPB, Aboagye EO, Adams JE, Aerts HJW, Barrington SF, Beer AJ, et al. Imaging biomarker roadmap for cancer studies. *Nat Rev Clin Oncol* (2017) 14:169–86. doi: 10.1038/nrclinonc.2016.162
88. Sullivan DC, Obuchowski NA, Kessler LG, Raunig DL, Gatsonis C Huang EP, et al. Metrology standards for quantitative imaging biomarkers. *Radiology* (2015) 277:813–25. doi: 10.1148/radiol.2015142202
89. Collins GS, Reitsma JB, Altman DG, Moons KGTransparent reporting of a multivariable prediction model for individual prognosis or diagnosis (TRIPOD): The TRIPOD statement. *Br J Cancer* (2020) 112:251–9. doi: 10.1038/bjc.2014.639
90. McCulloch P, Altman DG, Campbell WB, Flum DR, Glasziou P, Marshall JC, et al. No surgical innovation without evaluation: the IDEAL recommendations. *Lancet* (2009) 374(9695):1105–12. doi: 10.1016/S0140-6736(09)61116-8
91. Kim A, Thompson E, Governale L, Santa C, Cahill K, Kieran M, et al. Recurrence after gross-total resection of low-grade pediatric brain tumors: the frequency and timing of postoperative imaging. *J Neurosurg Pediatr* (2014) 14:356–64. doi: 10.3171/2014.6.PEDS1321
92. Zaazoue MA, Manley PE, Mehdar MA, Ullrich NJ, Dasenbrock HH, Chordas CA, et al. Optimizing Postoperative Surveillance of Pediatric Low-Grade Glioma Using Tumor Behavior Patterns. *Neurosurgery* (2020) 86:288–97. doi: 10.1093/neuros/nyz072
93. Clement P, Booth T, Borovečki F, Emblem KE, Figueiredo P, Hirschler L, et al. GliMR: Cross-Border Collaborations to Promote Advanced MRI Biomarkers for Glioma. *J Med Biol Eng* (2020). doi: 10.1007/s40846-020-00582-z
94. Society of Neuro-Oncology. (2020). https://soc-neuro-onc.org/WEB/About_Content/News_Pages/RANO_at_SNO.aspx.
95. Equator Network. (2020). https://www.equator-network.org/.
96. Bossuyt PM, Reitsma JB, Bruns DE, Gatsonis CA, Glasziou PP, Irwig L, et al. STARD Group. STARD 2015: An Updated List of Essential Items for Reporting Diagnostic Accuracy Studies. *Radiology* (2015) 277(3):826–32. doi: 10.1148/radiol.2015151516
97. Collins GS, Reitsma JB, Altman DG, Moons KG. Transparent reporting of a multivariable prediction model for individual prognosis or diagnosis (TRIPOD): the TRIPOD Statement. *Eur J Clin Invest* (2015) 45(2):204–14. doi: 10.1111/eci.12376
98. Schulz KF, Altman DG, Moher DCONSORT Group. CONSORT 2010 statement: updated guidelines for reporting parallel group randomized trials. *Ann Intern Med* (2010) 152(11):726–32. doi: 10.7326/0003-4819-152-11-201006010-00232
99. Husereau D, Drummond M, Petrou S, Carswell C, Moher D, Greenberg D, et al. CHEERS Task Force. Consolidated Health Economic Evaluation Reporting Standards (CHEERS) statement. *Int J Technol Assess Health Care* (2013) 29(2):117–22. doi: 10.1017/S0266462313000160

Conflict of Interest: TB, speaker's bureau for AbbVie and Siemens Healthineers. Craig Buckley, Head of Research and Innovation – Siemens Healthineers GB&I. JC, BrainMiner Founder. Involved in machine learning enterprise and business. JK, involved in enterprise and business. MM, BrainMiner Founder. Involved in machine learning enterprise and business. SO, BrainMiner Founder. Involved in machine learning enterprise and business. MP, received payment for consultancy work from Merck not related to cancer. AW, unrestricted educational grant, Bayer Schering, consultancy work and honoraria not related to cancer.

The remaining authors declare that the research was conducted in the absence of any commercial or financial relationships that could be construed as a potential conflict of interest.

frontiers in Neurology

ORIGINAL RESEARCH
published: 22 February 2021
doi: 10.3389/fneur.2021.642241

Machine Learning Analytics of Resting-State Functional Connectivity Predicts Survival Outcomes of Glioblastoma Multiforme Patients

Bidhan Lamichhane[1], Andy G. S. Daniel[2], John J. Lee[3], Daniel S. Marcus[3], Joshua S. Shimony[3] and Eric C. Leuthardt[1,2,4,5,6,7]**

[1] Department of Neurological Surgery, Washington University School of Medicine, St. Louis, MO, United States, [2] Department of Biomedical Engineering, Washington University in St. Louis, St. Louis, MO, United States, [3] Mallinckrodt Institute of Radiology, Washington University School of Medicine, St. Louis, MO, United States, [4] Department of Neuroscience, Washington University School of Medicine, St. Louis, MO, United States, [5] Department of Mechanical Engineering and Materials Science, Washington University in St. Louis, St. Louis, MO, United States, [6] Center for Innovation in Neuroscience and Technology, Washington University School of Medicine, St. Louis, MO, United States, [7] Brain Laser Center, Washington University School of Medicine, St. Louis, MO, United States

OPEN ACCESS

Edited by:
Ravi Prakash Reddy Nanga, University of Pennsylvania, United States

Reviewed by:
Victoria M. Leavitt, Columbia University Irving Medical Center, United States
Bhim M. Adhikari, University of Maryland, Baltimore, United States

***Correspondence:**
Eric C. Leuthardt
leuthardte@wustl.edu
Bidhan Lamichhane
bidhanlamichhane@wustl.edu

Specialty section:
This article was submitted to Applied Neuroimaging, a section of the journal Frontiers in Neurology

Received: 15 December 2020
Accepted: 03 February 2021
Published: 22 February 2021

Citation:
Lamichhane B, Daniel AGS, Lee JJ, Marcus DS, Shimony JS and Leuthardt EC (2021) Machine Learning Analytics of Resting-State Functional Connectivity Predicts Survival Outcomes of Glioblastoma Multiforme Patients. Front. Neurol. 12:642241. doi: 10.3389/fneur.2021.642241

Glioblastoma multiforme (GBM) is the most frequently occurring brain malignancy. Due to its poor prognosis with currently available treatments, there is a pressing need for easily accessible, non-invasive techniques to help inform pre-treatment planning, patient counseling, and improve outcomes. In this study we determined the feasibility of resting-state functional connectivity (rsFC) to classify GBM patients into short-term and long-term survival groups with respect to reported median survival (14.6 months). We used a support vector machine with rsFC between regions of interest as predictive features. We employed a novel hybrid feature selection method whereby features were first filtered using correlations between rsFC and OS, and then using the established method of recursive feature elimination (RFE) to select the optimal feature subset. Leave-one-subject-out cross-validation evaluated the performance of models. Classification between short- and long-term survival accuracy was 71.9%. Sensitivity and specificity were 77.1 and 65.5%, respectively. The area under the receiver operating characteristic curve was 0.752 (95% CI, 0.62–0.88). These findings suggest that highly specific features of rsFC may predict GBM survival. Taken together, the findings of this study support that resting-state fMRI and machine learning analytics could enable a radiomic biomarker for GBM, augmenting care and planning for individual patients.

Keywords: brain tumor, resting state functional connectivity, biomarker, overall survival, short and long-term survival, classification, support vector machine

INTRODUCTION

Glioblastoma multiforme (GBM) is the most frequently occurring brain malignancy. The median survival time is very poor, ranging from 12 to 14.6 months following diagnosis and after receiving the therapeutic standard of care (1, 2). Only 3–5% of GBM patients survive longer than 3 years after diagnosis (3). Facing such abbreviated lifespans, decisions of care balancing aggressiveness of

treatment with impacts on quality of life, are critical to patients. As a result, the identification of novel prognostic biomarkers may have substantial and meaningful impact for individual patients making decisions for their terminal care.

Currently, a tissue diagnosis is required for definitive histopathologic confirmation and optimizing the next steps of care. Factors currently known to be associated with survival include age, Karnofsky performance status (KPS) (4), O6-methylguanine–DNA methyltransferase promoter (MGMT) hypermethylation (5), and mutations in isocitrate dehydrogenase (IDH) 1 or 2 (6, 7). Furthermore, gene expression–based molecular classification of GBM (8), epidermal growth factor receptor amplification (EGFR) (9) and CpG island methylator phenotype status have emerged as additional potential predictors of treatment response and outcome (10). Although such molecular information has improved the clinical assessment of GBM and has been used to better inform clinical trials (5–8, 10, 11), there remains unmet clinical need for accessible, non-invasively acquired biomarkers that predict clinical prognosis and response to therapy for individual patients *prior to surgical intervention and biopsy*.

There are numerous efforts in imaging radiomics to map image features to molecular data. As an example, investigators have correlated quantitative computed tomography (CT) image features to gene expression data of non-small cell lung cancer to predict survival (12, 13). Similarly in GBM, prior work has demonstrated associations between imaging and gene expression (14). These insights have been used to predict response to treatment of gliomas (9). Further, by forming clustering patterns on structural MRI across patients, these patterns can be used to identify GBM phenotypic subtypes (15). In addition to the molecular and genetic features, the synaptic input of neurons on glioblastoma cells has been shown to be a powerful influence of promoting tumor growth (16). Currently, there is no imaging biomarker of this synaptic interaction.

Increasingly, it has become clear that brain networks and their alterations associated with GBM have an impact on survival. Stoecklein et al. demonstrated that resting-state functional connectivity (rsFC) measured by MRI is affected by gliomas throughout the whole brain and this information indicated individual glioma disease burden (17). Daniel et al. took these findings further to show that functionally connected voxels can be routinely found within glioblastoma tumors and that intra-tumor connectivity strength is a prognostic marker for overall survival (18). What is currently lacking is a methodology that leverages these group-level scientific findings and provides an actionable imaging biomarker that can inform and guide clinical care of individual patients.

In this study, we examined whether rsFC between pre-defined regions of interest (ROIs) can enable machine learning algorithms to predict overall survival (OS) for individual patients. For this, we used resting-state functional MRI with blood oxygen level-dependent (BOLD) signals acquired in 64 de novo GBM patients prior to standard of care treatment with surgery and chemoradiation. Retrospectively, patients' clinical course and rsFC between ROIs trained a support vector machine (SVM) to predict OS. In this work we provide evidence that the alterations of functional organization of the brain can provide insights into predicting a GBM patient's oncologic course.

MATERIALS AND METHODS

Participants

A total of 64 patients with a pathologic diagnosis of GBM were included in this study. Patients were recruited from the neurosurgery brain tumor service, initially as part of a National Institutes of Health (NIH) funded tumor database project (NIH 5R01NS066905). Inclusion criteria stipulated that each patient was newly diagnosed with a brain tumor, that they underwent surgical treatment of the tumor, that the pathology was GBM, and that there was a pre-surgical indication for structural MRI and resting-state functional MRI as determined by the treating neurosurgeon. Exclusion criteria were age <18 years and prior surgery for a brain tumor. All patients provided written informed consent and the study was approved by the Institutional Review Board of the Washington University in St. Louis.

Group Construction and Patient Demographics

GBM patients were classified into two groups with respect to the median duration of OS: 14.6 months (1). Patients surviving <14.6 months were grouped as short-term survival (STS) while those surviving 14.6 months or longer were grouped as long-term survival (LTS). Demographic, clinical and molecular characteristics of STS and LTS groups are summarized in **Table 1**.

MRI Acquisition

Imaging was done on Siemens Trio or Skyra MRI scanners operating at 3T. Patients were scanned using a standard presurgical tumor protocol. Structural imaging included T1-weighted magnetization prepared rapid acquisition gradient echo (MPRAGE) and T2-weighted fast spin-echo. Resting-state functional MRI was acquired using echo-planar imaging sequences (voxel size = 3 mm cubic; echo time = 27 ms; repetition time = 2.2–2.9 s; field of view = 256 mm; flip angle = 90°) for a total of 320 frames.

Resting-State Functional Connectivity (rsFC) Pre-processing

We used standard pre-processing approaches previously described (19, 20). Denoising methods included slice timing corrections which removed systematic slice intensity differences due to interleaved acquisition, and head motion corrections within and across runs. Atlas transformations were achieved by the composition of affine transforms connecting functional imaging volumes with T2-weighted and T1-weighted structural images. Thereby, we registered volumetric BOLD time series to an isotropic 3 mm atlas space. Additional preprocessing included spatial smoothing (isotropic 6 mm full-width half-maximum Gaussian blur), removal of linear temporal trends from voxels in each scanning run, and temporal low-pass filtering to retain frequencies <0.1 Hz. Spurious variances were reduced by regression of nuisance waveforms derived from head motion correction and time series sampled from regions of white matter and cerebrospinal fluid. The whole-brain (global)

TABLE 1 | Patients' demographic, clinical, and molecular characteristics of patient population by group.

Summary of characteristics			
	Short term survival ($n = 35$)	**Long term survival ($n = 29$)**	***P*-value**
Age in years (range)	62.6 ± 11.6 (27–83)	58.5 ± 9.1 (41–79)	0.114
Sex			
Male	21 (60.0%)	24 (82.8%)	0.058
Female	14 (40.0%)	5 (17.2%)	
CE volume (cm^3)	37.6 ± 28.7	22.9 ± 28.7	0.004
FLAIR volume (cm^3)	109.4 ± 67.6	83.4 ± 76.5	0.074
KPS, *n* (%)			
>70%	6 (21.4%)	13 (52.0%)	0.025
Missing	7	4	
Extent of resection			
Gross-total	11 (31.4%)	10 (34.5%)	
Subtotal	13 (37.1%)	14 (48.3%)	
Laser	7 (20.0%)	1 (3.5%)	
Biopsy	4 (11.4%)	4 (13.8%)	
MGMT status			
Methylated	12 (37.5%)	13 (52.0%)	0.297
Non-methylated	20 (62.5%)	12 (48.0%)	
Missing	3	4	
IDH mutation			
Mutated	0	0	
Wild type	34	29	
Missing	1	0	
EGFR amplification			
Positive	6 (30.0%)	12 (63.2%)	0.056
Negative	14 (70.0%)	7 (36.8%)	
Missing	15	10	
Overall survival in days	242.1 ± 118.0	840.9 ± 372.6	<0.00001

STS, short-term survival (<14.6 months); LTS, long-term survival (≥14.6 months); CE, contrast enhancement; FLAIR, fluid-attenuated inversion recovery; KPS, Karnofsky performance status; MGMT, methylguanine methyltransferase; IDH, isocitrate dehydrogenase; EGFR, epidermal growth factor receptor.

signal was removed as a nuisance regressor. Frame censoring was performed to minimize the impact of head motion on FC computations. Thus, for each volumetric frame, if the root-mean-square of voxel intensities within brain regions changed significantly compared to the previous frame, the frame was censored. Significant changes were defined as those that exceeded 0.5% of root-mean-square voxel intensities.

Resting-State Functional Connectivity (rsFC) Analysis

The BOLD time series for pre-defined volumetric ROIs were obtained by averaging the voxel time series within each ROI. The rsFC between any pair of ROIs was then defined as Pearson's product moment correlation coefficient between ROI-specified time series. We used the set of 300 ROIs from the study by Seitzman et al. [see (21), for detail]. Briefly summarized, this set of 300 spherical ROIs comprise 264 previously described ROIs (22) with the addition of subcortical and cerebellar ROIs. Thus, the ROI set comprised 239 cortical, 34 subcortical, and 27 cerebellar ROIs. The cortical ROIs belong to one of 13 resting-state networks (RSNs): the cingulo-opercular network (CO), frontoparietal network (FPN), dorsal attention network (DAN), ventral attention network (VAN), salience (SAL) network, somatomotor dorsal (SMD) network, somatomotor lateral (SML) network, visual (VIS) network, auditory (AUD) network, medial temporal lobe (MTL) network, reward (REW) network, parietomedial (PMe) network, the default-mode network (DMN), and cerebellum regions (all cerebellum ROIs). Finally, we identified a collection of twelve ROIs which overlapped with atlas regions for white matter and tentorium, excluding their assignment to any of the 13-resting state functional network. This was consistent with methodological precedence for avoiding confounding of resting-state inferences by ROIs encompassing non-gray matter (22), also see **Supplementary Material**. Thus, for each subject, a 288 × 288 functional connectivity (FC) matrix was computed.

Classification Using Machine Learning

We used the Caret package available within RStudio to implement our machine learning classifier [(23), rstudio.com]. We used a support vector machine (SVM) with linear kernel because of its favorable reported predictive performance in medical knowledge discovery with small amounts of training data (24). Because of the limited number of patients in the present study and our aim to minimizing bias in the estimate of classification accuracy, we used the leave-one-out (LOO) cross-validation method. An overview is illustrated in **Figure 1**. Our use of LOO cross-validation adhered to standard prescriptions for cross-validation implemented in the Caret package. For pedagogical overviews of cross-validation and SVM we recommend the cross-disciplinary textbook by Hastie et al. (25).

This analysis included 64 patients, thus 64-folds of LOO cross-validations. For example, for the first cross-validation fold, all data from one patient were withheld and data from the 63 remaining patients were used for feature selection, training the SVM and tuning hyperparameters. Then, the fold-1 model was tested against the held-out data. In the next cross-validation fold, all data from a different patient were withheld and data from the 63 remaining patients were used for feature selection, retraining the SVM and retuning hyperparameters. Then, the fold-2 model was tested against the held-out data and so on until we predicted (tested) all 64-subjects by running such 64-folds.

The Pearson product moment correlation of 288 ROIs specified in section Resting-State Functional Connectivity (rsFC) Analysis is represented by a correlation matrix of size 288 × 288 (**Figure 1**, step 1). Diagonal matrix elements are exactly unity and non-informative while upper triangular matrix elements are symmetric to lower triangular matrix elements. Consequently, we count the informative correlations over ROIs to be 41,328, equivalent to number of combinations $\left(\frac{288}{2}\right)$. We defined the Fisher z-transformation of this set of informative correlations to be the original features for rsFC. Since the number of original

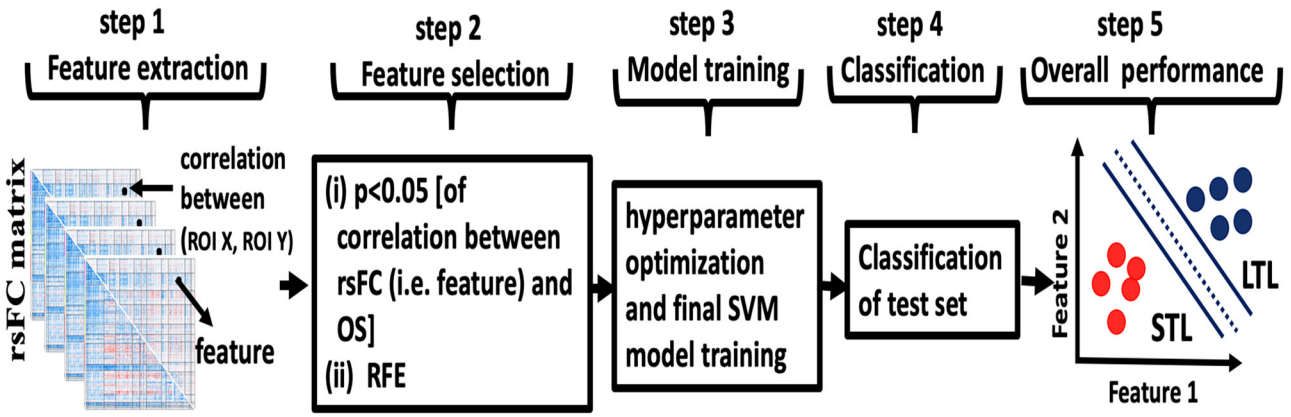

FIGURE 1 | Overview of machine learning. **Step 1**: the rsFC matrix of size 288 × 288 was computed for each patient. The features were rsFC between pairs of ROIs (for example, the correlation between ROI X and ROI Y represented by dots in step 1). **Step 2**: feature selection was performed in two steps using only the lower triangular rsFC matrix to exclude self and symmetric connections. First (i), features with correlation with patients' days of overall survival OS ($p < 0.05$, uncorrected) were selected for heuristic filtering. Then (ii), recursive feature elimination (RFE) was used to select the best predicting feature subset. **Step 3**: hyperparameter optimization and final SVM model training was performed. **Step 4**: the trained model from the cross-validation fold was tested against the single held-out subject. Steps 1–4 were repeated for each fold of leave-one-out cross-validation. **Step 5**: following all cross-validation folds, accuracy, AUC, sensitivity, and specificity for the full sample set were computed.

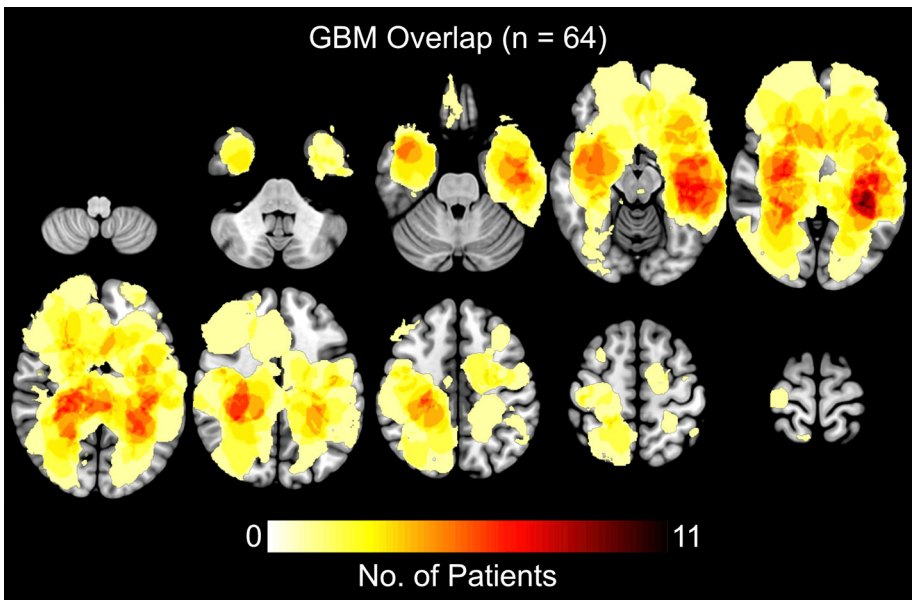

FIGURE 2 | Heatmaps showing the distribution of tumor density, defined by contrast-enhanced (CE) T1w boundaries, in the full sample of 64 patients.

features, 41,328, is much higher than the number of patients, we used feature selection to avoid overfitting our SVM.

Feature selection was performed in two steps (26, 27) (**Figure 1**, step 2). First, using all patient training data (except the withheld subject's data), we computed the correlation of original features for rsFC to OS expressed as continuous time of survival. We discarded features with p-value >0.05 (uncorrected) for heuristic filtering. The p-value for correlations was not used for significance testing of any kind. Second, we used recursive feature elimination (RFE) (28) which also ranks features according to their predictive ability. However, features tend to also be correlated with one another and so the multivariate discriminant classifier retains high dimensionality. RFE repeatedly, and recursively, evaluates the rank of features for predictively ability, eliminating the worst performing features. Within the RFE framework, we used 4-fold internal cross-validation (not to be confused with external LOO cross-validation) with ten iterations to obtain ranked selected features for rsFC. Internal cross-validations and iterations are necessary for RFE to correctly eliminate large numbers of features. Using heuristic p-value

filtering and RFE, we reduced rsFC features from 41,328 to the best performing features subset. Our strategy submitted these best performing features to SVM.

As with other machine learning algorithms, SVM may perform poorly until hyperparameters are tuned for the problem domain. The caret package enabled tuning SVM scaling and model complexity cost using grid search (**Figure 1**, step3). Thus, the main parameters, the cost in case of linear SVM, was estimated by using the grid-search algorithm at the scale of $c =$ 1:10. We used 4-fold cross-validation for hyperparameter tuning following feature extraction, feature selection (p-value filtration and RFE), and in model training. Following training on 63 patients of the training set from LOO, we tested classification performance on the single held-out patient of the test set from LOO (**Figure 1**, step 4). Upon completion of 64 LOO folds, we ascertained the performance of the final classifier, computing accuracy, specificity and sensitivity values using the standard confusion matrix (see **Supplementary Material** for detail). To evaluate overall model performance, we also performed Receiver-operating Characteristic (ROC) curve analysis.

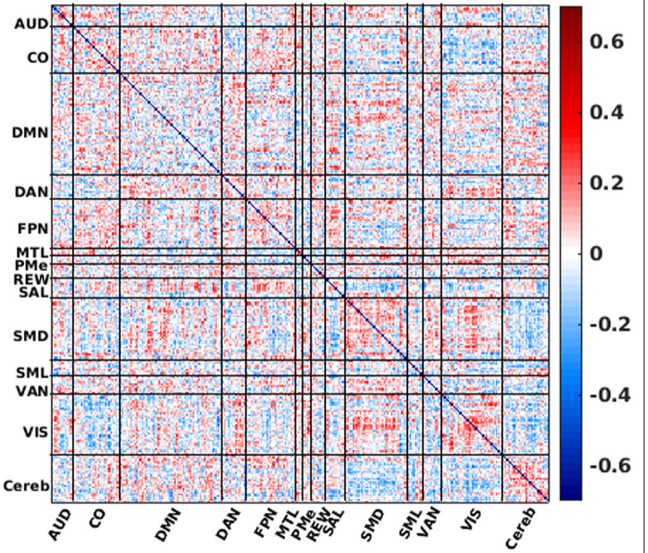

FIGURE 3 | Correlation between rsFC (Fisher's z transformed pairwise ROI correlation) and OS. The horizontal and vertical axis of the plot is the ROI number sorted by the resting-state network. The surface color represents the correlation between OS and ROI-to-ROI rsFC. Correlation strength between ROI pair and OS is represented by colorbar. AUD, auditory; CO, cingulo-opercular; DMN, default-mode network; DAN, dorsal attention network; FPN, frontoparietal network; MTL, medial temporal lobe; PMe, parietomedial network; REW, reward network; SAL, salience network; SMD, somatomotor dorsal network; SML, somatomotor lateral network; VAN, ventral attention network; VIS, visual network; and Cereb, cerebellum regions (all).

RESULTS

A total of 64 patients diagnosed with *de novo* GBM were partitioned into two groups, STS and LTS, based on overall survival (OS). The summary of patient's clinical, molecular, and genetic characteristic of present sample were also reported in **Table 1**. To test the significance of differences in summary characteristics between two groups, we performed the Mann-Whitney U-test (for the continuous variables; age, CE and FLAIR volume, KPS) and Fisher's exact test (for the categorical variables: Sex, MGMT status, IDH mutation, EGFR) and p-value of resultant test were also reported (**Table 1**). Furthermore, the heterogeneity of GBM location, size, and morphology is illustrated in **Figure 2**. These heatmaps represent the distribution of tumor density in the entire patient cohort as defined by contrast-enhanced (CE) T1w boundaries segmented by using the software application ITK-SNAP (29). The distribution shows no systematic asymmetry or focality that could significantly bias the results.

Correlation Between Resting-State Functional Connectivity and Overall Survival (OS)

Figure 3 illustrates how each element of the matrix of canonical functional connectivities correlates with OS. That is, for each element of functional connectivity between ROIs, the vector of measured functional connectivities for 64 patients was correlated with the vector of days of OS for the patients. Please note that the surface color in the **Figure 3** represents the correlation between OS and ROI-to-ROI rsFC. **Figure 3** demonstrates that there are no obvious patterns by which OS may be inferred directly from rsFC. Matrix elements in red denoting positive correlations with OS intersperse with matrix elements in blue denoting negative correlations with OS. This absence of semantic patterns motivates techniques of feature reduction and inference by machine learning. The strategy of heuristic filtering using uncorrected p-values <0.05 pruned 41,328 unique matrix elements to $\sim$1,550 selected matrix elements (the number may change slightly from the fold to fold of LOO cross-validation). The strategy of wrapping using RFE pruned selected matrix elements to just 60 using a principled feature reduction technique (28). The 60 final matrix elements were given to SVM for classification (also see **Supplementary Material** for details)

Machine Learning Classification of Short-Term Survival (STS) and Long-Term Survival (LTS) GBM Patients

The performance of our classification schemes in predicting short vs. long term survival are presented in **Table 2**. Briefly; within-patient classification accuracy was 71.88%. Similarly, the sensitivity and specificity were 77.14 and 65.52%, respectively. The area under the curve (AUC) value was 0.752 (95% CI, 0.62–0.88). The receiver operating characteristic (ROC) curves for stratifying patients is shown in **Figure 4**.

The Most Predictive Features

In order to assess the predictive contribution of each features, we sorted the top 60 contributing features as follows. During model training, feature selection was performed on the training set within each LOO fold, producing variations of selected

TABLE 2 | Classification performance summary of SVM classifier.

SVM (LOO)	Accuracy	Sensitivity	Specificity	AUC	*C*
STS vs. LTS	71.88%	77.14%	65.52%	0.752	1

Regarding C, although we used the grid-search algorithm at the scale of c = 1:10 to optimize C, all selected C were 1.

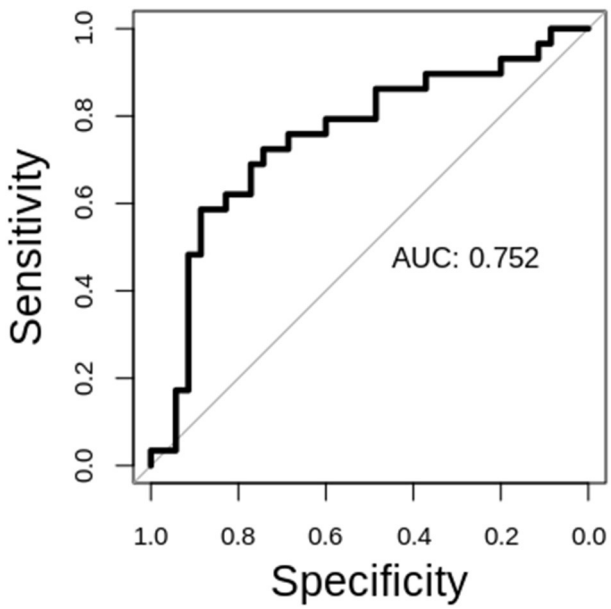

FIGURE 4 | ROC analysis for the STS vs. LTS classification.

features across cross-validation folds. We stored the 60 top-ranking features from SVM-RFE from each LOO fold. We then sorted features according to their frequency of occurrence in all 64 LOO folds. **Figure 5** illustrates, as network adjacency maps, the RSN distribution of the selected features using vertices for ROIs (node) and edges for correlations of selected features with OS. Of the top 60 features, 27 were reproducibly found in all 64 LOO folds, invariant to tumor and physiologic variability across patients [for completeness, anatomical distribution of these top 60 and 27 shared features (separately) were also plotted, see **Supplementary Figures 1, 2**, respectively].

DISCUSSION

Anatomic and functional imaging currently is routinely utilized prior to and during the resection of brain tumors. This technology has been shown to improve the extent of tumor resection (30), and as a result, improve survival statistics (31). That said, it is not routine prior to resections to make use of imaging that reflect the functional organization of the brain and its interaction with the tumor to provide insight into long-term prognosis. Beyond, guiding the specific surgery *per se*, deep insight into the aggressiveness of the tumor informs fundamental decision making about the total course of care. Historically, task-based fMRI has been employed as a means of pre-operatively localizing function (32). During the past decade, it has been shown that the representation of multiple motor, sensory, and cognitive functions can be mapped by analysis of intrinsic brain activity, acquisition of which requires only that the patient hold still during fMRI (33–35). Thus, resting-state fMRI provides a much more complete functional map of the brain than does task-based fMRI; moreover, rs-fMRI is more reliable and much more time-efficient. Finally, the robustness of this mapping modality enables the identification of functional tissue both within a tumor (providing insight into glial-neuronal interactions) and throughout the brain (providing measures of global functional distortions (17, 18, 36–38), What has remained a challenge has been dealing with the complexity and magnitude of the resting-state fMRI data to provide reliable and actionable insights that can enhance clinical care.

Machine learning approaches creates the opportunity to organize large amounts of data to support more generalized and actionable interpretations. In the context of prognostic radiomics for GBM there are several considerations that merit attention. First, in the supervised context, as done in this work, predictions were formulated by direct comparisons of abundant functional data and outcome measurements. Recursive feature elimination (RFE) with support vector machines (SVM) were chosen because they outperformed many popular classification algorithms in a survey of neuroimaging studies of brain disorders: simple thresholding, centroid methods, minimum distance, discriminant function analysis, Gaussian process, spectral clustering, fused lasso, random forests, perceptrons, stacked auto-encoder neural networks, SVM without RFE (39, 40). Second, appropriately selecting features, which determine the dimensionality of a machine learning model, is critical for SVM in the face of limited outcome data, such as the OS of GBM patients. Valid selection of features can help increase prediction accuracies and can also help interpretability. This work made use of a heuristic filtering method that calculated correlations and used uncorrected *p*-values to prune features. RFE then served as a wrapper method to further prune features that were most appropriate for the problem of predicting OS for GBM patients. Third, a linear SVM provided classification. While our feature selection choices provided limited interpretability of feature subsets (network topographies and patterns in neuroanatomy were not evident), feature selection did improve clinically relevant prediction accuracies. Specifically, this work demonstrated that patients with GBM can be partitioned into short term and long-term survival groups using features extracted from resting-state fMRI (**Table 2** and **Figure 4**). These findings complement previous work demonstrating the potential

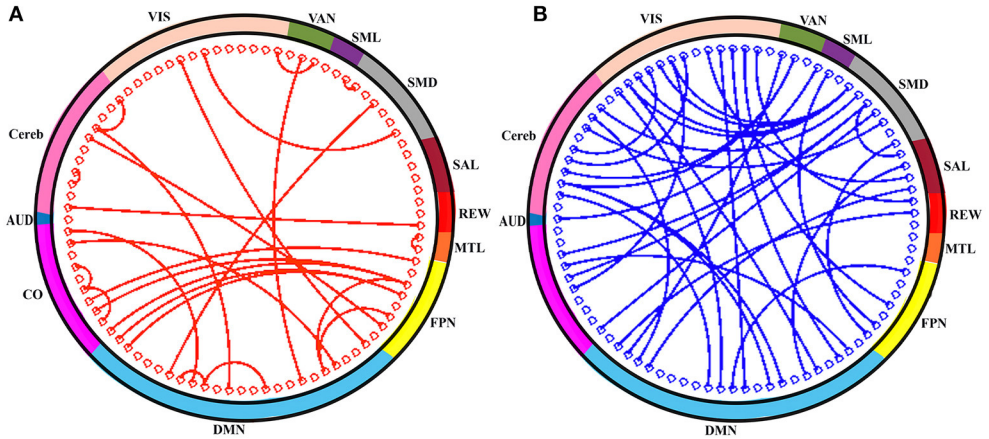

FIGURE 5 | The top-60 frequently selected features are shown in circle. **(A)** Red connection (line) indicates the positive correlation of connections (i.e., rsFC) with OS and that of negatively correlated connections are in blue **(B)**. The color of the outer sphere represents the resting-state network (RSN) that the ROIs belongs to. AUD, auditory; CO, cingulo-opercular network; DMN, default-mode network; FPN, frontoparietal network; MTL, medial temporal lobe; REW, reward network; SAL, salience network; SMD, somatomotor dorsal network; SML, somatomotor lateral network; VAN, ventral attention network; VIS, visual network; and Cereb, cerebellum regions (all).

of rsFC as a biomarker of OS in GBM patients (18). Notably, this work demonstrates predictions of OS for individual patients.

While the prediction of OS is clinically important a caution is warranted in interpreting the features used to make those predictions because of the nature of support vectors in determining decision hypersurfaces in high-dimensional data. The 60 most frequently selected features are plotted in **Figure 5** (anatomical distribution of these features is also plotted, see **Supplementary Figure 1**). Unlike other methods, such as linear discriminant analysis in which features are ascribed shared covariances that occupy the space of dominant features, our use of RFE-SVM selects features which serve as kernel bases optimally separating features which are most ambiguous along the decision boundary. Consequently, while having optimal benefits for generating decision hypersurfaces, our selected features for rsFC in fact visualize anatomy and network adjacencies that are most ambiguous for predicting OS. The difficulty of interpreting features selected by machine learning algorithms is a common problem of neuroimaging research. Many features contribute to the classification of OS because of the complexity of factors that determine OS. Broadly distributed features have been found in many previous investigations of rsFC in GBM patients (41–43).

FC studies have markedly advanced our knowledge of human brain function and its organization. Thus, rsFC has been used to characterize individuals' functional brain organization in patients with a broad range of neurosurgical diseases including GBM. Relatively recently, there were reports of significant alteration of brain functional connectivity in GBM (42, 43). We, for the first time, directly tested the relationship of such changes with OS in GBM patients (**Figure 3**). We emphasize the advantages of rsFC over task-based MRI. For instance, resting-state functional MRI can be acquired in patients that are unable to cooperate with a task, such as cognitively impaired patients as they do not need to perform a task (20, 44, 45). Moreover, task-based fMRI conventionally is restricted to mapping the representation of motor and speech function, which omits other important functions (e.g., executive function, attention, etc.) and does not perform a whole brain assessment. Even the waking state during fMRI is not required as essentially the same functional maps are obtained even if the patient is asleep or sedated (46–48). Thus, rsFC provides information complementary to that obtained from structural imaging of brain tumors. Notably, rsFC throughout the brain is affected by gliomas, even in the non-lesional hemisphere (41–43). This was one of the key motivations for this study.

To our knowledge, no previous studies have examined correlations between rsFC and individual OS as a filtering heuristic. While weak correlations have no role for testing hypothesis, they can provide intermediate data for consumption by more principled algorithms, such as RFE and SVM. These weak correlative relationships may be interpretable in the context that functional connectivity across networks correlates with a patient's cognitive function (41, 49, 50). In cases of high grade GBM, reports describe marked decline in neurocognitive functioning during the course of a patient's disease (51). Moreover, poorer performance on initial cognitive testing is associated with shorter survival (52). Here we demonstrate that a trained SVM predicts short and long-term survival in GBM patients based on rsFC measures. Previous work in GBM patients have shown that cognitive impairment in GBM patients can be associated with both increases and decreases in rsFC (53, 54).

The ability of several rsFC ROI pairs to predict OS further extends our previous report that intratumor rsFC may be a prognostic marker for overall survival (18). This finding aligned with previous reports that brain tumors can lead to various cognitive deficits and are related to alterations in local and interhemispheric rsFC across functional networks (49, 50, 55, 56). Here we showed that particular ROI-pair

dependent reductions and increases in rsFC are associated with OS prediction, suggesting that connectivity alterations at specific cortical locations play an important role in influencing outcomes. Thus, local and global rsFC changes in GBM patients may act as a biomarker for prognosis and disease monitoring.

LIMITATIONS

A common deficiency of neuroimaging studies is limitations of sample size in the presence of data with high dimensional sets of features (57). The difficulties of machine learning methods under these restrictions include overfitting and the inability to adequately represent the complexity of the underlying study problem. Feature selection did not account for tumor location, tumor staging, tumor grading, and aspects of patient demography, such as age, sex, and ethnicity. However, inclusion of such additional features in the classifier are likely to improve the performance of the classifier described in this work. There remain issues regarding reproducibility and generalizability of results. Partial solutions include recruiting larger numbers of patients for study and testing models with unseen data. In this work, we used LOO on all available patient data.

CONCLUSION AND FUTURE WORK

In summary, our results demonstrate that resting-state functional connectivity provides prognostic biomarkers for individual patients with GBM. This work demonstrates prognostic classification of short-term survival vs. long-term survival and suggests how future work may attain more precise predictions of years of survival for individual patients. Such efforts may require extensive longitudinal data to attain clinical utility but such precision predictions would have substantial and meaningful impact for patients with GBM making decisions for their terminal care.

DATA AVAILABILITY STATEMENT

Tumor data will be made available upon request to Eric C. Leuthardt.

ETHICS STATEMENT

The studies involving human participants were reviewed and approved by Institutional Review Board of the Washington University in St. Louis. The patients/participants provided their written informed consent to participate in this study.

AUTHOR CONTRIBUTIONS

BL and EL designed the study. AD, BL, and DM collected and assembled the data. JL and JS assisted in pre-processing of the data. BL and AD performed the post-processing data analysis. BL prepared the first draft. All authors critically reviewed and edited the manuscript.

FUNDING

This research was supported by the National Cancer Institute of the National Institute for Health via grant R01CA203861.

ACKNOWLEDGMENTS

We would like to thank EL's, JS's, and DM's lab team for helpful input and discussions regarding the data analysis of this study.

SUPPLEMENTARY MATERIAL

The Supplementary Material for this article can be found online at: https://www.frontiersin.org/articles/10.3389/fneur.2021.642241/full#supplementary-material

REFERENCES

1. Stupp R, Mason WP, van den Bent MJ, Weller M, Fisher B, Taphoorn MJB, et al. Radiotherapy plus concomitant and adjuvant temozolomide for glioblastoma. *N Engl J Med.* (2005) 352:987–96. doi: 10.1056/NEJMoa043330
2. Stupp R, Hegi ME, Mason WP, van den Bent MJ, Taphoorn MJ, Janzer RC, et al. Effects of radiotherapy with concomitant and adjuvant temozolomide versus radiotherapy alone on survival in glioblastoma in a randomised phase III study: 5-year analysis of the EORTC-NCIC trial. *Lancet Oncol.* (2009) 10:459–66. doi: 10.1016/S1470-2045(09)70025-7
3. Krex D, Klink B, Hartmann C, Von Deimling A, Pietsch T, Simon M, et al. Long-term survival with glioblastoma multiforme. *Brain.* (2007) 130:2596–606. doi: 10.1093/brain/awm204
4. Laws ER, Parney IF, Huang W, Anderson F, Morris AM, Asher A, et al. Survival following surgery and prognostic factors for recently diagnosed malignant glioma: data from the glioma outcomes project. *J Neurosurg.* (2003) 99:467–73. doi: 10.3171/jns.2003.99.3.0467
5. Hegi ME, Liu L, Herman JG, Stupp R, Wick W, Weller M, et al. Correlation of O6-methylguanine methyltransferase (MGMT) promoter methylation with clinical outcomes in glioblastoma and clinical strategies to modulate MGMT activity. *J Clin Oncol.* (2008) 26:4189–99. doi: 10.1200/JCO.2007.11.5964
6. Sanson M, Marie Y, Paris S, Idbaih A, Laffaire J, Ducray F, et al. Isocitrate dehydrogenase 1 codon 132 mutation is an important prognostic biomarker in gliomas. *J Clin Oncol.* (2009) 27:4150–4. doi: 10.1200/JCO.2009.21.9832
7. Yan H, Parsons DW, Jin G, McLendon R, Rasheed BA, Yuan W, et al. IDH1 and IDH2 mutations in gliomas. *N Engl J Med.* (2009) 360:765–73. doi: 10.1056/NEJMoa0808710
8. Verhaak RGW, Hoadley KA, Purdom E, Wang V, Qi Y, Wilkerson MD, et al. Integrated genomic analysis identifies clinically relevant subtypes of glioblastoma characterized by abnormalities in PDGFRA, IDH1, EGFR, and NF1. *Cancer Cell.* (2010) 17:98–110. doi: 10.1016/j.ccr.2009.12.020
9. Haas-Kogan DA, Prados MD, Tihan T, Eberhard DA, Jelluma N, Arvold ND, et al. Epidermal growth factor receptor, protein kinase B/Akt, and glioma response to erlotinib. *J Natl Cancer Inst.* (2005) 97:880–7. doi: 10.1093/jnci/dji161
10. Noushmehr H, Weisenberger DJ, Diefes K, Phillips HS, Pujara K, Berman BP, et al. Identification of a CpG island methylator phenotype that defines a distinct subgroup of glioma. *Cancer Cell.* (2010) 17:510–22. doi: 10.1016/j.ccr.2010.03.017
11. Sturm D, Witt H, Hovestadt V, Khuong-Quang DA, Jones DTW, Konermann C, et al. Hotspot mutations in H3F3A and IDH1 Define distinct epigenetic and biological subgroups of glioblastoma. *Cancer Cell.* (2012) 22:425–37. doi: 10.1016/j.ccr.2012.08.024

12. Gevaert O, Xu J, Hoang CD, Leung AN, Xu Y, Quon A, et al. Non-small cell lung cancer: identifying prognostic imaging biomarkers by leveraging public gene expression microarray data–methods and preliminary results. *Radiology.* (2012) 264:387–96. doi: 10.1148/radiol.12111607
13. Nair VS, Gevaert O, Davidzon G, Napel S, Graves EE, Hoang CD, et al. Prognostic PET 18F-FDG uptake imaging features are associated with major oncogenomic alterations in patients with resected non-small cell lung cancer. *Cancer Res.* (2012) 72:3725–34. doi: 10.1158/0008-5472.CAN-11-3943
14. Gevaert O, Mitchell LA, Achrol AS, Xu J, Echegaray S, Steinberg GK, et al. Glioblastoma multiforme: exploratory radiogenomic analysis by using quantitative image features. *Radiology.* (2014) 273:168–74. doi: 10.1148/radiol.14131731
15. Itakura H, Achrol AS, Mitchell LA, Loya JJ, Liu T, Westbroek EM, et al. Magnetic resonance image features identify glioblastoma phenotypic subtypes with distinct molecular pathway activities. *Sci Transl Med.* (2015) 7:1–11. doi: 10.1126/scitranslmed.aaa7582
16. Venkatesh HS, Morishita W, Geraghty AC, Silverbush D, Woo PJ, Taylor KR, et al. Electrical and synaptic integration of glioma into neural circuits. *Nature.* (2020) 573:539–45. doi: 10.1038/s41586-019-1563
17. Stoecklein VM, Stoecklein S, Galiè F, Ren J, Schmutzer M, Unterrainer M, et al. Resting-state fMRI detects alterations in whole brain connectivity related to tumor biology in glioma patients. *Neuro Oncol.* (2020) 22:1388–98. doi: 10.1093/neuonc/noaa044
18. Daniel AGS, Park KY, Roland JL, Dierker D, Gross J, Humphries JB, et al. Functional connectivity within glioblastoma impacts overall survival. *Neuro Oncol.* (2020) 1–10. doi: 10.1093/neuonc/noaa189
19. Power JD, Mitra A, Laumann TO, Snyder AZ, Schlaggar BL, Petersen SE. Methods to detect, characterize, and remove motion artifact in resting state fMRI. *Neuroimage.* (2014) 84:320–41. doi: 10.1016/j.neuroimage.2013.08.048
20. Leuthardt EC, Guzman G, Bandt SK, Hacker C, Vellimana AK, Limbrick D, et al. Integration of resting state functional MRI into clinical practice–a large single institution experience. *PLoS ONE.* (2018) 13:e0198349. doi: 10.1371/journal.pone.0198349
21. Seitzman BA, Gratton C, Marek S, Raut RV, Dosenbach NUF, Schlaggar BL, et al. A set of functionally-defined brain regions with improved representation of the subcortex and cerebellum. *Neuroimage.* (2020) 206:116290. doi: 10.1016/j.neuroimage.2019.116290
22. Power JD, Cohen AL, Nelson SM, Wig GS, Barnes KA, Church JA, et al. Functional network organization of the human brain. *Neuron.* (2011) 72:665–78. doi: 10.1016/j.neuron.2011.09.006
23. Kuhn M. Building predictive models in R using the caret package. *J Stat Softw.* (2008) 28:1–26. doi: 10.18637/jss.v028.i05
24. Arslan AK, Colak C, Sarihan ME. Different medical data mining approaches based prediction of ischemic stroke. *Comput Methods Programs Biomed.* (2016) 130:87–92. doi: 10.1016/j.cmpb.2016.03.022
25. Hastie T, Tibshirani R, Friedman J. *The Elements of Statistical Learning (Sections 7.10 and Chapter 12).* 2nd ed. New York, NY: Springer US (2008).
26. Chen G, Ward BD, Xie C, Li W, Wu Z, Jones JL, et al. Classification of Alzheimer disease, mild cognitive impairment, and normal cognitive status with large-scale network analysis based on resting-state functional MR imaging. *Radiology.* (2011) 259:213–21. doi: 10.1148/radiol.10100734
27. Liu F, Xie B, Wang Y, Guo W, Fouche JP, Long Z, et al. Characterization of post-traumatic stress disorder using resting-state fMRI with a multi-level parametric classification approach. *Brain Topogr.* (2014) 28:221–37. doi: 10.1007/s10548-014-0386-2
28. Guyon I, Weston J, Barnhill S. Gene selection for cancer classification using support vector machines. *Mach Learn.* (2002) 46:389–422. doi: 10.1023/A:1012487302797
29. Yushkevich PA, Piven J, Hazlett HC, Smith RG, Ho S, Gee JC, et al. User-guided 3D active contour segmentation of anatomical structures: significantly improved efficiency and reliability. *Neuroimage.* (2006) 31:1116–28. doi: 10.1016/j.neuroimage.2006.01.015
30. Slavin KV. Neuronavigation in neurosurgery: current state of affairs. *Expert Rev Med Devices.* (2008) 5:1–3. doi: 10.1586/17434440.5.1.1
31. Lacroix M, Abi-Said D, Fourney DR, Gokaslan ZL, Shi W, DeMonte F, et al. A multivariate analysis of 416 patients with glioblastoma multiforme: prognosis, extent of resection, and survival. *J Neurosurg.* (2001) 95:190–8. doi: 10.3171/jns.2001.95.2.0190
32. McGirt MJ, Mukherjee D, Chaichana KL, Than KD, Weingart JD. Quinones-Hinojosa A. Association of surgically acquired motor and language deficits on overall survival after resection of glioblastoma multiforme. *Neurosurgery.* (2009) 65:463–70. doi: 10.1227/01.NEU.0000349763.42238.E9
33. Lee MH, Hacker CD, Snyder AZ, Corbetta M, Zhang D, Leuthardt EC, et al. Clustering of resting state networks. *PLoS ONE.* (2012) 7:e40370. doi: 10.1371/journal.pone.0040370
34. Hacker CD, Laumann TO, Szrama NP, Baldassarre A, Snyder AZ, Leuthardt EC, et al. Resting state network estimation in individual subjects. *Neuroimage.* (2013) 82:616–33. doi: 10.1016/j.neuroimage.2013.05.108
35. Mitchell TJ, Hacker CD, Breshears JD, Szrama NP, Sharma M, Bundy DT, et al. A novel data-driven approach to preoperative mapping of functional cortex using resting-state functional magnetic resonance imaging. *Neurosurgery.* (2013) 73:963–9. doi: 10.1227/NEU.0000000000000141
36. Håberg A, Kvistad KA, Unsgård G, Haraldseth O. Preoperative blood oxygen level-dependent functional magnetic resonance imaging in patients with primary brain tumors: clinical application and outcome. *Neurosurgery.* (2004) 54:902–5. doi: 10.1227/01.neu.0000114510.05922.f8
37. Derks J, Dirkson AR, de Witt Hamer PC, van Geest Q, Hulst HE, Barkhof F, et al. Connectomic profile and clinical phenotype in newly diagnosed glioma patients. *Neuroimage Clin.* (2017) 14:87–96. doi: 10.1016/j.nicl.2017.01.007
38. Liu L, Zhang H, Wu J, Yu Z, Chen X, Rekik I, et al. Overall survival time prediction for high-grade glioma patients based on large-scale brain functional networks. *Brain Imaging Behav.* (2019) 13:1333–51. doi: 10.1007/s11682-018-9949-2
39. Arbabshirani MR, Plis S, Sui J, Calhoun VD. Single subject prediction of brain disorders in neuroimaging: promises and pitfalls. *Neuroimage.* (2017) 145:137–65. doi: 10.1016/j.neuroimage.2016.02.079
40. Qiao C, Lu L, Yang L, Kennedy PJ. Identifying brain abnormalities with schizophrenia based on a hybrid feature selection technology. *Appl Sci.* (2019) 9:1–23. doi: 10.3390/app9102148
41. Maesawa S, Bagarinao E, Fujii M, Futamura M, Motomura K, Watanabe H, et al. Evaluation of resting state networks in patients with gliomas: connectivity changes in the unaffected side and its relation to cognitive function. *PLoS ONE.* (2015) 10:e0118072. doi: 10.1371/journal.pone.0118072
42. Catalino MP, Yao S, Green DL, Laws ER, Golby AJ, Tie Y. Mapping cognitive and emotional networks in neurosurgical patients using resting-state functional magnetic resonance imaging. *Neurosurg Focus.* (2020) 48:E9. doi: 10.3171/2019.11.FOCUS19773
43. Manan HA, Franz EA, Yahya N. Functional connectivity changes in patients with brain tumours—a systematic review on resting state-fMRI. *Neurol Psychiatry Brain Res.* (2020) 36:73–82. doi: 10.1016/j.npbr.2020.03.003
44. Rosazza C, Aquino D, D'Incerti L, Cordella R, Andronache A, Zacà D, et al. Preoperative mapping of the sensorimotor cortex: comparative assessment of task-based and resting-state fMRI. *PLoS ONE.* (2014) 9:e98860. doi: 10.1371/journal.pone.0098860
45. Lee MH, Miller-Thomas MM, Benzinger TL, Marcus DS, Hacker CD, Leuthardt EC, et al. Clinical resting-state fMRI in the preoperative setting. *Top Magn Reson Imaging.* (2016) 25:11–8. doi: 10.1097/rmr.0000000000000075
46. Vincent JL, Patel GH, Fox MD, Snyder AZ, Baker JT, Van Essen DC, et al. Intrinsic functional architecture in the anaesthetized monkey brain. *Nature.* (2007) 447:83–6. doi: 10.1038/nature05758
47. Larson-Prior LJ, Zempel JM, Nolan TS, Prior FW, Snyder A, Raichle ME. Cortical network functional connectivity in the descent to sleep. *Proc Natl Acad Sci USA.* (2009) 106:4489–94. doi: 10.1073/pnas.0900924106
48. Breshears JD, Gaona CM, Roland JL, Sharma M, Bundy DT, Shimony JS, et al. Mapping sensorimotor cortex with slow cortical potential resting-state networks while awake and under anesthesia. *Neurosurgery.* (2012) 71:305–16. doi: 10.1227/NEU.0b013e318258e5d1
49. Fox ME, King TZ. Functional connectivity in adult brain tumor patients: a systematic review. *Brain Connect.* (2018) 8:381–97. doi: 10.1089/brain.2018.0623
50. Ghinda DC, Wu JS, Duncan NW, Northoff G. How much is enough—can resting state fMRI provide a demarcation for neurosurgical resection in glioma? *Neurosci Biobehav Rev.* (2018) 84:245–61. doi: 10.1016/j.neubiorev.2017.11.019

51. Bosma I, Vos MJ, Heimans JJ, Taphoorn MJB, Aaronson NK, Postma TJ, et al. The course of neurocognitive functioning in high-grade glioma patients. *Neuro Oncol.* (2007) 9:53–62. doi: 10.1215/15228517-2006-012
52. Johnson DR, Wefel JS. Relationship between cognitive function and prognosis in glioblastoma. *CNS Oncol.* (2013) 2:195–201. doi: 10.2217/cns.13.5
53. Lang S, Gaxiola-Va, Opoku-Darko M, Partlo LA, Goodyear BG, Kelly JJP, et al. Functional connectivity in frontoparietal network: indicator of preoperative cognitive function and cognitive outcome following surgery in patients with glioma. *Srp Arh Celok Lek.* (2017) 16:87–98. doi: 10.2298/SARH170718174T
54. Jütten K, Mainz V, Delev D, Gauggel S, Binkofski F, Wiesmann M, et al. Asymmetric tumor-related alterations of network-specific intrinsic functional connectivity in glioma patients. *Hum Brain Mapp.* (2020) 41:4549–61. doi: 10.1002/hbm.25140
55. Zhang N, Xia M, Qiu T, Wang X, Lin C, Guo Q, et al. Reorganization of cerebro-cerebellar circuit in patients with left hemispheric gliomas involving language network: a combined structural and resting-state functional MRI study. *Hum. Brain Mapp.* (2018) 39:4802–19. doi: 10.1002/hbm.24324
56. Yuan B, Zhang N, Yan J, Cheng J, Lu J, Wu J. Resting-state functional connectivity predicts individual language impairment of patients with left hemispheric gliomas involving language network. *Neuroimage Clin.* (2019) 24:102023. doi: 10.1016/j.nicl.2019.102023
57. Saeys Y, Inza I, Larrañaga P. A review of feature selection techniques in bioinformatics. *Bioinformatics.* (2007) 23:2507–17. doi: 10.1093/bioinformatics/btm344

Conflict of Interest: EL has equity in Neurolutions, Inner Cosmos, and Sora Neuroscience. Washington University has equity in Neurolutions. DM owns stock in Radiologics and Sora Neuroscience.

The remaining authors declare that the research was conducted in the absence of any commercial or financial relationships that could be construed as a potential conflict of interest.

frontiers in Oncology

ORIGINAL RESEARCH
published: 23 March 2021
doi: 10.3389/fonc.2021.648528

Effect of Applying Leakage Correction on rCBV Measurement Derived From DSC-MRI in Enhancing and Nonenhancing Glioma

Fatemeh Arzanforoosh[1*], *Paula L. Croal*[2,3], *Karin A. van Garderen*[1], *Marion Smits*[1], *Michael A. Chappell*[2,3,4] *and Esther A. H. Warnert*[1]

[1] Department of Radiology and Nuclear Medicine, Erasmus MC, Rotterdam, Netherlands, [2] Radiological Sciences, Mental Health and Clinical Neurosciences, School of Medicine, University of Nottingham, Nottingham, United Kingdom, [3] Sir Peter Mansfield Imaging Centre, School of Medicine, University of Nottingham, Nottingham, United Kingdom, [4] NIHR Nottingham Biomedical Research Centre, Queen's Medical Centre, University of Nottingham, Nottingham, United Kingdom

OPEN ACCESS

Edited by:
Ravi Prakash Reddy Nanga, University of Pennsylvania, United States

Reviewed by:
Nico Sollmann, Technical University of Munich, Germany
Ashley M. Stokes, Barrow Neurological Institute (BNI), United States

***Correspondence:**
Fatemeh Arzanforoosh
f.arzanforoosh@erasmusmc.nl

Specialty section:
This article was submitted to Neuro-Oncology and Neurosurgical Oncology, a section of the journal Frontiers in Oncology

Received: 31 December 2020
Accepted: 25 February 2021
Published: 23 March 2021

Citation:
Arzanforoosh F, Croal PL, van Garderen KA, Smits M, Chappell MA and Warnert EAH (2021) Effect of Applying Leakage Correction on rCBV Measurement Derived From DSC-MRI in Enhancing and Nonenhancing Glioma. Front. Oncol. 11:648528. doi: 10.3389/fonc.2021.648528

Purpose: Relative cerebral blood volume (rCBV) is the most widely used parameter derived from DSC perfusion MR imaging for predicting brain tumor aggressiveness. However, accurate rCBV estimation is challenging in enhancing glioma, because of contrast agent extravasation through a disrupted blood-brain barrier (BBB), and even for nonenhancing glioma with an intact BBB, due to an elevated steady-state contrast agent concentration in the vasculature after first passage. In this study a thorough investigation of the effects of two different leakage correction algorithms on rCBV estimation for enhancing and nonenhancing tumors was conducted.

Methods: Two datasets were used retrospectively in this study: 1. A publicly available TCIA dataset (49 patients with 35 enhancing and 14 nonenhancing glioma); 2. A dataset acquired clinically at Erasmus MC (EMC, Rotterdam, NL) (47 patients with 20 enhancing and 27 nonenhancing glial brain lesions). The leakage correction algorithms investigated in this study were: a unidirectional model-based algorithm with flux of contrast agent from the intra- to the extravascular extracellular space (EES); and a bidirectional model-based algorithm additionally including flow from EES to the intravascular space.

Results: In enhancing glioma, the estimated average contrast-enhanced tumor rCBV significantly (Bonferroni corrected Wilcoxon Signed Rank Test, $p < 0.05$) decreased across the patients when applying unidirectional and bidirectional correction: 4.00 ± 2.11 (uncorrected), 3.19 ± 1.65 (unidirectional), and 2.91 ± 1.55 (bidirectional) in TCIA dataset and 2.51 ± 1.3 (uncorrected), 1.72 ± 0.84 (unidirectional), and 1.59 ± 0.9 (bidirectional) in EMC dataset. In nonenhancing glioma, a significant but smaller difference in observed rCBV was found after application of both correction methods used in this study: 1.42 ± 0.60 (uncorrected), 1.28 ± 0.46 (unidirectional), and 1.24 ± 0.37 (bidirectional) in TCIA dataset and 0.91 ± 0.49 (uncorrected), 0.77 ± 0.37 (unidirectional), and 0.67 ± 0.34 (bidirectional) in EMC dataset.

Conclusion: Both leakage correction algorithms were found to change rCBV estimation with BBB disruption in enhancing glioma, and to a lesser degree in nonenhancing glioma. Stronger effects were found for bidirectional leakage correction than for unidirectional leakage correction.

Keywords: dynamic susceptibility contrast (DSC), relative cerebral blood volume (rCBV), unidirectional leakage correction, bidirectional leakage correction, glioma

INTRODUCTION

Dynamic susceptibility contrast (DSC)-MRI is a technique that uses rapid measurements of MRI signal change following the injection of a gadolinium-based contrast agent (GBCA) (1). Perfusion parameters derived from DSC-MRI are increasingly utilized as image-based biomarkers for management of patients with brain cancer. Of particular interest is relative cerebral blood volume (rCBV). It is the most widely used parameter derived from DSC-MRI for predicting brain tumor aggressiveness (2, 3). rCBV also has the potential to predict overall survival of brain tumor patients (4) and can be used in brain tumor monitoring, where it may have value in early detection of local recurrence or malignant transformation, and can aid in differentiation of posttreatment changes from tumor recurrence (5).

A particular challenge in using DSC-MRI for the determination of rCBV in brain tumors is that the presence of a leaky blood-brain barrier (BBB) may confound measurements (6). GBCA leads to shortening of effective transverse relaxation time T_2^* and shortening of longitudinal relaxation time T_1. In T_2^*-weighted DSC-MRI acquisition, the shortening of T_2^* results in signal loss induced by the passage of the paramagnetic contrast agent. This forms the basis of rCBV estimation. In lesions with a disrupted BBB, GBCA leaks into the extravascular extracellular space (EES), reducing both T_2^* time and T_1 time even further. In DSC-based perfusion quantification, this phenomenon violates underlying assumptions and thus could lead either to an under- or overestimation of rCBV, depending on the dominant leakage effect (7). A disrupted BBB is present in enhancing glioma, defined as a glial tumor in which a signal increase is clearly seen on T_1-weighted imaging after injection of a GBCA.

Various strategies have been proposed to address the GBCA leakage issue in DSC-MRI; however, no universally accepted method currently exists (8). Many of these techniques concentrate on the reduction of T_1 effects, such as application of a preload bolus injection of contrast agent or optimizing acquisition parameters such as echo time, repetition time and flip angle (9, 10). Using a preload prior to the bolus injection for the DSC acquisition is done to saturate the EES and thereby diminish the T_1 induced signal intensity increase during the subsequent DSC-MRI GBCA administration (11). A number of post-processing methods have also been proposed to correct both T_2^* – and T_1-related leakage effects, either by themselves or in addition to advanced acquisition methods (12–15). Among first published post processing methods for addressing GBCA leakage in glioma was the model-based approach by Boxerman–Schmainda–Weisskoff (12). Known as the BSW leakage correction method, it aims to correct both T_2^* – and T_1-related leakage effects by modeling the temporal curves of transverse relaxation rate changes in tumor voxels using two terms: one derived from the average relaxivity in nonenhancing tissues, where there is no contrast agent leakage, and the other term that models contrast agent flux from the intravascular space to the EES, with the assumption of no contrast agent back flux.

The BSW method has been widely used and implemented by several commercial software vendors (16). It has been shown that rCBV measurements resulting from a DSC acquisition acquired after a preload and with using the BSW method agree well with histology in spatially correlated tissue biopsies in patients diagnosed with high grade glioma (17, 18). Despite this promising result, limitations of the BSW approach prompted researchers to look for modifications to this leakage correction method. Leigh et al. (13) introduced an arrival time correction to this model, in order to solve mismatch of mean transit time between normal and malignant tissue. Bjørnerud et al. (14) estimated leakage from the residue function, obtained *via* singular value decomposition (SVD), to distinguish between T_1 and T_2^* dominant extravasation effects. Recently, the BSW model was extended with bidirectional contrast agent exchange, additionally including flow from EES to the intravascular space (15, 19). Considering that contrast agent exchange is in principle bidirectional, this modification could potentially improve the accuracy of rCBV estimates.

In light of the rising use of rCBV and other DSC-based biomarkers and with current recommendations for acquiring DSC-MRI data including a preload bolus (20), there is an increasing demand for guidance on accurate leakage correction in clinical settings. Moreover, the necessity of using model-based postprocessing leakage correction has been highlighted for high-grade gliomas (20), where typically a contrast-enhancing lesion is seen in T_1-weighted postcontrast images. However, to the best of our knowledge, the effect of using leakage correction algorithm on nonenhancing glioma, when there is no visually detectable contrast enhancing lesion in T_1-weighted postcontrast, has not been investigated. Fully understanding the effects of applying leakage correction for rCBV estimation can help the radiologists and technicians using commercial or free software for analyzing DSC-MRI data decide if they need to "tick the box" of leakage correction for both enhancing and nonenhancing tumor. Therefore, this study focuses on a thorough investigation of the effect of using the well-known BSW leakage correction algorithm (12) as well as its recent modified leakage correction algorithm (19) on rCBV estimation in both enhancing and nonenhancing glioma, using two different datasets acquired

with different parameters and different GBCA dosage. In the following, we will refer to the former method as the unidirectional and the latter as the bidirectional leakage correction algorithm.

MATERIALS AND METHODS

The Theory

In DSC-MRI, the dynamic signal drop caused by passage of an intravascular GBCA bolus is assumed to be proportional to the change in concentration of GBCA over time, causing a proportional change in relaxation rate (21), as expressed by equation [1]:

$$C(t) \propto \Delta R_2^*(t) = -(1/T_E) \times (ln(S(t)/S_0)) \quad (1)$$

where $\Delta R_2^*(t)$ is the inverse of the change in T_2^* relaxation time (relaxivity-time curve), C(t) is the tracer concentration at time t, S(t) is the intensity time-signal, S_0 is the baseline signal in the voxel prior to the contrast bolus arrival, and T_E is the echo time. The uncorrected rCBV is estimated by trapezoidal integration between entrance t_0 and exit t_1 time points of the bolus in the relaxivity-time curve:

$$rCBV = \int_{t_0}^{t_1} \Delta R_2^*(t)\, dt \quad (2)$$

In the unidirectional leakage correction algorithm, the measured relaxivity change $\Delta R_2^*(t)$ for each voxel can be modeled as a linear combination of the whole-brain average relaxivity-time curve $\overline{\Delta R_2^*}(t)$ in nonenhancing voxels and its time integral:

$$\Delta R_2^*(t) \approx K_1\, \overline{\Delta R_2^*}(t) - K_2 \int_0^t \overline{\Delta R_2^*}(t')\, dt' \quad (3)$$

where K_1 (sec^{-1}) is a susceptibility scaling factor, K_2 (sec^{-1}) is a permeability related parameter for intra- to extravascular contrast flux and both are estimated by a linear least square fit of the measured $\Delta R_2^*(t)$ to equation [3]. Thus, the unidirectional corrected relaxivity-time curve $\Delta R^*_{2\,\mathrm{unidir}}$ and $rCBV_{unidir}$ can be calculated for each voxel:

$$\Delta R^*_{2\,unidir}(t) = \Delta R_2^*(t) + K_2 \int_0^t \overline{\Delta R_2^*}(t')\, dt' \quad (4)$$

$$rCBV_{unidir} = \int_{t_0}^{t_1} \Delta R^*_{2\,unidir}(t)\, dt \quad (5)$$

In the bidirectional leakage correction algorithm, the assumption is that contrast agent flows back and forth between the intravascular and extravascular compartment. This is implemented by adding an extra term to equation [3] where $\Delta R_2^*(t)$ can be modeled as follows:

$$\Delta R_2^*(t) \approx K_1\, \overline{\Delta R_2^*}(t) - K_2 \int_0^t \overline{\Delta R_2^*}(t')\, e^{-K_{ep}(t-t')} dt' \quad (6)$$

where K_{ep} is the transfer coefficient for extra- to intravascular contrast flux and substituting K_{ep}=0 yields the unidirectional leakage correction equation [3]. After applying least square fitting, and obtaining K_1, K_2 and K_{ep} the bidirectional corrected relaxivity-time curve $\Delta R^*_{2\,\mathrm{bidir}}$ and $rCBV_{bidir}$ can be calculated for each voxel:

$$\Delta R^*_{2\,bidir}(t) = \Delta R_2^*(t) + K_2 \int_0^t \overline{\Delta R_2^*}(t')\, e^{-k_{ep}(t-t')}\, dt' \quad (7)$$

$$rCBV_{bidir} = \int_{t_0}^{t_1} \Delta R^*_{2\,bidir}(t)\, dt \quad (8)$$

Note that we did not impose any constraints for fitting K_{ep}, K_2 and K_1 in any of those methods. This allows K_2 to be positive or negative in both methods to account for T_1 and T_2^* leakage effects.

Patients and MR Imaging

Two datasets were used retrospectively in this study. The first dataset, "Glioma DSC-MRI Perfusion Data", is publicly available in The Cancer Imaging Archive (TCIA) (22, 23). This dataset contains 49 patients (51 ± 16 years, 31 male) with coregistered DSC-MRI and post contrast T_1-weighted SPGR images of nonenhancing (n = 14) and enhancing (n = 35) glioma. These MR images were acquired at 1.5T or 3T on systems from two vendors (GE Healthcare, Waukesha, WI, US; Siemens, Erlangen, DE). All patients had received 0.1 mmol/kg of gadobenate dimeglumine (MultiHance, Bracco Diagnostics, Cranbury, NJ, US) during DSC-MRI acquisition with gradient-echo echo-planar imaging (Repetition Time (T_R): 1.1/1.25 s, Echo Time (T_E): 30 ms, Flip Angle (FA): 70/72/80°, 120 dynamics, voxel size: 0.85 × 0.85 × 6.5 mm^3, 13 slices), preceded by the injection of 0.05 mmol/kg of the same contrast agent as preload bolus, except for one patient who had received 0.01 mmol/kg for preload. A power injector was used for contrast agent injection with antecubital injection and typically set at a rate of 3 ml/s. The parameters for T_1-weighted postcontrast are not consistent between all patients (T_R ranging from 34 ms to 666 ms, T_E ranging from 2.3 ms to 21 ms).

The second dataset collected at the Erasmus MC (EMC, Rotterdam, the Netherlands) contained 47 patients (50 ± 10 years, 32 male) with coregistered T_1-weighted (FSPGR) and DSC-MRI images from patients with confirmed enhancing (n = 20) and nonenhancing (n = 27) glioma. These patients underwent MRI scans at 3T (Discovery MR750, GE, Waukesha, USA) with preload administration of 7.5 ml of gadobutrol 1.0 mmol/ml (Gadovist®1.0, Bayer AG, Leverkusen, DE) followed by administration of the same dose of gadobutrol during DSC acquisition with GRE echo-planar imaging (T_R: 2 s, T_E:45 ms, FA: 90°, 50 dynamics, voxel size: 2 × 2 × 5 mm^3, 26 slices). The contrast agent injection was done by power injector with an injection rate of 5 ml/s of the bolus as well as the saline flush (20 ml, following the contrast agent bolus). Additionally, high resolution inversion recovery T_1-weighted pre- and postcontrast images (T_R: 2.1 ms, T_E: 4.6 ms, voxel size: 0.5 × 0.5 × 0.8 mm^3), structural images of T_2-weighted (T2W) (T_R: 0.14 s, T_E: 8.4 s,

voxel size: $0.46 \times 0.46 \times 5.00$ mm^3) and FLAIR (Fluid-Attenuated Inversion Recovery) (T_R: 1.7 s, T_E: 90 ms, voxel size: $0.54 \times 0.54 \times 0.79$ mm^3) were collected in this dataset. The complete protocol is part of routine clinical imaging and all patients provided informed written consent to have their information stored in an Institutional Review Board Approved Neuro-Oncology database for use in future investigations.

In both datasets separation of enhancing and nonenhancing glioma patients was done by visual inspection of pre- and post-contrast T_1-weighted imaging, by a certified neuroradiologist with more than 12 years of experience for EMC dataset and a neuroradiologist with more than 20 years of experience for TCIA dataset

Volume of Interest Delineation

For the TCIA dataset the provided volumes of interest (VOI) were used. These were binary masks of the whole brain, the contrast enhanced part of the tumor mask for enhancing glioma (CET), non-contrast enhancing part of tumor for nonenhancing glioma (NCET) and normal appearing white matter mask (NAWM) (8). These masks had been drawn manually on structural images by an experienced radiologist and all were coregistered to the DSC-MRI dataset.

For the EMC dataset, we used HD-BET for brain extraction of the T_1-weighted images to generate brain masks (24). FAST (FMRIB's Automated Segmentation Tool) (25) was used to generate probability maps of white matter, grey matter and cerebrospinal fluid. The NAWM mask was obtained by thresholding and binarizing probability maps of white matter (probability>0.90) in the contralateral part of brain. This binarized map was eroded using **FSL** tools (http://www.fmrib.ox.ac.uk/fsl/) to generate NAWM masks comparable in size with the NAWM masks in TCIA dataset. The generated NAWM mask encompasses on average 50 voxels covering multiple slices and was used for rCBV normalization.

For tumor segmentation, first structural images of T_1-weighted precontrast, T_2-weighted and FLAIR were registered to T_1-weighted postcontrast using the Elastix toolbox (version 2.5) (26). Then, based on these 4 structural images, NCET mask for nonenhancing as well as CET mask for enhancing glioma were delineated using HD-GLIO (27, 28).

Relative Cerebral Blood Volume Measurements

In processing the DSC datasets, two first brain volumes from each individual DSC dataset were removed to make sure that the GRE signal had reached steady state. Then, all masks as well as other volumes of the DSC dataset were rigidly registered to the third volume of DSC-MRI dataset using FLIRT (FMRIB's Linear Image Registration Tool) (29, 30) (see **Figure 1**).

In-house code developed in Python 3.6 (http://www.python.org) was used for image analysis. To ensure sufficient contrast-to-noise for the time curves, we excluded voxels exhibiting a drop of fewer than 5 standard deviations from the baseline signal from the analysis (31). DSC signal–time curves were converted to relaxivity–time curves using equation [1]. To fit equation [4] and equation [7], relaxivity–time curves of nonenhancing voxels were selected and averaged to produce $\overline{\Delta R_2^*}(t)$ needed in both leakage correction methods. Those nonenhancing voxels were selected from voxels in the brain mask where the absolute difference between average signal of the tail (final 10 time points) and the baseline (timepoints prior to the contrast bolus arrival) was less than one standard deviation of the baseline signal (12).

Trapezoidal integration between entrance and exit bolus time points of the 3 relaxivity–time curves, uncorrected, unidirectionally and bidirectionally corrected, was then used to obtain rCBV, $rCBV_{unidir}$, $rCBV_{bidir}$ respectively (32). These maps were normalized by dividing all intensities by the mean intensity of the contralateral NAWM of each rCBV map. "rCBV" subsequently refers to this normalized rCBV. Additionally, the permeability related parameters of K_2 and K_{ep} for the bidirectional correction algorithm (equation [6]) and K_2 for unidirectional correction (equation [3]) have been provided.

Data Analysis and Statistical Method

For each patient the median values of each normalized map (rCBV, $rCBV_{unidir}$, $rCBV_{bidir}$) as well as permeability related parameters (K_{2_unidir}, K_{2_bidir} and K_{ep_bidir}) within VOIs were computed and used for comparison. These VOIs were CET for enhancing glioma and the NCET for nonenhancing glioma. Data were tested for normality using the Shapiro-Wilk test, with non-parametric statistical tests selected accordingly. Comparison of parameters was done across each glioma group of enhancing and

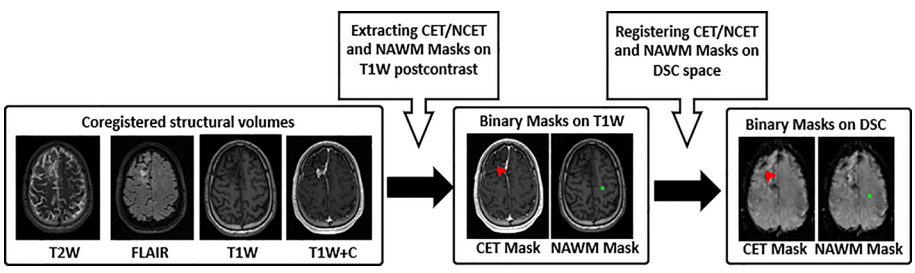

FIGURE 1 | Pre-processing workflow. 1) T_2-weighted (T2W), FLAIR, T_1-weighted precontrast (T1W) and postcontrast (T1W+C) images used for CET and NCET, and NAWM segmentation, 2) Binary mask of CET/NCET (red color) and NAWM (green color) mask on the structural data, 3) Registered Binary mask of CET/NCET on the third volume of DSC-MR imaging. CET, Contrast Enhanced Tumor; NCET, Non Contrast Enhanced Tumor; NAWM, Normal Appearing White Matter.

nonenhancing in each dataset by Wilcoxon Signed Rank Test combined with Holm–Bonferroni correction to counteract the problem of multiple comparisons. Moreover, the percentage difference between uncorrected rCBV and both corrected rCBV values were computed and averaged across the enhancing and nonenhancing group per dataset.

Goodness-of-Fit

Voxelwise goodness of fit was computed *via* calculation of the coefficient of determination, adjusted R-squared for both correction models. This involves the measurement of the difference of $\Delta R_2^*(t)$ (equation [1]) and its unidirectional (equation [3]) model fit for every time point:

$$R_{adj}^2 = 1 - \left[\frac{(1-R^2)(n-1)}{n-k-1}\right] \tag{9}$$

$$R^2 = 1 - SS_{res}/SS_{tot} \tag{10}$$

where n is the number of time points in the $\Delta R_2^*(t)$ curve, and k is the number of variables in the model, i.e. 2 and 3 for the unidirectional and bidirectional model, respectively. In equation [10], SS_{tot} is the total sum of squares and SS_{res} is the sum of squares of residuals:

$$SS_{tot} = \sum_t (\Delta R_2^*(t) - \overline{\Delta R_2^*(t)})^2 \tag{11}$$

$$SS_{res} = \sum_t (\Delta R_{2\,corr}^*(t) - \Delta R_2^*(t))^2 \tag{12}$$

Where $\Delta R_2^*(t)$ is the uncorrected relaxivity-time curve, $\overline{\Delta R_2^*(t)}$ is the mean $\Delta R_2^*(t)$ for each voxel, and $\overline{\Delta R_{2corr}^*(t)}$ is the corrected relaxivity-time curve, either bidirectionally or unidirectionally.

The average adjusted R-squared was calculated for the CET and NCET VOIs for each group of patients in each dataset.

Predicting Glioma Grade With Relative Cerebral Blood Volume

As a proof of principle, we assessed the statistical correlation between rCBV (both corrected and uncorrected) and histopathologic tumor grade using the Spearman rank correlation test (r_s). In the TCIA dataset all scans were collected shortly before surgery (5 days on average), at which time tumor grade was determined from the resected tumor tissue. This was not the case for the EMC dataset, where scans were acquired at various time points after tumor resection and as a result the initially established tumor grading information might no longer be valid for this imaging dataset to be used for grade prediction.

RESULTS

Table 1 lists histopathologic diagnosis of both enhancing and nonenhancing glioma patients in TCIA dataset. The WHO grade II tumors included 13 glioma patients (4 enhancing and 9 nonenhancing); the grade III included 5 glioma patients (1 enhancing and 4 nonenhancing); and the grade IV included 31 glioma patients (30 enhancing and 1 nonenhancing).

TABLE 1 | Summary of clinical description of patients in TCIA dataset.

Tumor Grade	Diagnosis	Enhancing Glioma	Nonenhancing Glioma
		Number of patients/Total %	Number of patients/Total %
IV	Glioblastoma multiforme	61.2%	2%
III	Anaplastic Astrocytoma III	2%	6.1%
	Mixed Anaplastic Astrocytoma/ Oligodendrogliomas III	0	2%
II	Astrocytoma II	6.1%	6.1%
	Mixed Astrocytoma/ Oligodendrogliomas II	0	12.2%
	Ependymoma II	2%	0

Both unidirectional and bidirectional correction reduced the tail of the uncorrected relaxivity-time curves of the CET VOI in enhancing tumors and the NCET VOI in nonenhancing tumors. Examples of these curves can be seen in **Figure 2**. As exemplified in this figure, a stronger reduction was reached when bidirectional leakage correction was applied. More specifically, the bidirectional corrected relaxivity–time curve in the CET VOI dropped faster initially, but the curve eventually slowed down; however, the unidirectional corrected relaxivity–time curve dropped almost linearly over time. In nonenhancing glioma, the mean relaxivity–time curves of NCET VOI showed smaller differences between either of the two leakage correction algorithms.

In the CET VOI (i.e. in enhancing glioma) the mean rCBV was significantly decreased when using either correction algorithm in both datasets. In the TCIA dataset uncorrected rCBV was 4.00 ± 2.11 which significantly ($p<0.001$) decreased with unidirectional correction to 3.19 ± 1.65 (20.2%) and with bidirectional correction to 2.91 ± 1.55 (27.1%) (**Figure 3**). Similar results were found in the EMC dataset with uncorrected rCBV being 2.5 ± 1.30, decreasing significantly ($p<0.001$) with unidirectional correction to 1.72 ± 0.84 (31.5%) and with bidirectional correction to 1.59 ± 0.90 (36.6%). In the NCET VOI in nonenhancing glioma, small but significant ($p<0.05$) differences were observed between uncorrected and corrected rCBV in both datasets when applying either of two leakage correction algorithms (see **Table 2**). Moreover, in both datasets and in both enhancing and nonenhancing tumors bidirectionally corrected rCBV values were significantly lower compared to unidirectionally corrected rCBV.

Visual inspection of uncorrected rCBV and corrected $rCBV_{unidir}$ and $rCBV_{bidir}$ maps is consistent with the above stated findings. As shown in **Figure 4**, the difference between three rCBV maps of a nonenhancing tumor is not clearly perceived, while in the enhancing tumor the difference between rCBV with and without correction is detectable in the CET VOI.

Variation of permeability parameters of both correction methods has been depicted in **Figure 5** for both datasets. The mean value of K_2 in both datasets across enhancing and nonenhancing groups is

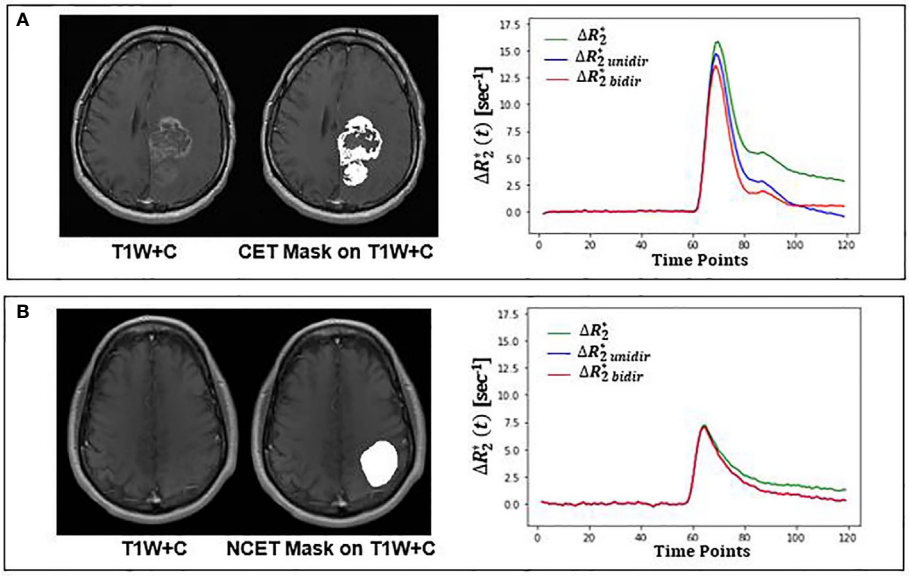

FIGURE 2 | Leakage correction effect on relaxivity-time curve for an enhancing (top) and nonenhancing (bottom) tumor from TCIA dataset. **(A)** Structural T_1-weighted postcontrast (T1W+C) image overlaid with CET VOI on the left; mean uncorrected (green), bidirectional (red) and unidirectional (blue) corrected relaxivity-time in CET VOI on the right. **(B)** Structural T_1-weighted postcontrast (T1W+C) image overlaid with NCET VOI on the left; mean uncorrected (green), bidirectional (red) and unidirectional (blue) corrected relaxivity-time in NCET VOI on the right. CET, Contrast Enhanced Tumor, NCET, Non Contrast Enhanced Tumor.

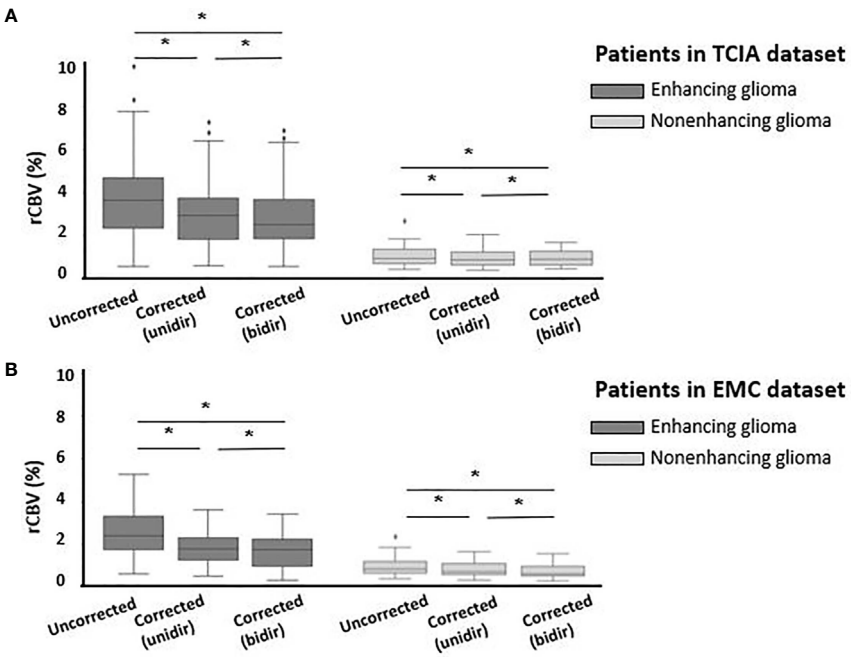

FIGURE 3 | Boxplots of uncorrected, unidirectional corrected and bidirectional corrected rCBV values from left to right **(A)** for enhancing glioma (n = 35) (dark gray) and for nonenhancing glioma (n = 14) (light gray) in TCIA dataset; **(B)** for enhancing glioma (n = 20) (dark gray) and nonenhancing glioma (n = 27) (light gray) in EMC dataset. *Significantly different, $p < 0.05$.

TABLE 2 | Patient averages of uncorrected and corrected rCBV and the resulting P-Value from statistical analysis.

		Uncorrected	Unidirectional Leakage Correction		Bidirectional Leakage Correction	
		rCBV (mean ± std)	rCBV (mean ± std)	Difference percentage (P-Value)	rCBV (mean ± std)	Difference percentage (P-Value)
TCIA dataset	**Enhancing Glioma**	4.00 ± 2.11	3.19 ± 1.65	20.2% P < 0.001	2.91 ± 1.55	27.1% P < 0.001
	Nonenhancing Glioma	1.42 ± 0.60	1.28 ± 0.46	9.5% P < 0.001	1.24 ± 0.37	12.6% P = 0.02
EMC dataset	**Enhancing Glioma**	2.51 ± 1.30	1.72 ± 0.84	31.5% P < 0.001	1.59 ± 0.90	36.6% P < 0.001
	Nonenhancing Glioma	0.91 ± 0.46	0.77 ± 0.37	14.6% P < 0.001	0.67 ± 0.34	25.9% P < 0.001

The difference Percentage is the percentage of relative change between each of leakage corrected and uncorrected rCBV.

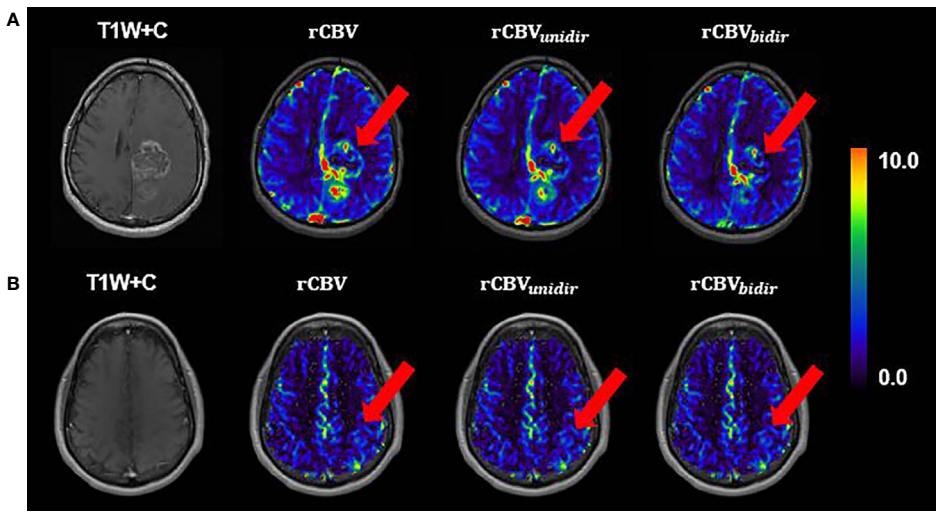

FIGURE 4 | A slice example of T_1-weighted postcontrast overlaid with uncorrected, unidirectional corrected and bidirectional corrected rCBV maps from left to right, respectively, **(A)** for enhancing glioma patient **(B)** for nonenhancing glioma; both from TCIA dataset.

negative, with a close to zero value for nonenhancing ones. This value for enhancing tumors is K_{2_unidir} = -0.03 ± 0.02 (sec^{-1}) and K_{2_bidir} = -0.05 ± 0.08 (sec^{-1}) for TCIA dataset; K_{2_unidir} = -0.05 ± 0.04 (sec^{-1}) and K_{2_bidir} = -0.06 ± 0.04 (sec^{-1}) for EMC dataset. The transfer coefficient K_{ep_bidir} that appears in the bidirectional model, representing the extra- to intravascular contrast flux, had a positive mean value of 0.02 ± 0.05 (sec^{-1}) and 0.01 ± 0.02 (sec^{-1}) for enhancing tumors of EMC and TCIA respectively.

Evaluation of model fitting by averaging adjusted R-squared value across patients showed limited differences between the bidirectional (0.87 ± 0.12) and unidirectional (0.87 ± 0.12) models in TCIA dataset, while in EMC dataset adjusted R-squared of the bidirectional model (0.86 ± 0.05) was slightly higher compared to the unidirectional model (0.83 ± 0.06).

Table 3 shows corrected and uncorrected rCBV measurements for each grade and each tumor type in the TCIA dataset. The average rCBV values were higher for grade IV and III compared to grade II and decreased after application of either of leakage correction algorithm. Across the 49 patients in TCIA dataset, tumor grade and rCBV were significantly correlated with or without leakage correction algorithm (see **Figure 6**).

DISCUSSION

This study investigated the effect of two known leakage correction algorithms on rCBV measurements in both enhancing and nonenhancing glioma in two independent datasets. The leakage correction algorithms used in this study are based on unidirectional contrast agent transport from the intravascular to extravascular spaces and on bidirectional contrast agent transport between these two spaces. The result of this study showed that in enhancing glioma, when the BBB is disrupted, application of either of these two leakage correction methods decreased rCBV measurements. The decrease in rCBV measurements in enhancing glioma after applying leakage correction algorithms likely originates from initial rCBV overestimation due to dominance of T_2^* effects in the leaky area.

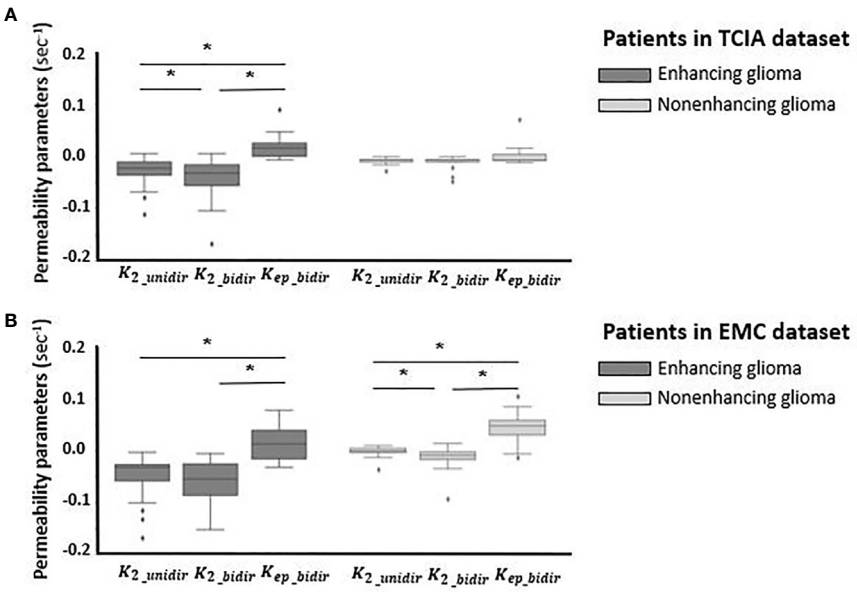

FIGURE 5 | Boxplots of permeability parameters of K_2 in unidirectional correction method and K_2 and K_{ep} in bidirectional correction method from left to right **(A)** for enhancing glioma (n = 35) (dark gray) and for nonenhancing glioma (n = 14) (light gray) in TCIA dataset; **(B)** for enhancing glioma (n = 20) (dark gray) and nonenhancing glioma (n = 27) (light gray) in EMC dataset. *Significantly different, $p < 0.05$.

TABLE 3 | Patient averages of uncorrected and corrected rCBV for the different tumor types and the grades in TCIA.

Tumor Grade	Diagnosis	Uncorrected		Unidirectional Leakage Correction		Bidirectional Leakage Correction	
		rCBV (mean ± std)		rCBV (mean ± std)		rCBV (mean ± std)	
		Type	grade	Type	grade	Type	grade
IV	**Glioblastoma multiforme**	3.90 ± 1.87	3.90 ± 1.87	3.13 ± 1.53	3.13 ± 1.53	2.88 ± 1.46	2.88 ± 1.46
III	**Anaplastic Astrocytoma** III	3.57 ± 4.25	3.45 ± 3.69	2.83 ± 2.99	2.73 ± 2.6	2.56 ± 2.66	2.44 ± 2.32
	Mixed Anaplastic Astrocytoma/Oligodendrogliomas III	2.94		2.31		1.94	
II	**Astrocytoma** II	1.58 ± 1.05	1.66 ± 1.18	1.46 ± 0.86	1.45 ± 0.84	1.44 ± 0.79	1.38 ± 0.67
	Mixed Astrocytoma/Oligodendrogliomas II	1.24 ± 0.48		1.13 ± 0.4		1.14 ± 0.38	
	Ependymoma II	4.65		3.29		2.48	

We have seen different effect size of leakage correction in the two investigated datasets, with a stronger reduction on average in rCBV for the EMC dataset. Previously it has been shown that the leakage of contrast agent into the extravascular extracellular space results in increased T_1 and T_2^* effect, by shortening both T_1 and T_2^* relaxation time. Depending on which of two has dominant effect in the leaky area, the tail of relaxivity-time curve gets artificially either lower or upper than the baseline (11). In the EMC protocol applying higher dose of preload, combined with long T_E and high FA, the measured signal would be less sensitive to change in T_1 effect and more sensitive to change in T_2^* effect, compared to TCIA dataset. Stronger T_2^* effect dominance in the enhanced area results in highly elevated tail in relaxivity-time curve. Thus, when applying either of leakage correction algorithms on the curve, the effect size would appear stronger.

In line with previous consensus (20) our result highlights the necessity of using either leakage correction algorithm for rCBV measurements in enhancing glioma. However, when using these algorithms in the absence of contrast agent leakage effects, interpretation should be done with caution. The result of this study shows that both leakage correction algorithms significantly altered rCBV estimation in nonenhancing glioma. Although, this alteration was not noticeable in most patients, there might be a risk of overfitting in using these leakage correction algorithms in nonenhancing glioma. One explanation for this phenomenon could be the elevated steady-state contrast agent concentration in the vasculature after first passage. This might interfere with the performance of these algorithms and cause rCBV misestimation after application of leakage correction methods. Another possible explanation for this result could be that these algorithms are able to detect subtle leakage effects which are not yet clearly visible on a T_1 postcontrast image. Since there are no histopathological rCBV measurements to serve as a gold standard for rCBV in nonenhancing tumor caution needs to be taken with application of leakage correction in nonenhancing areas.

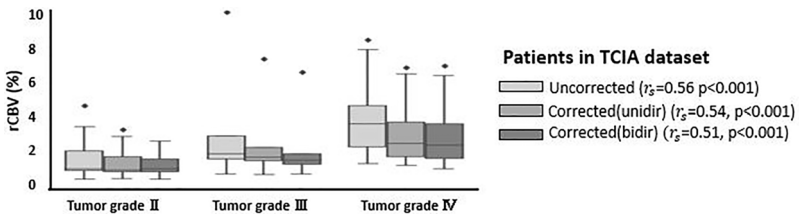

FIGURE 6 | Boxplots of uncorrected, unidirectional corrected and bidirectional corrected rCBV values per each grade (grade II, III, and IV). r_s represents the correlation coefficient between rCBV and tumor grade, derived from Spearman rank correlation test. *Significantly different, $p < 0.05$.

Comparing the performance of the uni- vs bidirectional leakage algorithms, each method has its own pros and cons. The goodness-of-fit analysis showed slightly higher adjusted R-squared for bidirectional method. However, the bidirectional leakage correction takes twice as long to compute as the unidirectional one, which may be clinically undesirable. Analyses of the permeability parameters for nonenhancing patients shows that K_2 obtained from unidirectional algorithm is plausibly close to zero in both datasets, whereas K_2 and K_{ep} resulted from bidirectional model are changing in a broader range specially for nonenhancing group in EMC datasets. The likely reason for this unexpected behavior could be the number of time points (50 time points) collected in EMC dataset, as previous investigations have indicated that the leakage correction algorithm performed best with the collection of 120 time points (14).

It is worthwhile to note that in TCIA dataset, including both enhancing and nonenhancing glioma, a significant correlation was found between tumor grading and all three rCBV calculations, including uncorrected, unidirectionally and bidirectionally corrected rCBV. Therefore, the unexpected finding of significant effects of leakage correction on rCBV on nonenhancing tumor may not be an issue for standard application of leakage correction in clinical settings. However, generalization of this finding requires further corroboration in multiple clinical studies.

A limitation of this study is the retrospective nature which leads to both datasets not following the standardized DSC-MRI acquisition protocol (20). In consensus study it has been suggested that using a full-dose of 0.1 mmol/kg for both preload and bolus injection dose, along with DSC acquisition parameters of 60° for FA and T_E of 40–50 ms at 1.5 T and 20–35 ms at 3 T, provide overall best accuracy and precision for rCBV estimates. As with many retrospective studies, the DSC-MRI acquisition protocol used for both TCIA and EMC datasets do not fall within the standardized acquisition protocol, as described in the method section. For instance, in TCIA dataset the preload is 0.05 mmol/kg which is half of what is recommended currently; and in EMC dataset, the dose protocol is not based on weight but on contrast volume (7.5ml). With the standard "full dose" defined as 0.1 mmol/kg, only patients weighing 75 kg (~165 lb) received a full dose, while patients under and over this weight would receive more than and less than a full dose, respectively. Therefore, future work should be focused on examining datasets with the most recent standard protocol and a ground truth for MRI-derived perfusion parameter utilizing spatially-correlated biopsy samples.

In summary, this work evaluated the effect of leakage correction on rCBV estimates, indicating stronger effects for bidirectional than for unidirectional leakage correction as well as larger effects in enhancing tumors than in nonenhancing tumors. From a clinical perspective, our work highlights that using rCBV as a universal biomarker still requires further development in standardization of validation of both acquisition and post-processing procedures. The fact that the application of a correction algorithm affects the estimated rCBV indicates that the use of published threshold values (8) for determining tumor type, molecular profile or grade has to be done with great caution, taking the methodology for establishing such thresholds into account.

DATA AVAILABILITY STATEMENT

A publicly available datasets was analyzed in this study. Data can be found here: https://wiki.cancerimagingarchive.net/display/Public/QIN-BRAIN-DSC-MRI.

ETHICS STATEMENT

The studies involving human participants were reviewed and approved by the first dataset used in this study. "Glioma DSC-MRI Perfusion Data" is publicly available in The Cancer Imaging Archive (TCIA). For the second dataset, the complete protocol is part of routine clinical imaging, and all patients provided informed written consent to have their information stored in an Institutional Review Board Approved Neuro-Oncology database for use in future investigations. The patients/participants provided their written informed consent to participate in this study.

AUTHOR CONTRIBUTIONS

The study was conceptualized by EW, PC, and MC. The manuscript was written by FA. Image processing and statistical analysis were done by FA with the help of KG for tumor segmentation and PC for statistical analysis. The result has been evaluated by FA, EW, PC, and MC for the technical point of view and MS for the clinical point of view as an experienced

radiologist. MS also provided one of the clinical datasets used in this work. All authors helped in interpreting the data and critically reviewed the manuscript and commented on the final version. All authors contributed to the article and approved the submitted version.

FUNDING

FA conducted this work funded by a Short Term Scientific Mission from Glioma MR Imaging 2.0, an Action funded by the European Cooperation in Science and Technology. EW is funded by a "Veni Vernieuwingsimpuls" from the Dutch Research Council entitled "Food for thought: Oxygen delivery to the brain," grant number 91619121.

ACKNOWLEDGMENTS

We acknowledge Pr. Kathleen Schmainda for kindly providing grading information for TCIA dataset and Martin Craig for his contributions that improved the quality of the processing.

REFERENCES

1. Villringer A, Rosen BR, Belliveau JW, Ackerman JL, Lauffer RB, Buxton RB, et al. Dynamic imaging with lanthanide chelates in normal brain: Contrast due to magnetic susceptibility effects. *Magn Reson Med* (1988) 6:164–74. doi: 10.1002/mrm.1910060205
2. Law M, Yang S, Babb JS, Knopp EA, Golfinos JG, Zagzag D, et al. Comparison of cerebral blood volume and vascular permeability from dynamic susceptibility contrast-enhanced perfusion MR imaging with glioma grade. *Am J Neuroradiol* (2004) 25:746–55.
3. Kremer S, Grand S, Remy C, Esteve F, Lefournier V, Pasquier B, et al. Cerebral blood volume mapping by MR imaging in the initial evaluation of brain tumors. *J Neuroradiol* (2002) 29:105–13.
4. Law M, Oh S, Babb JS, Wang E, Inglese M, Zagzag D, et al. Low-grade gliomas: Dynamic susceptibility-weighted contrast-enhanced perfusion MR imaging - Prediction of patient clinical response. *Radiology* (2006) 238:658–67. doi: 10.1016/S0098-1672(08)70489-2
5. Sugahara T, Korogi Y, Tomiguchi S, Shigematsu Y, Ikushima I, Kira T, et al. Posttherapeutic intraaxial brain tumor: The value of perfusion-sensitive contrast-enhanced MR imaging for differentiating tumor recurrence from nonneoplastic contrast-enhancing tissue. *Am J Neuroradiol* (2000) 21:901–9.
6. Paulson ES, Schmainda KM. Comparison of dynamic susceptibility-weighted contrast-enhanced MR methods: Recommendations for measuring relative cerebral blood volume in brain tumors. *Radiology* (2008) 249:601–13. doi: 10.1148/radiol.2492071659
7. Kluge A, Lukas M, Toth V, Pyka T, Zimmer C, Preibisch C. Analysis of three leakage-correction methods for DSC-based measurement of relative cerebral blood volume with respect to heterogeneity in human gliomas. *Magn Reson Imaging* (2016) 34:410–21. doi: 10.1016/j.mri.2015.12.015
8. Schmainda KM, Prah MA, Rand SD, Liu Y, Logan B, Muzi M, et al. Multisite concordance of DSC-MRI analysis for brain tumors: Results of a National Cancer Institute Quantitative Imaging Network Collaborative Project. *Am J Neuroradiol* (2018) 39:1008–16. doi: 10.3174/ajnr.A5675
9. Quarles CC, Gochberg DF, Gore JC, Yankeelov TE. A theoretical framework to model DSC-MRI data acquired in the presence of contrast agent extravasation. *Phys Med Biol* (2009) 54:5749–66. doi: 10.1088/0031-9155/54/19/006
10. Hu LS, Baxter LC, Pinnaduwage DS, Paine TL, Karis JP, Feuerstein BG, et al. Optimized preload leakage-correction methods to improve the diagnostic accuracy of dynamic susceptibility-weighted contrast-enhanced perfusion MR imaging in posttreatment gliomas. *Am J Neuroradiol* (2010) 31:40–8. doi: 10.3174/ajnr.A1787
11. Shiroishi MS, Castellazzi G, Boxerman JL, D'Amore F, Essig M, Nguyen TB, et al. Principles of T2∗-weighted dynamic susceptibility contrast MRI technique in brain tumor imaging. *J Magnetic Resonance Imaging* (2015) 41:296–313. doi: 10.1002/jmri.24648
12. Boxerman JL, Schmainda KM, Weisskoff RM. Relative cerebral blood volume maps corrected for contrast agent extravasation significantly correlate with glioma tumor grade, whereas uncorrected maps do not. *Am J Neuroradiol* (2006) 27:859–67.
13. Leigh R, Jen SS, Varma DD, Hillis AE, Barker PB. Arrival Time Correction for Dynamic Susceptibility Contrast MR Permeability Imaging in Stroke Patients. *PLoS One* (2012) 7(12):e52656. doi: 10.1371/journal.pone.0052656
14. Bjornerud A, Sorensen AG, Mouridsen K, Emblem KE. T1-and T2-dominant extravasation correction in DSC-MRI: Part I-theoretical considerations and implications for assessment of tumor hemodynamic properties. *J Cereb Blood Flow Metab* (2011) 31:2041–53. doi: 10.1038/jcbfm.2011.52
15. Leu K, Boxerman JL, Lai A, Nghiemphu PL, Pope WB, Cloughesy TF, et al. Bidirectional Contrast agent leakage correction of dynamic susceptibility contrast (DSC)-MRI improves cerebral blood volume estimation and survival prediction in recurrent glioblastoma treated with bevacizumab. *J Magn Reson Imaging* (2016) 44:1229–37. doi: 10.1002/jmri.25227
16. Hu LS, Kelm Z, Korfiatis P, Dueck AC, Elrod C, Ellingson BM, et al. Impact of software modeling on the accuracy of perfusion MRI in glioma. *Am J Neuroradiol* (2015) 36:2242–9. doi: 10.3174/ajnr.A4451
17. Hu LS, Eschbacher JM, Dueck AC, Heiserman JE, Liu S, Karis JP, et al. Correlations between perfusion MR imaging cerebral blood volume, microvessel quantification, and clinical outcome using stereotactic analysis in recurrent high-grade glioma. *Am J Neuroradiol* (2012) 33:696–76. doi: 10.3174/ajnr.A2743
18. Prah MA, Al-Gizawiy MM, Mueller WM, Cochran EJ, Hoffmann RG, Connelly JM, et al. Spatial discrimination of glioblastoma and treatment effect with histologically-validated perfusion and diffusion magnetic resonance imaging metrics. *J Neurooncol* (2018) 136:13–21. doi: 10.1007/s11060-017-2617-3
19. Leu K, Boxerman JL, Cloughesy TF, Lai A, Nghiemphu PL, Liau LM, et al. Improved leakage correction for single-echo dynamic susceptibility contrast perfusion MRI estimates of relative cerebral blood volume in high-grade gliomas by accounting for bidirectional contrast agent exchange. *Am J Neuroradiol* (2016) 37:1440–6. doi: 10.3174/ajnr.A4759
20. Boxerman JL, Quarles CC, Hu LS, Erickson BJ, Gerstner ER, Smits M, et al. Consensus recommendations for a dynamic susceptibility contrast MRI protocol for use in high-grade gliomas. *Neuro Oncol* (2020) 22:1262–75. doi: 10.1093/neuonc/noaa141
21. Covarrubias DJ, Rosen BR, Lev MH. Dynamic Magnetic Resonance Perfusion Imaging of Brain Tumors. *Oncologist* (2004). doi: 10.1634/theoncologist.9-5-528
22. Schmainda KM, Prah MA, Connelly JM RS. Glioma DSC-MRI perfusion data with standard imaging and ROIs. *Cancer Imaging Arch* (2016).
23. Clark K, Vendt B, Smith K, Freymann J, Kirby J, Koppel P, et al. The cancer imaging archive (TCIA): Maintaining and operating a public information repository. *J Digit Imaging* (2013) 26:1045–57. doi: 10.1007/s10278-013-9622-7
24. Isensee F, Schell M, Pflueger I, Brugnara G, Bonekamp D, Neuberger U, et al. Automated brain extraction of multisequence MRI using artificial neural networks. *Hum Brain Mapp* (2019) 40:4952–64. doi: 10.1002/hbm.24750
25. Zhang Y, Brady M, Smith S. Segmentation of brain MR images through a hidden Markov random field model and the expectation-maximization algorithm. *IEEE Trans Med Imaging* (2001) 20:45–57. doi: 10.1109/42.906424
26. Klein S, Staring M, Murphy K, Viergever MA, Pluim JPW. Elastix: A toolbox for intensity-based medical image registration. *IEEE Trans Med Imaging* (2010) 29:196–205. doi: 10.1109/TMI.2009.2035616

27. Isensee F, Petersen J, Kohl SAA, Jäger PF, Maier-Hein KH. nnU-Net: Breaking the Spell on Successful Medical Image Segmentation. *Nature Methods* (2019) 2. doi: 10.1038/s41592-020-01008-z
28. Kickingereder P, Isensee F, Tursunova I, Petersen (Jørgen) J, Neuberger U, Bonekamp D, et al. Automated quantitative tumour response assessment of MRI in neuro-oncology with artificial neural networks: a multicentre, retrospective study. *Lancet Oncol* (2019) 20:728–40. doi: 10.1016/S1470-2045(19)30098-1
29. Jenkinson M, Smith S. A global optimisation method for robust affine registration of brain images. *Med Image Anal* (2001) 5:143–56. doi: 10.1016/S1361-8415(01)00036-6
30. Jenkinson M, Bannister P, Brady M, Smith S. Improved optimization for the robust and accurate linear registration and motion correction of brain images. *Neuroimage* (2002) 17:825–41. doi: 10.1006/nimg.2002.1132
31. Bell LC, Stokes AM, Quarles CC. Analysis of postprocessing steps for residue function dependent dynamic susceptibility contrast (DSC)-MRI biomarkers and their clinical impact on glioma grading for both 1.5 and 3T. *J Magn Reson Imaging* (2020) 51:547–53. doi: 10.1002/jmri.26837
32. Willats L, Calamante F. The 39 steps: Evading error and deciphering the secrets for accurate dynamic susceptibility contrast MRI. *NMR BioMed* (2013) 26:913–31. doi: 10.1002/nbm.2833

Conflict of Interest: The authors declare that the research was conducted in the absence of any commercial or financial relationships that could be construed as a potential conflict of interest.

frontiers in Neurology

ORIGINAL RESEARCH
published: 14 April 2021
doi: 10.3389/fneur.2021.636573

Contralesional Structural Plasticity in Different Molecular Pathologic Subtypes of Insular Glioma

Zhenxing Huang[1,2], *Gen Li*[1,2], *Zhenye Li*[1,2], *Shengjun Sun*[2,3], *Yazhuo Zhang*[2,4], *Zonggang Hou*[1,2*] *and Jian Xie*[1,2*]

[1] Department of Neurosurgery, Beijing Tiantan Hospital, Capital Medical University, Beijing, China, [2] China National Clinical Research Centre for Neurological Diseases, Beijing, China, [3] Neuroimaging Center, Beijing Neurosurgical Institute, Capital Medical University, Beijing, China, [4] Beijing Neurosurgical Institute, Capital Medical University, Beijing, China

Neuroplasticity may preserve neurologic function in insular glioma, thereby improving prognosis following resection. However, the anatomic and molecular bases of this phenomenon are not known. To address this gap in knowledge, the present study investigated contralesional compensation in different molecular pathologic subtypes of insular glioma by high-resolution three-dimensional T1-weighted structural magnetic resonance imaging. A total of 52 patients with insular glioma were examined. We compared the gray matter volume (GMV) of the contralesional insula according to histological grade [low-grade glioma (LGG) and high-grade glioma (HGG)] and molecular pathology status [isocitrate dehydrogenase (IDH) mutation, telomerase reverse-transcriptase (*TERT*) promoter mutation, and 1p19q codeletion] by voxel-based morphometry (VBM). A cluster of 320 voxels in contralesional insula with higher GMV was observed in glioma with IDH mutation as compared to IDH wild-type tumors by region of interest-based VBM analysis (family-wise error-corrected at $p < 0.05$). The GMV of the entire contralesional insula was also larger in insular glioma patients with IDH mutation than in patients with wild-type IDH. However, there was no association between histological grade, *TERT* promoter mutation, or 1p19q codeletion and GMV in the contralesional insula. Thus, IDH mutation is associated with greater structural compensation in insular glioma. These findings may be useful for predicting neurocognitive and functional outcomes in patients undergoing resection surgery.

Keywords: insular glioma, neuroplasticity, brain structural plasticity, molecular pathology, VBM

OPEN ACCESS

Edited by:
Manoj Kumar,
National Institute of Mental Health and Neurosciences (NIMHANS), India

Reviewed by:
Tianming Qiu,
Fudan University, China
Madhura Ingalhalikar,
Symbiosis International University, India

****Correspondence:***
Zonggang Hou
houzg2006@163.com
Jian Xie
xiejian0630@126.com

Specialty section:
This article was submitted to Neuro-Oncology and Neurosurgical Oncology, a section of the journal Frontiers in Neurology

Received: *01 December 2020*
Accepted: *08 March 2021*
Published: *14 April 2021*

Citation:
Huang Z, Li G, Li Z, Sun S, Zhang Y, Hou Z and Xie J (2021) Contralesional Structural Plasticity in Different Molecular Pathologic Subtypes of Insular Glioma. Front. Neurol. 12:636573. doi: 10.3389/fneur.2021.636573

INTRODUCTION

Neuroplasticity occurs across the human life span. Developmental and adaptive plasticity underlie experience-related changes resulting from modification of the environment, physical exercise, or cognitive training (1). Additionally, reactive functional and structural plasticity is responsible for restoring normal brain function following injury, a process known as cortical remodeling or reorganization (2). Neuroimaging studies have revealed that this process occurs in both the lesioned and intact hemispheres in stroke, brain trauma, and glioma (3–10).

The pattern of cortical remodeling in glioma has been reported to be hierarchical (6). The compensation could be launched firstly within the lesioned area and then enlarged to

the peritumor area. If it was still insufficient, the ipsilateral and even the contralateral hemispheres could be recruited to the remodeling process. And this hierarchical pattern is especially suited for low-grade gliomas (LGGs), because they exhibited a slow-growing, less-invasive feature, which left enough time for this remodeling process. As it happens, the insular cortex is a common location for LGGs (11, 12); it is also involved in multiple brain functions, acting as a hub for neural circuits involved in language processing, emotion, cognitive control, and decision making (13). Most insular glioma patients are diagnosed following seizure or headache or during routine physical examination, and tumor resection typically has an acceptable neurologic outcome (14, 15), implying that neuroplastic changes occur during gliomagenesis. Along this perspective, Almairac et al. (7) observed structural remodeling in unilateral low-grade insular glioma patients, whereby gray matter volume (GMV) of the contralesional insula was increased relative to healthy control subjects. It was speculated that the slow rate of growth and low invasiveness of low-grade insular glioma suited that hierarchical remodeling pattern well.

It should be noted that the 2016 World Health Organization (WHO) classification for glioma added the molecular subtype [isocitrate dehydrogenase (IDH) or telomerase reverse-transcriptase promoter (TERTp) mutation and 1p19q codeletion], which is highly associated with tumor invasiveness and prognosis (16, 17). There were even evidence that the IDH wild-type LGGs should be treated as glioblastomas (GBMs, Grade IV), as they shared similar clinical and genetic characteristics (18). Therefore, except classical histological grading, different molecular subtypes might also reflect different biological behaviors and might lead to different neuroplastic results. However, most studies investigating neuroplasticity in glioma have compared patients and healthy control subjects, without examining differences that exist according to the histological grade or molecular pathologic subtype of glioma.

Therefore, we designed the present study to investigate contralesional compensation in different histological grades, especially molecular pathologic subtypes of insular glioma by high-resolution three-dimensional (3D) T1-weighted (T1W) structural magnetic resonance imaging (MRI) and voxel-based morphometry (VBM) analysis.

MATERIALS AND METHODS

Participants and Grouping

A total of 52 patients diagnosed with unilateral insular glioma at Beijing Tiantan Hospital were enrolled in this study. Detailed information on molecular pathology including 6-*O*-methylguanine (O6-MeG)-DNA methyltransferase (MGMT) promoter methylation status, IDH mutation, TERTp mutation, and 1p19q codeletion was available for all patients. MGMT promoter methylation has been shown to inhibit apoptosis and increase sensitivity to temozolomide (19, 20), but as it has little clinical significance in gliomagenesis, it was not investigated in this study.

The patients were grouped as IDH mutation (IDH-mu) and IDH wild type (IDH-wt), TERTp-mu and TERTp-wt, and 1p19q codeletion (1p19q-codel) and non-1p19q-codel. Additionally, we also involved histological pathology, where patients were grouped as LGG (WHO II) and high-grade glioma (WHO III and IV, HGG). The study was approved by the Institutional Review Board of the Beijing Tiantan Hospital. All the participants signed a written informed consent form.

The number of patients was relatively small when they were further grouped according to the side of the brain in which the lesion was located (left vs. right). Therefore, in order to enhance statistical power, all left-tumor MRIs were flipped along the X axis in the FMRIB Software Library (FSL) before preprocessing. Then the right and left insula could be consistently referred to as the "lesioned insula" and "contralesional insula," respectively. Statistical analyses were performed with the flipped images and focused on the contralesional insula. However, this flipping operation could introduce bias because of the asymmetry between certain brain regions in the left and right hemispheres (21). In order to exclude this possibility, we compared the contralesional insula between the right- and left-sided tumors; as we did not observe any differences, we applied the flipping operation to our dataset.

Aging can affect GMV; hence, studies comparing patients and healthy participants typically consider age as an uninteresting variable (3, 7, 22). It should be noted that HGG, IDH-wt, and TERTp-mu in glioma were found to be closely related to older age (16, 23), which was also the case in our study (**Table 1**). Therefore, setting patient age as a covariate in our analyses could eliminate the effects of different molecular pathologic subtypes on GMV, which we should avoid in the present study. On the other hand, recent studies have reported that the decline in insular volume slows or even stops during aging (24, 25), suggesting that age has little effect on GMV of the insular cortex. Nonetheless, given that GMV starts to decrease at the age of 40 years (26, 27), which was also the median age in our cohort, we compared GMV of the contralesional insula between patients aged $\geq$40 years and those aged <40 years. As no difference was found, we considered that age did not affect GMV of the contralesional insula, and it was not included as a covariate in the statistical analysis.

MRI

3D T1W structural images were acquired at our center with two different scanners: the Ingenia 3.0T (Philips, Amsterdam, The Netherlands) (P) and Prisma 3.0T (Siemens, Munich, Germany) (S). The acquisition program was as follows: resolution = 1 × 1 × 1 mm, field of view = 256 × 256 mm, slice thickness = 1 mm, flip angle = 8°, repetition time = 6.49/1.56 s, and echo time = 3.042/1.56 ms (for P/S). In addition, conventional magnetic resonance (MR) sequences including T2-weighted (T2W), fluid-attenuated inversion recovery (FLAIR) and T1W images with intravenous injection of a gadolinium contrast agent were routinely acquired.

Lesion Tracing

In order to visualize the lesion in the insula and calculate tumor volume (TV), the tumor mask was delineated in T2W or FLAIR images by a neurosurgeon with 8 years of

TABLE 1 | Demographic characteristic of different grades and molecular pathology statuses.

Variables	Grade and molecular pathology status										
	IDH-mu	IDH-wt	*P*	TERT-mu	TERT-wt	*P*	1p19q-codel	Non-1p19q-codel	*P*	LGG	HGG	*P*
Total no.	38	14	NA	21	31	NA	14	38	NA	26	26	–
Gender, M/F, *n*	23/15	8/6	0.83	13/8	18/13	0.78	7/7	24/14	0.39	16/10	15/11	0.778
Age (Mean ± SD), years	38.84 ± 9.94	53.57 ± 12.48	<0.001	46.95 ± 10.69	40 ± 12.93	0.047	41.29 ± 11.32	43.37 ± 12.94	0.6	37.04 ± 0.51	48.58 ± 12.50	<0.001
TV (Mean ± SD), ml	54.15 ± 42.65	57.58 ± 24.74	0.78	51.95 ± 32.84	57.19 ± 42.22	0.63	45.99 ± 28.27	58.42 ± 41.4	0.31	41.81 ± 32.13	68.34 ± 40.22	0.011
Scanner type, P/S, *n*	4/34	4/10	NA	2/19	6/25	NA	1/13	7/31	NA	3/23	5/21	NA
Grade II (*n* = 26)	26	0	NA	11	15	NA	11	15	NA	–	–	–
Grade III (*n* = 16)	9	7	NA	7	9	NA	3	13	NA	–	–	–
Grade IV (*n* = 10)	3	7	NA	3	7	NA	0	10	NA	–	–	–

SD, Standard deviation; TV, Tumor volume; P, Philips Ingenia 3.0T scanner; S, Siemens Prisma 3.0T scanner; NA, Not applicable.

experience using MRIcron (https://www.mccauslandcenter.sc.edu/crnl/tools). Lesion masks and corresponding images for tracing were normalized to standard Montreal Neurological Institute (MNI) space using SPM12 (https://www.fil.ion.ucl.ac.uk/spm/software/spm12/). A reconfirmation procedure was performed by the neurosurgeon after normalization for more accurate matching to the original lesion range. The normalized and rechecked lesion masks were used for lesion overlap with MRIcroGL (https://www.mccauslandcenter.sc.edu/mricrogl).

Image Preprocessing

Structural image preprocessing was performed with SPM12 and the CAT12 toolbox in MATLAB. The images were manually reoriented to the anterior commissure, which was defined as the origin (mm coordinates: 0, 0, 0). The "Segment Data" module of CAT12 was used to segment the structural images into the gray matter (GM), white matter, and cerebrospinal fluid. In this process, the original structural images were normalized to MNI-152 standard space with an isotropic voxel resolution of 1.5 × 1.5 × 1.5 mm, and we also modulated the spatial normalized data in order to maintain its original GMV. We checked the data quality to verify the segmentation and normalization results. Total intracranial volume (TIV) was determined using the "Estimate TIV" module. The modulated GM maps of each participant were smoothed with an 8-mm full-width at half-maximum Gaussian kernel. VBM analyses were performed on the smoothed images generated during the last preprocessing step.

Statistical Analysis

VBM analysis was applied to imaging data. Based on the general linear model, the two-sample *t*-test was used for three types of comparisons: (1) left-sided vs. right-sided tumor patients to exclude the effect of brain structural asymmetry; (2) patients aged ≥40 vs. <40 years to exclude the effect of aging; and (3) LGG vs. HGG, IDH-mu vs. IDH-wt, TERTp-mu vs. TERTp-wt, and 1p19q-codel vs. non-1p19q-codel to evaluate the effect of molecular pathology on contralesional compensation in insular glioma.

As we focused only on alterations in the contralesional (left) insular cortex, we generated a left insular mask as the region of interest (ROI) using the WFU_PickAtlas toolbox (https://www.nitrc.org/projects/wfu_pickatlas/) based on the automated anatomical labeling template. We used this mask in the three abovementioned comparisons. The ROI-based analysis highlights the changing patterns of certain brain areas and provides enhanced statistical control (7). Patient sex, TIV, TV, and MR scanner type were covariates in all of the comparisons. An absolute masking threshold of 0.2 was also set in all comparisons (28). A voxel-level family-wise error (FWE) correction at $P < 0.05$ with a spatial extent threshold of 50 voxels was regarded as significant. For comparisons that passed the FWE correction in VBM, we further compared the GMV of significant clusters and the entire insula. Non-imaging data for continuous and categorical variables were analyzed with the two-sample *t*-test and chi-squared test,

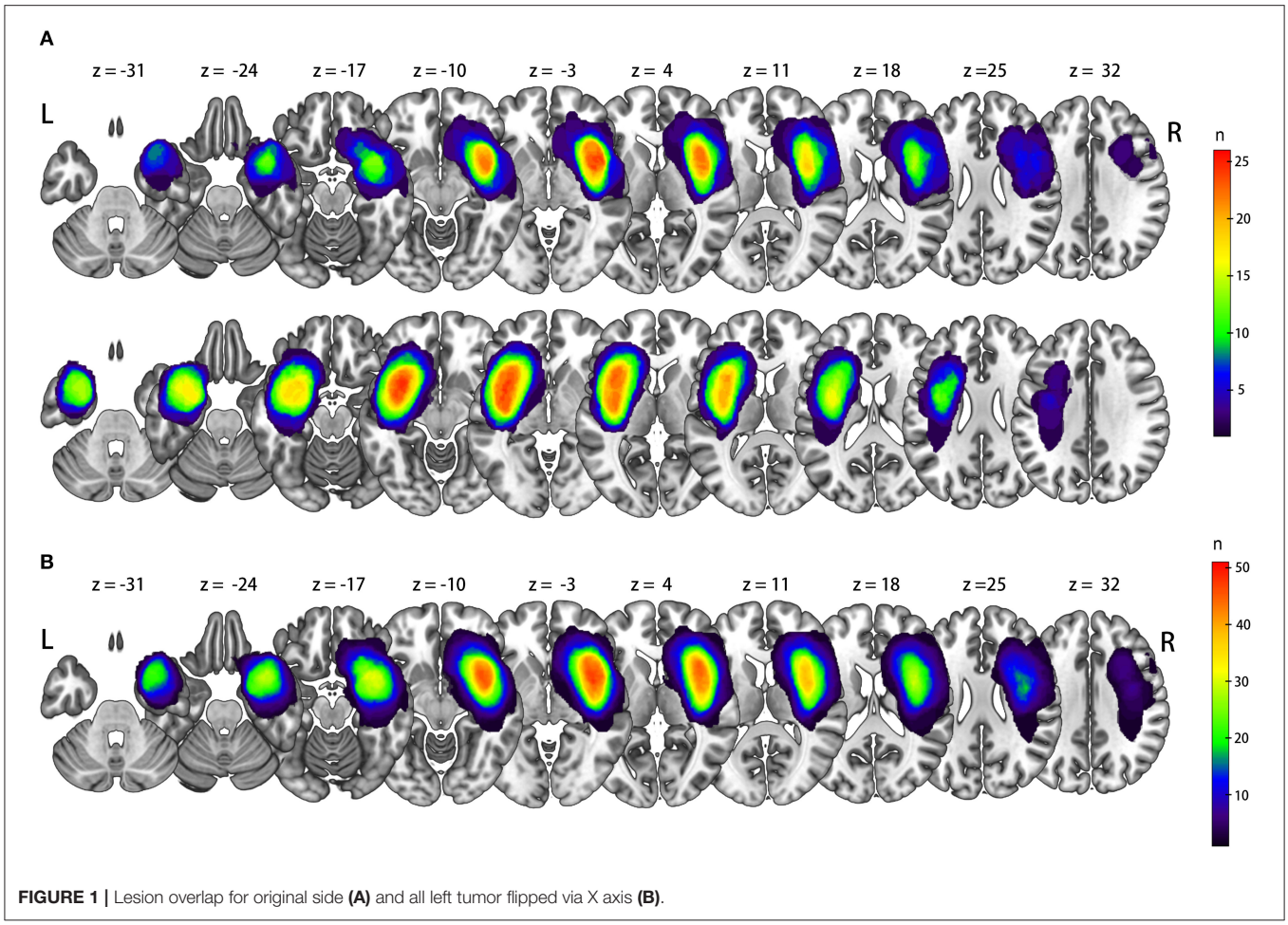

FIGURE 1 | Lesion overlap for original side **(A)** and all left tumor flipped via X axis **(B)**.

TABLE 2 | Demographic characteristic of different tumor sides and age.

Variables	Left tumor	Right tumor	*P*	Age ≥40 years	Age <40 years	*P*
Total No.	26	26	NA	28	24	NA
Gender, M/F, *n*	15/11	16/10	0.778	18/10	13/11	0.459
Age (Mean ± SD), years	44.42 ± 13.76	41.19 ± 11.02	0.354	51.89 ± 8.84	32.21 ± 5.85	<0.001
TV (Mean ± SD), ml	65.21 ± 37.12	44.93 ± 37.74	0.056	53.88 ± 30.75	56.46 ± 46.52	0.812
Scanner type, P/S, *n*	8/18	0/26	NA	4/24	4/20	NA

SD, Standard deviation; TV, Tumor volume; P, Philips Ingenia 3.0T scanner; S, Siemens Prisma 3.0T scanner; NA, Not applicable.

respectively. A $P < 0.05$ in a two-tailed test was considered statistically significant.

RESULTS

Clinical and Demographic Characteristic of Study Population

In 52 patients with insular glioma (Grade II, $n = 26$; Grade III, $n = 16$; Grade IV, $n = 10$; male, $n = 31$; female, $n = 21$; median age, 40 years old), 26 tumors were located in the left insula, and 26 were located in the right insula. The lesion overlap is shown in **Figure 1A**. We flipped the image of left-sided tumors so that in all 52 patients, the tumor was in the right insula, and the left side was contralesional (**Figure 1B**). Detailed information on the molecular pathology of the tumors is shown in **Table 1**, and detailed demographic data are shown in **Table 2**.

ROI-Based VBM Analysis

We examined whether the GMV of the contralesional insula differed between patients with left and right insular gliomas. The results of this comparison showed that no voxels survived the FWE correction. We next compared patients aged ≥40

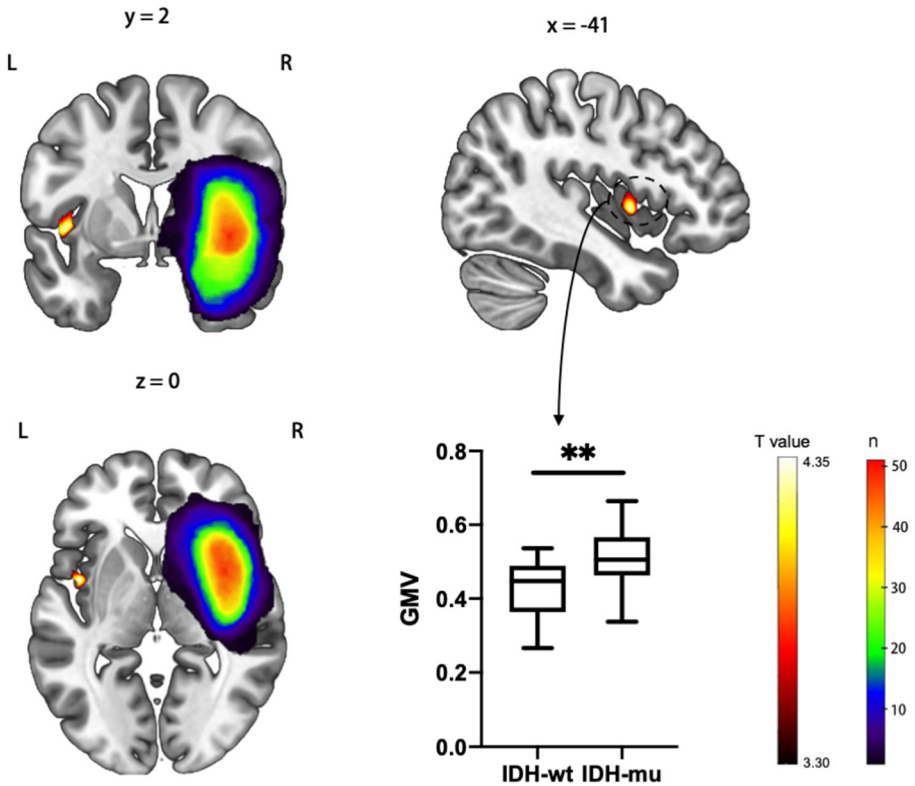

FIGURE 2 | *T* statistical parametrical map of IDH-mu > IDH-wt in ROI (left insula) based VBM analysis. The box plot showed the GMV of significant clusters between IDH-wt and IDH-mu insular glioma. $^{**}P < 0.01$.

TABLE 3 | VBM analysis for IDH-mu > IDH-wt.

Cluster size (voxels)	*P*-value	Peak MNI coordinates			*t* score peak level	Anatomy location
		x	*y*	*z*		
320	0.003	−44	2	0	4.39	Anterior insular cortex
		−39	−9	15	3.58	Posterior insular cortex

and <40 years to determine whether aging affected the GMV of the contralesional insula. This comparison also did not reveal significant voxels. Thus, tumor side and patient age were unrelated to the GMV of contralesional insula in our cohort.

Next, we first compared the GMV between LGG and HGG, and the results showed that no voxel survived the FWE correction. And the GMV in the entire contralesional insular cortex was also indifferent (**Figure 3** and **Table 4**).

Then, we investigated whether molecular pathology in glioma is associated with the observed contralesional structural reorganization. A cluster of 320 voxels located in both anterior and posterior insular cortexes showed a significantly increased GMV in IDH-mu relative to IDH-wt (**Figure 2** and **Table 3**). We extracted the GMV value of the significant cluster and the entire insula and found that they were both significantly higher in IDH-mu than in IDH-wt (**Figure 3** and **Table 4**).

However, no voxel survived in the comparison of TERTp-mu vs. TERTp-wt and 1p19q-codel vs. non-1p19q-codel. Moreover, we did not observe any GMV differences in the entire contralesional cortex in the comparisons (**Figure 3** and **Table 4**).

DISCUSSION

The results of this study demonstrated for the first time that IDH mutation in insular glioma leads to morphologic compensation in the contralesional insula. TERTp mutation and 1p19q codeletion did not have this effect. The reorganization in the contralesional hemisphere could be the result of disinhibition (29), which has been observed in stroke patients on a functional level (30–32). However, glioma is a progressive disease that causes increasing damage over time. Structural reorganization with tumor growth has been observed not only in the region adjacent to the lesion but also in the contralateral hemisphere (6). Contralesional plasticity was shown to be positively correlated with the degree of impairment (29). Under these circumstances, functional plasticity of existing synapses—which depends on synaptic efficacy (33)—may not be sufficient to restore neuronal

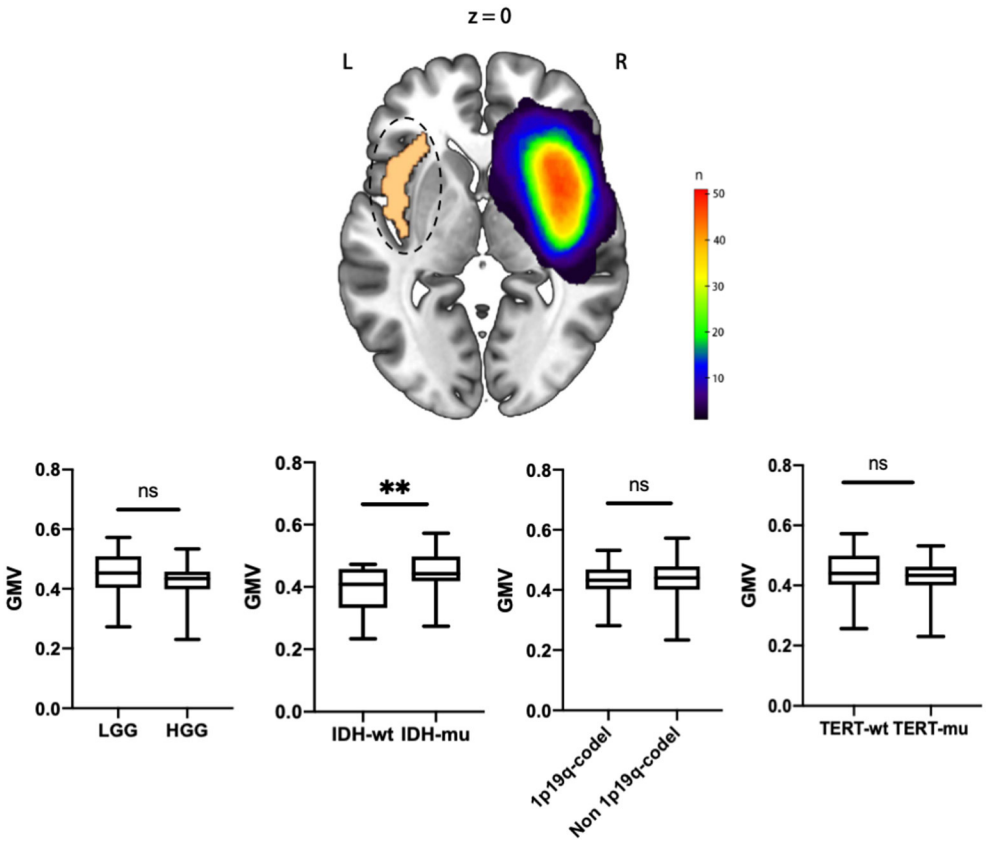

FIGURE 3 | The entire contralesional insula GMV comparisons between different histological grade and molecular pathology status. $^{**}P < 0.01$ ns, for not significant.

TABLE 4 | *t*-test for GMV in different groups.

Variables	GMV (mean ± SD)											
	LGG	HGG	*P*	IDH-mu	IDH-wt	*P*	TERT-mu	TERT-wt	*P*	1p19q-codel	Non-1p19q-codel	*P*
Active region	–	–	–	0.511 ± 0.075	0.427 ± 0.086	0.0011	–	–	–	–	–	–
Entire contralesional insular cortex	0.449 ± 0.074	0.415 ± 0.071	0.096	0.448 ± 0.064	0.390 ± 0.082	0.0096	0.421 ± 0.067	0.440 ± 0.078	0.377	0.431 ± 0.062	0.433 ± 0.078	0.909

activity when structural plasticity involving synaptogenesis and axonal remodeling are required (34–36). Thus, structural remodeling of the contralesional hemisphere in insular glioma patients may depend on the duration between the onset of the lesion and detection and the extent of damage within this duration.

Along with this perspective, we could infer that insular glioma patients with IDH mutation had a longer disease course than those with wild-type IDH and accumulate damage to the insula slowly. In fact, IDH mutation has also been reported to be an early event in gliomagenesis that precedes the occurrence of TERTp mutation and 1p19q codeletion (37), which might be the reason for the absence of contralesional reorganization in the latter two genetic alterations. IDH catalyzes the conversion of isocitrate into α-ketoglutarate (α-KG), whereas the enzyme produced by the mutated IDH gene further converts α-KG into 2-hydroxyglutarate (α-HG). Excess α-HG inhibits α-KG-dependent enzymes and causes alterations in cellular metabolism, epigenetic regulation, redox state, and DNA repair, all of which contribute to carcinogenesis including acute myeloid leukemia (AML), chondrosarcoma, and glioma (38, 39). However, IDH mutation in AML and chondrosarcoma has been linked to worse prognosis, while the opposite is true for glioma (38). This phenomenon implied the complex role in gliomagenesis. On one hand, IDH mutation may inhibit complement activation and help the tumor evade immune surveillance, leading to gliomagenesis (40, 41). On the other hand, IDH mutation reduced cytoprotection and apoptosis resistance in tumor cells and increased the number of antitumor immune cells (M1 tumor-associated macrophages), resulting

in tumor suppression (42, 43). And the better prognosis of IDH-mu glioma patients implied that the tumor suppression role overwhelmed its promotion role, which led to a longer disease course and allowed contralesional reorganization to proceed as observed in the present study.

Moreover, opposite to the IDH subtype, we did not observe a compensation in the contralesional insular cortex in different histological grades. These results implied that the effect on contralesional compensation on the IDH subtype was more significant than histological classification, also provided evidence for different structural remodeling patterns in different IDH subtypes, and also supported the distinctive biological behavior between them (44). As for GBM, the most malignant type in histological classification could be divided into primary GBM (always IDH-wt) and secondary GBM (always IDH-mu). Our result implied the insular secondary GBM patients had a relatively long disease course, which is consistent with its feature of increasing the malignancy grade of a lower grade glioma over time (45).

There were some limitations to this study. Firstly, the sample in this study was relatively small. Secondly, we did not evaluate neurocognitive performance in our patients, and therefore, it is unclear whether the observed reorganization of the brain structure had functional significance. And functional MRI could provide additional information on this point. Additionally, we did not determine whether an association between molecular pathologic subtype in glioma and contralesional structural reorganization exists in tumors located outside the insula, although this warrants further study. Nonetheless, our results provide evidence for contralesional plasticity in the brain of patients with insular glioma and a possible molecular basis for this observation. These findings may have clinical significance in that insular glioma patients with IDH mutation may be candidates for more complete resection when an intraoperative pathologic diagnosis is available.

DATA AVAILABILITY STATEMENT

The raw data supporting the conclusions of this article will be made available by the authors, without undue reservation.

ETHICS STATEMENT

The studies involving human participants were reviewed and approved by the Institutional Review Board of the Beijing Tiantan Hospital. Written informed consent to participate in this study was provided by the participants' legal guardian/next of kin.

AUTHOR CONTRIBUTIONS

ZHu designed the study, analyzed the data, and drafted the manuscript. JX provided the clinical and imaging data. GL and ZL performed the literature search. SS, YZ, ZHo, and JX reviewed and edited the manuscript. All authors contributed to the article and approved the submitted version.

FUNDING

This study was supported by the National Natural Science Foundation of China (ID: 81771792) and the Beijing Municipal Science and Technology Commission (Z171100000117002).

REFERENCES

1. Raz N, Lindenberger U. Life-span plasticity of the brain and cognition: from questions to evidence and back. *Neurosci Biobehav Rev.* (2013) 37(9 Pt B):2195–200. doi: 10.1016/j.neubiorev.2013.10.003
2. Ismail FY, Fatemi A, Johnston MV. Cerebral plasticity: Windows of opportunity in the developing brain. *Eur J Paediatr Neurol.* (2017) 21:23–48. doi: 10.1016/j.ejpn.2016.07.007
3. Yuan T, Zuo Z, Ying J, Jin L, Kang J, Gui S, et al. Structural and functional alterations in the contralesional medial temporal lobe in glioma patients. *Front Neurosci.* (2020) 14:10. doi: 10.3389/fnins.2020.00010
4. Cao Y, D"Olhaberriague L, Vikingstad EM, Levine SR, Welch KMA. Pilot Study of functional MRI to assess cerebral activation of motor function after poststroke hemiparesis. *Stroke.* (1998) 29:112–22.
5. Pineiro R, Pendlebury S, Johansen-Berg H, Matthews PM. Functional MRI detects posterior shifts in primary sensorimotor cortex activation after stroke: evidence of local adaptive reorganization? *Stroke.* (2001) 32:1134–9. doi: 10.1161/01.str.32.5.1134
6. Fisicaro RA, Jost E, Shaw K, Brennan NP, Peck KK, Holodny AI. Cortical plasticity in the setting of brain tumors. *Top Magn Reson Imaging.* (2016) 25:25–30. doi: 10.1097/rmr.0000000000000077
7. Almairac F, Duffau H, Herbet G. Contralesional macrostructural plasticity of the insular cortex in patients with glioma: a VBM study. *Neurology.* (2018) 91:e1902–8. doi: 10.1212/wnl.0000000000006517
8. Han K, Davis RA, Chapman SB, Krawczyk DC. Strategy-based reasoning training modulates cortical thickness and resting-state functional connectivity in adults with chronic traumatic brain injury. *Brain Behav.* (2017) 7:e00687. doi: 10.1002/brb3.687
9. Xu J, Elazab A, Liang J, Jia F, Zheng H, Wang W, et al. Cortical and subcortical structural plasticity associated with the glioma volumes in patients with cerebral gliomas revealed by surface-based morphometry. *Front Neurol.* (2017) 8:266. doi: 10.3389/fneur.2017.00266
10. Liu D, Chen J, Hu X, Hu G, Liu Y, Yang K, et al. Contralesional homotopic functional plasticity in patients with temporal glioma. *J Neurosurg.* (2020) 134:1–9. doi: 10.3171/2019.11.Jns191982
11. Duffau H, Capelle L. Preferential brain locations of low-grade gliomas. *Cancer.* (2004) 100:2622–6. doi: 10.1002/cncr.20297
12. Li Z, Li G, Liu Z, Pan Y, Hou Z, Wu L, et al. Transcortical approach for insular gliomas: a series of 253 patients. *J Neuro Oncol.* (2020) 147:59–66. doi: 10.1007/s11060-020-03390-2
13. Gogolla N. The insular cortex. *Curr Biol.* (2017) 27:R580–6. doi: 10.1016/j.cub.2017.05.010
14. Wu AS, Witgert ME, Lang FF, Xiao L, Bekele BN, Meyers CA, et al. Neurocognitive function before and after surgery for insular gliomas. *J Neurosurg.* (2011) 115:1115–25. doi: 10.3171/2011.8.Jns11488
15. Herbet G, Maheu M, Costi E, Lafargue G, Duffau H. Mapping neuroplastic potential in brain-damaged patients. *Brain.* (2016) 139(Pt 3):829–44. doi: 10.1093/brain/awv394
16. Eckel-Passow JE, Lachance DH, Molinaro AM, Walsh KM, Decker PA, Sicotte H, et al. Glioma groups based on 1p/19q, IDH, and TERT promoter mutations in tumors. *N Engl J Med.* (2015) 372:2499–508. doi: 10.1056/NEJMoa1407279

17. Herveyjumper SL, Berger MS. Insular glioma surgery: an evolution of thought and practice. *J Neurosurg.* (2019) 130:9–16. doi: 10.3171/2018.10.JNS181519
18. Carabenciov ID, Buckner JC. Controversies in the therapy of low-grade gliomas. *Curr Treat Options Oncol.* (2019) 20:25. doi: 10.1007/s11864-019-0625-6
19. Patel M, Vogelbaum MA, Barnett GH, Jalali R, Ahluwalia MS. Molecular targeted therapy in recurrent glioblastoma: current challenges and future directions. *Expert Opin Investig Drugs.* (2012) 21:1247–66. doi: 10.1517/13543784.2012.703177
20. Hegi ME, Diserens AC, Gorlia T, Hamou MF, de Tribolet N, Weller M, et al. MGMT gene silencing and benefit from temozolomide in glioblastoma. *N Engl J Med.* (2005) 352:997–1003. doi: 10.1056/NEJMoa043331
21. Ocklenburg S, Friedrich P, Güntürkün O, Genç E. Voxel-wise grey matter asymmetry analysis in left- and right-handers. *Neurosci Lett.* (2016) 633:210–4. doi: 10.1016/j.neulet.2016.09.046
22. Yuan T, Ying J, Zuo Z, Gui S, Gao Z, Li G, et al. Structural plasticity of the bilateral hippocampus in glioma patients. *Aging.* (2020) 12:10259–74. doi: 10.18632/aging.103212
23. Hartmann C, Meyer J, Balss J, Capper D, Mueller W, Christians A, et al. Type and frequency of IDH1 and IDH2 mutations are related to astrocytic and oligodendroglial differentiation and age: a study of 1,010 diffuse gliomas. *Acta Neuropathol.* (2009) 118:469–74. doi: 10.1007/s00401-009-0561-9
24. Fjell AM, Westlye LT, Grydeland H, Amlien I, Espeseth T, Reinvang I, et al. Accelerating cortical thinning: unique to dementia or universal in aging? *Cereb Cortex.* (2014) 24:919–34. doi: 10.1093/cercor/bhs379
25. Storsve AB, Fjell AM, Tamnes CK, Westlye LT, Overbye K, Aasland HW, et al. Differential longitudinal changes in cortical thickness, surface area and volume across the adult life span: regions of accelerating and decelerating change. *J Neurosci.* (2014) 34:8488–98. doi: 10.1523/jneurosci.0391-14.2014
26. Hedman AM, van Haren NEM, Schnack HG, Kahn RS, Hulshoff Pol HE. Human brain changes across the life span: a review of 56 longitudinal magnetic resonance imaging studies. *Hum Brain Mapp.* (2012) 33:1987–2002. doi: 10.1002/hbm.21334
27. Battaglini M, Gentile G, Luchetti L, Giorgio A, Vrenken H, Barkhof F, et al. Lifespan normative data on rates of brain volume changes. *Neurobiol Aging.* (2019) 81:30–7. doi: 10.1016/j.neurobiolaging.2019.05.010
28. Ridgway GR, Litvak V, Flandin G, Friston KJ, Penny WD. The problem of low variance voxels in statistical parametric mapping; a new hat avoids a 'haircut'. *NeuroImage.* (2012) 59:2131–41. doi: 10.1016/j.neuroimage.2011.10.027
29. Di Pino G, Pellegrino G, Assenza G, Capone F, Ferreri F, Formica D, et al. Modulation of brain plasticity in stroke: a novel model for neurorehabilitation. *Nat Rev Neurol.* (2014) 10:597–608. doi: 10.1038/nrneurol.2014.162
30. Takeuchi N, Tada T, Chuma T, Matsuo Y, Ikoma K. Disinhibition of the premotor cortex contributes to a maladaptive change in the affected hand after stroke. *Stroke.* (2007) 38:1551–6. doi: 10.1161/STROKEAHA.106.470187
31. Shimizu T, Hosaki A, Hino T, Sato M, Komori T, Hirai S, et al. Motor cortical disinhibition in the unaffected hemisphere after unilateral cortical stroke. *Brain.* (2002) 125:1896–907. doi: 10.1093/brain/awf183
32. Lotze M, Markert J, Sauseng P, Hoppe J, Plewnia C, Gerloff C. The role of multiple contralesional motor areas for complex hand movements after internal capsular lesion. *J Neurosci.* (2006) 26:6096–102. doi: 10.1523/jneurosci.4564-05.2006
33. Heynen AJ, Yoon BJ, Liu CH, Chung HJ, Huganir RL, Bear MF. Molecular mechanism for loss of visual cortical responsiveness following brief monocular deprivation. *Nat Neurosci.* (2003) 6:854–62. doi: 10.1038/nn1100
34. Butz M, W?Rg?Tter F, Ooyen AV. Activity-dependent structural plasticity. *Brain Res Rev.* (2009) 60:287–305. doi: 10.1016/j.brainresrev.2008.12.023
35. Draganski B, May A. Training-induced structural changes in the adult human brain. *Behaviou Brain Res.* (2008) 192:137–42. doi: 10.1016/j.bbr.2008.02.015
36. Stroemer RP, Kent TA, Hulsebosch CE. Neocortical neural sprouting, synaptogenesis, and behavioral recovery after neocortical infarction in rats. *Stroke.* (1995) 26:2135–44.
37. Ohba S, Hirose Y. Biological significance of mutant isocitrate dehydrogenase 1 and 2 in gliomagenesis. *Neurol Med Chir.* (2016) 56:170–9. doi: 10.2176/nmc.ra.2015-0322
38. Molenaar RJ, Maciejewski JP, Wilmink JW, van Noorden CJF. Wild-type and mutated IDH1/2 enzymes and therapy responses. *Oncogene.* (2018) 37:1949–60. doi: 10.1038/s41388-017-0077-z
39. Koivunen P, Lee S, Duncan CG, Lopez G, Lu G, Ramkissoon S, et al. Transformation by the (R)-enantiomer of 2-hydroxyglutarate linked to EGLN activation. *Nature.* (2012) 483:484–8. doi: 10.1038/nature10898
40. Zhang L, Sorensen MD, Kristensen BW, Reifenberger G, McIntyre TM, Lin F. D-2-Hydroxyglutarate is an intercellular mediator in IDH-mutant gliomas inhibiting complement and T cells. *Clin Cancer Res.* (2018) 24:5381–91. doi: 10.1158/1078-0432.Ccr-17-3855
41. Philip B, Yu DX, Silvis MR, Shin CH, Robinson JP, Robinson GL, et al. Mutant IDH1 promotes glioma formation *in vivo*. *Cell Rep.* (2018) 23:1553–64. doi: 10.1016/j.celrep.2018.03.133
42. Houillier C, Wang X, Kaloshi G, Mokhtari K, Guillevin R, Laffaire J, et al. IDH1 or IDH2 mutations predict longer survival and response to temozolomide in low-grade gliomas. *Neurology.* (2010) 75:1560–6. doi: 10.1212/WNL.0b013e3181f96282
43. Liu PS, Wang H, Li X, Chao T, Teav T, Christen S, et al. α-ketoglutarate orchestrates macrophage activation through metabolic and epigenetic reprogramming. *Nat Immunol.* (2017) 18:985–94. doi: 10.1038/ni.3796
44. Sanson M, Marie Y, Paris S, Idbaih A, Laffaire J, Ducray F, et al. Isocitrate Dehydrogenase 1 codon 132 mutation is an important prognostic biomarker in gliomas. *J Clin Oncol.* (2009) 27:4150–4. doi: 10.1200/JCO.2009.21.9832
45. Aldape K, Zadeh G, Mansouri S, Reifenberger G, von Deimling A. Glioblastoma: pathology, molecular mechanisms and markers. *Acta Neuropathol.* (2015) 129:829–48. doi: 10.1007/s00401-015-1432-1

Conflict of Interest: The authors declare that the research was conducted in the absence of any commercial or financial relationships that could be construed as a potential conflict of interest.

frontiers in Oncology

ORIGINAL RESEARCH
published: 17 June 2021
doi: 10.3389/fonc.2021.683367

Uncovering a Distinct Gene Signature in Endothelial Cells Associated With Contrast Enhancement in Glioblastoma

Fan Yang[1†], Yuan Xie[2†], Jiefu Tang[3†], Boxuan Liu[4†], Yuancheng Luo[5], Qiyuan He[2], Lingxue Zhang[2], Lele Xin[2], Jianhao Wang[1], Sinan Wang[2], Shuqiang Zhang[2], Qingze Cao[2], Liang Wang[6], Liqun He[1,7*] and Lei Zhang[2,4*]*

[1] Department of Neurosurgery, Tianjin Medical University General Hospital, Tianjin Neurological Institute, Key Laboratory of Post-Neuro-injury Neuro-Repair and Regeneration in Central Nervous System, Ministry of Education and Tianjin City, Tianjin, China, [2] Key Laboratory of Ministry of Education for Medicinal Plant Resource and Natural Pharmaceutical Chemistry, National Engineering Laboratory for Resource Developing of Endangered Chinese Crude Drugs in Northwest of China, College of Life Sciences, Shaanxi Normal University, Xi'an, China, [3] Trauma Center, The First Affiliated Hospital of Hunan University of Medicine, Huaihua, China, [4] Precision Medicine Center, The Second People's Hospital of Huaihua, Huaihua, China, [5] School of Life Science, University of Liverpool, Liverpool, United Kingdom, [6] Department of Neurosurgery, Tangdu Hospital of the Fourth Military Medical University (Air Force Medical University of PLA), Xi'an, China, [7] Department of Immunology, Genetics and Pathology, Uppsala University, Rudbeck Laboratory, Uppsala, Sweden

Purpose: Glioblastoma (GBM) is the most aggressive and lethal type of brain tumors. Magnetic resonance imaging (MRI) has been commonly used for GBM diagnosis. Contrast enhancement (CE) on T1-weighted sequences are presented in nearly all GBM as a result of high vascular permeability in glioblastomas. Although several radiomics studies indicated that CE is associated with distinct molecular signatures in tumors, the effects of vascular endothelial cells, the key component of blood brain barrier (BBB) controlling vascular permeability, on CE have not been thoroughly analyzed.

Methods: Endothelial cell enriched genes have been identified using transcriptome data from 128 patients by a systematic method based on correlation analysis. Distinct endothelial cell enriched genes associated with CE were identified by analyzing difference of correlation score between CE-high and CE–low GBM cases. Immunohistochemical staining was performed on in-house patient cohort to validate the selected genes associated with CE. Moreover, a survival analysis was conducted to uncover the relation between CE and patient survival.

Results: We illustrated that CE is associated with distinct vascular molecular imprints characterized by up-regulation of pro-inflammatory genes and deregulation of BBB related genes. Among them, PLVAP is up-regulated, whereas TJP1 and ABCG2 are down-regulated in the vasculature of GBM with high CE. In addition, we found that the high CE is associated with poor prognosis and GBM mesenchymal subtype.

OPEN ACCESS

Edited by:
Manoj Kumar, National Institute of Mental Health and Neurosciences (NIMHANS), India

Reviewed by:
Alessia Pellerino, University Hospital of the City of Health and Science of Turin, Italy
Haridha Shivram, Genentech, Inc., United States

****Correspondence:***
Lei Zhang
zlsnnu@gmail.com;
lei.zhang@snnu.edu.cn
Liqun He
liqun.he@igp.uu.se
Liang Wang
drwangliang@126.com

†These authors have contributed equally to this work

Specialty section:
This article was submitted to Neuro-Oncology and Neurosurgical Oncology, a section of the journal Frontiers in Oncology

Received: *20 March 2021*
Accepted: *27 May 2021*
Published: *17 June 2021*

Citation:
Yang F, Xie Y, Tang J, Liu B, Luo Y, He Q, Zhang L, Xin L, Wang J, Wang S, Zhang S, Cao Q, Wang L, He L and Zhang L (2021) Uncovering a Distinct Gene Signature in Endothelial Cells Associated With Contrast Enhancement in Glioblastoma. Front. Oncol. 11:683367. doi: 10.3389/fonc.2021.683367

Conclusion: We provide an additional insight to reveal the molecular trait for CE in MRI images with special focus on vascular endothelial cells, linking CE with BBB disruption in the molecular level. This study provides a potential new direction that may be applied for the treatment optimization based on MRI features.

Keywords: contrast enhancement, MRI, endothelial cell, radiomics, glioblastoma

INTRODUCTION

Glioblastoma (GBM), the most aggressive and lethal type of brain tumors, is characterized by extensive vascular abnormality in both morphological and molecular levels (1). Microvascular proliferation and high vascular permeability are the hallmarks of GBM (2). Abnormal vasculature in GBM promotes tumor growth and relapses by inducing hypoxia and providing specialized niches for glioma stem-like cells (GSCs), and has been identified as a target for GBM treatment (3). MRI is a powerful non-invasive diagnostic tool for GBM and it is routinely used in clinical, providing *in vivo* portraits of tumors with multidimensional information including structure, location, composition, functional/physiological features as well as vascular parameters (4, 5). Tumor neoangiogenesis can be determined by the cerebral blood volume (CBV), which can be calculated from dynamic susceptibility contrast MRI (DSC-MRI) (6, 7). The leakiness of GBM vasculature can be detected by the conventional contrast-enhanced MRI following intravenous administration of gadolinium-based contrast agents (8). As a result of diffusion of contrast molecules out of vessels and accumulation within extracellular space in tumors, contrast-enhancing hyper-intense regions on T1-weighted (T1W) sequences are presented in nearly all GBM (9). These contrast-enhancing regions are the typical target for surgical resection (9).

Contrast enhancement (CE) is associated with distinct molecular imprints, and the plethora of radiomics studies have conclusively correlated CE with distinct molecular imprint including hypoxia signatures (10–14). However, most of these investigations were focused on tumors cells. The effect of vascular endothelial cells (ECs), the key component of blood brain barrier (BBB), on CE has not been thoroughly analyzed. In this study, we aim to understand how ECs affect CE in the tumors, and to uncover the endothelial-specific molecular imprints for CE.

MATERIALS AND METHODS

Patients Cohorts

External cohort: 128 GBM cases (5) with publicly available transcriptome data and MRI records [The Cancer Imaging Archive (TCIA) (http://www.cancerimagingarchive.net/)] were included in this study (**Table S1**). Patients' clinical information and processed RNA-sequencing data were obtained from the database of The Cancer Genome Atlas (TCGA) (http://cancergenome.nih.gov). The tumor segmentation information containing enhancing tumor volume (EV), central non-enhancing tumor volume (NV), complete tumor volume (CV: the sum of EV and NV) were obtained from the previous study (5).

Internal cohort: Our in-house GBM samples (14 cases) were collected at the Tangdu Hospital of the Fourth Military Medical University (Air Force Medical University of PLA) (**Table S1**). Pathological characterizations were performed according to the WHO criteria (2016). The MRI and biopsies were collected before radio- and chemotherapy, and the patients did not receive any anti-angiogenic therapy. All the patients have received corticosteroid (Dexamethasone) before surgery.

MRI Imaging Acquisition and Preprocessing Procedures

MRI scans were performed for in-house patients with a 3.0T MRI system (MR750; GE Healthcare, Milwaukee, WI, USA) before surgery. MRI sequence included T1-weighted imaging, contrast-enhanced T1-weighted imaging, fast T2-weighted imaging, and fluid-attenuated inversion recovery imaging (FLAIR). Tumor segmentation and component volumes were analyzed according to the previous description (5). In brief, after skull-stripping with Brain Extraction Tool (BET) (15), T1-weighted images were registered to Montreal Neurological Institute (MNI) 152 standard space using the FMRIB's Linear Image Registration Tool (FLIRT) in FMRIB software library (FSL) (16). For individual subject, all imaging modalities were co-registered to their native T1-weighted images space. MRI volumes were smoothed using Smallest Univalue Segment Assimilating Nucleus (SUSAN) to reduce intensity noise (17). Then, the automated hybrid generative-discriminative method (GLISTRboost) was used to segment the enhancing tumor volume (EV), central non-enhancing tumor volume (NV), and the complete tumor volume (CV) (18). The segmentation was confirmed by experienced neuroradiology expert and was revised if necessary.

Immunohistochemical Analysis

Tissue sections of formalin-fixed, paraffin-embedded samples were deparaffinized and dehydrated prior to antigen retrieval followed by blocking as previously described (19). Then the sections were incubated with primary antibody towards PLVAP (HPA002279, Sigma), ABCG2 (ab24115, Abcam), and TJP1 (HPA001637, Sigma) followed by incubation with biotinylated secondary antibody and streptavidin conjugated to HRP (Vector Laboratories). The staining was developed with the DAB substrate kit (SK-4100, Vector Laboratories) according to the manufacturer's protocol.

The images of immunohistochemical staining for VWF, CLDN5, CDH5, PECAM1, and ELTD1 in tumor were

obtained from The Human Protein Atlas database (https://www.proteinatlas.org/).

Identification of Endothelial Cell-Enriched (EC-Enriched) Genes and Gene Ontology (GO) Analysis

We used a correlation-based method (20) to identify endothelial-specific genes in the bulk transcriptome dataset from TCGA. Spearman correlation coefficients between known EC marker genes (*CDH5*, *CLDN5*, *VWF*) and all other protein coding genes were calculated. The raw P values and the False Discovery Rate (FDR) adjusted P values were also calculated. Genes with mean correlation coefficient more than 0.3 were identified as EC-enriched genes.

GO analysis for EC-enriched genes was performed using the web-based Gene Ontology tool (http://geneontology.org/), and only GO terms for biological processes were included in the analysis.

Identification of CE-High and CE-Low Associated EC-Enriched Genes

Contrast enhancement high (CE-high) and contrast enhancement low (CE-low) tumors associated EC-enriched genes were identified by analyzing differential correlation score. In brief, according to enhancing volume/complete tumor volume ratio (EV/CV ratio), patients with top-20 and bottom-20 EV/CV ratio were selected and dichotomized into CE-high or CE-low group respectively. Correlation coefficients of EC-enriched genes to EC marker genes (*CDH5*, *CLDN5*, *VWF*) were calculated in CE-low tumor group and CE-high tumor group respectively, and then the difference between the two correlation coefficients (CE-high tumors and CE-low tumors) yields the differential correlation scores for each EC-enriched gene. Genes with differential correlation score >0.1 were classified as CE-high associated genes, whereas genes with differential correlation score < −0.4 were classified as CE-low associated genes.

Functional annotation of CE-high or CE-low associated EC genes were performed using the web-based Gene Ontology tool (http://geneontology.org/), and the GO terms with a FDR < 0.05 were considered significantly enriched.

Survival Analysis

One hundred twenty-eight patients from TCGA database were dichotomized into CE-high or CE-low subgroups (median cutoff). Survival curves were plotted by the Kaplan-Meier method. Univariate test (log-rank) and multivariate test (Cox proportional hazards model) were used to compare survival of two subgroups.

Statistical Analysis

Statistical analysis was performed using GraphPad Prism (GraphPad Software) and R (v 4.0.3). All the Pearson correlation coefficients analysis were performed in R with cor.test function from the stats package. The survival curves of mice and patients were analyzed by log rank test. The following p values indicate statistical significance: *p < 0.05.

RESULTS

Identification of Endothelial-Enriched Genes in GBM

To explore the effect of vascular ECs on contrast enhancement in MRI, we first identified EC-enriched genes by a systematic approach through performing the correlation analysis of the expression profiles of all gene transcripts to the known EC marker gene as previously described (20, 21). A high average correlation coefficient with those EC marker genes indicates the enrichment of the genes in EC (20, 21). We analyzed transcriptome data from 128 GBM cases with available MRI records in TCGA (**Table S1**) to produce the average correlation values between EC marker genes (*CDH5*, *CLDN5*, *VWF*) and the other >20,000 protein encoding genes, yielding 343 EC-enriched genes manifesting correlation coefficient >0.3 (**Figures 1A, B** and **Table S2**). The top 10 most highly enriched genes, including *VWF*, *TMEM204*, *GPR116*, *CLDN5*, *CDH5*, *PECAM1*, *ELTD1*, *TIE1*, *GPR4*, and *MMRN2*, are known EC enriched transcripts (21, 22). Expression of VWF, CLDN5, CDH5, PECAM1, and ELTD1 in the GBM vasculature were confirmed by immunohistochemistry (**Figure 1B**). Gene Ontology analysis of these 343 EC-enriched gene transcripts uncovered that the top significantly enriched biological process categories were all related to EC function (vasculature/blood vessel development), as well as numerous other endothelial related terms including blood vessel morphogenesis, circulatory system morphogenesis, tube development, and angiogenesis (**Figure 1C** and **Table S2**).

Contrast Enhancement Is associated With a Distinct Molecular Signature in ECs Characterized by Upregulation of Pro-inflammatory Genes and Deregulation of BBB-Related Genes

To uncover the CE associated molecular signatures in vasculature, we analyzed MRI records of 128 GBM cases available in The Cancer Imaging Archive (TCIA) (https://www.cancerimagingarchive.net/) (**Table S1**). To evaluate the degree of CE for GBMs, we generated the ratio between the enhancing volume and the complete tumor volume (sum of the enhancing part and the central non-enhancing part) in the 128 TCGA GBM cases (**Figure 2A** and **Table S1**). Top- and bottom-20 patients were selected and dichotomized into contrast enhancement high (CE-high) or contrast enhancement low (CE-low) groups according to their enhancing volume/complete tumor volume ratio (EV/CV ratio) (**Figure 2A** and **Table S1**). In order to identify CE associated vascular genes, we first analyzed the correlation coefficients of the 343 EC-enriched genes to the EC markers in CE-low and CE-high groups respectively, and produced a differential correlation score (between CE-high and CE-low) for each gene. The scores indicate "degree" of EC-enrichment. High differential correlation score indicates that the gene gains EC-enrichment in CE-high tumors, which is likely due to (1) loss of expression in CE-low ECs, or (2) gain of expression in CE-high ECs. Forty-two genes with higher correlation coefficient in CE-high tumors (differential

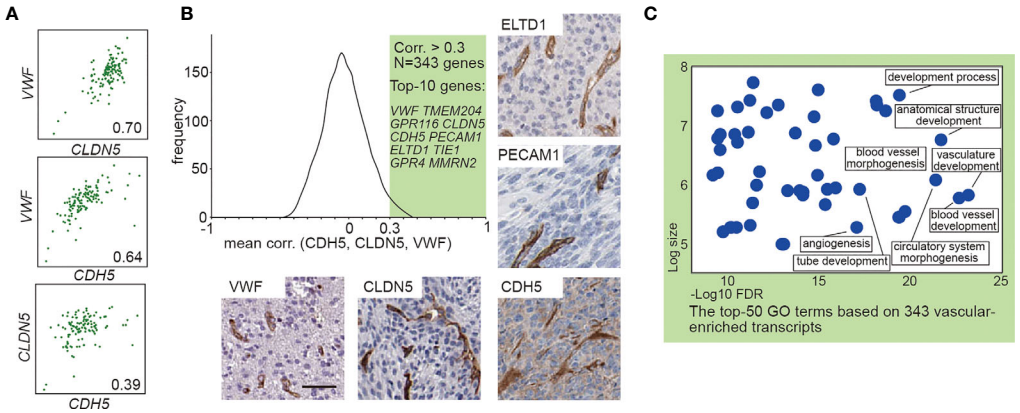

FIGURE 1 | Transcript-based analysis identifies endothelial-enriched genes in GBM. **(A)** Correlation analysis between *VWF*, *CLDN5*, and *CDH5*. **(B)** Frequency distribution plot and immunohistochemical staining of 343 EC genes. The frequency distribution illustrates the distribution of the average correlation coefficients between the known EC marker (*VWF*, *CLDN5*, and *CDH5*) and the other >20,000 protein encoding genes. The immunohistochemical staining (VWF, CLDN5, CDH5, PECAM1, and ELTD1) in human GBM were obtained from Human Protein Atlas: www.hpr.se). Scale bar = 50 μm. **(C)** The enriched GO terms of the 343 EC enriched genes. The x-axis shows the enrichment statistics false discovery rate (minus log scale) and the y-axis shows the number of genes in the GO term (log scale).

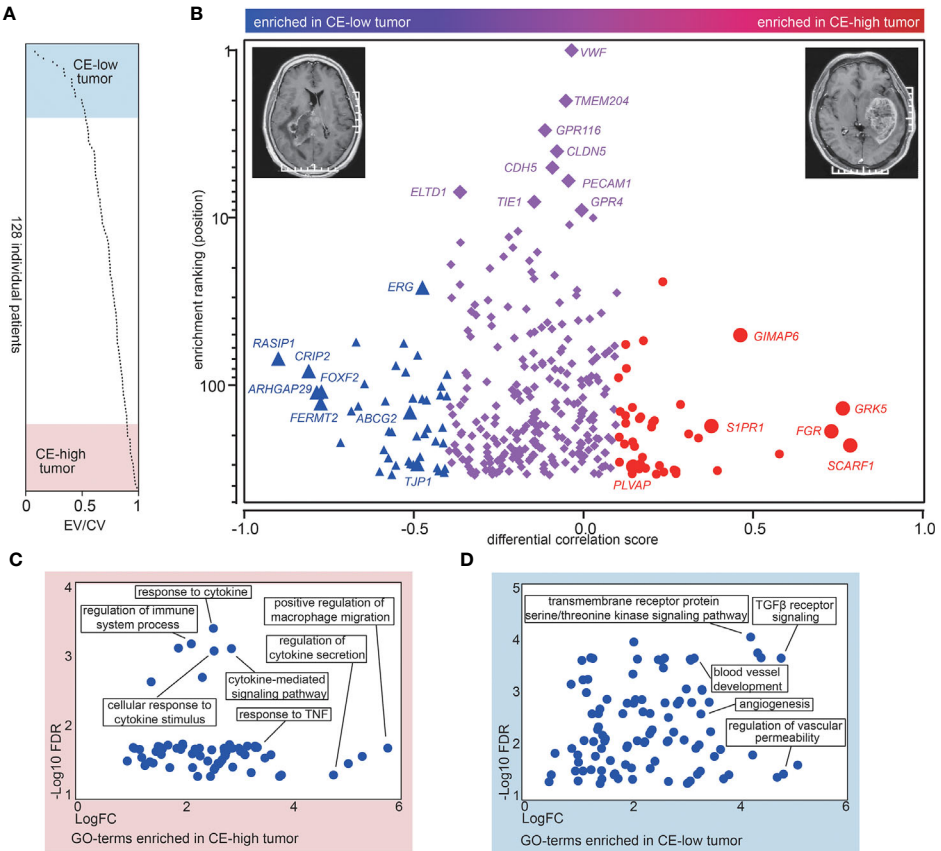

FIGURE 2 | CE is associated with a distinct molecular signature. **(A)** Overview of the ratios between the enhancing volume to the complete tumor volume (EV/CV ratio) in the 128 TCGA patients. The ratios are sorted from low to high. **(B)** The differential corr. score (difference between mean corr. with CE-low and CE-high transcripts) was plotted *versus* "EC-enrichment ranking" (position of correlation coefficients categorized as 343 EC-enriched genes, highest corr. = ranking 1). The red circles represent CE-high associated genes and the blue triangles represent CE-low associated genes. **(C, D)** Gene ontology analysis of CE-high **(C)** and CE-low **(D)** associated vascular genes. The x-axis shows the enrichment fold (log scale) and the y-axis shows the false discovery rate (log scale).

correlation score > 0.1) were classified as CE-high associated genes, including *SCARF1*, *GRK5*, *FGR*, *GIMAP6*, *S1PR1*, and *PLVAP* (**Figure 2B**, red circles; **Table S3**). On the other hand, 44 genes with higher correlation coefficient in CE-low tumors (differential correlation score < −0.4) were classified as CE-low associated genes including *RASIP1*, *CRIP1*, *ARHGAP29*, *FERMT2*, *ERG*, *FOXF2*, *ABCG2*, *TJP1*, and *COL1A2* (**Figure 2B**, blue triangles; **Table S3**). Interestingly, *TJP1* and *COL1A2* were used as markers for classical and mesenchymal subtype classification (23, 24).

Function annotation of the 42 CE-high associated vascular genes revealed significant enrichment of GO terms connected to "regulation of macrophage," "response to cytokine/TNF," as well as "response to cytokine secretion" (**Figure 2C**), whereas analysis of CE-low associated vascular genes uncovered GO terms including "blood vessel development," "TGFβ receptor signaling," and "regulation of vascular permeability" (**Figure 2D**). Taken together, these results indicate that CE are associated with alteration of genes involved in pro-inflammatory response and BBB integrity in vascular ECs.

Increased PLVAP Expression and Decreased ABCG2 and TJP1 Expression in Vasculature in CE-High GBMs

To validate our findings showing the association of CE with deregulation of BBB related genes in the GBM vasculature, we performed immunohistochemical staining for PLVAP, ABCG2, and TJP1 on in-house CE-high or CE-low GBM cases. All three proteins had vascular staining patterns (**Figures 3A–C**). As expected, PLVAP was up-regulated in the vasculature in CE-high GBMs, while ABCG2 and TJP1 were upregulated in the vasculature of CE-low GBMs (**Figures 3A–C**).

Contrast Enhancement Is Associated With Poor Prognosis and Mesenchymal Subtype

The identification of the association of CE with pro-inflammation led us to further investigate CE in different molecular subtypes of GBM. It has been shown that mesenchymal subtype was the most pro-inflammatory subtype of GBM, which associated with higher immune-associated signaling pathways and immune cells infiltration compared to other non-mesenchymal subtypes including pro-neural and classical subtypes (25, 26). As expected, EV/CV ratio was significantly higher in mesenchymal subtypes (**Figure 4A**). The association of CE-high phenotype with mesenchymal subtype was supported by Kourosh's study with 43 patients (27).

We next set out to assess whether CE correlates with patient survival. By dichotomizing patients into two groups of equal size according to EV/CV ratio, we found that the CE-high group was associated with shorter survival (**Figure 4B**, P = 0.0211, log-rank test). In addition, association of high contrast enhancement with poor prognosis was observed in younger patients (<60 years old) but not in older patients (≥ 60 years old) (**Figures S1A, B**). CE

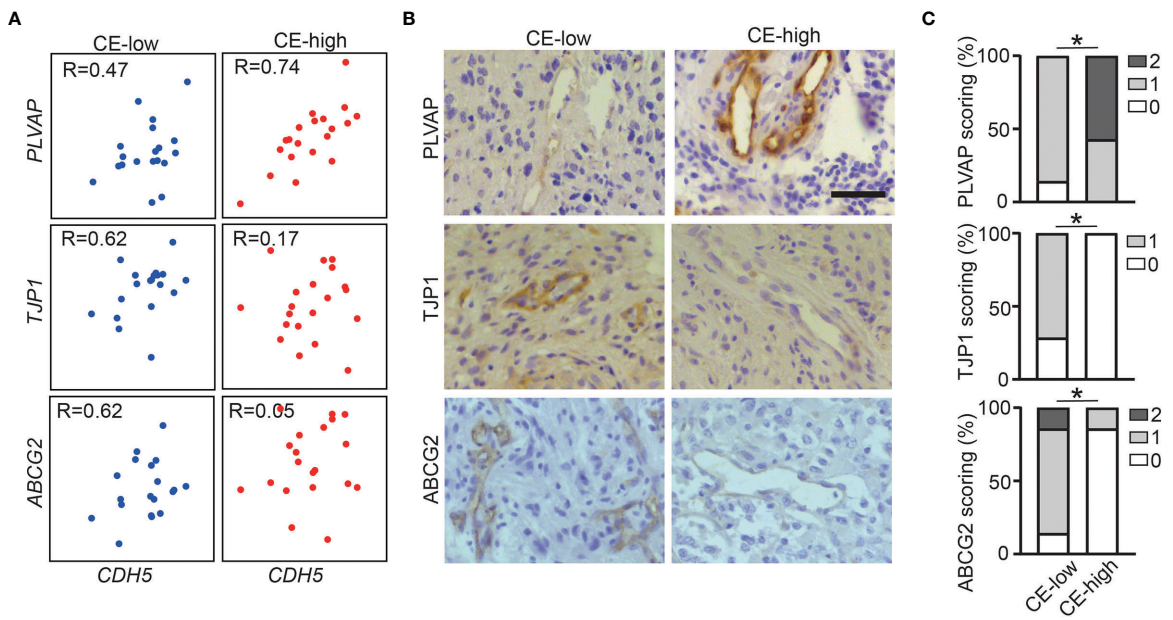

FIGURE 3 | Increased PLVAP expression and decreased ABCG2 and TJP1 expression in vasculature of CE-high GBM. **(A)** Correlation plots show expression of CDH5 *versus* selected genes (*PLVAP*, *TJP1*, and *ABCG2*) in CE-low (Bottom-20 EV/CV cases in TCGA dataset) and CE-high (Top-20 EV/CV cases in TCGA dataset). **(B)** Immunohistochemistry staining of PLVAP, TJP1, ABCG2 in CE-low and CE-high groups. **(C)** Quantification of immunohistochemistry staining of PLVAP, TJP1, ABCG2 in CE-low and CE-high groups. Staining was scored semi-quantitatively on scale from 0 to 2 (0, no vessels stained; 1, minority of vessels stained; and 2, majority of vessels stained) (Mann-Whitney test, *p < 0.05). Scale bar = 50 μm.

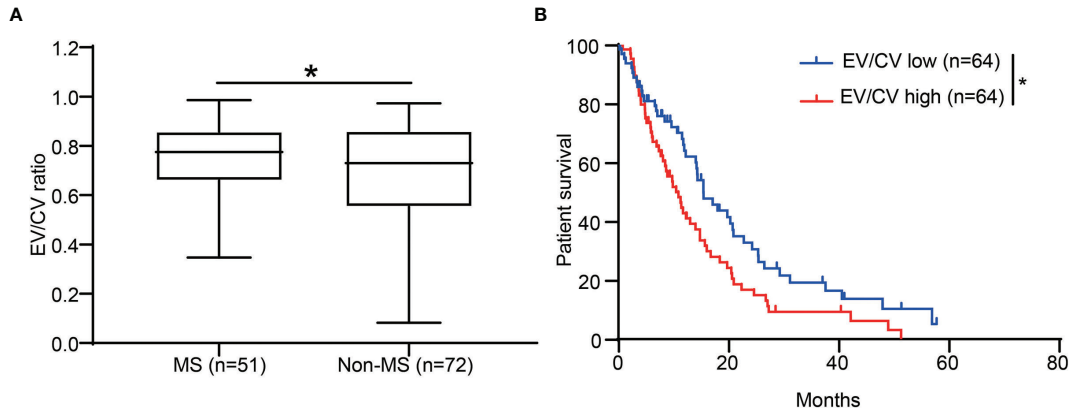

FIGURE 4 | CE was associated with patient survival and enriched in the GBM mesenchymal subtype. **(A)** The ratio of EV/CV was enriched in mesenchymal subtype. Student's t-test, *p < 0.05 **(B)** Kaplan-Meier graph showing patient survival in EV/CV low and EV/CV high groups. Log-rank test, *P < 0.05.

did not significantly correlate to the survival when correcting for age in a multivariate analysis (**Table S4**), indicating CE is not an independent prognostic marker.

DISCUSSION

It has been shown in several studies that CE is associated with inter- and intro-tumoral molecular signature in GBM (10–14). By comparing gene expression in specimen from 22 incompletely contrast-enhancing and 30 completely contrast-enhancing untreated glioblastoma, it revealed that CE was associated with distinct transcriptome signature characterized by increased VEGFA expression (10). These results were supported by Diehn et al. study with 22 GBM patients revealing a strong association between CE and hypoxia signature including VEGFA (11). In addition, with biopsies derived from distinct tumor regions by MRI-guided stereotactic sampling techniques, intro-tumoral heterogeneity of CE was investigated (12–14). Transcriptome analysis of biopsy from paired enhancing and peri-tumoral non-enhancing region from 13 treatment-naïve GBM patients indicated that enhanced regions were characterized by increased level of hypoxia, cellular density, and vascular hyperplasic together with elevated relative cerebral blood volume (CBV) and reduced apparent diffusion coefficient (ADC) (12, 13). Similarly, Van Meter et al. studied the molecular profiles of contrast enhancing region and central non-enhancing necrotic region and showed an enrichment of angiogenesis and hypoxia signature in central non-enhancing necrotic region (14).

In present study, we have integrated public dataset with our in-house patient cohort to provide additional molecular trait for CE with special focus on vascular ECs. ECs are key component of BBB, controlling the vascular permeability and leakiness (28). However, the direct molecular imprint of CE in ECs has not been studied before. Here, we used an unbiased approach to identify CE-low and CE-high associated EC-enriched genes. In contrast to direct comparison, this correlation-based method allows identification cell-type-enriched transcriptome using bulk RNA-seq data. We demonstrated that CE-high in GBM are associated with upregulation of pro-inflammatory genes and deregulation of BBB related genes in EC. The results were supported by the previous study with 148 GBM cases revealing a strong association of CE with an elevated inflammatory response (29).

Alteration of BBB-related genes in CE-high GBM vasculature is noteworthy. In the present study, we provide evidence in the molecular level linking CE with BBB alteration in EC characterized by up-regulation of PLVAP and down-regulation of TJP1 and ABCG2 in vasculature of CE-high GBMs. Plasma lemma vesicle-associated protein (*PLVAP*) is a vascular marker of BBB disruption, and can be induced in vasculature and associated with vascular leakage (30). In normal physiological condition, PLVAP expression is only restricted to vasculature in choroid plexus and circumventricular organs where the ECs are fenestrated to allow exchange between blood and cerebrospinal fluid (CSF) (31). PLVAP could increase vascular permeability by promoting transcytosis in ECs through forming the diaphragms of caveolae, fenestrae, and trans-endothelial channels (31). TJP1, also known as ZO-1, is essential for tight junction formation (32, 33). At BBB, TJP1 link the claudins and occludins to the actin cytoskeleton, sealing ECs (32, 33). *ABCG2* encode breast cancer resistance protein (BCRP), which is the ATP-binding cassette transporter mediating efflux of xenobiotics including temozolomide and other low molecular weight anti-cancer drugs from the endothelium away from the neuro parenchymal space (34). The deregulation of these important proteins indicates that CE may serve as an imaging biomarker for BBB disruption. Interestingly, steroids and anti-angiogenic therapy play an essential role on vascular permeability, and how the steroid and anti-angiogenic treatments affect ECs leading to CE alteration deserves further investigation.

In conclusion, we have shown that CE in GBM was associated with BBB alterations in vascular ECs. Considering the established key role of BBB on systemically delivery of pharmacological

agents into the brain, whether CE is associated with drug delivery and could be a non-invasive image biomarker for monitoring the drug delivery deserves further investigation. Considering the established key role of BBB on systemical delivery of pharmacological agents into the brain, our results support further research to develop CE as a potential non-invasive image biomarker for predicting drug delivery in the future.

CONCLUSION

Our study provided additional insights to reveal molecular trait for CE in MRI images with special focus on vascular ECs in glioblastoma. We demonstrated that high CE was associated with distinct gene signatures characterized by deregulation of BBB-related genes and up-regulation of pro-inflammatory genes.

DATA AVAILABILITY STATEMENT

The datasets presented in this study can be found in online repositories. The names of the repository/repositories and accession number(s) can be found in the article.

ETHICS STATEMENT

The studies involving human participants were reviewed and approved by the Ethics Committee of Shaanxi Normal University. The patients/participants provided their written informed consent to participate in this study.

AUTHOR CONTRIBUTIONS

LZ, LH, and LW conceived the project. FY, YX, JT, and BL performed the experiments, YL, QH, LXZ, LX, JW, SW, SZ, and QC analyzed data. LZ, LH, and LW wrote the manuscript with significant input from FY and YX. All authors contributed to the article and approved the submitted version.

FUNDING

This work was supported by the National Natural Science Foundation of China (NSFC)/the Swedish Foundation for International Cooperation in Research and Higher Education (STINT) Mobility Program (No. 81911530166), the NSFC (No. 81702489, 82002659, 81870978, 81772661), the National Key R&D Program of China (No. 2018YFC1313003), the Natural Science Foundation of Shaanxi Province (No. 2021KW-46, 2020JQ-429, 2020JZ-30), Tianjin Natural Science Foundation (No. 18JCYBJC94000), the Natural Science Foundation of Hunan Province (No. 2020JJ4071), Fundamental Research Funds for the Central University (No. GK202003050, GK202003048), the Natural Science Foundation of Huaihua City (2020R3118, 2020R3116).

ACKNOWLEDGMENTS

We would like to thank all of the Neurosurgery clinicians and staff from Tangdu Hospital of Airforce Military Medical University that assist with the collection of samples. We would also like to thank the patients and their families for their participation in this study.

SUPPLEMENTARY MATERIAL

The Supplementary Material for this article can be found online at: https://www.frontiersin.org/articles/10.3389/fonc.2021.683367/full#supplementary-material

Supplementary Table 1 | Patients' information

Supplementary Table 2 | Endothelial enriched genes identified by correlation analysis

Supplementary Table 3 | Contrast enhancement associated endothelial enriched genes

Supplementary Table 4 | Multivariate survival analysis with contrast enhancement

REFERENCES

1. Dieterich LC, Mellberg S, Langenkamp E, Zhang L, Zieba A, Salomaki H, et al. Transcriptional Profiling of Human Glioblastoma Vessels Indicates a Key Role of VEGF-A and TGFbeta2 in Vascular Abnormalization. *J Pathol* (2012) 228(3):378–90. doi: 10.1002/path.4072
2. Zhang L, Kundu S, Feenstra T, Li X, Jin C, Laaniste L, et al. Pleiotrophin Promotes Vascular Abnormalization in Gliomas and Correlates With Poor Survival in Patients With Astrocytomas. *Sci Signaling* (2015) 8(406):ra125. doi: 10.1126/scisignal.aaa1690
3. Dimberg A. The Glioblastoma Vasculature as a Target for Cancer Therapy. *Biochem Soc Trans* (2014) 42(6):1647–52. doi: 10.1042/BST20140278
4. Bernabeu-Sanz A, Fuentes-Baile M, Alenda C. Main Genetic Differences in High-Grade Gliomas may Present Different MR Imaging and MR Spectroscopy Correlates. *Eur Radiol* (2021) 31(2):749–63. doi: 10.1007/s00330-020-07138-4
5. Cao H, Erson-Omay EZ, Li X, Gunel M, Moliterno J, Fulbright RK. A Quantitative Model Based on Clinically Relevant MRI Features Differentiates Lower Grade Gliomas and Glioblastoma. *Eur Radiol* (2020) 30(6):3073–82. doi: 10.1007/s00330-019-06632-8
6. Boxerman JL, Schmainda KM, Weisskoff RM. Relative Cerebral Blood Volume Maps Corrected for Contrast Agent Extravasation Significantly Correlate With Glioma Tumor Grade, Whereas Uncorrected Maps do Not. *AJNR Am J Neuroradiol* (2006) 27(4):859–67.
7. Heiland DH, Demerath T, Kellner E, Kiselev VG, Pfeifer D, Schnell O, et al. Molecular Differences Between Cerebral Blood Volume and Vessel Size in Glioblastoma Multiforme. *Oncotarget* (2017) 8(7):11083–93. doi: 10.18632/oncotarget.11522
8. Yohay K, Wolf DS, Aronson LJ, Duus M, Melhem ER, Cohen KJ. Vascular Distribution of Glioblastoma Multiforme at Diagnosis. *Interv Neuroradiol* (2013) 19(1):127–31. doi: 10.1177/159101991301900119
9. Ellingson BM, Bendszus M, Boxerman J, Barboriak D, Erickson BJ, Smits M, et al. Consensus Recommendations for a Standardized Brain Tumor Imaging

Protocol in Clinical Trials. *Neuro Oncol* (2015) 17(9):1188–98. doi: 10.1093/neuonc/nov095
10. Pope WB, Chen JH, Dong J, Carlson MR, Perlina A, Cloughesy TF, et al. Relationship Between Gene Expression and Enhancement in Glioblastoma Multiforme: Exploratory DNA Microarray Analysis. *Radiology* (2008) 249 (1):268–77. doi: 10.1148/radiol.2491072000
11. Diehn M, Nardini C, Wang DS, McGovern S, Jayaraman M, Liang Y, et al. Identification of Noninvasive Imaging Surrogates for Brain Tumor Gene-Expression Modules. *Proc Natl Acad Sci U S A* (2008) 105(13):5213–8. doi: 10.1073/pnas.0801279105
12. Barajas RFJr., Hodgson JG, Chang JS, Vandenberg SR, Yeh RF, Parsa AT, et al. Glioblastoma Multiforme Regional Genetic and Cellular Expression Patterns: Influence on Anatomic and Physiologic MR Imaging. *Radiology* (2010) 254 (2):564–76. doi: 10.1148/radiol.09090663
13. Barajas RFJr., Phillips JJ, Vandenberg SR, McDermott MW, Berger MS, Dillon WP, et al. Pro-Angiogenic Cellular and Genomic Expression Patterns Within Glioblastoma Influences Dynamic Susceptibility Weighted Perfusion MRI. *Clin Radiol* (2015) 70(10):1087–95. doi: 10.1016/j.crad.2015.03.006
14. Van Meter T, Dumur C, Hafez N, Garrett C, Fillmore H, Broaddus WC. Microarray Analysis of MRI-Defined Tissue Samples in Glioblastoma Reveals Differences in Regional Expression of Therapeutic Targets. *Diagn Mol Pathol* (2006) 15(4):195–205. doi: 10.1097/01.pdm.0000213464.06387.36
15. Smith SM. Fast Robust Automated Brain Extraction. *Hum Brain Mapp* (2002) 17(3):143–55. doi: 10.1002/hbm.10062
16. Woolrich MW, Jbabdi S, Patenaude B, Chappell M, Makni S, Behrens T, et al. Bayesian Analysis of Neuroimaging Data in FSL. *Neuroimage* (2009) 45(1 Suppl):S173–86. doi: 10.1016/j.neuroimage.2008.10.055
17. Smith SM, Brady JM. Susan—a New Approach to Low Level Image Processing. *Int J Comput Vision* (1997) 23(1):45–78. doi: 10.1023/A:1007963824710
18. Bakas S, Zeng K, Sotiras A, Rathore S, Akbari H, Gaonkar B, et al. Glistrboost: Combining Multimodal MRI Segmentation, Registration, and Biophysical Tumor Growth Modeling With Gradient Boosting Machines for Glioma Segmentation. *Brainlesion* (2016) 9556:144–55. doi: 10.1007/978-3-319-30858-6_1
19. Zhang Y, Xie Y, He L, Tang J, He Q, Cao Q, et al. 1p/19q Co-Deletion Status is Associated With Distinct Tumor-Associated Macrophage Infiltration in IDH Mutated Lower-Grade Gliomas. *Cell Oncol (Dordr)* (2021) 44(1):193–204. doi: 10.1007/s13402-020-00561-1
20. Dusart P, Hallstrom BM, Renne T, Odeberg J, Uhlen M, Butler LM. A Systems-Based Map of Human Brain Cell-Type Enriched Genes and Malignancy-Associated Endothelial Changes. *Cell Rep* (2019) 29(6):1690–706.e4. doi: 10.1016/j.celrep.2019.09.088
21. Butler LM, Hallstrom BM, Fagerberg L, Ponten F, Uhlen M, Renne T, et al. Analysis of Body-wide Unfractionated Tissue Data to Identify a Core Human Endothelial Transcriptome. *Cell Syst* (2016) 3(3):287–301.e3. doi: 10.1016/j.cels.2016.08.001
22. Ziegler J, Zalles M, Smith N, Saunders D, Lerner M, Fung KM, et al. Targeting ELTD1, an Angiogenesis Marker for Glioblastoma (GBM), Also Affects VEGFR2: Molecular-Targeted MRI Assessment. *Am J Nucl Med Mol Imaging* (2019) 9(1):93–109.
23. Verhaak RG, Hoadley KA, Purdom E, Wang V, Qi Y, Wilkerson MD, et al. Integrated Genomic Analysis Identifies Clinically Relevant Subtypes of Glioblastoma Characterized by Abnormalities in PDGFRA, Idh1, EGFR, and NF1. *Cancer Cell* (2010) 17(1):98–110. doi: 10.1016/j.ccr.2009.12.020
24. Wang Q, Hu B, Hu X, Kim H, Squatrito M, Scarpace L, et al. Tumor Evolution of Glioma-Intrinsic Gene Expression Subtypes Associates With Immunological Changes in the Microenvironment. *Cancer Cell* (2017) 32 (1):42–56.e6. doi: 10.1016/j.ccell.2017.06.003
25. Martinez-Lage M, Lynch TM, Bi Y, Cocito C, Way GP, Pal S, et al. Immune Landscapes Associated With Different Glioblastoma Molecular Subtypes. *Acta Neuropathol Commun* (2019) 7(1):203. doi: 10.1186/s40478-019-0803-6
26. Doucette T, Rao G, Rao A, Shen L, Aldape K, Wei J, et al. Immune Heterogeneity of Glioblastoma Subtypes: Extrapolation From the Cancer Genome Atlas. *Cancer Immunol Res* (2013) 1(2):112–22. doi: 10.1158/2326-6066.CIR-13-0028
27. Naeini KM, Pope WB, Cloughesy TF, Harris RJ, Lai A, Eskin A, et al. Identifying the Mesenchymal Molecular Subtype of Glioblastoma Using Quantitative Volumetric Analysis of Anatomic Magnetic Resonance Images. *Neuro Oncol* (2013) 15(5):626–34. doi: 10.1093/neuonc/not008
28. Daneman R, Prat A. The Blood-Brain Barrier. *Cold Spring Harb Perspect Biol* (2015) 7(1):a020412. doi: 10.1101/cshperspect.a020412
29. Treiber JM, Steed TC, Brandel MG, Patel KS, Dale AM, Carter BS, et al. Molecular Physiology of Contrast Enhancement in Glioblastomas: An Analysis of The Cancer Imaging Archive (Tcia). *J Clin Neurosci* (2018) 55:86–92. doi: 10.1016/j.jocn.2018.06.018
30. Bosma EK, van Noorden CJF, Schlingemann RO, Klaassen I. The Role of Plasmalemma Vesicle-Associated Protein in Pathological Breakdown of Blood-Brain and Blood-Retinal Barriers: Potential Novel Therapeutic Target for Cerebral Edema and Diabetic Macular Edema. *Fluids Barriers CNS* (2018) 15(1):24. doi: 10.1186/s12987-018-0109-2
31. Benz F, Wichitnaowarat V, Lehmann M, Germano RF, Mihova D, Macas J, et al. Low Wnt/Beta-Catenin Signaling Determines Leaky Vessels in the Subfornical Organ and Affects Water Homeostasis in Mice. *Elife* (2019) 8. doi: 10.7554/eLife.43818
32. Lochhead JJ, Yang J, Ronaldson PT, Davis TP. Structure, Function, and Regulation of the Blood-Brain Barrier Tight Junction in Central Nervous System Disorders. *Front Physiol* (2020) 11:914. doi: 10.3389/fphys.2020.00914
33. Hashimoto Y, Campbell M. Tight Junction Modulation at the Blood-Brain Barrier: Current and Future Perspectives. *Biochim Biophys Acta Biomembr* (2020) 1862(9):183298. doi: 10.1016/j.bbamem.2020.183298
34. de Gooijer MC, de Vries NA, Buckle T, Buil LCM, Beijnen JH, Boogerd W, et al. Improved Brain Penetration and Antitumor Efficacy of Temozolomide by Inhibition of ABCB1 and ABCG2. *Neoplasia* (2018) 20(7):710–20. doi: 10.1016/j.neo.2018.05.001

Conflict of Interest: The authors declare that the research was conducted in the absence of any commercial or financial relationships that could be construed as a potential conflict of interest.

frontiers in Neurology

ORIGINAL RESEARCH
published: 22 July 2021
doi: 10.3389/fneur.2021.648092

Developing a Radiomics Signature for Supratentorial Extra-Ventricular Ependymoma Using Multimodal MR Imaging

*Apoorva Safai[1†], Sumeet Shinde[1†], Manali Jadhav[1], Tanay Chougule[1], Abhilasha Indoria[2], Manoj Kumar[2], Vani Santosh[3], Shumyla Jabeen[2], Manish Beniwal[4], Subhash Konar[4], Jitender Saini[2] and Madhura Ingalhalikar[1]**

[1] Symbiosis Center for Medical Image Analysis, Symbiosis Institute of Technology, Symbiosis International University, Pune, India, [2] Department of Neuroimaging & Interventional Radiology, National Institute of Mental Health & Neurosciences, Bangalore, India, [3] Department of Neuropathology, National Institute of Mental Health & Neurosciences, Bangalore, India, [4] Department of Neurosurgery, National Institute of Mental Health & Neurosciences, Bangalore, India

OPEN ACCESS

Edited by:
Jan Kassubek,
University of Ulm, Germany

Reviewed by:
Heiko Niessen,
Boehringer Ingelheim, Germany
Hans-Peter Müller,
University of Ulm, Germany

***Correspondence:**
Madhura Ingalhalikar
madhura@scmia.edu.in;
mingalhalikar@gmail.com

[†]These authors share first authorship

Specialty section:
This article was submitted to Applied Neuroimaging, a section of the journal Frontiers in Neurology

Received: 31 December 2020
Accepted: 14 June 2021
Published: 22 July 2021

Citation:
Safai A, Shinde S, Jadhav M, Chougule T, Indoria A, Kumar M, Santosh V, Jabeen S, Beniwal M, Konar S, Saini J and Ingalhalikar M (2021) Developing a Radiomics Signature for Supratentorial Extra-Ventricular Ependymoma Using Multimodal MR Imaging. Front. Neurol. 12:648092. doi: 10.3389/fneur.2021.648092

Rationale and Objectives: To build a machine learning-based diagnostic model that can accurately distinguish adult supratentorial extraventricular ependymoma (STEE) from similarly appearing high-grade gliomas (HGG) using quantitative radiomic signatures from a multi-parametric MRI framework.

Materials and Methods: We computed radiomic features on the preprocessed and segmented tumor masks from a pre-operative multimodal MRI dataset [contrast-enhanced T1 (T1ce), T2, fluid-attenuated inversion recovery (FLAIR), apparent diffusion coefficient (ADC)] from STEE ($n = 15$), HGG-Grade IV (HGG-G4) ($n = 24$), and HGG-Grade III (HGG-G3) ($n = 36$) patients, followed by an optimum two-stage feature selection and multiclass classification. Performance of multiple classifiers were evaluated on both unimodal and multimodal feature sets and most discriminative radiomic features involved in classification of STEE from HGG subtypes were obtained.

Results: Multimodal features demonstrated higher classification performance over unimodal feature set in discriminating STEE and HGG subtypes with an accuracy of 68% on test data and above 80% on cross validation, along with an overall above 90% specificity. Among unimodal feature sets, those extracted from FLAIR demonstrated high classification performance in delineating all three tumor groups. Texture-based radiomic features particularly from FLAIR were most important in discriminating STEE from HGG-G4, whereas first-order features from T2 and ADC consistently ranked higher in differentiating multiple tumor groups.

Conclusions: This study illustrates the utility of radiomics-based multimodal MRI framework in accurately discriminating similarly appearing adult STEE from HGG subtypes. Radiomic features from multiple MRI modalities could capture intricate and complementary information for a robust and highly accurate multiclass tumor classification.

Keywords: radiomics, ependymoma, high grade glioblastoma, classification, GBM, glioblastoma multiforme, MRI

INTRODUCTION

Supratentorial ependymoma are relatively rare neoplasms, which constitute 3–5% of adult intracranial tumors and present with a wide histopathological spectrum (1). Existing literature illustrates that more than 25% of adult ependymoma can be mis-diagnosed, thus, elevating the importance of an accurate diagnosis (2). This is especially true in delineating extra-ventricular supratentorial ependymomas (STEE) from high-grade gliomas (HGG) as the appearance of ependymoma may closely resemble that of a glioblastoma on a magnetic resonance image (MRI) (2–4). STEEs generally appear hypointense on T1-weighted imaging, hyperintense on T2-weighted imaging, with an intermediate to high signal intensity on fluid-attenuated inversion recovery (FLAIR) images and may demonstrate ring- or wreath-like contrast enhancement on gadolinium based T1-weighted imaging as shown in **Figure 1** (2, 5–8). Moreover, these lesions demonstrate marked heterogeneity within the tumor. Cystic formation can be noted very frequently, and calcifications are also common that can be seen in ∼50% of ependymomas (4, 7, 9). Diffusion-weighted imaging (DWI) from ependymoma demonstrates restricted diffusion within the solid tumor compartment indicating high cellularity of the lesion, while perfusion MRI shows marked increase in cerebral blood volume. Finally, MR spectroscopy demonstrates elevated choline and reduced N-acetyl-aspartate metabolism in tumor lesions (6). The abovementioned features are also observed in HGG-grade III (HGG-G3) referred to as anaplastic astrocytoma and HGG-grade IV (HGG-G4) also known as glioblastoma (3, 10), which are central nervous system neoplasms accounting for 59% of the commonly occurring primary brain tumors (11). Although the pathogenesis and treatment strategy of ependymoma differs significantly from gliomas, and a standard course of management in the case of STEE is not yet established, e.g., chemotherapy and radiotherapy as an adjuvant to resection is a conventional treatment protocol for gliomas (12–14); however, it is not included as part of the accepted standard of care in case of STEE (15). The European Association of Neuro-Oncology guidelines published in 2017 advocate gross total resection followed by adjuvant radiotherapy in grade 3 tumors and adjuvant radiotherapy in low-grade neoplasms if residual tumor is present. Chemotherapy is not advised in adult tumors, although chemotherapy is indicated in children and adults with recurrent tumor in whom primary treatment with resection and radiotherapy has been exhausted (15). It is, therefore, crucial to predict the tumor type to optimize treatment planning and assess the therapeutic interventions, which can subsequently facilitate better outcomes.

Radiomics is an emerging translational field that can extract quantitative features beyond the level of human perception, with an intent to create tumor phenotypic signatures to aid in prognosis, stratification, disease tracking, and treatment response evaluation (16). These features are generally based on geometry (shape), intensity characteristics (histogram), entropy, and numerous image textures that are extracted from the tumoral region. Multivariate classification framework based on these features can facilitate a single probabilistic marker for the tumor type under consideration. The complete analysis aims at delineating tumor types with the ultimate goal of supporting clinical decisions that may consequently improve patient outcomes.

Overall, there is scarce literature regarding neuroimaging findings in ependymomas especially those seen in adult patients. Existing work has demonstrated the utility of a radiomics-based machine learning approach in differential diagnosis of pediatric ependymoma from medulloblastoma and pilocytic astrocytoma on multiple 3D MRI modalities. These studies have reported high classification performance of texture-based features using both conventional T1- and T2-weighted images (17–19) as well as on advanced ADC maps (20, 21) in varying combinations. Recently, studies have also demonstrated the role of radiomics in evaluating treatment response of natural killer cell infusion therapy (22) and novel network-driven approach using proton therapy (23) in pediatric ependymoma. A radiomics-based signature of adult STEE tumors is yet to be established. Apart from ependymomas, radiomics has also shown potential in creating phenotypic signatures of glioma genotypes such as isocitrate dehydrogenase (IDH) (24–26), epidermal growth factor receptor (EGFR) (27), and O^6-methylguanine-DNA-methyl-transferase (MGMT) (28–31). In glioblastoma, multimodal MRI-based quantitative radiomic features have shown to predict tumor recurrence (32) with better performance than traditional qualitative approaches such as visualization of contrast-enhanced MRI and perfusion kinematic changes in discriminating recurrence from radiation necrosis (33, 34). These studies provide outcomes that evidently encourage the use of radiomics-based multimodal MRI in combination with machine learning framework to create an imaging marker of adult STEE tumor, which can accurately delineate it from HGG tumors.

This study aims to characterize adult STEEs using an underlying phenotypic radiomics-based signature from multimodal MRI images, which not only predicts but also portrays the textural patterns that mark the uniqueness of these tumors on MRI and discriminate them from HGG, thereby serving as a potential biomarker. Such a non-invasive differential prognostic signature of STEE can aid in better diagnosis, improve clinical decision making, and timely therapeutic intervention with better outcomes.

MATERIALS AND METHODS

Study Cohort and Imaging

Our dataset consisted of a clinical cohort of 75 adult tumor patients that included 15 patients (age = 27.2 ± 11.73 years, M:F = 8:7) with grade 2 and grade 3 STEEs, 36 patients with HGG-G3 (age = 39.30 ± 11.64 years, M:F = 22:14), and 24 HGG-G4 patients (age = 48.8 ± 15.76 years, M:F = 11:13). All patients included in this study had undergone surgical resection and standard post-surgical care and were identified retrospectively after reviewing the medical records. Final diagnosis was confirmed based on the histopathological examination of the resected tissue. Out of the complete cohort, 77% scanned were performed on a Philips Achieva 3.0 T MRI scanner, while others were scanned on a 3.0 T Siemens Skyra MRI system. Multiple sequences were acquired as standard clinical MRI;

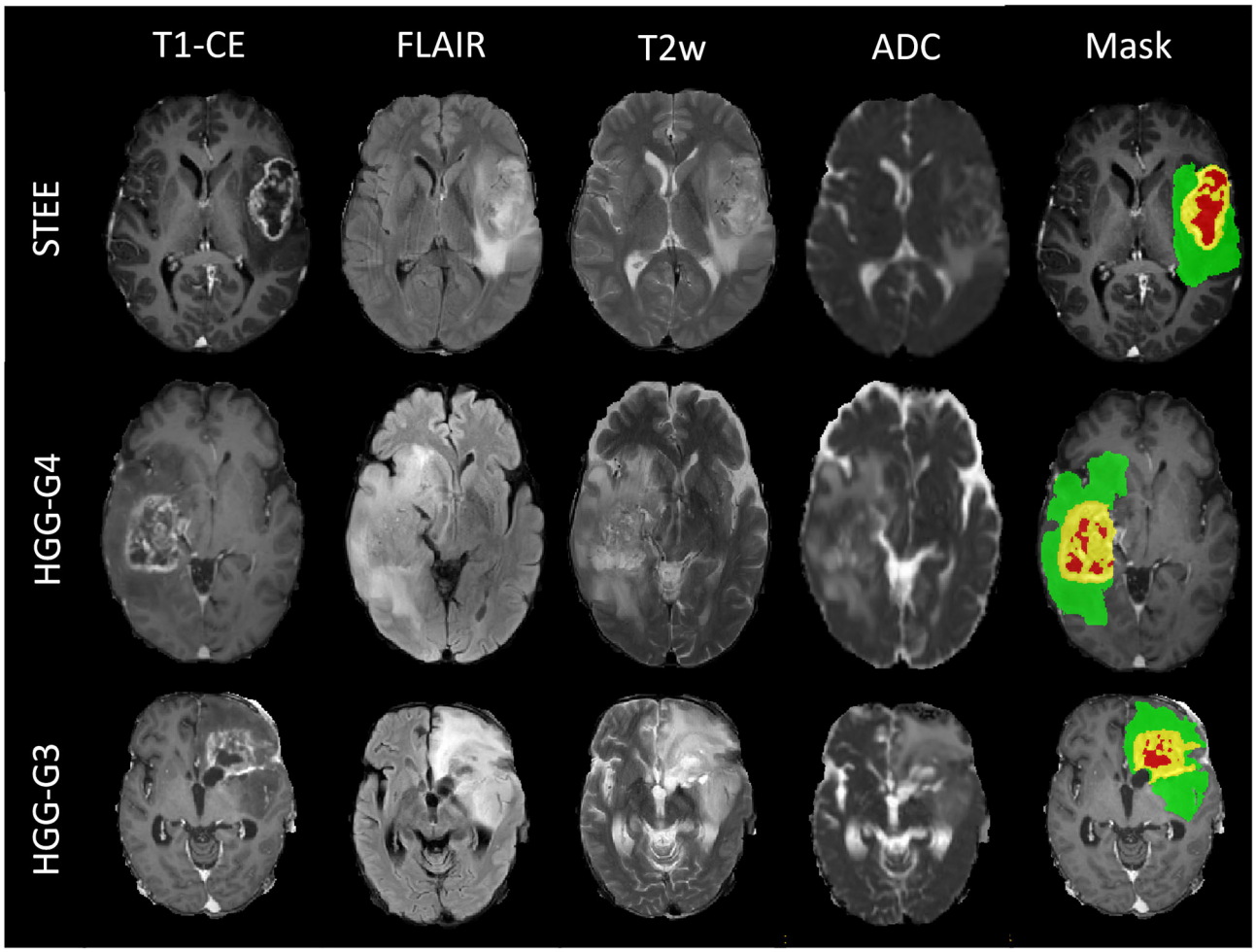

FIGURE 1 | Multimodal magnetic resonance image (MRI) sequences of one supratentorial extraventricular ependymoma (STEE), high-grade gliomas-grade 4 (HGG-G4), and HGG-G3 tumor case with their tumor segmented masks, which shows similarly appearing necrosis tissue (red), diffused enhancement (yellow), and edema tissue (green) in all three tumor groups.

however, we restricted our analysis to gadolinium-enhanced T1-weighted (T1ce), fluid attenuation inversion recovery (FLAIR), T2-weighted imaging, and apparent diffusion coefficient (ADC) maps. T1ce scans were obtained using TR/TE = 8.0/3.7 ms using TFE sequence on Philips scanner, while TR/TE = 1,800–2,200/2.3–2.6 ms using T1 MPRAGE sequence on Siemens with 1 × 1 × 1 mm isotropic resolution. T2-weighted imaging protocol consisted of TR/TE ranging from 3,600 to 6,000/80 to 99 ms and 0.5 × 0.5 mm resolution in the axial plane. FLAIR images were acquired using TR/TE/TI of 11,000/125/2,800 within the plane resolution of 0.5 × 0.5 mm. ADC maps were acquired using the DWI sequence. The institute review ethics committee approved the study and the informed consent of the patient was waived off as it was a retrospective study.

Image Processing and Radiomics

The detailed pre-processing of MRI images and radiomics pipeline implemented in this study is shown in **Figure 2**. Initially, for all the subjects, FLAIR, T2, and ADC maps were resampled to 1.0 mm iso-voxel and registered to T1ce image using a 6 degree of freedom rigid body transformation. T1ce images were further registered to standard MNI-spaced image using affine transformation, and this transformation matrix was further applied to FLAIR, T2, and ADC maps to have them all in a uniform sampling space with a common origin. All registration steps were performed using advanced normalization tool (ANTs) toolbox (35). Brain extraction for all co-registered modalities was performed using FSL's BET (36), followed by segmentation of enhancing tumor, edema, and necrosis using a deep learning model (DeepMedic) (37). This multiscale 3D convolutional neural network (CNN) model was trained on multimodal images (T1ce, T2, and FLAIR images) and labels from BRATS-2018 (https://www.med.upenn.edu/sbia/brats2018/data.html) data (training n = 206, validation n = 52). The segmented output masks were corrected manually by an expert annotator (M.J), followed by

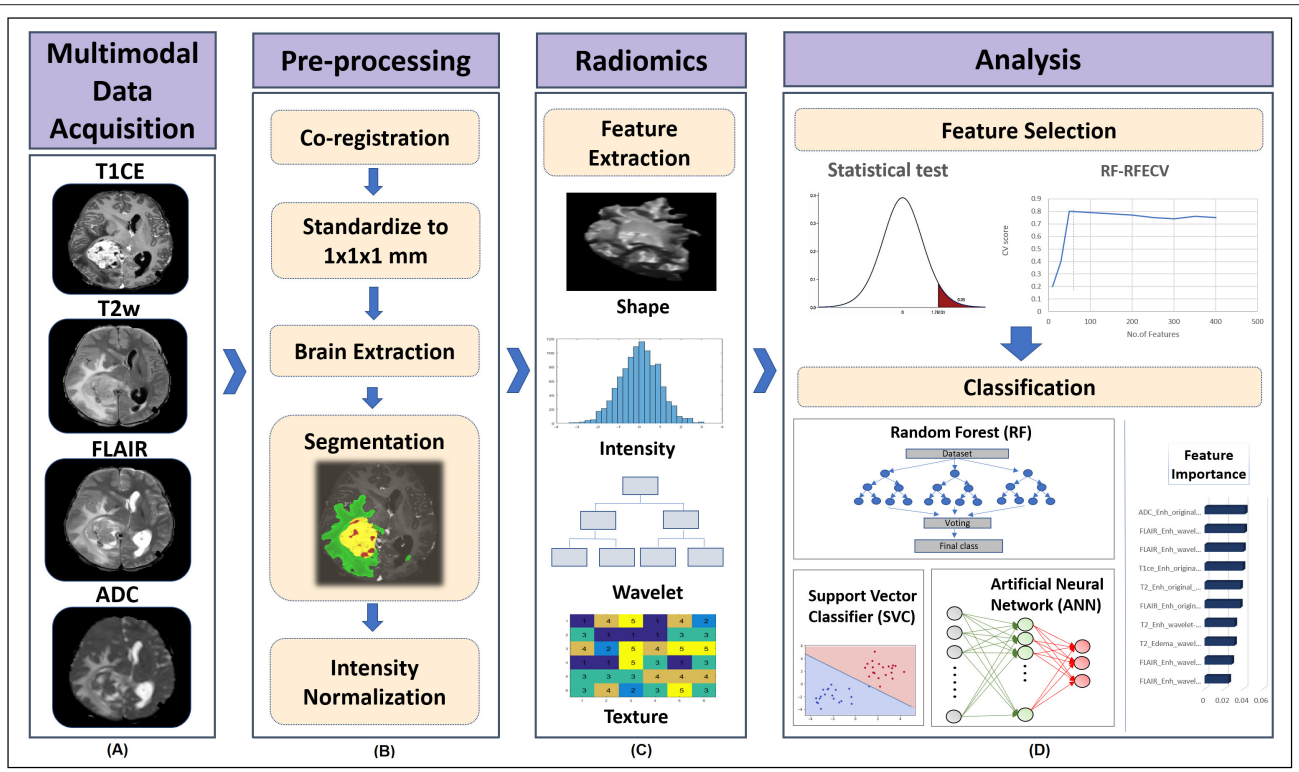

FIGURE 2 | Processing pipeline implemented for classification of tumor subgroups includes **(A)** Acquisition of multiple MRI modalities such as gadolinium enhanced T1-weighted (T1ce), fluid attenuation inversion recovery (FLAIR), T2-weighted imaging, and apparent diffusion coefficient (ADC) maps. **(B)** Pre-processing of MRI scans to segment different tumor tissues involved co-registration of FLAIR, T2, and ADC scans to T1ce scan and standardizing all modalities to 1 mm iso voxel size using advanced normalization tool (ANTs) software, brain extraction using all modalities using FSL's BET, segmentation of enhancing tumor, edema, and necrosis using deep learning (DeepMedic) model and its manual correction followed by intensity normalization. **(C)** Radiomic features such as shape, intensity-based histograms, and texture features were computed from original segmented mask of each tumor tissue using PyRadiomics. **(D)** Dual stage feature selection was performed on normalized radiomic features of each modality, where the first stage involved extraction of significantly varying features between tumor groups using ANOVA F-test with a *p*-value cut-off of 1 xe^{-06}. The second stage of feature selection was performed on features selected from stage 1 by implementing Random Forest based Recursive Feature Elimination with Cross Validation (RF-RFECV), such that initially a RF model was fit in a 5 fold-CV framework, with elimination of features at each cross validation (CV) based on their feature importance score and the model was recursively retrained on updated feature set until a minimum of 10 features were obtained that gave high accuracy across all the CVs. Classification performance of selected multimodal radiomic features in distinguishing different tumor groups was assessed by implementing a multiclass classification modal using RF, support vector classifier (SVC) and artificial neural network (ANN) classifiers. SVC coefficients were used to obtain the most important features.

intensity normalization and computation of radiomic features using PyRadiomics 2.2.0 library (38). The feature set used included 3D shape-based features, statistical features, gray-level co-occurrence matrix (GLCM), gray-level dependent matrix (GLDM), gray-level run length matrix (GLRLM), gray-level size zone matrix (GLSZM), and neighboring gray tone difference matrix (NGTDM). These features were also computed on filtered images where the filters used were Laplacian, wavelets, Gaussian, curvature flow, box mean, and box sigma. For each subject, a total of 11,274 features were computed, comprising 1,409 features from each of the four modalities, making a total of 5,637 features for each of the two tumor masks (edema and T1ce-based tumor tissue enhancing). We excluded the third region of interest (necrosis/cyst) from further analysis due to its heterogeneous tissue composition, which involved parts of non-enhancing tumor, cysts in some cases, and tumor necrosis.

Feature Selection

Multivariate classifiers may overfit on the input radiomic features, due to their enormously large size compared with the available sample size. To alleviate this issue, feature selection was performed to obtain an optimum feature set by removing redundant features and reducing feature dimensionality of the computed radiomic features. First, a 75–25% train-test split was applied on the dataset, with 56 subjects in the training set and 19 subjects in the test set. We then normalized all radiomic features using min–max normalization and implemented a two-stage feature selection strategy on the training dataset. In the first stage, features from each modality were statistically compared between groups using an ANOVA F-test. A *p*-value cutoff of $1 \times e^{-06}$ was applied per modality to obtain up to 50 significant radiomic features per modality. The second stage of feature selection was performed on the selected features obtained from stage 1 by implementing random

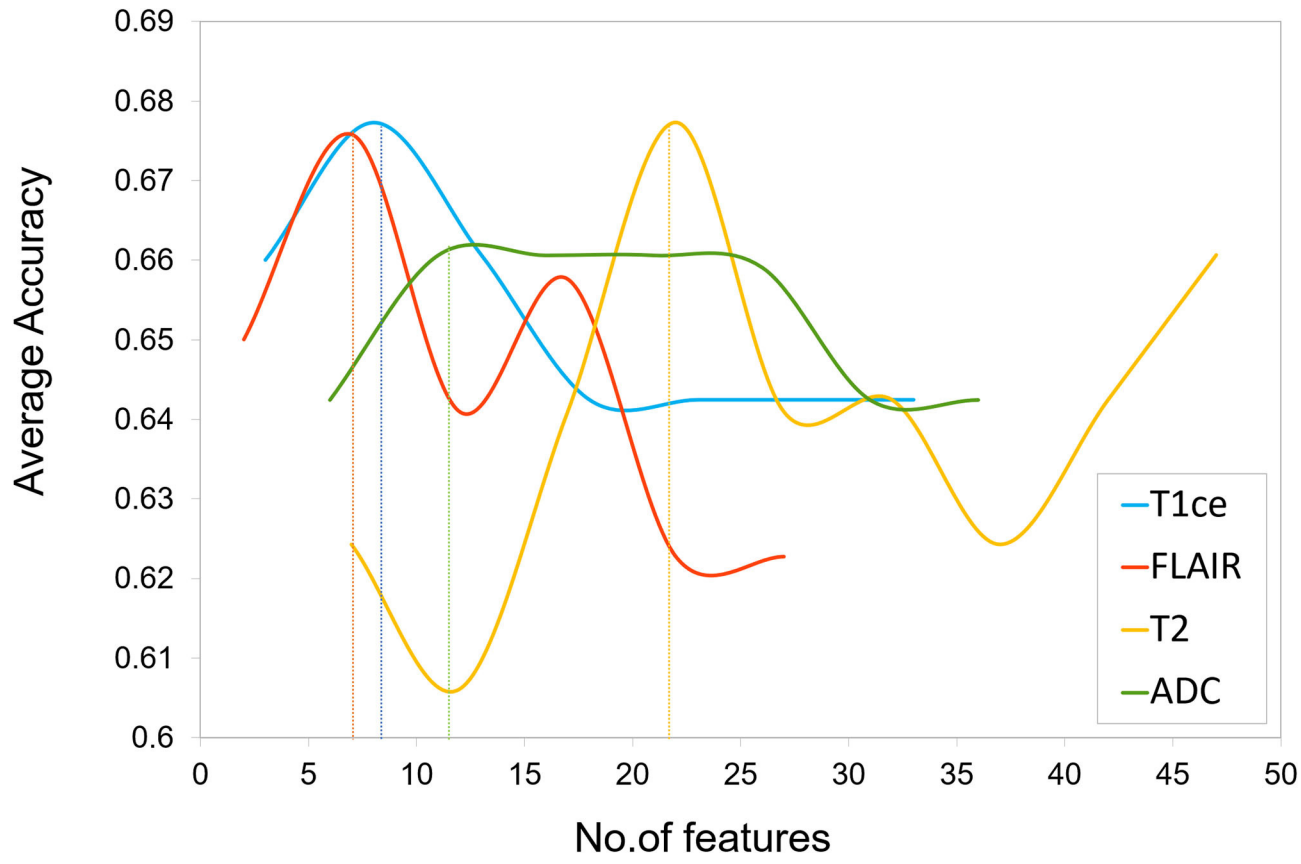

FIGURE 3 | Feature selection plot of number of features vs. average cross validation (CV) accuracy for each unimodal MRI feature set obtained by implementing Random Forest based Recursive Feature Elimination with Cross Validation (RF-RFECV) on training data. The vertical dotted line indicates a threshold on number of features below which a drop in average accuracy was observed.

forest-based recursive feature elimination with cross validation (RF-RFECV) (39–41). This two-stage feature selection process was applied individually on all four modalities. RF-RFECV was implemented by first fitting a random forest (RF) model (42) in a cross-validation (CV) framework on the training data using a fivefold CV. The least important features were eliminated (minimum step size-5) after every CV based on their feature importance scores pertaining to that CV, and an averaged fivefold CV accuracy was noted at every elimination. In the next step, the model was recursively retrained on updated feature set until a minimum of 10 features were obtained that gave high accuracy across all the CVs as shown in **Figure 3**. Thus, for each modality, a specific number of important selected radiomic features were used as input in the classification models.

Classification Models

To distinguish between STEE, HGG-G3, and HGG-G4 tumor types, we performed multiclass classification using the radiomic feature set of each modality individually in a unimodal setup, as well as by combining features from all modalities in a multimodal setup. Additionally, we employed multiple machine learning classification algorithms such as random forest (RF), support vector classifier (SVC), and artificial neural network (ANN) on both unimodal and multimodal feature sets to evaluate classification performance using different models. Random forests are decision tree-based ensemble learning classification algorithms that involve fitting multiple decision tree classifiers on random subsamples of the data and predicting the final class by aggregating votes or predictions from different decision trees. RF algorithms control overfitting of the model that may occur in a single decision tree (42). SVC is a supervised learning algorithm that performs linear or non-linear classification by transforming data to a higher dimensional space using a kernel function and constructing an optimal hyperplane. The hyperplane classifies data points into different classes by maximizing the distance between the nearest point on its either side (43). ANN is a biologically inspired feed forward neural networks that consists of an input layer, hidden layer, and output layer with nodes that act as activation functions and a back-propagation algorithm that trains the model for classification (44). We implemented RF classification model using 10,000 trees, maximum depth =

TABLE 1 | Classification results from unimodal and multimodal feature sets (testing/cross) validation (CV).

Classifier	Accuracy	Sensitivity	Specificity	F1-score	AUROC
A) Classification based on T1ce feature set					
RF	0.52/0.69	0.00/0.00	0.93/0.93	0.39/0.52	0.70/0.70
SVC	0.47/0.62	0.50/0.36	0.73/0.77	0.36/0.54	0.75/0.76
ANN	0.52/0.71	0.00/0.18	1.00/0.91	0.38/0.60	0.54/0.80
B) Classification based on FLAIR feature set					
RF	**0.63/0.53**	0.5/0.18	0.93/0.73	0.61/0.44	**0.76/0.73**
SVC	**0.63/0.67**	0.5/0.18	0.93/0.91	0.61/0.57	**0.79/0.80**
ANN	**0.57/0.75**	0.50/0.36	0.86/0.93	0.53/0.68	**0.75/0.85**
C) Classification based on T2 feature set					
RF	0.42/0.67	0.00/0.27	0.73/0.84	0.30/0.59	0.67/0.79
SVC	0.47/0.58	0.25/0.18	0.86/0.75	0.40/0.48	0.75/0.78
ANN	0.73/0.67	1.00/0.54	0.86/0.75	0.72/0.60	0.78/0.83
D) Classification based on ADC feature set					
RF	0.57/0.67	0.25/0.27	0.93/0.88	0.51/0.58	0.78/0.78
SVC	0.42/0.64	0.25/0.27	0.73/0.82	0.31/0.55	0.75/0.82
ANN	0.52/0.69	0.00/0.27	0.93/0.86	0.39/0.60	0.64/0.80
E) Classification based on multimodal feature set					
RF	0.53/0.75	0.50/0.36	0.80/0.95	0.49/0.73	0.77/0.80
SVC	**0.68/0.80**	**0.75/0.45**	**0.93/0.95**	**0.68/0.74**	**0.78/0.84**
ANN	**0.68/0.87**	**0.75/0.81**	**0.93/0.91**	**0.68/0.85**	**0.78/0.94**

Accuracy and f1-score (macro averaged) are overall classification scores, whereas sensitivity and specificity are for STEE class.
AUROC, area under receiver operating curve; RF, random forest; SVC, Support Vector Classifier; ANN, artificial neural network; FLAIR, Fluid Attenuated Inversion Recovery; ADC, apparent diffusion coefficient; STEE, Supratentorial Extraventricular Ependymoma.
Highlighted scores indicate high classification performance.

TABLE 2 | Class-specific performance metrices of classifiers on unimodal and multimodal feature sets.

Classifier	Class	Precision	Recall	F1-score
A) Class-specific performance metrices of SVC on unimodal feature set				
T1ce	STEE	0.33/0.29	0.50/0.36	0.40/0.32
	HGG-G4	0.00/0.54	0.00/0.39	0.00/0.45
	HGG-G3	0.58/0.83	0.78/0.89	0.67/0.86
FLAIR	STEE	**0.67/0.33**	**0.50/0.18**	**0.57/0.24**
	HGG-G4	**0.75/0.57**	**0.50/0.67**	**0.60/0.62**
	HGG-G3	**0.58/0.83**	**0.78/0.89**	**0.67/0.86**
T2	STEE	0.33/0.15	0.25/0.18	0.29/0.17
	HGG-G4	0.17/0.40	0.17/0.33	0.17/0.36
	HGG-G3	0.70/0.89	0.78/0.93	0.74/0.91
ADC	STEE	0.20/0.27	0.25/0.27	0.22/0.27
	HGG-G4	0.00/0.56	0.00/0.50	0.00/0.53
	HGG-G3	0.64/0.83	0.78/0.89	0.70/0.86
B) Class-specific performance metrices on multimodal feature set				
RF	STEE	0.50/0.38	0.25/0.27	0.33/0.32
	HGG-G4	0.50/0.58	0.50/0.61	0.50/0.59
	HGG-G3	0.64/0.83	0.78/0.89	0.70/0.86
SVC	STEE	**0.75/0.71**	**0.75/0.45**	**0.75/0.56**
	HGG-G4	**0.60/0.70**	**0.50/0.78**	**0.55/0.74**
	HGG-G3	**0.70/0.90**	**0.78/0.96**	**0.74/0.93**
ANN	STEE	**0.75/0.69**	**0.75/0.82**	**0.75/0.75**
	HGG-G4	**0.50/0.88**	**0.50/0.83**	**0.50/0.86**
	HGG-G3	**0.78/0.96**	**0.78/0.93**	**0.78/0.94**

HGG, high-grade gliomas. Highlighted scores indicate high classification performance.

2 and a maximum of square root of input features per tree with "Gini" criterion as the loss. SVC was implemented using a linear kernel on the training dataset having a c value of 1. A three-layer ANN was implemented with a single hidden layer of five hidden units followed by a softmax activation function at the output layer. The model was optimized using Adam optimizer, with a learning rate = 0.005 and binary cross entropy as the loss function. All three classification models were trained on a training set of 56 subjects and tested on 19 subjects, in both unimodal as well as in multimodal setup. Additionally, a leave-one-out-type cross validation (LOOCV) was implemented on the training set for each classifier to validate the model. To avoid classification bias in favor of majority class due to our unbalanced group samples and to attain robust prediction, we augmented the training data using a borderline Synthetic Minority Oversampling Technique (SMOTE) (45). Classification performance of the three classifier models were compared by evaluating their performance metrices, which included macro-averaged accuracy, F1-score, and AUROC (area under receiver operating curve), whereas the class-specific classification performance was evaluated using precision, recall, F1-score, and AUROC. To determine the most discriminative features involved in classification, we further obtained SVC coefficients for each pair of classes for unimodal as well as multimodal feature sets, with a high coefficient score implying high contribution of the feature in the classification of tumor groups.

RESULTS

Clinical and Radiological Characteristics of Tumors

Qualitative MRI features of patients with STEE, HGG-G3, and HGG-G4 are depicted in **Figure 1**. It demonstrates the similarity in the imaging findings of STEE and HGG with common occurrences of edema, heterogenous enhancement, necrosis, hemorrhage, and diffusion restriction in all three tumor groups. Detailed radiological findings for STEEs are reported in (4).

Feature Selection and Classification of Unimodal Radiomic Features

The two-stage feature selection process on each MRI modality generated an optimum final feature set per modality (T1ce-10 features, FLAIR-10 features, T2-22 features, ADC-11 features) based on the maximum average CV accuracy obtained using RF-RFECV, as shown in **Figure 3**. The performance of classification models using each unimodal feature set is mentioned in **Table 1**. Among all modalities, radiomic features obtained from FLAIR showed highest test accuracy of more than 60% using RF and SVC classifiers, respectively. ANN showed a test accuracy of 57%,

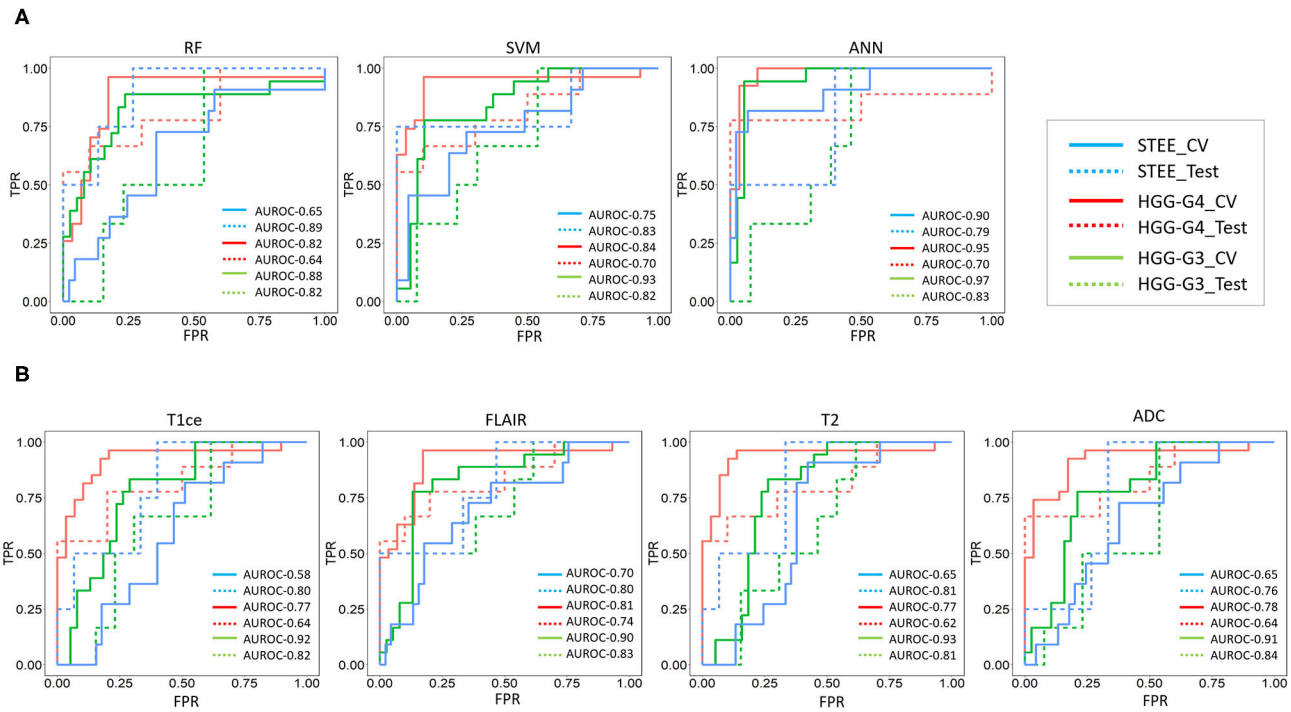

FIGURE 4 | (A) Receiver operating characteristic (ROC) curves for classification on multimodal feature set- ROC curves for multimodal features-based classification of multiple tumor groups (STEE: supratentorial extraventricular ependymoma, HGG-G4: high-grade glioma-grade 4, HGG-G3: high-grade glioma-grade3) using random forest (RF), support vector classifier (SVC), and artificial neural network (ANN) classifiers based on CV and test data. **(B)** ROC curves for SVC on unimodal features set-ROC curves unimodal [gadolinium enhanced T1-weighted (T1ce), fluid attenuation inversion recovery (FLAIR), T2-weighted imaging, and apparent diffusion coefficient (ADC)] feature-based SVC classification of multiple tumor groups using CV and test data.

a maximum CV accuracy of 75%, and AUROC of 85% among the three classifiers. More than 75% AUROC were observed consistently across all classifiers, along with high F1-score and sensitivity using FLAIR modality. High specificity was observed across all models for all modalities. As SVC model provided balanced performance throughout all modalities, we further assessed classification performance for each tumor group in a one vs. all manner using the SVC model as shown in **Table 2A**. Overall, all modalities gave high performance in identifying the HGG-G3 group, while FLAIR modality showed high precision in distinguishing all three tumor groups. In accordance with SVC results, RF and ANN classifiers also showed high performance on FLAIR and additionally on ADC and T2 modalities, respectively, as shown in **Supplementary Table 1**.

Classification Performance of Multimodal Radiomic Features

Classification performance of RF, SVC, and ANN models on multimodal feature set is provided in **Table 1E**. Both SVC and ANN showed 68% accuracy, 75% sensitivity, and 93% specificity on test data, while on CV, both classifiers demonstrated more than 80% accuracy and 90% specificity, along with 81% sensitivity using the ANN classifier. All classifiers showed an AUROC of 78% or more on test and CV; a maximum of 94% was attained on CV of ANN as shown in **Table 1D** and **Figure 4**, respectively. Higher accuracy and AUROC were obtained on multimodal feature set compared with unimodal feature sets, across all classifiers. Similar to the unimodal feature set, all classifiers showed high performance in identifying the HGG-G3 group on multimodal feature set as shown in **Table 2B**.

Feature importances evaluated on multimodal feature set using SVC are shown in **Table 3**. Radiomic features of FLAIR on enhancement tissue, T2, and ADC on edema tissue were the commonly occurring top 10 features that were most discriminative between any two tumor groups. Particularly, the texture-based GLRLM (gray-level run length matrix) feature–run length non-uniformity (RLN) was among the topmost frequently occurring important feature in distinguishing STEE from HGG-G4 as reported in **Table 3A**. From T2 and ADC modality, first-order features and texture-based NGTDM (neighboring gray tone difference matrix)-busyness and GLDM (gray-level dependence matrix)–high gray-level emphasis (HGLE) features on edema tissue were important in classifying STEE from HGG-G3. The first-order features and GLRLM features were important in distinguishing the HGG-G4 from the HGG-G3 tumor group. Interestingly, the GLDM feature from T2 edema was significantly distinct between the STEE and HGG-G4 tumor groups and was also found to be the most important feature in classifying HGG-G3 from HGG-G4 and STEE,

TABLE 3 | Feature importances obtained using SVC coefficient scores on multimodal feature set.

Sr.no.	Features	Coefficients	*p*-value	*t*-stat
A) STEE vs. HGG-G4				
1	ADC_Edema_wavelet-LHL_firstorder_InterquartileRange	1.214	0.554	**0.598**
2	FLAIR_Enh_wavelet-LHH_glrlm_RunLengthNonUniformity	1.114	0.591	0.546
3	FLAIR_Enh_wavelet-HLL_glrlm_RunLengthNonUniformity	0.987	0.831	0.216
4	FLAIR_Enh_wavelet-LHL_glrlm_RunLengthNonUniformity	0.967	0.790	0.269
5	T2_Edema_wavelet-HHL_gldm_HighGrayLevelEmphasis	0.790	0.055	−1.983
6	ADC_Enh_original_shape_LeastAxisLength	0.768	0.233	−1.225
7	T2_Edema_gradient_firstorder_Mean	0.759	0.586	0.550
8	FLAIR_Enh_wavelet-HHH_glrlm_GrayLevelNonUniformity	0.620	0.602	0.530
9	T2_Edema_gradient_firstorder_Median	0.579	0.497	0.687
10	T1ce_Enh_wavelet-HLH_ngtdm_Busyness	0.564	0.960	−0.051
B) STEE vs. HGG-G3				
1	T2_Edema_wavelet-HHL_gldm_HighGrayLevelEmphasis	1.145	0.000	−7.229
2	T2_Edema_gradient_firstorder_Median	0.949	0.000	7.181
3	ADC_Edema_wavelet-LHL_firstorder_InterquartileRange	0.762	0.000	5.028
4	T2_Edema_wavelet-HHH_glrlm_RunEntropy	0.598	0.000	−5.882
5	ADC_Edema_gradient_firstorder_Mean	0.582	0.000	5.493
6	T2_Enh_wavelet-LHL_ngtdm_Busyness	0.414	0.005	3.241
7	T2_Enh_wavelet-LHH_ngtdm_Busyness	0.378	0.004	3.254
8	ADC_Edema_gradient_firstorder_Median	0.360	0.000	5.111
9	T2_Edema_gradient_firstorder_Mean	0.351	0.006	3.160
10	T2_Enh_wavelet-HLH_ngtdm_Busyness	0.347	0.000	5.729
C) HGG-G4 vs. HGG-G3				
1	T2_Edema_wavelet-HHL_gldm_HighGrayLevelEmphasis	0.721	0.000	−5.617
2	ADC_Edema_gradient_firstorder_Median	0.647	0.000	6.007
3	ADC_Edema_gradient_firstorder_Mean	0.586	0.000	5.902
4	T2_Edema_gradient_firstorder_Median	0.532	0.000	6.415
5	ADC_Edema_wavelet-LHL_firstorder_InterquartileRange	0.500	0.000	5.134
6	T2_Edema_square_glrlm_RunVariance	0.419	0.000	−5.658
7	T2_Edema_lbp-2D_glrlm_RunVariance	0.419	0.000	−5.658
8	T2_Edema_gradient_glrlm_RunVariance	0.419	0.000	−5.658
9	T2_Edema_exponential_glrlm_RunVariance	0.419	0.000	−5.658
10	T1ce_Edema_square_glrlm_RunVariance	0.419	0.000	−5.658

Highlighted scores indicate high classification performance.

respectively. Overall, the first-order features from T2 and ADC on edema tissue were highlighted as the commonly seen important features in discriminating STEE and HGG tumor subtypes, whereas FLAIR-based GLRLM texture feature on enhancement was particularly important in classifying STEE from HGG-G4.

DISCUSSION

Radiological manifestations of STEEs are complicated and can often be mis-diagnosed as HGGs, which are frequently occurring neoplasms of the brain. This study aims at identifying multimodal imaging signatures of STEE tumors through a detailed radiomics-based quantitative evaluation. Our results demonstrate that coalescence of multiple MRI modalities leads to a superior classification performance compared with a single modality. FLAIR, T2, and ADC emerged as the highly discriminative modalities, whereas texture and higher-order statistical features were able to capture intricate imaging markers that could aid in accurately predicting STEE from HGG tumors.

Differential diagnosis of STEE is more challenging compared with infratentorial ependymomas as the latter mostly manifests in the ventricles, whereas STEE may appear outside the ventricles, in cortical regions, similar to other high-grade tumors such as anaplastic astrocytoma and glioblastoma (2, 5). Necrosis, internal hemorrhages, tissue heterogeneity, ring enhancement, significant edema, choline/N-acetylasepartate metabolic ratio on MR spectroscopy, occurrence of tumor in brain parenchyma, and infiltration into the contralateral frontal hemisphere (2, 5–7, 9) are some of the common characteristics of these tumors. Radiographic imaging markers of STEE tumors manifest on conventional MRI sequences as a heterogenous signal intensity on T1- and T2-weighted images and as variable appearance on FLAIR images (2, 5–8). Cyst and calcification are commonly occurring attributes of STEE tumors (4, 7, 9). Higher ADC values close to the white matter are also observed in these tumors (4). DWI and perfusion imaging illustrate restricted diffusion and high relative cerebral blood volume values, respectively, in STEEs, which are similar to high-grade anaplastic astrocytoma and glioblastoma (46). However, till date, there is no consensus on an established differential diagnosis of STEE, primarily due to its rare occurrence, which makes it difficult to conduct research studies and develop a validated biomarker. This often results in mis-diagnosis and poor prognosis of STEEs.

We investigated multiclass classification performance of unimodal as well as multimodal feature sets using RF, SVC, and ANN classifiers. Both SVC and ANN classifiers illustrated high classification performance. Multimodal features demonstrated consistently high AUROC of more than 75% and high CV accuracy of more than 80% from these two classifiers for each tumor type, as shown in **Table 1E** and **Figure 4**, suggesting that a multiparametric MRI framework would be more efficient and robust in classifying STEE from HGGs compared with a single modality. Among the unimodal feature sets, radiomic features computed from FLAIR modality provided maximum macro average classification accuracy of more than 55% as shown in **Table 1B**, which is significantly higher compared with the baseline 33% accuracy for multiclass classification. Moreover, in comparison with other modalities, FLAIR features demonstrated consistently high AUROC for all tumor types while assessing class-specific comparison of SVC as shown in **Figure 4** and **Table 2B**. T2 and ADC modalities performed better in delineating HGG-G3 tumors from other tumor groups as shown in **Table 2B**.

For a comprehensive understanding of each modality's contribution in classification of different tumor types in a multiparametric framework, we ranked the most important features based on the SVC coefficient score obtained from multimodal feature sets as shown in **Table 3**. Overall, first-order features such as mean, median, and interquartile range of edema tissue from T2 and ADC along with GLDM-HGLE feature from T2 were the commonly occurring most discriminative features in classifying different tumor groups. The GLDM-HGLE feature implies a larger concentration of high gray-level intensities. It was most significant ($p = 0.05$) in classifying STEE from HGG-G4 and was found to be lower in STEE compared with the HGG groups and higher in HGG-G3 compared with HGG-G4. Among other texture features, the GLRLM feature indicative of homogeneity within the particular tissue types was the commonly occurring important feature in the classification of STEE from HGG-G4. STEE was found to be more homogenous than HGG-G4 on enhancement tissue of FLAIR. NGTDM-busyness was important in classifying STEE from HGG-G3 and was higher in STEE on edema tissue of T2 modality. The busyness feature indicates a rapid change in intensities within a pixel and its neighborhood. Thus, texture-based features signifying concentration of high intensities, homogeneity, and intensity fluctuations between pixel neighborhoods were some of the key radiomics attributes that could distinguish different tumor types.

There were a few limitations to this study. The sample size of different tumor groups was unbalanced. Owing to the extremely rare occurrence of STEEs, acquiring a large number of MRI scans of these tumors is difficult. However, we controlled for this limitation by implementing data augmentation using the SMOTE technique, which provided a balanced dataset for our multiclass classification. Another limitation was that multiscanner data were used in the analysis. To control for scanner differences, we normalized the intensity of the data during pre-processing stage, prior to classification.

In conclusion, this study develops a potential quantitative radiomics signature for accurately differentiating STEE from HGGs using multimodal MRI. Radiomics features from FLAIR modality can aid predominantly in the classification of STEE and HGG-G4 tumor, whereas a multiparametric radiomics approach constituting particularly of FLAIR, ADC, and T2 modalities could provide intricate and complementary information that could aid in highly accurate classification of STEE and HGGs tumors. This work, thus, emphasizes the utility of radiomics-based multimodal MRI framework in pre-operative clinical diagnosis and effective treatment planning.

DATA AVAILABILITY STATEMENT

The raw data supporting the conclusions of this article will be made available by the authors. There are ethical restrictions on sharing of clinical and imaging data as it contains sensitive patient information. Data access will be provided upon the approval of the Institutional Ethics Committee.

ETHICS STATEMENT

The studies involving human participants were reviewed and approved by Institute Ethics Committee NIMHANS and patient informed consent was waived off due to retrospective study.

AUTHOR'S NOTE

Adult Supratentorial Extraventricular Ependymoma (STEE) are rare neoplasms that are often misdiagnosed as high-grade gliomas (HGG) due to their similar radiological manifestation on MRI. However, the pathogenesis and treatment plan of ependymoma differs significantly from gliomas, and hence an early and accurate diagnosis is crucial. Our proposed machine learning based diagnostic model can accurately distinguish adult STEE from HGG subtypes using quantitative radiomic signatures from a multi-model MRI data. Quantitative radiomic markers such as texture and first order statistics from multimodal MRI can capture intricate and complementary information and thus aid in a robust multiclass tumor classification of STEE and HGG subtypes.

AUTHOR CONTRIBUTIONS

AS, SS, MJ, TC, and AI: data analysis and processing. MK, JS, and MI: manuscript writing and editing. VS, SJ, MB, and SK: clinical evaluation.

SUPPLEMENTARY MATERIAL

The Supplementary Material for this article can be found online at: https://www.frontiersin.org/articles/10.3389/fneur.2021.648092/full#supplementary-material

REFERENCES

1. Gilbert MR, Ruda R, Soffietti, R. Ependymomas in adults. *Curr Neurol Neurosci Rep*. (2010) 10:240–7. doi: 10.1007/s11910-010-0109-3
2. Leng X, Tan X, Zhang C, Lin H, Qiu, S. Magnetic resonance imaging findings of extraventricular anaplastic ependymoma: a report of 11 cases. *Oncol Lett*. (2016) 12:2048–54. doi: 10.3892/ol.2016.4825
3. Shintaku M, Hashimoto, K. Anaplastic ependymoma simulating glioblastoma in the cerebrum of an adult. *Brain Tumor Pathol*. (2012) 29:31–6. doi: 10.1007/s10014-011-0057-x
4. Jabeen S, Konar SK, Prasad C, Mahadevan A, Beniwal M, Sadashiva N, et al. Conventional and advanced magnetic resonance imaging features of supratentorial extraventricular ependymomas. *J Comput Assist Tomogr*. (2020) 44:692–8. doi: 10.1097/RCT.0000000000001080
5. Byun J, Kim JH, Kim YH, Cho YH, Hong SH, Kim, et al. Supratentorial extraventricular ependymoma: retrospective analysis of 15 patients at a single institution. *World Neurosur*. (2018) 118:e1–e9. doi: 10.1016/j.wneu.2018.05.192
6. Yuh EL, Barkovich AJ, Gupta, N. Imaging of ependymomas: MRI and CT. *Childs Nerv Syst*. (2009) 25:1203–3. doi: 10.1007/s00381-009-0878-7
7. Mohaghegh MR, Chitsaz A, Okhovat AA, Pour, E.B. Supratentorial cortical ependymoma: an unusual presentation of a rare tumor. *Adv Biomed Res*. (2015) 4:72. doi: 10.4103/2277-9175.153896
8. Sun S, Wang J, Zhu M, Beejadhursing R, Gao P, Zhang X, et al. Clinical, radiological, and histological features and treatment outcomes of supratentorial extraventricular ependymoma: 14 cases from a single center. *J Neurosurg*. (2018) 128:1396–1402. doi: 10.3171/2017.1.JNS161422

9. Reni M, Gatta G,Mazza E,Vecht, C. Ependymoma. *Crit Rev Oncol Hematol.* (2007) 63:81–9. doi: 10.1016/j.critrevonc.2007.03.004
10. Wu J, Armstrong TS, Gilbert MR. Biology and management of ependymomas. *Neuro Oncol.* (2016) 18:902–13. doi: 10.1093/neuonc/now016
11. Dasgupta A, Gupta T, Jalali, R. Indian data on central nervous tumors: a summary of published work. *South Asian J Cancer.* (2016) 5:147–53. doi: 10.4103/2278-330X.187589
12. Watts, C. Surgical management of high-grade glioma: a standard of care. *CNS Oncol.* (2012) 1:181–92. doi: 10.2217/cns.12.26
13. Stupp R, Mason WP, van den Bent MJ, Weller M, Fisher B, Taphoorn MJ, et al. Radiotherapy plus concomitant and adjuvant temozolomide for glioblastoma. *N Engl J Med.* (2005) 352:987–6. doi: 10.1056/NEJMoa043330
14. Wang M, Zhang R, Liu X, Li D, Qiu C, Zhao P, et al. Supratentorial extraventricular ependymomas: a retrospective study focused on long-term outcomes and prognostic factors. *Clin Neurol Neurosurg.* (2018) 165:1–6. doi: 10.1016/j.clineuro.2017.12.013
15. Ruda R, Reifenberger G, Frappaz D, Pfister SM, Laprie A, Santarius T, et al. EANO guidelines for the diagnosis and treatment of ependymal tumors. *Neuro Oncol.* (2018) 20:445–56. doi: 10.1093/neuonc/nox166
16. Pope WB, ed. *Glioma Imapging: Physiologic, Metabolic, Molecular Approaches*. Switzerland: Springer Nature (2019). doi: 10.1007/978-3-030-27359-0
17. Fetit AE, Novak J, Peet AC, Arvanitits, T.N. Three-dimensional textural features of conventional MRI improve diagnostic classification of childhood brain tumours. *NMR Biomed.* (2015) 28:1174–84. doi: 10.1002/nbm.3353
18. Orphanidou-Vlachou E, Vlachos N, Davies NP, Arvanitis TN, Grundy RG, Peet AC, et al. Texture analysis of T1 - and T2 -weighted MR images and use of probabilistic neural network to discriminate posterior fossa tumours in children. *NMR Biomed.* (2014) 27:632–9. doi: 10.1002/nbm.3099
19. Li M, Wang H, Shang Z, Yang Z, Zhang, Wan Y. Ependymoma H, and pilocytic astrocytoma: differentiation using radiomics approach based on machine learning. *J Clin Neurosci.* (2020) 75:175–80. doi: 10.1016/j.jocn.2020.04.080
20. Rodriguez Gutierrez D, Awwad A, Meijer L, Manita M, Jaspan T, Dineen RA, et al. and textural features of MRI diffusion to improve classification of pediatric posterior fossa tumors. *AJNR Am J Neuroradiol.* (2014) 35:1009–5. doi: 10.3174/ajnr.A3784
21. Dong J, Li L, Liang S, Zhao S, Zhang B, Meng Y, et al. Differentiation between ependymoma and medulloblastoma in children with radiomics approach. *Acad Radiol.* (2020) 28:318–27. doi: 10.1016/j.acra.2020.02.012
22. Khatua S, Idris T, Kotrotsou A, Gupta S, Zaky WT, Gopalakrishnan V, et al. MRI based radiomic signature to predict treatment response to intraventricular natural killer (NK) cell infusion therapy for recurrent/refractory pediatric brain tumors. *Clini Trail.* (2019) 2019:e21511. doi: 10.1200/JCO.2019.37.15_suppl.e21511
23. Dominietto M, Pica A, Safai S, Lomax AJ, Weber DC, Capobianco, et al. Role of complex networks for integrating medical images and radiomic features of intracranial ependymoma patients in response to proton radiotherapy. *Front Med (Lausanne).* (2019) 6:333. doi: 10.3389/fmed.2019.00333
24. Lo CM, Weng RC, Cheng SJ, Wang HJ, Hsieh, K.L. Computer-aided diagnosis of isocitrate dehydrogenase genotypes in glioblastomas from radiomic patterns. *Medicine (Baltimore).* (2020) 99:e19123. doi: 10.1097/MD.0000000000019123
25. Wu S, Meng J, Yu Q, Li P, Fu, S. Radiomics-based machine learning methods for isocitrate dehydrogenase genotype prediction of diffuse gliomas. *J Cancer Res Clin Oncol.* (2019) 145:543–550. doi: 10.1007/s00432-018-2787-1
26. Tan Y, Zhang ST, Wei JW, Dong D, Wang XC, Yang GQ, et al. A radiomics nomogram may improve the prediction of IDH genotype for astrocytoma before surgery. *Europ Radiol.* (2019) 29:3325–37. doi: 10.1007/s00330-019-06056-4
27. Li Y, Liu X, Xu K, Qian Z, Wang K, Fan X, et al. MRI features can predict EGFR expression in lower grade gliomas: A voxel-based radiomic analysis. *Eur Radiol.* (2018) 28:356–62. doi: 10.1007/s00330-017-4964-z
28. Li ZC, Bai H, Sun Q, Li Q, Liu L, Zou Y, et al. Multiregional radiomics features from multiparametric MRI for prediction of MGMT methylation status in glioblastoma multiforme: A multicentre study. *Eur Radiol.* (2018) 28:3640–50. doi: 10.1007/s00330-017-5302-1
29. Xi YB, Guo F, Xu ZL, Li C, Wei W, Tian P, et al. Radiomics signature: A potential biomarker for the prediction of MGMT promoter methylation in glioblastoma. *J Magn Reson Imaging.* (2018) 47:1380–7. doi: 10.1002/jmri.25860
30. Wei J, Yang G, Hao X, Gu D, Tan Y, Wang X, et al. and habitat-based MRI radiomics signature for preoperative prediction of MGMT promoter methylation in astrocytomas with prognostic implication. *Eur Radiol.* (2019) 29:877–88. doi: 10.1007/s00330-018-5575-z
31. Hajianfar G, Shiri I, Maleki H, Oveisi N, Haghparast A, Abdollahi H, et al. Noninvasive O6 methylguanine-DNA methyltransferase status prediction in glioblastoma multiforme cancer using magnetic resonance imaging radiomics features: univariate and multivariate radiogenomics analysis. *World Neurosurg.* (2019) 132:e140–e61. doi: 10.1016/j.wneu.2019.08.232
32. Rathore S, Akbari H, Doshi J, Shukla G, Rozycki M, Bilello M, et al. Radiomic signature of infiltration in peritumoral edema predicts subsequent recurrence in glioblastoma: implications for personalized radiotherapy planning. *J Med Imaging (Bellingham).* (2018) 5:21219. doi: 10.1117/1.JMI.5.2.021219
33. Zhou M, Scott J, Chaudhury B, Hall L, Goldgof D, Yeom KW, et al. Radiomics in brain tumor: image assessment, quantitative feature descriptors, machine-learning approaches. *AJNR Am J Neuroradiol.* (2018) 39:208–16. doi: 10.3174/ajnr.A5391
34. Peng L, Parekh V, Huang P, Lin DD, Sheikh K, Baker B, et al. Distinguishing true progression from radionecrosis after stereotactic radiation therapy for brain metastases with machine learning and radiomics. *Int J Radiat Oncol Biol Phys.* (2018) 102:1236–43. doi: 10.1016/j.ijrobp.2018.05.041
35. Avants BB, Tustison NJ, Song G, Cook PA, Klein A, Gee JC, et al. A reproducible evaluation of ANTs similarity metric performance in brain image registration. *Neuroimage.* (2011) 54:2033–44. doi: 10.1016/j.neuroimage.2010.09.025
36. Smith, S.M. Fast robust automated brain extraction. *Hum Brain Mapp.* (2002) 17:143–55. doi: 10.1002/hbm.10062
37. Kamnitsas K, Ledig C, Newcombe VFJ, Simpson JP, Kane AD, Rueckert D, et al. Efficient multi-scale 3D CNN with fully connected CRF for accurate brain lesion segmentation. *Med Image Anal.* (2017) 36:61–78. doi: 10.1016/j.media.2016.10.004
38. Herz C, Fillion-Robin JC, Onken M, Riesmeier J, Lasso A, Pinter C, et al. DCMQI: an open source library for standardized communication of quantitative image analysis results using DICOM. *Cancer Res.* (2017) 77:e87–e90. doi: 10.1158/0008-5472.CAN-17-0336
39. Chen Q, Meng Z, Liu X, Jin Q, Su, R. Decision variants for the automatic determination of optimal feature subset in RF-RFE. *Genes (Basel).* (2018) 9:301. doi: 10.3390/genes9060301
40. Gregorutti B, Michel B, Saint-Pierre P. Correlation and variable importance in random forests. *Stat Comp.* (2017) 27:659–78. doi: 10.1007/s11222-016-9646-1
41. Guyon I, Weston J, Barnhill, Vapnik VS. Gene selection for cancer classification using support vector machines. *Mach Learn.* (2002) 46:389–422. doi: 10.1023/A:1012487302797
42. Breiman L. Random forests. *Mach Learn.* (2001). 45:5–32. doi: 10.1023/A:1010933404324
43. Cortes V, Vapnik C. Support-vector networks. *Mach Learn.* (1995) 20:273–97. doi: 10.1007/BF00994018
44. Wang SC. Artificial neural network. *Interdisc Comp Java Program.* (2003) 2003:81–100. doi: 10.1007/978-1-4615-0377-4_5
45. Chawla NV, Bowyer KW, Hall LO, Kegelmeyer WP. SMOTE: synthetic minority over-sampling technique. *J Artif Intellig Res.* (2002) 16:321–57. doi: 10.1613/jair.953
46. Mangalore S, Aryan S, Prasad C, Santosh, V. Imaging characteristics of supratentorial ependymomas: Study on a large single institutional cohort with histopathological correlation. *Asian J Neurosurg.* (2015) 10:276–81. doi: 10.4103/1793-5482.162702

Conflict of Interest: The authors declare that the research was conducted in the absence of any commercial or financial relationships that could be construed as a potential conflict of interest.

frontiers in Oncology

CLINICAL TRIAL
published: 30 August 2021
doi: 10.3389/fonc.2021.732704

An Integrated Radiomics Model Incorporating Diffusion-Weighted Imaging and ^{18}F-FDG PET Imaging Improves the Performance of Differentiating Glioblastoma From Solitary Brain Metastases

Liqiang Zhang[1†], Rui Yao[2†], Jueni Gao[1†], Duo Tan[2], Xinyi Yang[1], Ming Wen[1], Jie Wang[3], Xiangxian Xie[4], Ruikun Liao[5], Yao Tang[6], Shanxiong Chen[2*] and Yongmei Li[1*]*

[1] Department of Radiology, The First Affiliated Hospital of Chongqing Medical University, Chongqing, China, [2] College of Computer & Information Science, Southwest University, Chongqing, China, [3] Department of Nuclear Medicine, The First Affiliated Hospital of Chongqing Medical University, Chongqing, China, [4] Department of Radiology, Chongqing United Medical Imaging Center, Chongqing, China, [5] Department of Radiology, Chongqing General Hospital, Chongqing, China, [6] Department of Oncology, People's Hospital of Chongqing Hechuan, Chongqing, China

Background: The effectiveness of conventional MRI (cMRI)-based radiomics in differentiating glioblastoma (GBM) from solitary brain metastases (SBM) is not satisfactory enough. Therefore, we aimed to develop an integrated radiomics model to improve the performance of differentiating GBM from SBM.

Methods: One hundred patients with solitary brain tumors (50 with GBM, 50 with SBM) were retrospectively enrolled and randomly assigned to the training set (n = 80) or validation set (n = 20). A total of 4,424 radiomic features were obtained from contrast-enhanced T1-weighted imaging (CE-T1WI) with the contrast-enhancing and peri-enhancing edema region, T2-weighted imaging (T2WI), diffusion-weighted imaging (DWI)-derived apparent diffusion coefficient (ADC), and ^{18}F-fluorodeoxyglucose positron emission tomography (^{18}F-FDG PET) images. The partial least squares (PLS) regression with fivefold cross-validation is used to analyze the correlation between different radiomic features and different modalities. The cross-validity analysis was performed to judge whether a new principal component or a new feature dimension can significantly improve the final prediction effect. The principal components with effective interpretation in all radiomic features were projected to a low-dimensional space (2D in this study). The effective features of the new projection mapping were then sent to the random forest classifier to predict the results. The performance of differentiating GBM from SBM was compared between the integrated radiomics model and other radiomics models or nonradiomics methods using the area under the receiver operating characteristics curve (AUC).

OPEN ACCESS

Edited by:
Manoj Kumar,
National Institute of Mental Health and Neurosciences (NIMHANS), India

Reviewed by:
Shuai Ren,
Affiliated Hospital of Nanjing University of Chinese Medicine, China
Sridhar Goud,
National Institutes of Health (NIH), United States
Pardeep Kumar,
National Institute of Mental Health and Neurosciences, India

***Correspondence:**
Yongmei Li
lymzhang70@aliyun.com
Shanxiong Chen
csxpml@163.com
Yao Tang
ty15320328153@163.com

[†]These authors have contributed equally to this work and share first authorship

Specialty section:
This article was submitted to Neuro-Oncology and Neurosurgical Oncology, a section of the journal Frontiers in Oncology

Received: 29 June 2021
Accepted: 06 August 2021
Published: 30 August 2021

Citation:
Zhang L, Yao R, Gao J, Tan D, Yang X, Wen M, Wang J, Xie X, Liao R, Tang Y, Chen S and Li Y (2021) An Integrated Radiomics Model Incorporating Diffusion-Weighted Imaging and ^{18}F-FDG PET Imaging Improves the Performance of Differentiating Glioblastoma From Solitary Brain Metastases. Front. Oncol. 11:732704. doi: 10.3389/fonc.2021.732704

Results: Through the cross-validity analysis of partial least squares, hundreds of radiomic features were projected into a new two-dimensional space to complete the construction of radiomics model. Compared with the combined radiomics model using DWI + ^{18}F-FDG PET (AUC = 0.93, $p = 0.014$), cMRI + DWI (AUC = 0.89, $p = 0.011$), cMRI + ^{8}F-FDG PET (AUC = 0.91, $p = 0.015$), and single radiomics model using cMRI (AUC = 0.85, $p = 0.018$), DWI (AUC = 0.84, $p = 0.017$), and ^{18}F-FDG PET (AUC = 0.85, $p = 0.421$), the integrated radiomics model (AUC = 0.98) showed more efficient diagnostic performance. The integrated radiomics model (AUC = 0.98) also showed significantly better performance than any single ADC, SUV, or TBR parameter (AUC = 0.57–0.71, $p < 0.05$). The integrated radiomics model showed better performance in the training (AUC = 0.98) and validation (AUC = 0.93) sets than any other models and methods, demonstrating robustness.

Conclusions: We developed an integrated radiomics model incorporating DWI and ^{18}F-FDG PET, which improved the performance of differentiating GBM from SBM greatly.

Keywords: ^{18}F-FDG PET, diffusion-weighted imaging (DWI), apparent diffusion coefficient (ADC), glioblastoma, solitary brain metastases (SBM)

INTRODUCTION

As the most common malignant brain tumor in adults, metastasis is estimated to be at least 10 times more common than primary malignant central nervous system tumors (1). Glioblastoma (GBM) accounts for more than half of all primary brain malignancies (2). Differentiating GBM from solitary brain metastases (SBM) preoperatively is significantly critical for optimizing individualized therapeutic decision-making, as the medical staging, therapeutic strategies, and prognosis are different (3–5). *En bloc* resection is preferred for metastases, and stereotactic radiosurgery is also considered an effective strategy for metastases of less than 3–4 cm (6), and maximal resection of the tumor followed by radiotherapy and temozolomide chemotherapy should be considered for GBM (7). Generally speaking, metastasis usually presents as multiple nodular enhancing lesions with surrounding edema in the cortical gray-white matter junction, whereas GBM mostly has general characteristic image features, such as the invasion of the deep white matter and the presence of solitary ring-enhancing lesion (3, 8). In patients with multiple lesions and systemic cancer, brain metastasis identification may be easily performed using conventional MRI (cMRI). However, when metastasis presents with a solitary ring-enhancing lesion or an unknown clinical history, it is challenging to differentiate the two tumors due to their similar imaging features. Both GBM and SBM can present with irregular ring enhancement and intratumoral necrosis on contrast-enhanced T1-weighted imaging (CE-T1WI), surrounding edema on T2-WI and ring-hypermetabolic on ^{18}F-fluorodeoxyglucose positron emission tomography (^{18}F-FDG PET) images. Histopathology is the gold standard for the diagnosis of GBM or metastasis. Unfortunately, the present way for identifying GBM from SBM is to undertake a biopsy or open surgical resection invasively. However, when the tumors are located near eloquent areas or the patient is weak, biopsy or open surgical resection may risk morbidity and mortality. Therefore, an accurate noninvasive preoperative method would be preferable and sometimes necessary (9, 10).

It has been shown that infiltrating neoplastic cells have been found in surrounding edema of GBM, while peritumoral edema of metastasis consists essentially of vasogenic edema, indicating that there are some differences in cells, edema type, angiogenesis, etc. between the peri-enhancing edema regions of the two tumors. However, the surrounding edema of the two tumors showed no enhancement, hypometabolic, or no obvious diffusion limitation. Therefore, it is reasonable to assume that there are pathophysiological abnormalities in the peritumoral edema area that cannot be visually recognized besides the tumor enhancement area. We hope to find a new and more effective method to distinguish two tumors based on the difference between the metastatic vasogenic edema and GBM infiltrative edema containing tumor cells infiltrating the white matter.

With the rapid development of medical image analysis, radiomics has become a hot research topic. Radiomics can noninvasively extract quantitative features of lesions from magnetic resonance images, providing important reference information for tumor characterizations, treatment monitoring, and outcome prediction (11). Previous studies have established radiomics models based on cMRI sequences to differentiate GBM from SBM and achieved good results. Qian et al. (12) developed a CE-T1WI-based radiomics model to differentiate GBM from SBM, with a test AUC value of 0.90. A radiomics model based on T1WI, T2WI, and CE-T1WI trained by Dong et al. (13) has a test AUC value of 0.76. Artzi et al. (14) established a radiomics model based on postcontrast 3D-T1W gradient echo images, and the test mean accuracy was 0.85. The radiomics classifier based on CE-T1WI established by Su et al. (15) yielded good performance with AUC values of 0.82 and 0.81 in the training and validation cohorts to distinguish GBM from SBM. These results are barely satisfactory for having limited value in demonstrating heterogeneity, function, and tumor metabolism and still have room for improvement. Some studies have

reported that the mean diffusivity and minimum apparent diffusion coefficient (ADC) values of peritumoral edema seem lower in GBM than in SBM (16–18). Even though some other studies denied this result (19–21), diffusion-weighted imaging (DWI) seems to have the potential to distinguish GBM from SBM. Compared with cMRI, DWI can evaluate brain tumor diffusion and hypercellularity. ^{18}F-FDG PET imaging has been shown to be helpful for assessing surgery and radiotherapy as well as providing important imaging biomarkers for tumor metabolism evaluation (22–26). Therefore, DWI and ^{18}F-FDG PET imaging may show great potential for differentiating GBM from SBM. However, no studies have been reported to build a radiomics model incorporating DWI and ^{18}F-FDG PET imaging in differentiating GBM from SBM.

We hypothesized that a multivariate radiomics model incorporating DWI and ^{18}F-FDG PET could differentiate GBM from SBM more precisely than any other radiomics models or nonradiomics approaches, which will be more useful for clinicians to optimize clinical management decision-making. Thus, the study aimed to develop and validate a radiomics model using DWI and ^{18}F-FDG PET to improve the performance of differentiating GBM from SBM.

METHODS

Patient Enrollment

This retrospective study was approved by the local institutional review board, and the informed consent was obtained. The data and pathological information were obtained from The First Affiliated Hospital of Chongqing Medical University and the United Medical Imaging Center. We identified 128 consecutive patients who were pathologically confirmed with GBM or SBM on surgical resection or biopsy performed at the Department of Neurosurgery of our hospital. The inclusion criteria were as follows: (1) pathologically confirmed GBM or SBM; (2) all the lesions are solitary and limited to a single lobe, not across the lobes; (3) performed CE-T1WI, T2WI, DWI, and ^{18}F-FDG PET/CT examinations; (4) the interval between MRI and ^{18}F-FDG PET/CT examinations was less than 2 weeks; and (5) no history of preoperative radiotherapy or other medical treatments before surgery. A total of 28 patients were excluded according to the exclusion criteria (**Figure 1**). Finally, a total of 100 consecutive patients were included in the study. The patient selection process is presented in a flowchart in **Figure 1** in detail.

MR Imaging Acquisition

The MRI protocol for both training and validation sets included CE-T1WI, T2WI, DWI, and ^{18}F-FDG PET imaging.

MR images were obtained from the 3.0-T MRI system (Genesis Signa and Signa HDtx) with an eight-channel head coil (GE Medical Systems, Chicago, IL, USA). The main parameters of the T2WI sequence were as follows: repetition time/echo time (TR/TE) = 8,000/140 ms, flip angle = 90°, slice thickness = 5 mm, acquisition matrix = 256 × 256. The main parameters of the CE-T1WI sequence were as follows: TR/TE = 750/15 ms, slice thickness = 5 mm, acquisition matrix = 384 × 256. The main parameters of the DWI sequence were as follows: TR/TE = 6,379/70 ms; section thickness = 5 mm; intersection gap = 1.5 mm; matrix size = 128 × 128; FOV = 260 × 260 mm. The apparent diffusion coefficient (ADC) map (b = 1,000) was generated from DWI images.

^{18}F-FDG PET data acquisition was carried out with a PET/CT scanner (Philips Gemini TF 64 PET/CT scanner). The participants fasted for at least 6 h before ^{18}F-FDG administration and stopped any drugs that could affect brain metabolism for at least 12 h before the ^{18}F-FDG PET acquisition. Blood glucose levels were determined in all patients before ^{18}F-FDG administration, and blood glucose level was less than 8.0 mmol/L. PET/CT images of the head were acquired 60 min after intravenous injection of 370–555 MBq ^{18}F-FDG (produced

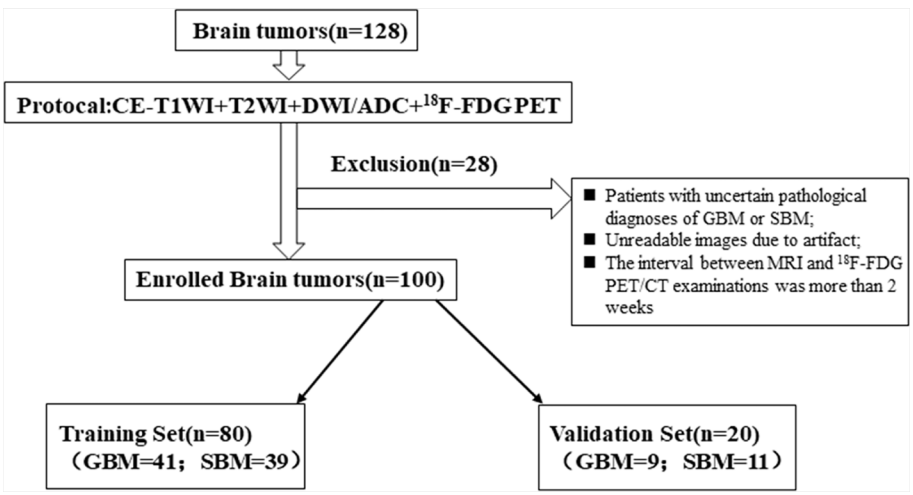

FIGURE 1 | The flowchart of patient selection process.

by Sumitomo accelerator of Japan with a radiochemical purity of >95%). PET images were acquired for one bed position (5 min/bed position), and a slice thickness of 2 mm. Low-dose CT images were obtained with a standardized protocol of 400 mAs, 120 Kv, matrix size of 512 × 512, and a slice thickness of 1 mm. The fusion images (a slice thickness of 2 mm) were obtained by computer iterative reconstruction and attenuation correction.

Image Preprocessing

For the CE-T1WI and T2WI data, signal intensity normalization was performed to reduce the variance in the T1-based signal intensity of the brain. We used the hybrid white-stripe method (22) for intensity normalization using the ANTsR and White Stripe packages (27, 28) in R, which incorporates processes of the statistical principles of image normalization, preserves ranks among the tissues, and matches the intensity of the tissues without upsetting the natural balance of the tissue intensities (29).

Skull stripping and tumor segmentation were performed by the 3D-Slicer Software (version 4.3, https://www.slicer.org) (30), an open-source software widely used for image visualization and segmentation. The tumor and perifocal edema contours were manually segmented using the fast-grow cut tool based on the T2WI imaging by two radiologists with 10 and 5 years of diagnostic experience, respectively, who were blinded to the final pathological result. The final region of interest (ROI) was determined by the two radiologists. If the divergence between segmentations was less than 5%, the final ROI was determined as the overlapping region of the two ROIs, otherwise, it was determined by the two radiologists. The segmented tumor contour was finally overlaid with source CE-T1WI, T2WI, ADC, and ^{18}F-FDG PET image.

Radiomics Feature Extraction

The radiomic features were composed of five groups of features: 18 first-order features, 14 shape features, 73 texture features, 273 LoG-transformed features, and 728 wavelet-transformed features. All patients had undergone CE-T1WI, T2WI, DWI, and ^{18}F-FDG PET, from which 1,106 radiomic features were derived, respectively. Finally, all radiomic features were extracted for group comparisons after z transformed. The entire feature extraction algorithm was fully automated, which yielded identical features regardless of the operators. The overall process of the radiomics pipeline is shown in **Figure 2**.

Feature Selection and Model Construction

In this study, we first used a *t*-test to screen radiomics features with significant independence, then applied partial least squares (PLS) to complete the regression analysis of those high-dimensional radiomics features in the training set. PLS regression method was applied using principal component analysis to extract and compress multiple independent variables X and multiple dependent variables Y into corresponding principal components U and V, respectively. Then, under the guidance of the canonical correlation principle and the multiple linear regression principle, the relationship can be analyzed between X and U, Y and V, and X and V. Thus, the relationship between X and Y can be studied. The PLS regression can project the high-dimensional data to the appropriate low-dimensional space and complete the effective feature selection of the data, which was chosen because the extracted radiomics features have the following two characteristics: (1) The number of feature dimensions extracted is far more than the number of patients. (2) Radiomics features exist in multiple correlations. PLS performs well in studies with small sample and multicollinearity among independent variables (radiomics features) and can emphasize the role of independent variables in the interpretation and prediction of dependent variables (classification of patients) when selecting feature vectors to remove the influence of useless noise on regression and make the radiomics model contain the least number of variables. As a result, final prediction performance gets better.

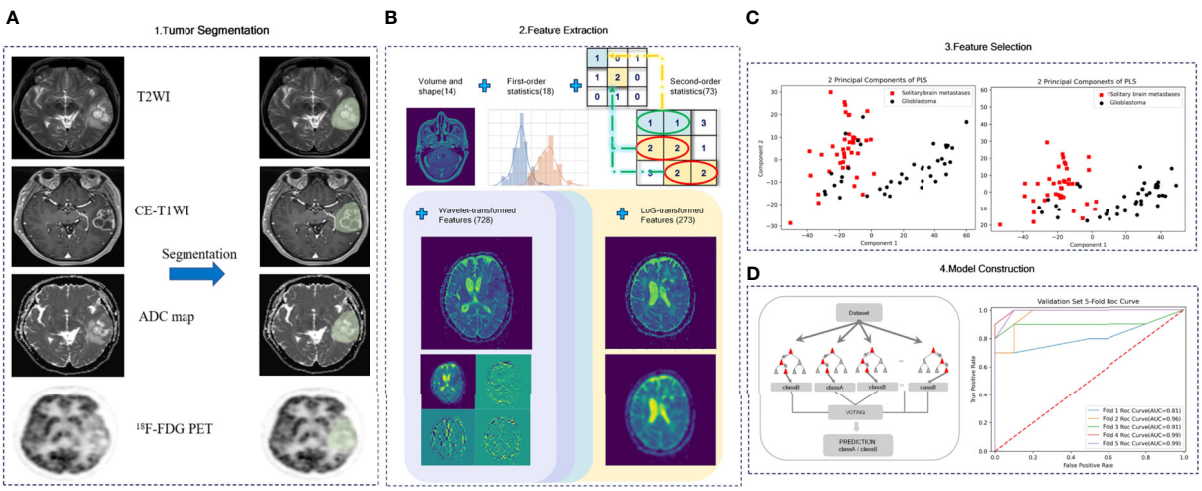

FIGURE 2 | Radiomics worklist. **(A)** Part 1 includes image acquisition, registration, and segmentation. Signal intensity normalization is conducted for CE-T1WI and T2WI. **(B)** Part 2 includes the extraction of radiomics features. **(C)** Part 3 includes feature selection. **(D)** Part 4 includes model construction.

To evaluate the robustness of the radiomics model and consider the number of data samples, we applied fivefold cross-validation. Cross-validity analysis was used to determine the final output dimension size of PLS regression; after that, all radiomics features with significant independence were projected to the new two-dimensional space through PLS regression. Then a variety of classical classifiers were used to predict the outcome using the selected effective features and the optimal random forest classifier is selected to construct the final radiomics model. Finally, the predictive efficiency of the radiomics model was compared under the different modality features combination.

Model Performance With Validation and Comparison of Diagnostic Performance

The accuracy of differentiating GBM from SBM using the above methods was assessed with the receiver operating characteristic (ROC) curve and the AUC values in two sets. The optimal thresholds of the AUC values were determined by maximizing the sum of the sensitivity and specificity values calculated for differentiating GBM from SBM.

The performance of the integrated radiomics model was compared with that of the three combined radiomics models, three single radiomics models, and five single nonradiomics methods. Bonferroni correction was applied to adjust the *p*-values for multiple comparisons. A Bonferroni-corrected significance level of $p < 0.008$ was used to compare the integrated radiomics model and six other radiomics models, and a value of $p < 0.01$ was used to compare between the integrated radiomics model and the five nonradiomics methods.

Statistical Analysis

Statistical analyses were performed using R software (version 3.3.3). Differences in clinical information between the training and validation sets were evaluated using Student's *t*-test and Chi-square tests, and $p < 0.05$ was considered statistically significant. The Student's *t*-test was used to assess differences in the imaging parameters between GBM and SBM in the training and validation sets.

RESULTS

Clinical Characteristics

All patients underwent biopsy or surgery, and their pathological examination results were assessed. Of the 80 enrolled patients in the training set, 41 (51.2%) were identified as GBM and 28 (36.8%) as SBM. Twenty patients in the validation set consisted of nine (45.0%) GBM and 11 (55.0%) SBM. The clinical characteristics of the training and validation sets are shown in **Table 1**. No significant differences were found between the patients with GBM and SBM regarding age and sex, which justified the applicability of the training and validation sets.

Radiomics Feature Extraction

In total, 4,424 radiomic features were extracted from the multiparametric MR data (1,106 features were derived from CE-T1WI, T2WI, ADC, and ^{18}F-FDG PET). Partial least squares regression was used to find the correlation between radiomic features and patient classification. After cross-validity analysis, the top-m principal components of radiomic features with significant improvement for prediction results were selected by truncation method, so that hundreds of radiomic features were projected into a new m-dimensional space. **Table 2** shows the corresponding numerical relationship between different modality combinations (columns) and the final projection mapping dimensions (rows). The table starts from the analysis with only one principal component and gradually increases the number of retained principal components until the cross-validity principle is no longer satisfied, to select the number of final effective feature dimensions. The specific performance is the corresponding Qh^2 value less than 0.0975, indicating that adding a new principal component or feature dimension based on the previous number of principal components no longer has an obvious improvement on the final prediction effect and then ends the increase of the principal component number. It can be obtained from **Table 2** that the effective principal components of almost all modality combinations are less than or equal to 3. At the same time, judging from the importance and cumulative proportion of each principal component to the outcome (**Figure 3**), even when there are only three principal components, the newly screened features can affect the final result by more than 50%. From this point of view, it is reasonable to use the partial least squares method to screen the effective features. Through the experimental test, the number of dimensions of the optimal result is 2.

In constructing a random forest model, not all the training data were used by each decision subtree, so these data can be used as test cases to measure the generalization performance of the model by calculating the classification error of out-of-bag estimation, which was 0.10 in the training cohort. The mean prediction accuracy of 84.00% (AUC = 0.9330) for fivefold cross-

TABLE 1 | Clinical characteristics of the patients.

Group	Training set			Validation set		
	GBM (*n* = 41)	SBM (*n* = 39)	*p*-Value	GBM (*n* = 9)	SBM (*n* = 11)	*p*-Value
Age	48.8 ± 11.2	49.6 ± 10.9	0.87	52.3 ± 10.3	51.8 ± 10.2	0.71
No of male patients	24 (58.5%)	17 (43.6%)	0.76	4 (44.4%)	5 (45.5%)	0.12
Biopsy	35 (85.4%)	31 (79.5%)		5 (55.6%)	7 (63.6%)	
Surgical resection	7 (14.6%)	8 (20.5%)		4 (44.4%)	4 (36.4%)	

Data are expressed as the mean ± standard deviation. Numbers in parentheses are percentages.

TABLE 2 | Score of crossvalidity analysis (Qh^2 score).

Modality combination	Number of principal components					Effective number
	1 Component	2 Components	3 Components	4 Components	5 Components	
ADC	1	0.2402	0.0498	None	None	2
PET	1	–0.0122	None	None	None	1
ADC+PET	1	0.1755	0.1990	–0.0559	None	3
T1+T2	1	0.1115	0.1243	0.1260	0.0369	4
T1+T2+ADC	1	0.0839	None	None	None	1
T1+T2+PET	1	0.2057	0.0183	None	None	2
T1+T2+ADC+PET	1	0.1829	0.0475	None	None	2

$Qh^2 \leq 0.0975$indicates that adding a new principal component or feature dimension based on the previous number of principal components no longer has an obvious improvement effect on the final prediction effect, and then ends the increase of the component number.

validation was achieved in the validation cohort (**Figure 4**). For a random forest classifier, the classification score matrix represents the possibility that the label comes from a specific category. As shown in **Figure 5**, the red line indicates the median, and in our radiomics classifier model, the average scores (white diamond in **Figure 5**) of correct prediction for samples with GBM label and SBM label are 0.9365 (95% CI: 0.9044–0.9686) and 0.8762 (95% CI: 0.8350–0.9174), respectively.

Model Performance and Comparison of Diagnostic Performance

The sensitivity and specificity of the integrated radiomics model in the training set were 92.5% and 98.7%, respectively. The AUC value was higher in the integrated radiomics model (AUC = 0.98) than in the combined radiomics models (DWI + ^{18}F-FDG PET: AUC = 0.93, p=0.014; Conventional + DWI: AUC = 0.89, p = 0.011; Conventional + ^{8}F-FDG PET: AUC = 0.91, p = 0.015), the single radiomics model using cMRI (AUC = 0.85, p = 0.018), DWI (AUC = 0.84, P = 0.017), ^{18}F-FDG PET (AUC = 0.85, p = 0.421) and single nonradiomics method (AUC = 0.57–0.71, $p < 0.05$), showing the integrated model with better performance (**Table 3**).

The sensitivity and specificity of the integrated radiomics model in the validation set were 83.5% and 84.9%, respectively. The AUC value was higher in the integrated radiomics model (AUC = 0.93) than in the combined radiomics models (DWI + ^{18}F-FDG PET: AUC = 0.81; Conventional + DWI: AUC = 0.86; Conventional + ^{8}F-FDG PET: AUC = 0.83), the single radiomics model using cMRI (AUC = 0.84), DWI (AUC = 0.83), and ^{18}F-FDG PET (AUC = 0.84) and the single nonradiomics method (AUC = 0.51–0.67), showing the integrated model with better performance as well. The comparison of diagnostic performance of the radiomics models in the validation is shown by the fivefold mean ROC curve for different combinations in **Figure 6**, and more evaluation indicator information can be seen in **Table 4**.

DISCUSSION

In the present study, we built seven radiomics models and five nonradiomics methods and compared their performance. By optimizing the radiomics models from single parameter, single and double sequences to multimodality, we finally concluded that the integrated radiomics model incorporating DWI and ^{18}F-FDG PET outperformed any other radiomics models and nonradiomics methods. The integrated radiomics models in the

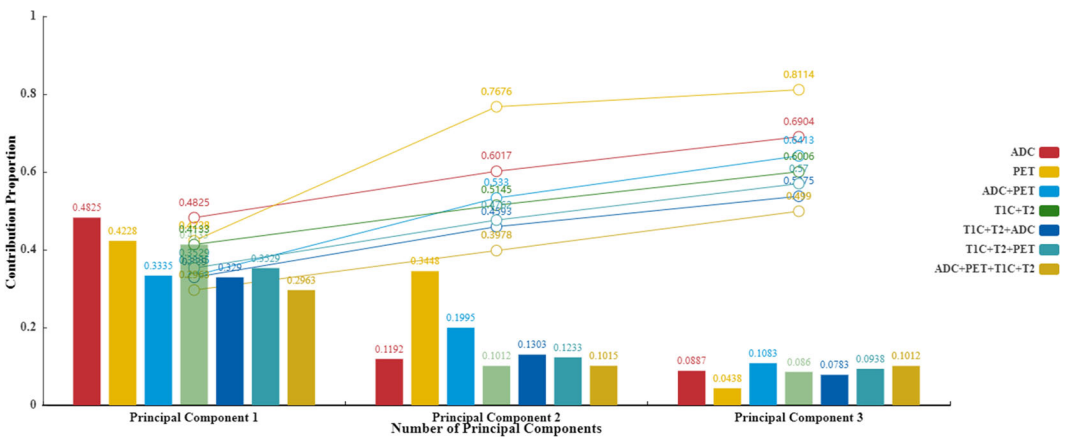

FIGURE 3 | Principal component contribution histogram and cumulative contribution rate line chart.

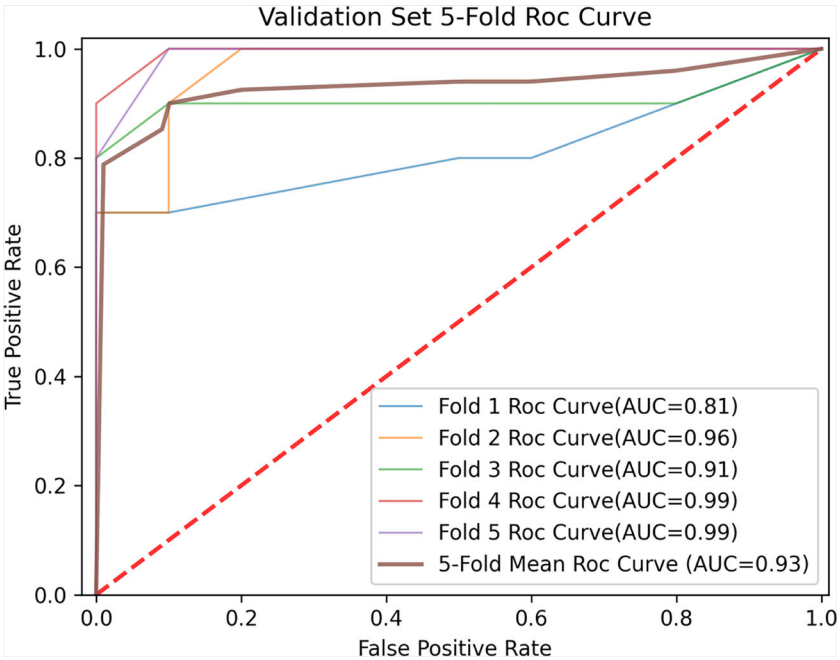

FIGURE 4 | Fivefold and mean receiver operating characteristic (ROC) curve for prediction in the validation cohort.

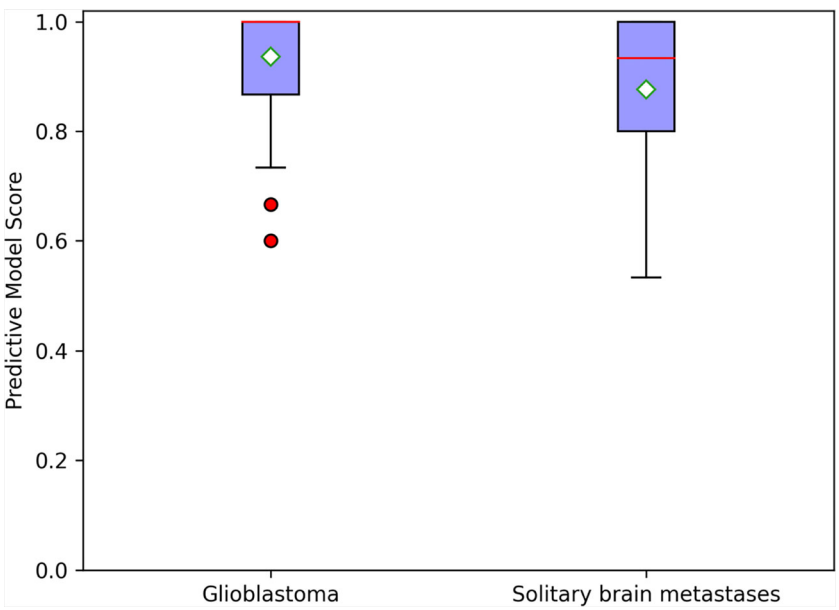

FIGURE 5 | Random forest classifier scores for glioblastoma and solitary brain metastases in the validation cohort; the red line indicates median, and the white diamond represents average prediction score.

training and validation sets have an AUC of 98% and 93%, a sensitivity of 92.5% and 83.5%, and a specificity of 98.7% and 84.9%, respectively. Some studies have used advanced imaging modalities (DWI and PET, etc.) to differentiate GBM from SBM. Lee et al. (29) analyzed patient age and sex, minimum ADC value, and ADC ratio of the two groups and found a statistical difference between GBM and metastasis. Kamson et al. (31) tested the accuracy of α[^{11}C]-methyl-L-tryptophan (AMT)–positron emission tomography (PET) to differentiate GBM from metastases and concluded that tumor/cortex AMT SUV

TABLE 3 | Comparison of diagnostic performance between integrated radiomics model and other methods in the training and validation sets.

Group		Training set				Validation set		
		AUC	*p*-Value*	Sensitivity	Specificity	AUC	Sensitivity	Specificity
Integrated radiomics model	Conventional + DWI+ ^{18}F-FDG PET	0.98 (0.93, 0.99)		92.5%	98.7%	0.93 (0.81, 0.97)	83.5%	84.9%
Combined radiomics model	DWI + ^{18}F-FDG PET	0.93 (0.89,0.97)	0.014	82.3%	91.2%	0.81 (0.67,0.89)	72.5%	78.1%
	Conventional + DWI	0.89 (0.83, 0.94)	0.011	92.1%	89.7%	0.86 (0.74, 0.93)	76.1%	86.8%
	Conventional + ^{18}F-FDG PET	0.91 (0.84, 0.95)	0.015	91.7%	94.7%	0.83 (0.74, 0.93)	80.4%	80.3%
Single radiomics model	Conventional MR	0.85 (0.74, 0.93)	0.018	82.6%	88.7%	0.84 (0.77, 0.91)	79.8%	76.1%
	DWI	0.84 (0.71, 0.87)	0.017	77.2%	75.8%	0.83 (0.78, 0.88)	82.2%	74.5%
	^{18}F-FDG PET	0.85 (0.72, 0.91)	0.421	66.4%	93.5%	0.84 (0.76, 0.89)	87.8%	72.2%
Single nonradiomics method	ADC max	0.59 (0.52, 0.65)	<0.001	56.4%	62.1%	0.51 (0.49, 0.72)	77.1%	61.3%
	ADC avg	0.57 (0.51, 0.63)	<0.001	61.4%	72.3%	0.53 (0.51, 0.64)	67.3%	77.3%
	SUV max	0.67 (0.62, 0.75)	<0.001	64.1%	53.4%	0.55 (0.47, 0.62)	62.1%	57.1%
	SUV avg	0.64 (0.59, 0.71)	<0.001	81.7%	74.3%	0.59 (0.56, 0.67)	69.3%	62.7%
	TBR max	0.71 (0.66, 0.77)	<0.001	80.4%	71.9%	0.67 (0.63, 0.77)	71.2%	89.3%

Numbers in parentheses are 95% confidence intervals.
ADC, apparent diffusion coefficient; SUV, standardized uptake value; TBR, tumor-to-background ratio.
**P-value refers to the significance among the differences of the AUCs between the integrated radiomics model and the other model or method.*

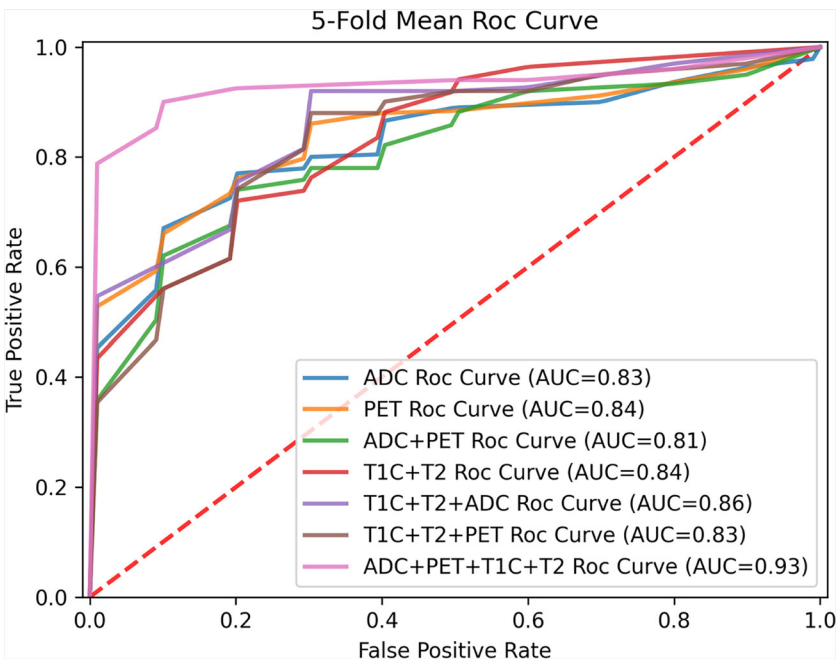

FIGURE 6 | Fivefold mean ROC curve for different modality combination.

ratios could distinguish GBM from metastases. However, their researches are just quantitative or semi-quantitative statistical analyses and limited to depict heterogeneous nature and excavate deeper information of GBM and metastases. As far as we know, this is the first radiomic study in brain tumors that combines MRI and ^{18}F-FDG PET. The CE-T1WI/T2WI, DWI, and

TABLE 4 | Comparison of more evaluation indicator information.

Modality combination	Evaluating indicator				
	ACC	Sensitivity	Specificity	PPV	NPV
ADC	0.76	0.828	0.745	0.7775	0.7565
PET	0.7699	0.878	0.722	0.7823	0.7695
ADC+PET	0.75	0.725	0.781	0.7710	0.7560
T1+T2	0.74	0.798	0.761	0.7388	0.7561
T1+T2+ADC	0.8099	0.761	0.868	0.8603	0.8085
T1+T2+PET	0.80	0.804	0.803	0.8191	0.8323
T1+T2+ADC+PET	0.84	0.835	0.849	0.8701	0.8728

^{18}F-FDG PET in the model provided structural, functional, and metabolic information at the same time and space, which makes our research more comprehensive and in-depth.

This study extended previous radiomic studies that only extracted features from cMRI sequences on enhancing tumor region or peri-enhancing edema region to differentiate GBM from SBM (12–15, 32–35). First, we incorporated DWI and ^{18}F-FDG PET based on cMRI sequences, which is the first of its kind. Second, the ROI of our study covers both enhancing tumor region and peri-enhancing edema region, which is larger than that of previous studies and is conducive to extracting more effective features. Third, we used the *t*-test to screen radiomics features with significant independence, and then used partial least squares regression to process these features further. The partial least squares regression with fivefold cross-validation was applied to analyze the correlation between different radiomics features within and between different imaging types in this study. Through cross-validity analysis to determine the final output dimension size of PLS regression, all radiomics features were mapped to the new two-dimensional space. After that, a variety of classical classifiers were used to predict classification outcomes using the new effective features, and the classifier with the best result (The random forest classifier is selected in this paper) will be selected to build the final radiomics model. Unlike the partial original radiomics features screened by LASSO in previous studies, we built the new interpretation dimensions according to the correlation between all radiomics features principal components and the corresponding label principal components to complete the construction of radiomics model. Even in a few new projection mapping dimensions, the final results are satisfactory. By comparing the diagnostic performance of models, we finally found an optimal integrated radiomics model to distinguish GBM from SBM. The integrated radiomics model achieved a noteworthy result, with AUCs of 0.98 (95% CI: 0.83–0.99) and 0.93 (95% CI: 0.81–0.97) in the training and validation sets, respectively, indicating the higher predictive performance of our study than the former ones.

Nevertheless, there are several limitations in this study. The total sample size was relatively small for the radiomics study, and a larger data set is needed to assess and adjust our model. Moreover, the validation set size is small, leading to the relatively low sensitivity of the integrated radiomics model. Finally, the study is a retrospective single-center study, and larger data sets from multicenter registration using different MR protocols should be interrogated to improve the radiomics model's stability further. If validated correctly and properly, this integrated model is expected to differentiate GBM from SBM before surgery, which can improve the diagnostic accuracy and provide help for the treatment plan and prognostic evaluation. Although the low-dimensional effective features screened by PLS can get a satisfactory performance, it ignores those principal components with large numbers but small contributions in feature screening, which may lead to a low cumulative contribution rate of the final screened effective features. Therefore, how to mine new information from these principal components with a large number but small contribution can be the future research direction.

In conclusion, our results confirm that the integrated radiomics model incorporating functional (DWI) and metabolic (^{18}F-FDG PET) sequences can achieve promising diagnostic efficiency for distinguishing between GBM and SBM with robustness. A large-scale multicenter study should be carried out to further confirm the preliminary results, thus making this noninvasive, simple and effective method applicable for routine clinical practice.

DATA AVAILABILITY STATEMENT

The raw data supporting the conclusions of this article will be made available by the authors, without undue reservation.

ETHICS STATEMENT

The studies involving human participants were reviewed and approved by The First Affiliated Hospital of Chongqing Medical University. The patients/participants provided their written informed consent to participate in this study. Written informed consent was obtained from the individual(s) for the publication of any potentially identifiable images or data included in this article.

AUTHOR CONTRIBUTIONS

Manuscript writing and statistical analysis: LZ, RY, and JG. Manuscript editing, supervised image segmentation, and

statistical analysis: RY. Image postprocessing, data provision, and informatics software support: DT and LZ. Supervised image postprocessing: JG, DT, and XY. Pathologic analysis: LZ, MW, YL, and SC. Clinical/oncologic database curation and oversight: YL, SC, and LZ. Database construction and data provision: XX, RL, SC, and JW. Database construction, clinical oversight, conceptual feedback, and project integrity: JG, DT, TY, YL, and SC. All authors contributed to the article and approved the submitted version.

FUNDING

This work was supported by the National Natural Science Foundation of China (31800823), the Medicine Scientific key Research Project of Chongqing Municipal Health and Family Planning Commission (2016ZDXM002), the Chongqing basic research and frontier exploration project of Chongqing Science & Technology Commission (cstc2018jcyjAX0584), the National Key Research & Development Plan of Ministry of Science and Technology of the People's Republic of China (2016YFC0107109). We thank the funders supporting the research.

ACKNOWLEDGMENTS

We thank other radiologists for helping the team with visualization. We also appreciate those patients who provided their images for our study. During the study process, our institution and radiology department provided a lot of support and convenience, to which we also express our deep gratitude.

REFERENCES

1. Ohgaki H, Kleihues P. Epidemiology and Etiology of Gliomas. *Acta Neuropathol* (2005) 109:93–108. doi: 10.1007/s00401-005-0991-y
2. Platta CS, Khuntia D, Mehta MP, Suh JH. Current Treatment Strategies for Brain Metastasis and Complications From Therapeutic Techniques: A Review of Current Literature. *Am J Clin Oncol* (2010) 33:398–407. doi: 10.1097/COC.0b013e318194f744
3. Cha S, Lupo JM, Chen MH, Lamborn KR, McDermott MW, Berger MS, et al. Differentiation of Glioblastoma Multiforme and Single Brain Metastasis by Peak Height and Percentage of Signal Intensity Recovery Derived From Dynamic Susceptibility-Weighted Contrast-Enhanced Perfusion MR Imaging. *AJNR Am J Neuroradiol* (2007) 28:1078–84. doi: 10.3174/ajnr.A0484
4. Giese A, Westphal M. Treatment of Malignant Glioma: A Problem Beyond the Margins of Resection. *J Cancer Res Clin Oncol* (2001) 127:217–25. doi: 10.1007/s004320000188
5. O'Neill BP, Buckner JC, Coffey RJ, Dinapoli RP, Shaw EG. Brain Metastatic Lesions. *Mayo Clin Proc* (1994) 69:1062–8. doi: 10.1016/S0025-6196(12)61374-3
6. Lin X, DeAngelis LM. Treatment of Brain Metastases. *J Clin Oncol* (2015) 33:3475. doi: 10.1200/JCO.2015.60.9503
7. Weller M, van den Bent M, Tonn JC, Stupp R, Preusser M, Cohen-Jonathan-Moyal E, et al. European Association for Neuro-Oncology (EANO) Guideline on the Diagnosis and Treatment of Adult Astrocytic and Oligodendroglial Gliomas. *Lancet Oncol* (2017) 18:e315–29. doi: 10.1016/S1470-2045(17)30194-8
8. Yang G, Jones TL, Howe FA, Barrick TR. Morphometric Model for Discrimination Between Glioblastoma Multiforme and Solitary Metastasis Using Three-Dimensional Shape Analysis. *Magn Reson Med* (2016) 75:2505–16. doi: 10.1002/mrm.25845
9. Blanchet L, Krooshof PW, Postma GJ, Idema AJ, Goraj B, Heerschap A, et al. Discrimination Between Metastasis and Glioblastoma Multiforme Based on Morphometric Analysis of MR Images. *AJNR Am J Neuroradiol* (2011) 32:67–73. doi: 10.3174/ajnr.A2269
10. Bernstein M, Parrent AG. Complications of CT-Guided Stereotactic Biopsy of Intra-Axial Brain Lesions. *J Neurosurg* (1994) 81:165–8. doi: 10.3171/jns.1994.81.2.0165
11. Lambin P, Rios-Velazquez E, Leijenaar R, Carvalho S, van Stiphout RGPM, Granton P, et al. Radiomics: Extracting More Information From Medical Images Using Advanced Feature Analysis. *Eur J Cancer* (2012) 48(4):441–6. doi: 10.1016/j.ejca.2011.11.036
12. Qian Z, Li Y, Wang Y, Li L, Li R, Wang K, et al. Differentiation of Glioblastoma From Solitary Brain Metastases Using Radiomic Machine-Learning Classifiers. *Cancer Lett* (2019) 451:128–35. doi: 10.1016/j.canlet.2019.02.054
13. Dong F, Li Q, Jiang B, Zhu X, Zeng Q, Huang P, et al. Differentiation of Supratentorial Single Brain Metastasis and Glioblastoma by Using Peri-Enhancing Oedema Region-Derived Radiomic Features and Multiple Classifiers. *Eur Radiol* (2020) 30:3015–22. doi: 10.1007/s00330-019-06460-w
14. Moran A, Idan B, Bashat Dafna B. Differentiation Between Glioblastoma, Brain Metastasis and Subtypes Using Radiomics Analysis. *J Magn Reson Imaging* (2019) 50:519–28. doi: 10.1002/jmri.26643
15. Su C-Q, Chen X-T, Duan S-F, Zhang JX, You YP, Lu SS, et al. A Radiomics-Based Model to Differentiate Glioblastoma From Solitary Brain Metastases. *Clin Radiol* (2021) 76:629.e11–.e18. doi: 10.1016/j.crad.2021.04.012
16. Byrnes TJ, Barrick TR, Bell BA, Clark CA. Diffusion Tensor Imaging Discriminates Between Glioblastoma and Cerebral Metastases *In Vivo*. *NMR BioMed* (2011) 24:54–60. doi: 10.1002/nbm.1555
17. Chiang IC, Kuo YT, Lu CY, Yeung K-W, Lin W-C, Sheu F-O, et al. Distinction Between High-Grade Gliomas and Solitary Metastases Using Peritumoral 3-T Magnetic Resonance Spectroscopy, Diffusion, and Perfusion Imaging. *Neuroradiology* (2004) 46:619–27. doi: 10.1007/s00234-004-1246-7
18. Pavlisa G, Rados M, Pavlisa G, Pavic L, Potocki K, Mayer D. The Differences of Water Diffusion Between Brain Tissue Infiltrated by Tumor and Peritumoral Vasogenic Edema. *Clin Imaging* (2009) 33:96–101. doi: 10.1016/j.clinimag.2008.06.035
19. Kono K, Inoue Y, Nakayama K, Shakudo M, Morino M, Ohata K, et al. The Role of Diffusion-Weighted Imaging in Patients With Brain Tumors. *AJNR* (2001) 22:1081–8.
20. Tsougos I, Svolos P, Kousi E, Fountas K, Theodorou K, Fezoulidis I, et al. Differentiation of Glioblastoma Multiforme From Metastatic Brain Tumor Using Proton Magnetic Resonance Spectroscopy, Diffusion and Perfusion Metrics at 3 T. *Cancer Imaging* (2012) 12:423–36. doi: 10.1102/1470-7330.2012.0038
21. Min ZG, Niu C, Rana N, Ji HM, Zhang M. Differentiation of Pure Vasogenic Edema and Tumorinfiltrated Edema in Patients With Peritumoral Edema by Analyzing the Relationship of Axial and Radial Diffusivities on 3. *0T MRI Clin Neurol Neurosurg* (2013) 115:1366–70. doi: 10.1016/j.clineuro.2012.12.031
22. Pauleit D, Floeth F, Hamacher K, Riemenschneider MJ, Reifenberger G, Muller HW, et al. O-(2-[18F]Fluoroethyl)-L-Tyrosine PET Combined With MRI Improves the Diagnostic Assessment of Cerebral Gliomas. *Brain* (2005) 128:678–87. doi: 10.1093/brain/awh399
23. Jansen NL, Suchorska B, Wenter V, Eigenbrod S, Schmid-Tannwald C, Zwergal A, et al. Dynamic 18f-FET PET in Newly Diagnosed Astrocytic Low-Grade Glioma Identifies High-Risk Patients. *J Nucl Med* (2014) 55:198–203. doi: 10.2967/jnumed.113.122333
24. Albert NL, Weller M, Suchorska B, Galldiks N, Soffietti R, Kim MM, et al. Response Assessment in Neuro-Oncology Working Group and European Association for Neuro-Oncology Recommendations for the Clinical Use of PET Imaging in Gliomas. *Neuro-Oncology* (2016) 18:1199–208. doi: 10.1093/neuonc/now058
25. Puttick S, Bell C, Dowson N, Rose S, Fay MPET. MRI, and Simultaneous PET/MRI in the Development of Diagnostic and Therapeutic Strategies for Glioma. *Drug Discov Today* (2015) 20(3):306–17. doi: 10.1016/j.drudis.2014.10.016

26. Wang K, Qiao Z, Zhao X, Li X, Wang X, Wu T, et al. Individualized Discrimination of Tumor Recurrence From Radiation Necrosis in Glioma Patients Using an Integrated Radiomics-Based Model. *Eur J Nucl Med Mol Imaging* (2020) 47(6):1400–11. doi: 10.1007/s00259-019-04604-0
27. Avants BB, Tustison NJ, Song G, Cook PA, Klein A, Gee JC. A Reproducible Evaluation of ANTs Similarity Metric Performance in Brain Image Registration. *Neuroimage* (2011) 54:2033–44. doi: 10.1016/j.neuroimage.2010.09.025
28. Shinohara RT, Sweeney EM, Goldsmith J, Shiee N, Mateen FJ, Calabresi PA, et al. Statistical Normalization Techniques for Magnetic Resonance Imaging. *NeuroImage Clin* (2014) 6:9–19. doi: 10.1016/j.nicl.2014.08.008
29. Lee EJ, terBrugge K, Mikulis D, Choi DS, Bae JM, Lee SK, et al. Diagnostic Value of Peritumoral Minimum Apparent Diffusion Coefficient for Differentiation of Glioblastoma Multiforme From Solitary Metastatic Lesions. *AJR Am J Roentgenol* (2011) 196:71–6. doi: 10.2214/AJR.10.4752
30. Fedorov A, Beichel R, Kalpathy-Cramer J, Finet J, Fillion-Robin JC, Pujol S, et al. 3d Slicer as an Image Computing Platform for the Quantitative Imaging Network. *Magn Reson Imaging* (2012) 30:1323–41. doi: 10.1016/j.mri.2012.05.001
31. Kamson David O, Sandeep M, Buth A, Muzik O, Kupsky William J, Robinette Natasha L, et al. Differentiation of Glioblastomas From Metastatic Brain Tumors by Tryptophan Uptake and Kinetic Analysis: A Positron Emission Tomographic Study With Magnetic Resonance Imaging Comparison. *Mol Imaging* (2013) 12(5):327–37. doi: 10.2310/7290.2013.00048
32. Sauerbrei W, Royston P, Binder H. Selection of Important Variables and Determination of Functional Form for Continuous Predictors in Multivariable Model Building. *Stat Med* (2007) 26:5512–28. doi: 10.1002/sim.3148
33. Tibshirani R. Regression Shrinkage and Selection *via* the Lasso. *J Roy Stat Soc B Met* (1996) 58(1):267–88. doi: 10.1111/j.2517-6161.1996.tb02080.x
34. Wu TT, Chen YF, Hastie T, Sobel E, Lange K. Genome-Wide Association Analysis by Lasso Penalized Logistic Regression. *Bioinf (Oxf Engl)* (2009) 25(6):714–21. doi: 10.1093/bioinformatics/btp041
35. Gui J, Li H. Penalized Cox Regression Analysis in the High-Dimensional and Low-Sample Size Settings, With Applications to Microarray Gene Expression Data. *Bioinf (Oxf Engl)* (2005) 21(13):3001–8. doi: 10.1093/bioinformatics/bti422

Conflict of Interest: The authors declare that the research was conducted in the absence of any commercial or financial relationships that could be construed as a potential conflict of interest.

Publisher's Note: All claims expressed in this article are solely those of the authors and do not necessarily represent those of their affiliated organizations, or those of the publisher, the editors and the reviewers. Any product that may be evaluated in this article, or claim that may be made by its manufacturer, is not guaranteed or endorsed by the publisher.

frontiers in Neurology

ORIGINAL RESEARCH
published: 24 September 2021
doi: 10.3389/fneur.2021.627247

Can High b Value Diffusion Be a Surrogate Marker for PET—A MR/PET Study in Neurooncology Set Up

Sandhya Mangalore, Sriharish Vankayalapati, Shumyla Jabeen, Arun Kumar Gupta and Pardeep Kumar*

Department of Neuroimaging and Interventional Radiology, National Institute of Mental Health and Neurosciences, Bangalore, India

OPEN ACCESS

Edited by:
Sanjeev Chawla, University of Pennsylvania, United States

Reviewed by:
Kavindra Nath, University of Pennsylvania, United States
Pradeep Kumar Gupta, University of Pennsylvania, United States

***Correspondence:**
Sandhya Mangalore
drsandym@gmail.com

Specialty section:
This article was submitted to Applied Neuroimaging, a section of the journal Frontiers in Neurology

Received: *08 November 2020*
Accepted: *24 May 2021*
Published: *24 September 2021*

Citation:
Mangalore S, Vankayalapati S, Jabeen S, Kumar Gupta A and Kumar P (2021) Can High b Value Diffusion Be a Surrogate Marker for PET—A MR/PET Study in Neurooncology Set Up. Front. Neurol. 12:627247. doi: 10.3389/fneur.2021.627247

Purpose: Hybrid whole-body magnetic resonance/positron emission tomography (MR/PET) systems are new diagnostic tools enabling the simultaneous acquisition of morphologic and multiparametric functional data, which allow for a diversified characterization of oncological diseases. This study aimed to compare the diagnostic ability of MRI with the diffusion-weighted image (DWI), and simultaneous integrated positron emission tomography MR/PET to detect malignant lesions and elucidate the utility and limitations of these imaging modalities in preoperative and postoperative follow up in cancer patients.

Material and Methods: A total of 45 patients undergoing simultaneous MR/PET for CNS ICSOL in our institution between January 2016 and July 2020 were considered in this study. Post-processing was done in Siemens syngo software to generate a b2000 image. This image was then inverted to grayscale and compared with the NAC image of PET.

Results: The lesion-based sensitivity, specificity, positive predictive value, and negative predictive value for DWI were 92.3, 83.3, 97.3, and 62.5%, respectively (at 95% CI and *p* was 0.000). The lesion-based sensitivity, specificity, positive predictive value, and negative predictive value for PET were 97.4, 71.4, 94.9, and 83.3%, respectively (at 95% CI and *p* was 0.000). The lesion-based sensitivity and specificity of DWI were comparable with those of PET.

Conclusions: Although DWI and FDG-PET reflect different tissue properties, there is an association between the measures of both methods in CNS tumors probably because of the coupling of cellularity with tumor metabolism as seen on FDG and other PET tracers. Our study shows that DWI acts as a surrogate biomarker for FDG PET and other tracers in tumors. The method of DWI image generation is simple, radiation-free, and cost-effective in a clinical setup. The simultaneous DWI-PET study provides evidence and confirms the role of DWI in surveillance imaging of tumors.

Keywords: PET-MR, CNS tumors, FDG-PET, high value diffusion weighted imaging, glioma

INTRODUCTION

The hybrid whole-body magnetic resonance positron emission tomography (MRPET) system is a new diagnostic tool. It enables the simultaneous acquisition of morphologic and multiple functional data and thus a diversified characterization of oncological diseases (1, 2).

Our study focuses on the use of simultaneous MR/PET. The temporal correlation of MRI and PET in a single sitting is possible with MR/PET and various MRI parameters and PET tracers can be compared with high spatial and temporal resolution. MRI is a multiparametric imaging technique and when combined with simultaneous PET is better than PET computed tomography.

Many MR/PET studies correlate with multiple advanced imaging parameters like diffusion-weighted imaging (DWI) and Perfusion weighted imaging (PWI) studies on the grading of gliomas, enabling the prediction of recurrence. It is possible to differentiate recurrence vs. radiation necrosis and the false negative in each modality is known (3–6). PET also has many tracers, each with its specificity and sensitivity (7–10).

Each modality has inherent limitations, for instance, false-positive uptake of FDG PET is due to the immediate effects of cyberknife and gamma knife, and post-radiotherapy related inflammatory changes (11). The resolution of PET at best is 4–6 mm (12). Many small lesions in the brain may be missed at this resolution in a post-operative case. MRI parameters on the other hand, such as PWI, MRS, contrast enhancement patterns have specificity and sensitivity and since these are ROI-based measurements, inherent flaws exist (12, 13). MRS and PWI can help grade tumors but since they use large voxel sizes, they have low specificity (14). Contrast enhancement pattern, which represents blood-brain barrier imaging, helps to correlate, but pseudoprogression and pseudo regression are known entities (15).

Though many DWI techniques have been discussed, no study had access to simultaneous MR/PET, especially in a neuro-oncology setup. However, the clinical benefits of simultaneous MR/PET imaging need to be balanced against the relatively high cost and availability of such an approach.

This paper discusses DWI as a potential MRI biomarker for FDG PET and other tracers. Moreover, this marker is simple, radiation-free, and cost-effective, making clinical translations more straightforward. This study compares DWI with PET images and aims to establish the sensitivity specificity and pitfalls in neurooncology.

We hypothesize that DWI and PET will have a good correlation as both show signal changes and uptake is based on cellularity. Though this paper mainly focuses on the role of MR/PET in cases of glioblastoma, we also briefly describe our experience with other histotypes of CNS tumors and also with other PET tracers as well.

MATERIALS AND METHODS

Approval was obtained from our institutional ethics committee. Patient consent was waived for this retrospective observational analysis of anonymized data. The study considered all patients with intra-cranial space-occupying-lesions (ICSOL) (all grades of gliomas and various other histotypes) evaluated with MR/PET in our institution between January 2016 and July 2020. A total of 45 cases with simultaneous MR/PET imaging are included in the study. All patients had histologically proven malignancies or suspected malignancies. Whole-brain PET images along with multiplanar and multi-sequence MR images were acquired in 3-D mode after i.v. injection of 18F-FDG using a simultaneous Siemens mMR Biograph PET/MR scanner. In a few cases different tracers like C-11methionine, F-18 choline was used as part of a clinical protocol.

This study aimed to compare the diagnostic ability of MRI with a diffusion-weighted image (DWI), and simultaneous integrated positron emission tomography MR/PET to detect malignant lesions and elucidate the utility and limitations of these imaging modalities in preoperative and postoperative follow up in cancer patients.

DWI Image Acquisition

A routine multiparametric MRI was conducted including T2, SWI, and fluid-attenuated inversion recovery (FLAIR) sequences, axial and 3D T1-weighted, and GdT1w-MRI.

DWI was acquired in the axial plane before injection of contrast material for all patients by fast echo-planar T2*-weighted gradient echo sequence and used for generating ADC maps. The sequence parameters were: b-values 0 and 1,000 s/mm^2,TR = 3,600 ms, TE = 81 ms, FOV = 23 cm, matrix = 128 × 128, voxel size-0.9 × 0.9 × 4 mm, 27 slices of 4 mm thickness 4 mm without spacing, NEX- 1.

Image Interpretation

Two radiologists interpreted the MR/PET images in a blinded fashion. The lesion-specific signal intensity on DWI and ADC is compared with metabolism on PET images. Histopathology, all imaging findings, and follow-up scans served as a standard of reference. The DWI images were post-processed using Siemens Heathineers syngo software (version 05.01.0000.0061). The MR basics module in the software package has options for calculating the high b value of trace images and hence we generated images at b2000 to suppress the T2 shine-through the effects of gliosis and edema and also at high value there was good background suppression and increased conspicuity of recurrent foci. For ease of visual correlation, in this study, we aimed to obtain a PET-like image from DWI by inverting the b2000 trace image to grayscale, which has the potential to be an excellent biomarker in the neuro-oncology workup.

Statistical Analysis

Data were collated offline on Microsoft Excel version 15.0.4 and statistical analysis was conducted with an online interactive statistics page using a 2 × 2 consistency table. Lesion-based sensitivity, specificity, negative predictive value, positive predictive value were calculated for DWI and PET modalities. The Yates corrected P-value < 0.005 was considered significant.

TABLE 1 | Brief summary of GLIOMA cases evaluated with MRI FDG-PET.

	MRI	Histopathology	DWI 2000	ADC 2000	PET	NAC vs. DWI	Other imaging findings
1	Recurrence	Anaplastic oligodendroglioma, nos - who grade iii; right fronto insular	Bright	Dark	Hyper metabolism	Match	Linear and nodular enhancement and elevated perfusion
2	Recurrence in background of radiation necrosis	Recurrent glioblastoma who grade -iv; molecular information:idh-1(r132h) - positive, atrx - loss of expression, p53 – positive mib-1 labeling is high (25–30%) at foci	Bright	Dark	Hyper metabolism	Match	Swiss cheese enhancement and elevated perfusion
3	Recurrence	Anaplastic oligodendroglioma, who grade iii; left frontal.	Bright	Dark	Hyper metabolism	Match	Homogenous enhancement with elevated perfusion
4	Radiation necrosis		Bright	Dark	Hypo metabolism		Homogenous enhancement
5	Radiation necrosis		Iso	Iso	Hypometabolism	Match	Swiss cheese enhancement with no elevated perfusion
6	Recurrence	Anaplastic oligodendroglioma - who grade-iii - right frontal.	Bright	Dark	Hyper metabolism	Match	Swiss cheese with nodular foci on enhancement. Volume underestimation on PET
7	Recurrence	Glioblastoma [idh-1 (r132h) mutant] - who grade iv; right frontal.	Bright	Dark	Hypermetabolism	Match	Nodular foci of enhancement with elevated perfusion
8	Recurrence	Glioblastoma, who grade-iv, left parietal.	Bright	Dark	Hyper metabolism	Match	Swiss cheese with nodular foci on enhancement and elevated perfusion
9	Recurrence		Bright	Dark	Few areas of Hyper metabolism	Match	Heterogeneous enhancement
10	Radiation necrosis	Anaplastic astrocytoma -who grade iii; corpus callosum	Iso	Iso	Hypometabolism	Match.	No foci of enhancement or elevated perfusion
11	Recurrence in background of radiation necrosis	Infiltrating anaplastic astrocytoma, left occipital.	Bright	Dark	Hypermetabolism	Match. Lesion is more evident on DWI	Swiss cheese with thick areas of enhancement and elevated perfusion. Overestimation on pet.
12	Radiation necrosis		Iso	Iso	Hypometabolism	Match	No foci of enhancement
13	Radiation necrosis	Anaplastic mixed oligo-astrocytoma, who grade-iii.	Iso	Iso	Hypometabolism	Match.	Heterogeneous enhancement along the resection cavity
14	Recurrence		Bright	Dark	Hypermetabolism	Match	Very thick nodular enhancement.
15	Recurrence		Bright	Dark	Hypermetabolism	Match	Extensive parenchymal enhancement with elevated perfusion
16	Recurrence	Glioblastoma (epithelioid variant) who grade iv; left frontal	Bright	Dark	Hypermetabolism	Match	Thick parenchymal enhancement. Overestimation on pet
17	Recurrence	Radiation necrosis with foci of glial neoplasm consistent with anaplastic glioma [idh 1 (r132h) negative, atrx retained expression]; left frontal.	Bright	Dark	Hypermetabolism	Match	Swiss cheese kind of appearance with overestimation on ASL
18	Recurrence	Glioblastoma, idh mutant, who grade iv, left frontal (recurrent).	Bright	Dark	Hypermetabolism	Match	Near homogenous enhancement with elevated perfusion on ASL
19	Recurrence	Glioblastoma who grade iv	Bright	Dark	Hypermetabolism	Match	Heterogeneous enhancement with elevated perfusion
20	Recurrence	Anaplastic oligodendroglioma, who grade iii; nos, right parieto occipital	Bright	Dark	Hyper metabolism	Match	Swiss cheese with nodular enhancement
21	Recurrence with metastasis in body	High grade glioma suggestive of pilocytic astrocytoma with malignant transformation (Dedifferentiation)	Bright	dark	Hypermetabolism	Match	Metastatic deposits in the occipital lobe; posterior fossa and left paravertebral region.

(Continued)

TABLE 1 | Continued

	MRI	Histopathology	DWI 2000	ADC 2000	PET	NAC vs. DWI	Other imaging findings
22	Recurrence	GBM with metastasis	Bright	Bright	Hypermetabolism	Match	Heterogeneous enhancement with elevated perfusion
23	Recurrence	Anaplastic oligodendroglioma grade iii,	Bright	Dark	Hypermetabolism	Match	Swiss cheese enhancement with nodular foci of enhancement with elevated perfusion.
24	Recurrence	Anaplastic oligodendroglioma who grade iii	Bright	Dark	Hypermetabolism	Match	Nodular focus of entertainment with elevated perfusion along margins
25	Recurrence in background of radiation necrosis		Bright	Dark	Hypermetabolism	Match	Areas of near heterogenous enhancement with elevated perfusion
	MRI	**Histopathology**	**ADC 2000**	**ADC values mean**	**SUV max**	**PET**	**Other imaging findings**
1	Recurrence	Anaplastic oligodendroglioma, nos - who grade iii; right fronto insular	Dark	667.58	5.8	Hyper metabolism	Linear and nodular enhancement and elevated perfusion
2	Recurrence in background of radiation necrosis	Recurrent glioblastoma who grade -iv; molecular information:idh-1 (r132h) - positive, atrx - loss of expression, p53 – positive mib-1 labeling is high (25–30%) at foci	Dark	825.3	8.2	Hyper metabolism	Swiss cheese enhancement and elevated perfusion
3	Recurrence	Anaplastic oligodendroglioma, who grade iii; left frontal.	Dark	906.6	21.9	Hyper metabolism	Homogenous enhancement with elevated perfusion
4	Radiation necrosis		Dark			Hypo metabolism	Homogenous enhancement
5	Radiation necrosis		Iso	1,636	7.5	Hypometabolism	Swiss cheese enhancement with no elevated perfusion
6	Recurrence	Anaplastic oligodendroglioma - who grade-iii - right frontal.	Dark	420	5	Hyper metabolism	Swiss cheese with nodular foci on enhancement. Volume underestimation on PET
7	Recurrence	Glioblastoma [idh-1 (r132h) mutant] - who grade iv; right frontal.	Dark	725.5	27	Hypermetabolism	Nodular foci of enhancement with elevated perfusion
8	Recurrence	Glioblastoma, who grade-iv, left parietal.	Dark	882	6.8	Hyper metabolism	Swiss cheese with nodular foci on enhancement and elevated perfusion
9	Recurrence		Dark	659.2	7.1	Few areas of Hyper metabolism	Heterogeneous enhancement
10	Radiation necrosis	Anaplastic astrocytoma -who grade iii; corpus callosum	iso	1,201		Hypometabolism	No foci of enhancement or elevated perfusion
11	Recurrence in background of radiation necrosis	Infiltrating anaplastic astrocytoma, left occipital.	Dark	831.7	11.9	Hypermetabolism	Swiss cheese with thick areas of enhancement and elevated perfusion. Overestimation on pet.
12	Radiation necrosis		Iso	818.8	5.9	Hypometabolism	No foci of enhancement
13	Radiation necrosis	Anaplastic mixed oligo-astrocytoma, who grade-iii.	Iso	1,340	10.6	Hypometabolism	Heterogeneous enhancement along the resection cavity
14	Recurrence		Dark	489		Hypermetabolism	Very thick nodular enhancement.
15	Recurrence		Dark	906	11.5	Hypermetabolism	Extensive parenchymal enhancement with elevated perfusion
16	Recurrence	Glioblastoma (epithelioid variant) who grade iv; left frontal	Dark	668	11	Hypermetabolism	Thick parenchymal enhancement. Overestimation on pet

(Continued)

TABLE 1 | Continued

	MRI	Histopathology	ADC 2000	ADC values mean	SUV max	PET	Other imaging findings
17	Recurrence	Radiation necrosis with foci of glial neoplasm consistent with anaplastic glioma [idh 1 (r132h) negative, atrx retained expression]; left frontal.	Dark	670	14.1	Hypermetabolism	Swiss cheese kind of appearance with overestimation on ASL
18	Recurrence	Glioblastoma, IDH mutant, who grade iv, left frontal (recurrent).	Dark	812.7	14.9	Hypermetabolism	Near homogenous enhancement with elevated perfusion on ASL
19	Recurrence	Glioblastoma who grade iv,	Dark			Hypermetabolism	Heterogeneous enhancement with elevated perfusion
20	Recurrence	Anaplastic oligodendroglioma, who grade iii; nos, right parieto occipital	Dark	405	3.5	Hyper metabolism	Swiss cheese with nodular enhancement
21	Recurrence with metastasis in body	High grade glioma suggestive of pilocytic astrocytoma with malignant transformation (Dedifferentiation)	dark			Hypermetabolism	Metastatic deposits in the occipital lobe; posterior fossa and left paravertebral region.
22	Recurrence	GBM with metastasis	Bright	414	54.7	Hypermetabolism	Heterogeneous enhancement with elevated perfusion
23	Recurrence	Anaplastic oligodendroglioma grade iii	Dark	439	7.7	Hypermetabolism	Swiss cheese enhancement with nodular foci of enhancement with elevated perfusion.
24	Recurrence	Anaplastic oligodendroglioma who grade iii	Dark	816	8	Hypermetabolism	Nodular focus of entertainment with elevated perfusion along margins
25	Recurrence in background of radiation necrosis		Dark	998	111.4	Hypermetabolism	Areas of near heterogenous enhancement with elevated perfusion

RESULTS

Anonymized MR/PET imaging data obtained in 45 patients with ICSOL were also used in the analysis and examined glioma of all grades ($n = 35$) and other histotypes ($n = 10$, including ependymoma, craniopharyngioma, meningioma, lymphoma, atypical rhabdoid tumor) with FDG tracer ($n = 31$), and other PET tracers such as C-11methionine ($n = 8$) and F-18 choline ($n = 3$).

Lesion-based sensitivity, specificity, positive predictive value and negative predictive value for DWI were 92.3, 83.3, 97.3, and 62.5% respectively (at 95% CI and $p < 0.05$). The lesion-based sensitivity, specificity, positive predictive value, and negative predictive value for PET were 97.4, 71.4, 94.9, and 83.3% respectively (at 95% CI and p is < 0.05). These lesion-based sensitivity, specificity of DWI were comparable with those of PET. The DWI showed significantly higher specificity than PET.

The salient observations noticed on visual analysis will also be discussed underneath as:

a) our experience with Glioma: high b value diffusion as a surrogate marker for FDG PET in the diagnosis of recurrence in brain tumors (**Table 1**).
b) Our experience with CNS tumors of other histotypes including the whole body work up (**Table 2**).
c) Our experience with other tracers (**Table 2**).

Using MRPET in Glioma to Differentiate Recurrence From Radiation Necrosis

A total of 25 post-operative patients with brain tumors were studied with preoperative histopathology and FDG MR/PET between 2016 and 2020.

Out of 25, 10 were Grade III and 8 were Grade IV tumors. A detailed histopathology report of glioma was not available in seven cases, as they were referred cases.

Among the 10 cases with Grade III, there were four who had IDH mutation, four were of p53 type and five were positive for ATRX. Among the eight cases with Grade IV tumor, two had IDH mutation, three were p53 subtype and one had ATRX mutation. The grade was based on a mitotic index. Of Grade IV cases, seven were of GBM tissue subtype and one was pilocytic astrocytoma subtype. In Grade III, six cases were of Oligodendroglioma subtype, one was of mixed Oligo astrocytoma subtype, and thee of anaplastic astrocytoma subtype.

MR/PET was done in 25 cases of glioma and reported as recurrence ($n = 20$) (**Figure 1**) and radiation necrosis ($n = 5$) (**Figure 2**) based on imaging findings. On follow-up, histopathology was available in 16 cases in the recurrence group. Recurrence on PET was noted in 20 cases with radiation necrosis in five cases. In Grade IV, five had a recurrence and among Grade III, seven had a recurrence, and three had necrosis on PET. We used PET as a reference to standardize DWI in differentiating necrosis vs. recurrence. When B2000 DWI and PET findings

TABLE 2 | Brief summary of other CNS histotypes cases evaluated with MRI FDG-PET and other PET tracers.

S.NO	Indication	Final diagnosis	DWI b-2000	ADC	PET	NAC vs. DWI	PET tracer	Comments
1	Primary tumor	Anaplastic Ependymoma	Bright	Dark	Hypermetabolism	Match	FDG	
2	Primary CNS lesion	Demyelination- clippers	Bright	Dark	Hyper etabolism	Match	FDG	HP after a month was Tcell lymphoma likely due to low tissue volume for both DWI and PET scan.
3	Brain and whole body PET	Lymphoma	Bright	Dark	Hypermetabolism	Match	FDG	HP came as demyelination but DWI PET matched as lymphoma – biopsy site should be planned properly
4	Recurrence With SMART syndrome	Anaplastic mixed oligo astrocytoma (WHO Grade III); left thalamus	Bright	Dark	Hypermetabolism	Small focus recurrence match PET and DWI Mismatch of large area of gyral uptake and normal DWI	FDG SPECT	Patient had sudden weakness and large uptake of FDG with DWI normal –SMART syndrome
5	Primary	Diffuse midline high grade glioma with thalamic extension	Bright	Dark	Hypermetabolism	Match	FDG	DWI PET showed high grade lesion. Surveillance imaging. DWI showed free diffusion likely due to post radiotherapy resolution.
6	Primary tumor	Pontine glioma	Center bright	Dark	Hypermetabolism	Match	FDG	
7	Recurrence	Case of Melanotic schwannoma with multiple intracranial and spinal dural deposits and also in the right pinna and left orbit.	iso	iso	Hypermetabolism	DWI is masked due to presence of susceptibility foci	FDG	In syndromes NF differentiating tumor undergoing high grade transformation is crucial possible with Whole body DWI imaging
8	Recurrence with metastasis in brain.	External auditory canal squamous cell carcinoma.	Bright	Dark	Hypermetabolism	Match	FDG	Near homogenous enhancement with intracranial extension to temporal lobe
9	Primary tumor	Lymphoma right external capsule	Bright	Dark	Hypermetabolism	Match	FDG	Remote hyper metabolism in bilateral frontal lobes mimicking multifocal lymphoma with no lesion noted on MRI.
10	Recurrence	k/c/o diffuse astrocytoma grade ii/iv	Bright	Dark	Hypermetabolism	Match	C11 METHIONINE	
11	Primary tumor	Low grade glioma oligodendroglioma	Subtle bright	Subtle dark	Subtle hyper metabolism	Match	C11 METHIONINE	
12	Post operative follow up scan.	No recurrence of glioma	iso	iso	Hypometabolism	Match	C11 METHIONINE	
13	Primary tumor	Gliosarcoma IDH wild type, who grade-iv-right parietal.	Bright	Dark	Hypermetabolism	Match	C 11 METHIONINE	
14	Pre surgical work up	Meningioma incidentally detected.	iso	iso	Hypermetabolism	Mismatch	C 11 METHIONINE	Methionine is taken up by low grade benign tumor such as meningioma. DWI appearance based on cellularity
15	Primary tumor	Diffuse midline glioma H3k27m mutant; who grade iv; left ventricle and thalamus	Bright	Dark	Hyper etabolism	Match	C11 METHIONINE	
16	Recurrence	Atypical teratoid rhabdoid tumor, who grade-iv, suprasellar.	Bright	Dark	Hypermetabolism	Match	C 11 METHIONINE	
17	Recurrence	Craniopharyngioma	iso	iso	Hypermetabolism	Mismatch	C 11 METHIONINE	Low grade tumors such as craniopharyngioma show c11 methionine uptake
18	Recurrence	Recurrence GBM	Bright	Dark	Hypermetabolism	Match	F18 CHOLINE	
19	GBM	GBM	Match	Match	Hypermetabolism	Match	F18 CHOLINE	
20	Primary tumor	Right parietal anaplastic clear cell Ependymoma. False negative PET is reported in clear cell variant of Ependymoma.	Bright	Dark	Hypometabolism	Mismatch	F 18 CHOLINE	Variable behavior on F18 choline PET is reported in clear cell variant

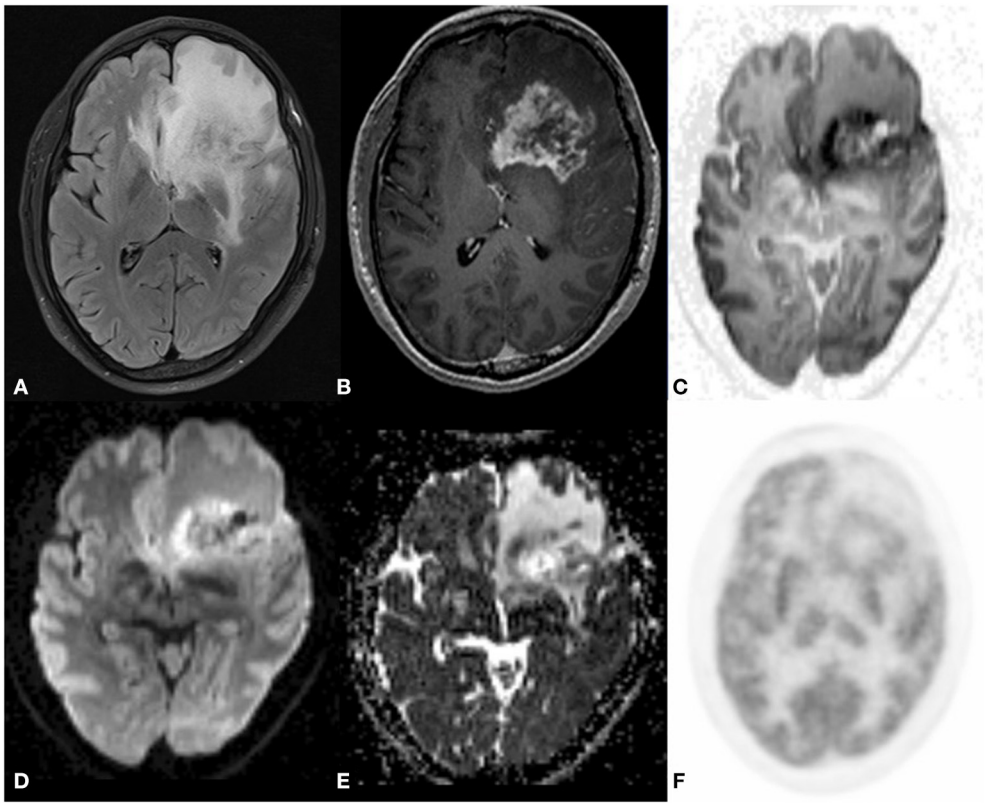

FIGURE 1 | A 43 year old male postoperative case of Glioblastoma IDH mutant in the left frontal lobe, 5 year follow up MRI FDG PET axial images T2-FLAIR **(A)** post-contrast T1 **(B)** Inverted DWI **(C)** DWI b2000 **(D)** ADC **(E)** NAC PET **(F)** showed a T2 heterogeneous hypointense lesion with Swiss cheese and nodular enhancement and elevated perfusion. The lesion shows DWI restriction with hypermetabolism on PET. There is a match on the inverted DWI image and the NAC PET image. Suggestive of recurrence.

were compared, very similar imaging findings were noted among both modalities concerning recurrence and the radiation necrosis group complementing each other.

On comparing PET -DWI for tumor volume, overestimation or underestimation of tumor volume was noted as compared to structural imaging. Since the intensity of PET is based on the uptake, tumors with high SUV can have a spillover effect with overestimation of tumor volumes in three cases and tumors with low SUV and below an absolute standard can appear smaller as noted in one case as compared to the DWI image. DWI is based on cellularity and FDG on metabolic uptake and hence this disparity in volume (1). In MRI of CNS tumors with the heterogeneous landscape, noting the volume of the tumor, cellularity on DWI, and ADC and SUV uptake measurements are important for prognosis and treatment response, which again highlights the need for multiparametric imaging.

On CEMRI, recurrence post-radiotherapy was considered when there was a nodular enhancement in the background of the Swiss cheese pattern of enhancement. On the correlation between DWI, PET, and CEMRI, false-positive recurrence was noted in two cases CEMRI but DWI and PET were suggestive of necrosis. Similarly, four cases showed false negative for recurrence on CE MRI when compared with DWI -PET.

PWI data was available in 22 cases. On post-processing ROI was placed on the enhancing portion on CEMRI.14 cases showed elevated perfusion values consistent with recurrence and the remaining eight cases did not show any elevated perfusion that was suggestive of necrosis. When the correlation between DWI, PET, and PWI was done, recurrence was missed in 4 cases i.e., false negative on PWI. This pitfall might be due to wrong ROI placement based on the standard enhancing portion on CEMRI rather than planning on either DWI or PET. Non-enhancing recurrence foci can be missed by using CEMRI if used as criteria to identify tumor foci (2).

There was a case of pseudoprogression correctly identified by DWI and FDG PET helping in differentiating thick nodular enhancement in that case is due to radiation necrosis with no recurrence. Though CEMRI and PWI techniques showed thick nodular enhancement with no abnormal perfusion.

In two cases simultaneous ASL was performed as part of the protocol. ASL, DWI, and PET volumes matched in both cases, and ASL which is a perfusion marker has good potential in tumor imaging. ASL is known to differentiate oligodendroglioma from astrocytoma irrespective of tumor grade and enhancement pattern and may aid in the pathological molecular typing of gliomas (3).

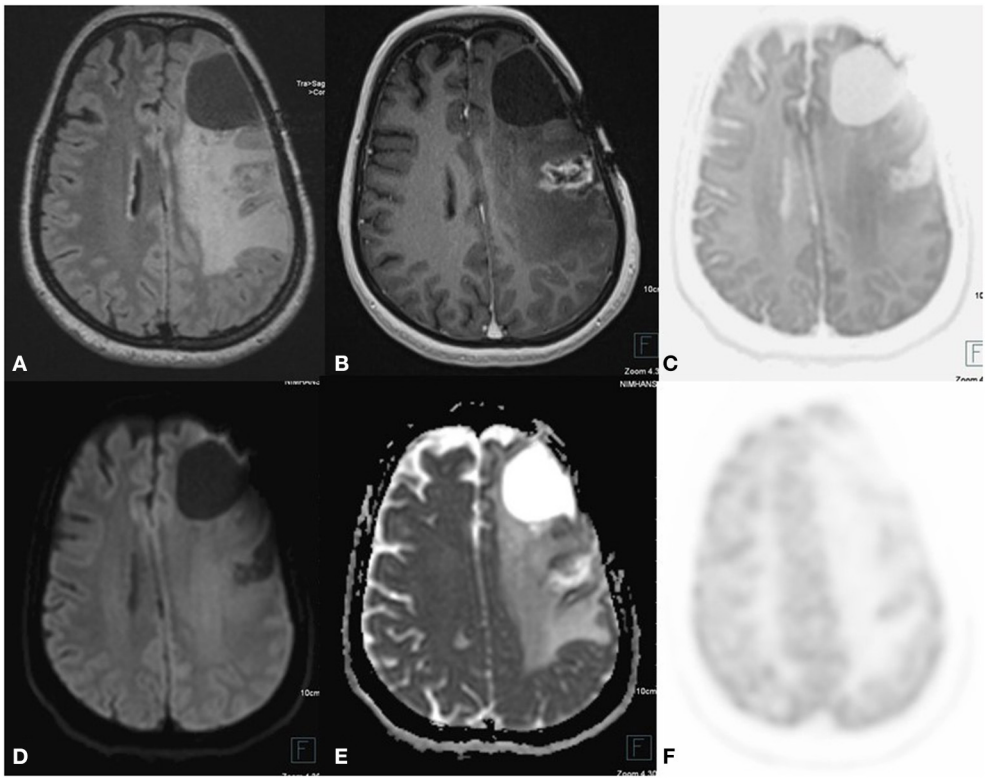

FIGURE 2 | A 24 year old female postoperative, post-RT case of Glioma left frontal lobe, 3 year follow up MRI FDG PET axial images T2-FLAIR **(A)** post-contrast T1 **(B)** Inverted DWI **(C)** DWI b2000 **(D)** ADC **(E)** NAC PET **(F)** show a postoperative cavity in the left frontal lobe with Swiss cheese-like enhancing lesion posterior to postoperative either no elevated perfusion. Neither DWI restriction nor elevated metabolism on PET is seen, which is suggestive of radiation necrosis.

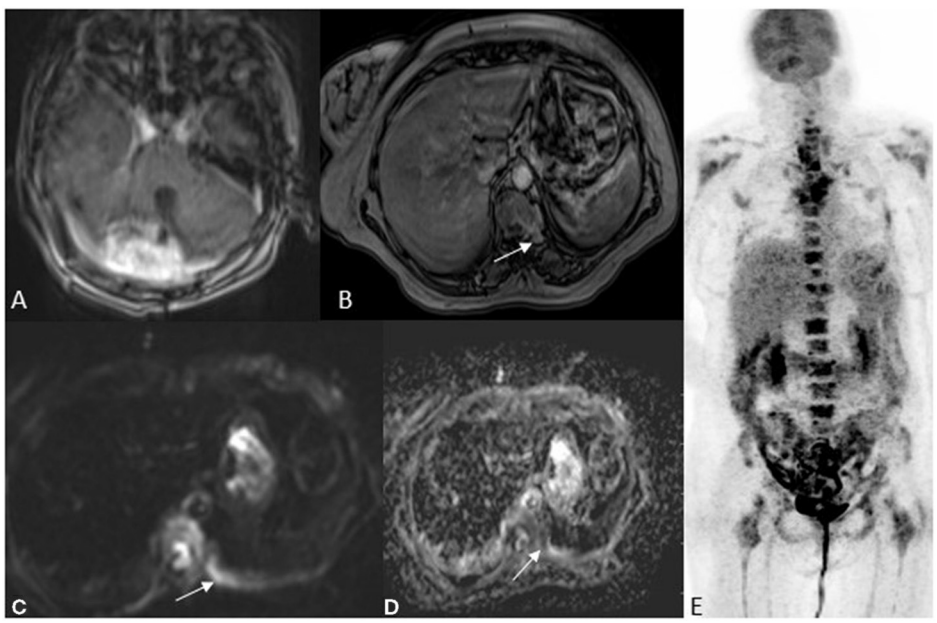

FIGURE 3 | A 52 year old female with imbalance, MRI FDG PET axial brain images T1 post-contrast **(A)** image showed an enhancing lesion in the right cerebellum. Whole-body MRI with fast sequences at axial hepatic sections **(B)** VIBE fat sat post-contrast **(C)** DWI b800 **(D)** ADC and NAC PET **(E)** showing an area of metastases to the vertebral body as an area of restricted diffusion and post-contrast enhancement. HPE was suggestive of Pilocytic astrocytoma with metastasis.

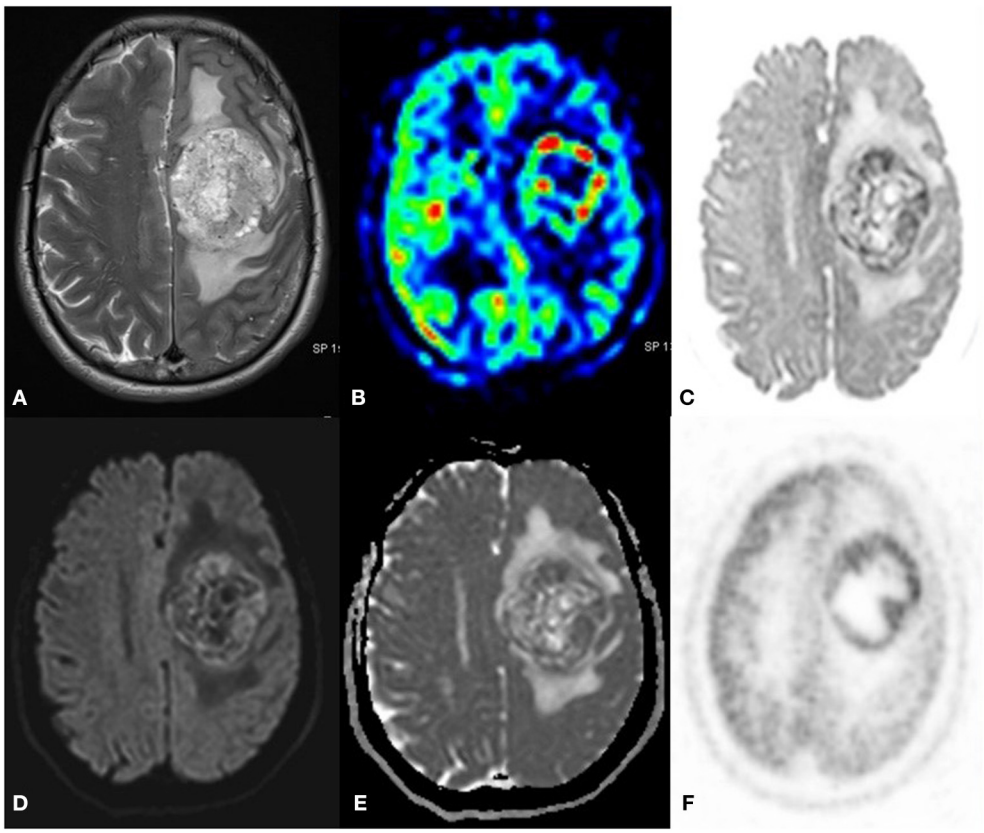

FIGURE 4 | A 55 year old male with a progressive right-side weakness for one and a half month, MRI FDG PET axial images T2 **(A)** ASL **(B)** Inverted DWI **(C)** DWI b2000 **(D)** ADC **(E)** NAC PET **(F)** showed a well-defined lobulated T2 heterogeneous iso- hyperintense with increased perfusion on ASL. The lesion shows DWI restriction with hypermetabolism on PET. There is a match on the inverted DWI image and the NAC PET image. HPE is suggestive of Anaplastic Ependymoma.

Pilocytic astrocytoma with metastases is very rare. There was a histopathologically proven case and MR/PET corroborated this, proving metastatic spread. Whole-body DWI correlated well with FDG PET (**Figure 3**) (case 21).

There was a case of multiple intracranial lesions referred to as metastases. A whole-body MRI PET revealed it as a primary CNS tumor with metastases and both PET and DWI matched in the diagnosis (case 22).

MRPET in Other CNS Tumor Histotypes

Cases denote serial numbers in **Table 2**. We had a case of anaplastic Ependymoma (**Figure 4**), DWI, and FDG PET correlated well to confirm recurrence and rule out radiation necrosis though contrast enhancement patterns that appeared like radiation necrosis (Case 1).

There were 2 MR/PET cases of brain stem lesions diagnosed as demyelination on MR/PET and lymphoma in another, which on histopathology turned out to be T cell lymphoma and demyelination, respectively (Case 2, 3).

In another case, there was a large area of uptake on FDG mimicking recurrence but DWI, which showed only a small focus of restriction and due to DWI and FDG PET mismatch. PET with other tracers was done and DWI correlated well with F18 choline helped in planning the biopsy site. The patient had a sudden onset of transient weakness before FDG was injected and hence was diagnosed with SMART syndrome (stroke-like migraine attacks after radiation therapy) (case 4) (**Figure 5**).

There was a case of midline glioma H3K27 mutant, with extension into the thalamus and cerebellar peduncles DWI and FDG PET correlated well, post-radiotherapy follow up, DWI showed free diffusion suggesting resolution of the lesion (Case 5).

Another case with MRI T1 hyperintensity and CT hyperattenuating lesion in the right cerebellum and brachium pontis, suggested melanoma and it proved to be melanotic schwannoma. MR PET whole body was asked to rule out metastatic spread or any syndromic association (NF syndrome) before planning excision. There was no diffusion restriction. The enhancement pattern was confounded by the precontrast T1 hyperintensity. The FDG pet showed uptake as expected in schwannomas.

Whole-body MRI PET confirmed the SOL to be primary with no associated syndrome or metastatic spread, as the primary or secondary status could not be commented on histopathology. PET behavior was similar to any schwannoma and showed

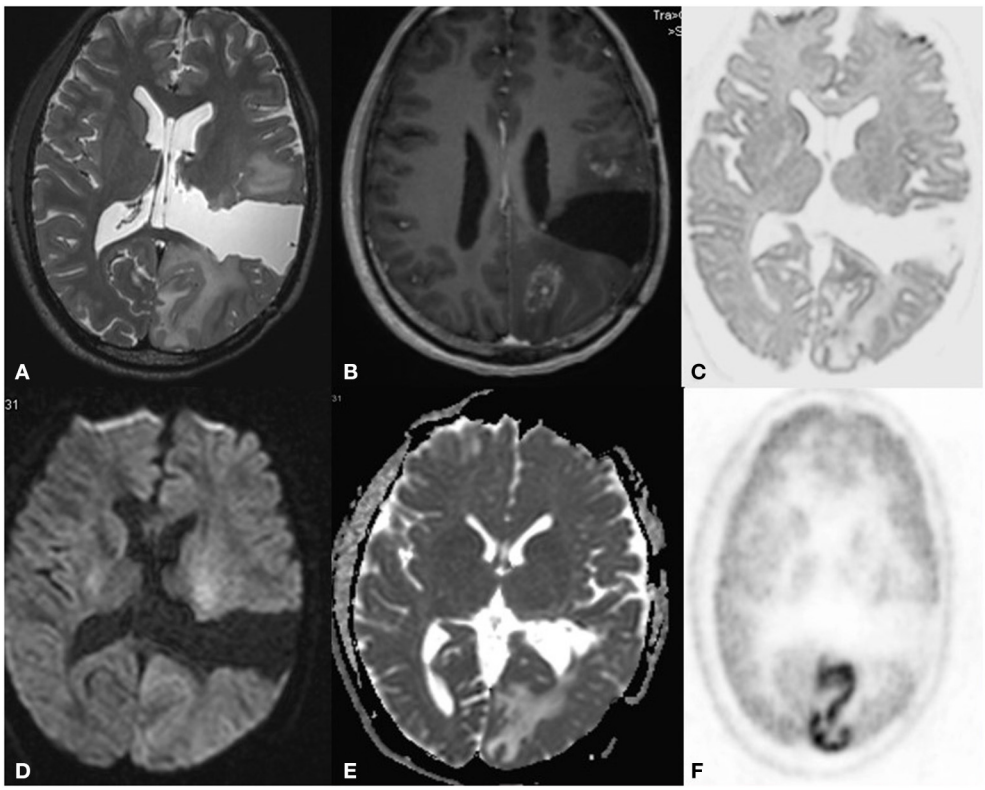

FIGURE 5 | A 32 year old male postoperative, post-radiotherapy case of Anaplastic mixed oligoastrocytoma left thalamus, 3 year follow up MRI FDG PET axial images T2W **(A)** post-contrast T1 **(B)** Inverted DWI **(C)** DWI b2000 **(D)** ADC **(E)** NAC PET **(F)** show a postoperative cavity in the left parietal region. Anterior and posterior to this there is a heterogeneously enhancing lesion with elevated perfusion. The lesion shows DWI restriction with hypermetabolism on PET. This is suggestive of recurrence, but there is a large area of gyral enhancement due to SMART Syndrome. There is a false positive uptake on PET.

uptake. The T1 image identified it as a melanotic variant and DWI labeled it as low grade (case 7). This case highlights the importance of multimodality and whole-body imaging.

There was a case of lymphoma in the right external capsule, DWI- FDG correlated well, but there was remote hypermetabolism in bilateral frontal lobes mimicking multifocal lymphoma with no lesion noted on MRI (Case 9).

Our Experience With Other Tracers

Tracers like F18 /C11 choline, C11 methionine, and Ammonia (NH3) PET were assessed.

DWI correlated well with FDG tracers like C11 methionine in cases of glioblastoma (Case 10–13) and F18 choline (Case 18–19) (**Figure 6**).

Methionine had better specific uptake in small foci of recurrence as compared to DWI, especially in low-grade glioma (Case 10).

There was a case of recurrence of glioma with an incidental meningioma (**Figure 7**), both recurrence and meningioma were picked by C11 methionine PET but DWI helped to differentiate the two. This case of meningioma showed no DWI restriction and had post-contrast brilliant enhancement. PET showed false-positive uptake irrespective of the grade of the tumor (Case 14).

There were cases of midline glioma in which both C11methionine PET and DWI correlated well. However, the intensity of uptake was more in methionine than DWI (Case 15).

Similar findings were noted in high-grade glioma recurrence in which DWI and methionine uptake was restricted to the tumor area, unlike FDG which has another non-specific uptake in the cortex, like in the case of SMART syndrome.

In the case of the recurrent atypical teratoid rhabdoid tumor (**Figure 8**), DWI and C11methionine PET correlated well to confirm recurrence (Case 16). In another case of recurrent craniopharyngioma, DWI showed no restriction but uptake is seen in C11 methionine PET (Case 17).

We had the case of a clear cell variant of Ependymoma (**Figure 9**), evaluated with MR F18 choline PET. MRI DWI showed small foci of recurrence in the background of radiation necrosis. PET showed faint to no uptake as it was a clear cell variant and F18 choline has variable behavior in this subtype (4) (Case 20).

In all cases where there was DWI and PET, the correlation grayscale inverted b2000 image corresponded with the NAC image of PET, which has the potential to be an excellent biomarker in neuro-oncology workup.

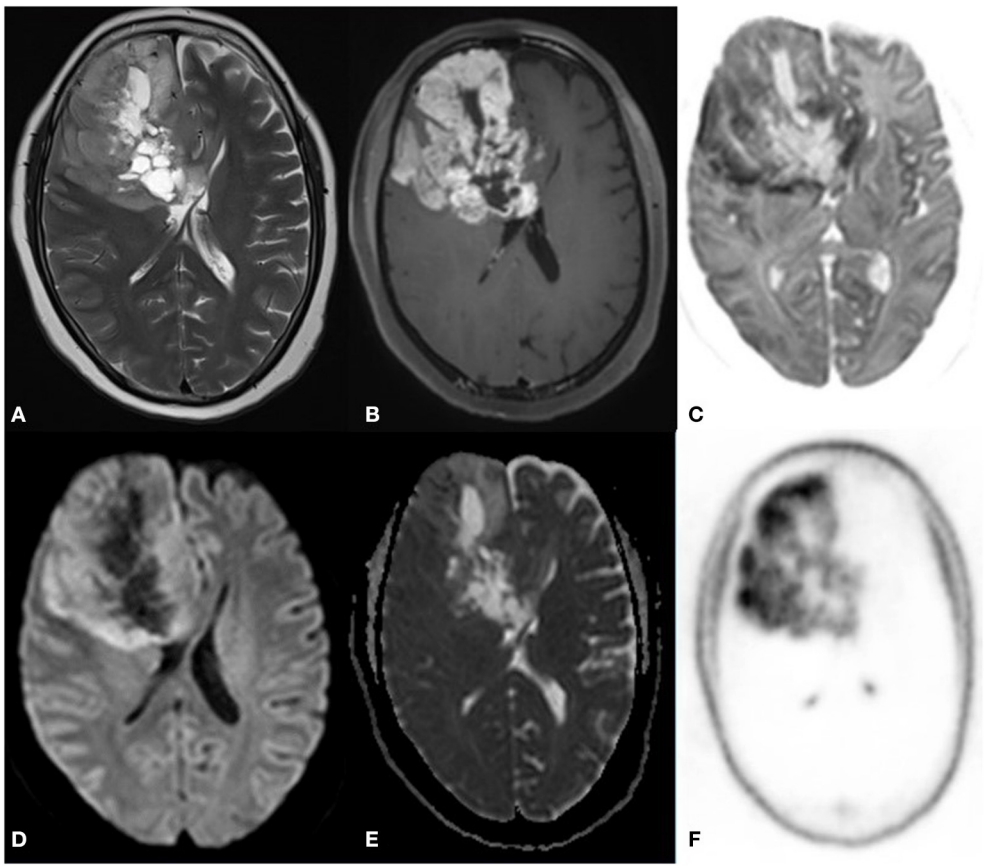

FIGURE 6 | A 52 year old female with a headache for 1 year with recent onset of a seizure. MRI PET (F18 CHOLINE) axial images T2W **(A)** post-contrast TW **(B)** Inverted DWI **(C)** DWI b2000 **(D)** ADC **(E)** NAC PET **(F)** shows Ill-defined infiltrative heterogeneous lesion in the right frontal lobe with invasion to corpus callosum showing intense heterogeneous enhancement. The lesion shows DWI restriction with hypermetabolism on PET. There is a match on the inverted DWI image and the NAC PET image, which is suggestive of Glioblastoma.

Discussion

This study evaluated the simultaneous acquisition of MR-DWI and PET data in the patients with suspected ICSOL, mainly focusing on gliomas and also other histotypes.

In lesion based sensitivity, the specificity of DWI was comparable with those of PET and in agreement with earlier published studies (5, 6).

In our study, we used the trace image as it nullifies T2 shine-through the effects of gliosis, and vasogenic edema, which is commonly associated with the tumor and postoperative and post-radiotherapy cases, and only tissue with increased cellularity is seen as bright on the trace image. A high b value (b2000) was generated to further decrease the background of the T2 effects and increase the contrast noise ratio. Synthetic high b value generation helps save time on the scanner and gives similar images, allowing retrospective analysis. We inverted this b2000 trace image to make it look like a PET AC corrected image. The ADC image does not have a good PET-like appearance and background parenchyma suppression is suboptimal to pick small foci.

This DWI-PET study suggests that DWI can be planned as a surrogate marker and saves time, which helps in surveillance imaging. Both DWI and PET have a resolution of 3–4 mm thick sections. In the case of tumor, DWI highlights cellularity and is immune from blood-brain barrier dysfunction and helpful in differentiating recurrence from enhancing radiation necrosis and in diagnosing non-enhancing recurrence (7). PWI and MRS have a good correlation but, since it is ROI-based, if the location of placement is wrong it can be misleading.

DWI and PET have a good one-on-one correlation (8). A combined DWI -PET increases true positive by nullifying the false positive and negative of both MRI and PET such as bleed, air/bone, the parenchyma interface artifacts of DWI, and the non-specific uptake of FDG (9).

Glioma is graded as 1–4 based on the cellularity/mitotic index. FDG PET has low sensitivity for grades 1 and 2, which is very similar to DWI (11). Excellent correlation was noted with FDG and DWI for tumor margin delineation in the background of radiation necrosis as compared to other MRI parameters (11). Tracers such as methionine and choline are better for

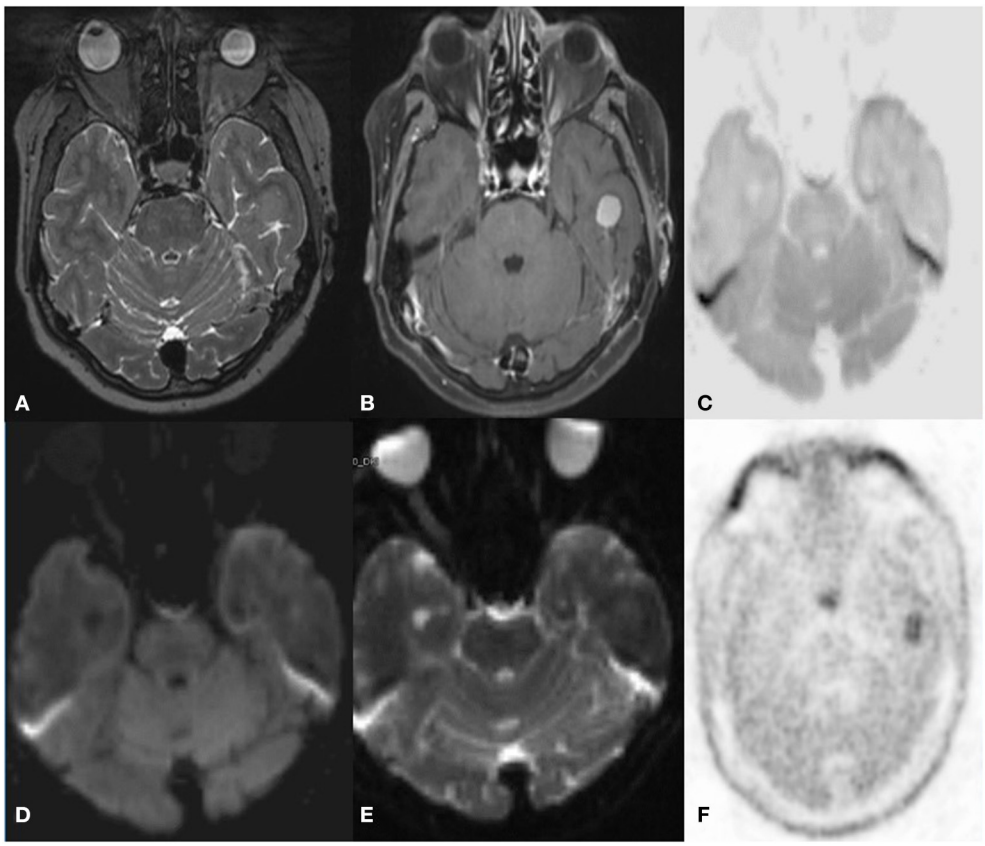

FIGURE 7 | A 59 year old female with Glioma, incidentally detected a lesion in follow up MRI C-11 Methionine PET axial images T2W **(A)** post-contrast T1 **(B)** Inverted DWI **(C)** DWI b2000 **(D)** ADC **(E)** NAC PET **(F)** shows a broad-based T2 hypointense intensely enhancing in the left inferior temporal convexity. The lesion shows no DWI restriction with hypermetabolism on PET. S/O meningioma. False-positive uptake of meningioma by methionine.

low-grade tumors and recurrence of the low-grade tumor as compared to DWI–FDG PET in combination with conventional MRI for characterizing the lesion further into a meningioma or a glioma etc.

The intensity of uptake and DWI grayscale matches with FDG but not with other tracers. Tumor volume was better delineated with DWI and methionine as compared to FDG and GHA wherein lesions with increased SUV often had exaggerated volumes and a spill-over effect. The FDG intensity reflects the metabolic behavior and can help plan the intensity of radiotherapy and prognosticate whereas MRI can help define borders (12).

This paper highlights the role of a high b value DWI weighted image trace image with grayscale inversion, which is excellent for achieving a PET-like image. Since a close correlation between DWI and FDG has been established, developing high b value DWI as a biomarker can help in treatment response assessment in close intervals without risk of contrast, radiation, and cost.

Our experience of DWI–PET with other histotypes of brain tumor and tracers highlighted the need to know false positive and negative rates associated with FDG and other tracers and interpret PET along with MRI parameters (13) such as DWI, ASL, PWI, MRS, SWI and CEMRI for further characterization and diagnosis. False-positive uptake in meningioma (9) was noted with free diffusion and brilliant enhancement. This type of MR correlation is very important in syndromes such as Neurofibromatosis wherein both glioma and meningioma can coexist and identify malignant transformation. Similarly, brain tuberculoma can show raised FDG uptake and can mimic tumors with high SUV (14) but MRI DWI can show free diffusion and aids in differentiating them (15).

Simultaneous MR/PET of the brain and whole body helps confirm whether a lesion is a primary CNS lesion rather than metastases/systemic lymphoma. Overall hybrid imaging has many advantages such as increasing the diagnostic accuracy to demarcate viable tumor margin, planning therapy, and patient management and treatment response (16). Knowledge of the advantages and pitfalls of each modality is required. CT MRI provides excellent cross-sectional imaging with MRI having a resolution of up to 1 mm as compared to PET, which has a resolution of 4 mm. Structural MRI has excellent spatial resolution and is well-suited to differentiate tumors from edema, hemorrhage other features such as raised ICP. Advanced MRI

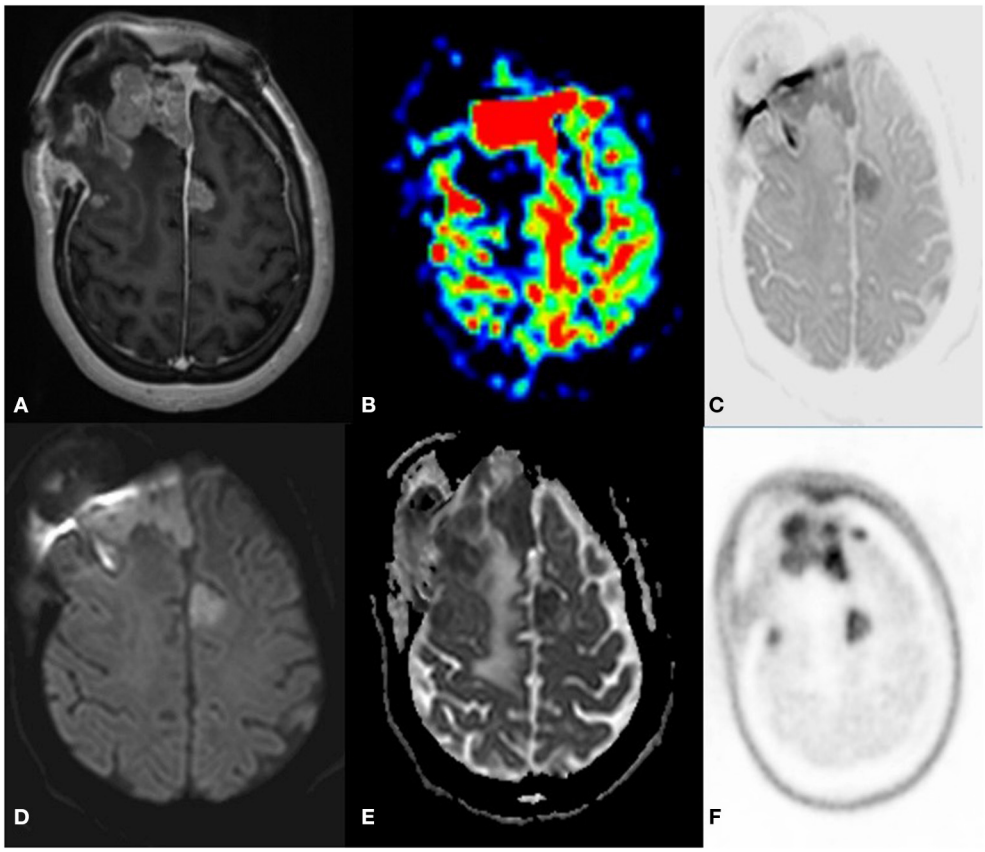

FIGURE 8 | A 33 year old female postoperative, post-radiotherapy case of Embryonal tumor compatible (atypical teratoid rhabdoid tumor) 1 year follow up MRI C-11 Methionine PET axial images post-contrast T1 **(A)** ASL **(B)** Inverted DWI **(C)** DWI b2000 **(D)** ADC **(E)** NAC PET **(F)** showed Multiple enhancing dural based lesions are seen in bilateral frontal convexity and anterior falx with elevated perfusion. The lesion shows DWI restriction with hypermetabolism on PET. There is a match on the inverted DWI image and the NAC PET image, which is suggestive of recurrence.

such as ASL, DWI, PWI, SWI, and MRS also provide blood flow cellularity and metabolic information (10).

PET tracers give information on subcellular processes based on the radiopharmaceutical used such as glucose/amino acid metabolism and so on. Though tumor biology is associated with tracers to map increased glucose consumption, increased expression of amino acid transporters, increased proliferation rate, increased membrane biosynthesis, increased perfusion, and hypoxia are available and a commonly used tracer is glucose consumption imaging. FDG reflects increased tumor glucose metabolism, glycolysis via the GLUT receptors, and apoptosis rate /mitotic index in tumors. Some low-grade tumors with increased expression of GLUT receptors such as pilocytic astrocytoma and neuroma etc. can show high uptake of FDG. In these cases, MRI DWI can help differentiate benign tumors from high-grade lesions (17).

Amino acid PET imaging such as ammonia, methionine, FET, FLT, FDOPA deals with part of tumor biology related to histopathology with the Ki-67 index, proliferating cell nuclear antigen, and microvessel density (18).

A knowledge of biological distribution of different tracers in brain is required before interpretation for example ammonia is transported by process of diffusion and others are carrier mediated and dependent on BBB damage. Areas which lack BBB such as choroid plexus and pituitary gland can show uptake (F-thymidine and F choline) (19). Choice of tracers for brain tumor in these location should be planned accordingly. FLT may have lower specificity for low grade tumors as compared to methionine PET.

Methionine has a better background suppression as compared to choline and thymidine and is preferred in tumor imaging. Normal distribution of this tracer should be known and non tumor conditions such as demyelination or abscess can also show methionine uptake (20).

F DOPA is another tracer but can be taken up by other sol such as meningioma etc. Overall since FDG, methionine and FDOPA uptake is affected by body metabolism and knowledge of patient preparation is required such as controlled sugars, seizure free, low protein diet, off dopaminergic drugs for the above tracers (21).

In our series we don't have experience with FET, FLT or FDOPA for tumour and its correlation with DWI or MRPWI.

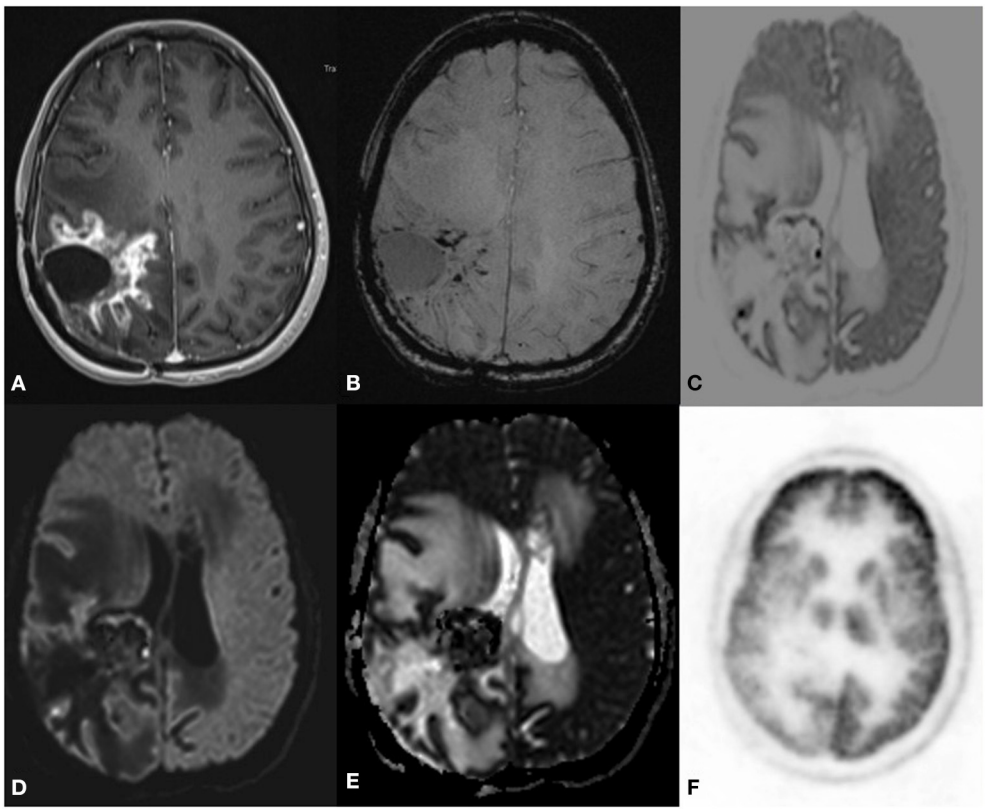

FIGURE 9 | A 34 year old female postoperative case of anaplastic clear cell Ependymoma, 7 year follow up MRI F-18 choline PET axial images SWI **(B)** postcontrast T1 **(A)** Inverted DWI **(C)** DWI b2000 **(D)** ADC **(E)** NAC PET **(F)** showed a Swiss cheese and nodular enhancement lesion in the right parietal region. The lesion shows DWI restriction with hypermetabolism on PET. There is a match on the inverted DWI image and the NAC PET image, which is suggestive of recurrence.

Hypoxia imaging with FMISO helps demarcate tumor margins and angiogenesis. Perfusion imaging with radio water reflects angiogenesis that correlates with VEGF and antigen ki6 on histopathology which make tumor more aggressive and resistant to radiotherapy (22). Molecular imaging with hybrid technology expands the scope of tracers and imaging *in vivo*. Newer chemistry derivatives can be used either with Gadolinium particles, Nano particles for MRI or radiotracers for PET or fluorescein for optical imaging. It is an exciting field for *in vivo* imaging (16).

This paper has some limitations. First, the limited sample size and study design involved visual interpretation rather than voxel-wise correlation by fusing DWI and PET images because of quick analysis, reproducibility, and non-time consumption. Rather than highlighting the differences between DWI and PET, this paper says that both are complementary. The difference between the image and the representative histopathological specimen limited the proof of concept.

The preliminary results of this study need to be confirmed in a larger patient population. Further studies are planned to extend parameter inclusion and quantification. The main strength of this paper is that this study involves a broader spectrum of CNS ICSOL imaged with multiple types of PET tracers and all cases have been followed up to establish the diagnosis.

CONCLUSION

The role of imaging is not about characterizing the lesion but trying to extract virtual histopathology-like features *in vivo* and, additionally, keep pace with newer modes of tumor treatment regimens that target different pathways of a tumor. This approach has led to the development of multimodality advanced hybrid imaging. Although DWI and FDG-PET reflect different tissue properties, there may very well be an association between the measures of both methods, most probably because of increased cellularity and the glucose metabolism of FDG-avid CNS lesions. Presently PET is an adjunct to MRI in neurooncology. DWI helps pick the lesion, calculate tumor volume, and predict appropriate early post-treatment tumor response. MRI is a good tool when multi-time point imaging is required for the diagnosis of a tumor, for planning therapy, post-treatment response, and further surveillance. DWI acts as a surrogate to FDG PET and has promising potentials for clinical translation.

DATA AVAILABILITY STATEMENT

The original contributions presented in the study are included in the article/supplementary material, further inquiries can be directed to the corresponding author/s.

ETHICS STATEMENT

The studies involving human participants were reviewed and approved by Ethics Committee Board, NIMHANS. Written informed consent for participation was not required for this study in accordance with the national legislation and the institutional requirements.

AUTHOR CONTRIBUTIONS

SM contributed to the original concept, image analysis, the manuscript draft, and clinical MRI reporting. SV and SJ undertook data collection and manuscript drafting. AK contributed to manuscript overview and inputs. PK contributed for production of PET tracers at the institute cyclotron. All authors contributed to the article and approved the submitted version.

ACKNOWLEDGMENTS

We extend thanks to the team working at MR/PET center NIMHANS.

REFERENCES

1. Im HJ, Bradshaw T, Solaiyappan M, Cho SY. Current methods to define metabolic tumour volume in positron emission tomography: which one is better? *Nucl Med Mol Imaging.* (2018) 52:5–15. doi: 10.1007/s13139-017-0493-6
2. Eichberg DG, Di L, Morell AA, Shah AH, Semonche AM, Chin CN, et al. Incidence of high grade gliomas presenting as radiographically non-enhancing lesions: experience in 111 surgically treated non-enhancing gliomas with tissue diagnosis. *J Neurooncol.* (2020) 147:671–9. doi: 10.1007/s11060-020-03474-z
3. Wang N, Xie S, Liu H, Chen G, Zhang W. Arterial spin labeling for glioma grade discrimination: correlations with IDH1 genotype and 1p/19q status. *Transl Oncol.* (2019) 12:749. doi: 10.1016/j.tranon.2019.02.013
4. Chang JM, Lee HJ, Goo JM, Lee H-Y, Lee JJ, Chung J-K, et al. False positive and false negative FDG-PET scans in various thoracic diseases. *Korean J Radiol.* (2006) 7:57. doi: 10.3348/kjr.2006.7.1.57
5. Stopa BM, Juhász C, Mittal S. Comparison of amino acid PET to advanced and emerging MRI techniques for neurooncology imaging: a systematic review of the recent studies. *Mol Imaging.* (2021) 2021:e8874078. doi: 10.1155/2021/8874078
6. Suzawa N, Maeda M, Matsushima N, Murashima S, Kobayashi S, Takeda K. Relationship between FDG uptake and apparent diffusion coefficients in solitary brain tumours: preliminary experience. *J Nucl Med.* (2009) 50:1234. doi: 10.1016/s1052-5149(02)00033-3
7. Valentini MC, Mellai M, Annovazzi L, Melcarne A, Denysenko T, Cassoni P, et al. Comparison among conventional and advanced MRI, 18F-FDG PET/CT, phenotype and genotype in glioblastoma. *Oncotarget.* (2017) 8:91636. doi: 10.18632/oncotarget.21482
8. Ishii S, Miyajima M, Nambu T, Watanabe H, Hakozaki M, Suenaga H, et al. Comparison of diagnostic performance between whole-body MRI with DWI and PET/MRI. *J Nucl Med.* (2018) 59:1372.
9. Valotassiou V, Leondi A, Angelidis G, Psimadas D, Georgoulias P. SPECT and PET imaging of meningiomas. *Sci World J.* (2012) 2012:412580. doi: 10.1100/2012/412580
10. Kao H-W, Chiang S-W, Chung H-W, Tsai FY, Chen C-Y. Advanced MR imaging of gliomas: an update. *BioMed Res Int.* (2013) 213:970586. doi: 10.1155/2013/970586
11. Marner L, Henriksen OM, Lundemann M, Larsen VA, Law I. Clinical PET/MRI in neurooncology: opportunities and challenges from a single-institution perspective. *Clin Transl Imaging.* (2017) 5:135. doi: 10.1007/s40336-016-0213-8
12. Moreau A, Febvey O, Mognetti T, Frappaz D, Kryza D. Contribution of different positron emission tomography tracers in glioma management: focus on glioblastoma. *Front Oncol.* (2019) 9:1134. doi: 10.3389/fonc.2019.01134
13. Fink JR, Muzi M, Peck M, Krohn KA. Multimodality brain tumour imaging: MR imaging, PET, and PET/MR imaging. *J Nucl Med.* (2015) 56:1554–61. doi: 10.2967/jnumed.113.131516
14. Hutomo F, Yudistiro R, Mulyanto ID, Budiawan H. False positive finding from malignancy-like lesions on FDG PET/CT: case report of tuberculosis patients. *BMC Med Imaging.* (2020) 20:26. doi: 10.1186/s12880-020-00427-w
15. Peng J, Ouyang Y, Fang WD, Luo TY, Li YM, Lv FJ, et al. Differentiation of intracranial tuberculomas and high grade gliomas using proton MR spectroscopy and diffusion MR imaging. *Eur J Radiol.* (2012) 81:4057–63. doi: 10.1016/j.ejrad.2012.06.005
16. Cal-Gonzalez J, Rausch I, Shiyam Sundar LK, Lassen ML, Muzik O, Moser E, et al. Hybrid imaging: instrumentation and data processing. *Front Phys.* (2018) 6:47. doi: 10.3389/fphy.2018.00047
17. Rosenkrantz AB, Friedman K, Chandarana H, Melsaether A, Moy L, Ding Y-S, et al. Current status of hybrid PET/MRI in oncologic imaging. *Am J Roentgenol.* (2015) 206:162–72. doi: 10.2214/AJR.15.14968
18. Surov A, Meyer HJ, Wienke A. Associations between PET parameters and expression of Ki-67 in breast cancer. *Transl Oncol.* (2019) 12:375. doi: 10.1016/j.tranon.2018.11.005
19. Miyake K, Shinomiya A, Okada M, Hatakeyama T, Kawai N, Tamiya T. Usefulness of FDG, MET and FLT-PET studies for the management of human gliomas. *J Biomed Biotechnol.* (2012) 2012:205818. doi: 10.1155/2012/205818
20. Qi Y, Liu X, Li J, Yao H, Yuan S. Fluorine-18 labeled amino acids for tumour PET/CT imaging. *Oncotarget.* (2017) 8:60581. doi: 10.18632/oncotarget.19943
21. Jacob MJ, Pandit AG, Jora C, Mudalsha R, Sharma A, Pathak HC. Comparative study of 18 F-DOPA, 13 N-Ammonia and F18-FDG PET/CT in primary brain tumours. *Indian J Nuclear Med.* (2011) 26:139. doi: 10.4103/0972-3919.103996
22. Xu Z, Li X-F, Zou H, Sun X, Shen B. 18 F-Fluoromisonidazole in tumour hypoxia imaging. *Oncotarget.* (2017) 8:94969–79. doi: 10.18632/oncotarget.21662

Conflict of Interest: The authors declare that the research was conducted in the absence of any commercial or financial relationships that could be construed as a potential conflict of interest.

Publisher's Note: All claims expressed in this article are solely those of the authors and do not necessarily represent those of their affiliated organizations, or those of the publisher, the editors and the reviewers. Any product that may be evaluated in this article, or claim that may be made by its manufacturer, is not guaranteed or endorsed by the publisher.

frontiers in Oncology

ORIGINAL RESEARCH
published: 29 September 2021
doi: 10.3389/fonc.2021.744827

Prediction of Malignant Transformation of WHO II Astrocytoma Using Mathematical Models Incorporating Apparent Diffusion Coefficient and Contrast Enhancement

Alex Mun-Ching Wong[1,2], *Tiing Yee Siow*[2,3], *Kuo-Chen Wei*[2,4], *Pin-Yuan Chen*[2,3], *Cheng Hong Toh*[2,3*] *and Mauricio Castillo*[5]

[1] Department of Medical Imaging and Intervention, Chang Gung Memorial Hospital at Keelung, Keelong, Taiwan, [2] College of Medicine, Chang Gung University, Tao-Yuan, Taiwan, [3] Department of Medical Imaging and Intervention, Chang Gung Memorial Hospital at Linkou, Tao-Yuan, Taiwan, [4] Department of Neurosurgery, Chang Gung Memorial Hospital at Linkou, Taoyuan, Taiwan, [5] Department of Radiology, University of North Carolina School of Medicine, Chapel Hill, NC, United States

Using only increasing contrast enhancement as a marker of malignant transformation (MT) in gliomas has low specificity and may affect interpretation of clinical outcomes. Therefore we developed a mathematical model to predict MT of low-grade gliomas (LGGs) by considering areas of reduced apparent diffusion coefficient (ADC) with increased contrast enhancement. Patients with contrast-enhancing LGGs who had contemporaneous ADC and histopathology were retrospectively analyzed. Multiple clinical factors and imaging factors (contrast-enhancement size, whole-tumor size, and ADC) were assessed for association with MT. Patients were split into training and validation groups for the development of a predictive model using logistic regression which was assessed with receiver operating characteristic analysis. Among 132 patients, (median age 46.5 years), 106 patients (64 MT) were assigned to the training group and 26 (20 MT) to the validation group. The predictive model comprised age (P = 0.110), radiotherapy (P = 0.168), contrast-enhancement size (P = 0.015), and ADC (P < 0.001). The predictive model (area-under-the-curve [AUC] 0.87) outperformed ADC (AUC 0.85) and contrast-enhancement size (AUC 0.67). The model had an accuracy of 84% for the training group and 85% respectively for the validation group. Our model incorporating ADC and contrast-enhancement size predicted MT in contrast-enhancing LGGs.

Keywords: malignant transformation, contrast enhancement, apparent diffusion coefficient, model prediction and validation, low-grade gliomas

OPEN ACCESS

Edited by:
Sanjeev Chawla, University of Pennsylvania, United States

Reviewed by:
Ingerid Reinertsen, SINTEF, Norway
Karsten Wrede, University of Duisburg-Essen, Germany

***Correspondence:**
Cheng Hong Toh
eldomtoh@hotmail.com

Specialty section:
This article was submitted to Neuro-Oncology and Neurosurgical Oncology, a section of the journal Frontiers in Oncology

Received: *21 July 2021*
Accepted: *14 September 2021*
Published: *29 September 2021*

Citation:
Wong AM-C, Siow TY, Wei K-C, Chen P-Y, Toh CH and Castillo M (2021) Prediction of Malignant Transformation of WHO II Astrocytoma Using Mathematical Models Incorporating Apparent Diffusion Coefficient and Contrast Enhancement. Front. Oncol. 11:744827. doi: 10.3389/fonc.2021.744827

INTRODUCTION

Malignant transformation (MT) of low-grade gliomas (LGGs) is the histopathologic progression of grade II World Health Organization (WHO) tumors to WHO grade III or IV tumors. LGGs account for 14.6% of gliomas in population-based studies (1) and may remain stable clinically and by imaging for years after initial diagnosis and treatment. MRI features suggesting disease progression include enlargement of non-enhancing areas and increasing enhancement on post-gadolinium T1-weighted images. However, tumors showing these features may remain WHO grade II or undergo MT and correct diagnosis requires histopathologic confirmation. Because of potential risks and costs associated with histopathologic confirmation, increased contrast enhancement is frequently used as a surrogate marker for MT in clinical practice, research studies, and clinical trials of LGG. In the widely used Response Assessment in Neuro-Oncology criteria (2), an increase of enhancement is regarded as MT.

In a recent study, the specificity of using increased contrast enhancement to detect MT was 57%, despite a sensitivity of 92% (3). Among LGGs with increasing contrast enhancement, the percentage of tumors that remained grade II ranges from 18-37% (3, 4). Also, increasing contrast enhancement may be associated with treatment-related changes (5, 6). This limited accuracy of using increasing contrast enhancement to diagnose MT was recognized in a consensus article recently published by the Society for Neuro-Oncology and the European Association of Neuro-Oncology (7). Therefore, using increasing contrast enhancement as a marker of MT may result in overtreatment of patients whose tumors remain low-grade, errors in the results of research studies, and misinterpretation of clinical benefits of new therapies. Because of the issues associated with increasing contrast enhancement, it is crucial to search for imaging markers that can accurately diagnose MT.

Diffusion-weighted imaging (DWI) identifies high-grade gliomas by their low apparent diffusion coefficient (ADC) values (8, 9). In a study investigating multiple diffusion tensor imaging parameters, ADC showed the highest diagnostic performance in differentiating between LGGs and high-grade gliomas (9). A recent study demonstrated the utility of DWI in predicting MT of LGGs (10). Since ADC values can be heterogeneous in previously treated LGGs (11), the choice of regions for ADC measurements affects its reproducibility and accuracy in diagnosing MT. To the best of our knowledge, the role of DWI in diagnosing MT has not been investigated among LGGs with increased contrast enhancement. In our study which used histopathology as the gold standard, we aimed to develop a regression model based on clinical and imaging factors to predict MT in a group of patients with LGGs with increased contrast enhancement on follow-up MRI studies.

MATERIALS AND METHODS

Patients

This retrospective study was performed after institutional review board approval. The need to obtain patient informed consent was waived by our review board (202100387B0). Patients were selected from our brain tumor database if they met the following criteria: 1) prior pathologic diagnosis of LGG and follow-up MRI studies performed between 2004 and 2020 showing increasing contrast enhancement; 2) having undergone surgery due to increased contrast enhancement with the resected tumor being grade II, III, or IV gliomas; 3) availability of DWI, and 4) removal of tumor regions with increased contrast enhancement confirmed by follow-up MRI. Increasing contrast enhancement was defined as new enhancement in previously non-enhancing regions, new separate lesions with contrast enhancement, or at least a 25% increase in the size of enhancement in previously enhancing regions at baseline. Baseline was the first follow-up MRI study after surgery. Increased contrast enhancement was confirmed by neuroradiologists who compared the baseline MRI and the most recent MRI before the next surgery. Patients with multiple surgeries for separate events of increasing contrast enhancement were included until they experienced MT. Each instance of increasing contrast enhancement was treated independently. Histopathologic diagnosis was made by a board-certified neuropathologist according to the 2000 WHO classification of CNS tumors before 2007, the 2007 WHO classification from 2007 to 2016, and the 2016 WHO classification after 2016. We excluded patients younger than 18 years of age at initial diagnosis, those with a diagnosis of radiation necrosis, and those in whom DWI showed susceptibility artifacts that hindered interpretation.

Between 2004 and 2020, 306 patients with LGGs were regularly followed up in our institution after initial diagnosis and treatment. On follow-up MRI studies, 132 patients had 149 instances of increasing contrast enhancement leading to surgery. Seven patients with 9 instances of radiation necrosis were excluded. Eight instances of increasing contrast enhancement were excluded due to the lack of DWI studies. Removal of brain regions with increasing contrast enhancement was confirmed in 44 instances with intraoperative MRI, in 34 with postoperative MRI performed within 1 week, and in 46 with postoperative MRI performed between 2-12 weeks. Our final study population consisted of 118 patients with 132 MRI studies (48 grade II, 40 grade III, and 44 grade IV). **Figure 1** shows the patient selection process.

Clinical and Imaging Information

Patient medical records were retrospectively reviewed to collect information including sex, age, and Karnofsky Performance Scale score (KPS) at the time of increased contrast enhancement, histologic subtypes (diffuse astrocytoma, oligoastrocytoma, or oligodendroglioma), isocitrate dehydrogenase 1 (IDH1) mutation status (12), disease duration (time interval between first histopathologic diagnosis of LGG and subsequent increased contrast enhancement), adjuvant therapy received before increased contrast enhancement, post-radiation therapy duration (time interval between the end of radiation therapy and subsequent increased contrast enhancement), and tumor grades associated with increased contrast enhancement. The first follow-up MRI studies after the last operation were reviewed for the presence of baseline residual tumor.

MRI Parameters

MRI examinations were performed at 1.5 T (N = 14) or 3.0 T (N = 118). All examinations included a T2-weighted sequence, DWI, and

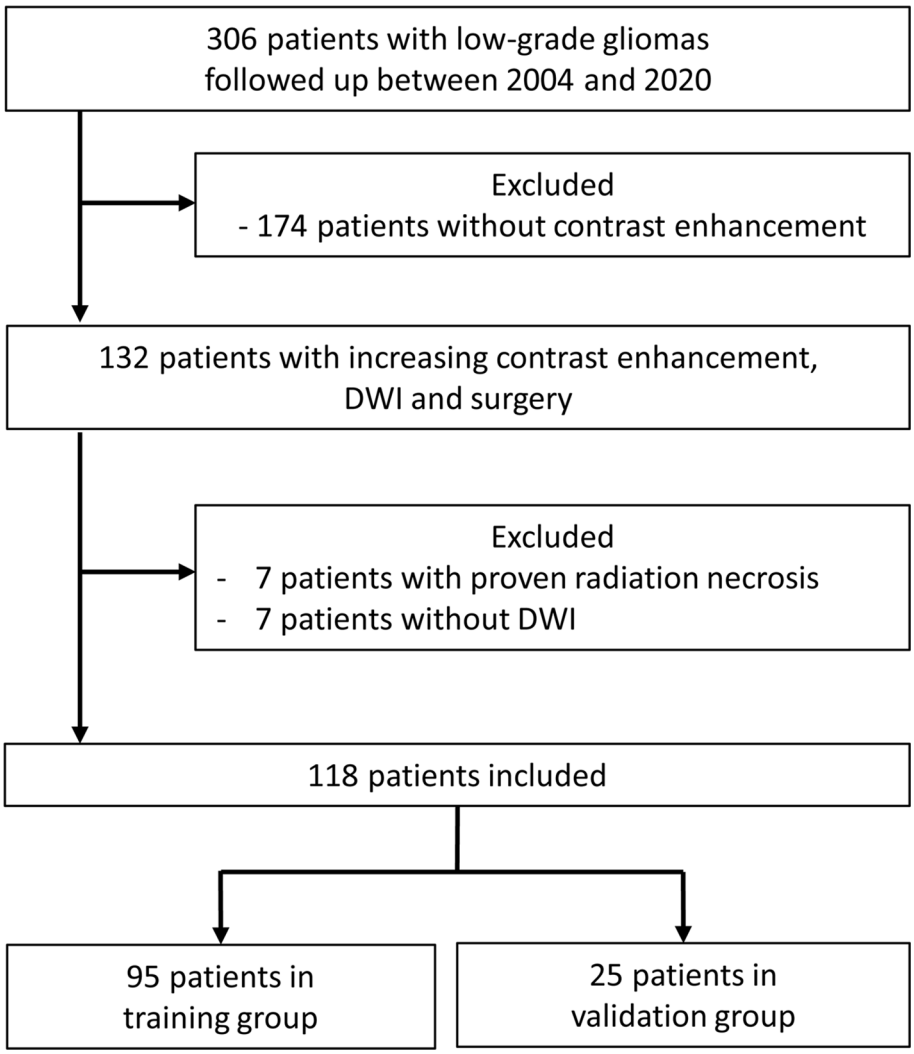

FIGURE 1 | Flowchart of patient selection process. DWI, diffusion-weighted imaging.

T1-weighted sequences acquired before and after administration of 0.1 mmol/kg body weight gadopentetate dimeglumine (Magnevist; Schering, Berlin, Germany). MRI parameters are provided in **Table 1**. Isotropic DWI and ADC maps were generated using software provided by the manufacturers.

Measurements of Tumor Size and ADC

All imaging data were transferred to an independent workstation and processed using nordicICE (nordic Image Control and Evaluation Version 2, Nordic Imaging Lab, Bergen, Norway). Co-registration of T2-weighted and post-contrast T1-weighted images to ADC maps were based on a 3D non-rigid transformation and mutual information. Adequacy of registration was visually assessed and manually adjusted. Blinded to the final pathologic results, 2 board-certified neuroradiologists with 20 and 17 years of experience independently measured contrast enhancement size, whole tumor size, and tumor ADC on all MRI studies. Post-contrast T1-weighted images in axial, coronal, and sagittal planes were used to localize increased contrast-enhancing tumor portions. These tumor portions were carefully chosen to include as much of the enhancing regions as possible and avoid the inclusion of necrosis, cysts, hemorrhage, edema, calcifications, and normal-appearing brain. Size of the contrast-enhancing regions was the product of the largest diameter of the increased contrast-enhancing portion and its perpendicular length on a single post-contrast transverse image. The size of the whole tumor, which included both enhancing and non-enhancing components, was measured on transverse T2-weighted images. If multiple lesions were present, the largest 3 were selected and their products were summed.

ADC was measured by placing a region of interest (ROI) of 30 mm^2 or larger on the tumor portion with increased contrast enhancement (**Figure 2**). The ROI was drawn to cover the largest axial tumor cross-section, after excluding necrosis, macroscopic hemorrhages, and calcifications.

TABLE 1 | MRI parameters.

Field strength	Vendor	Model	Patients	Sequence	TR (ms)	TE (ms)	TI (ms)	In-plane resolution (mm^2)	Slice thickness (mm)	Slice gap (mm)
3 T	Siemens	Magnetom Trio	87							
				T2W	4000	90		0.43 × 0.43	4	0
				Post-contrast MPRAGE	2000	2.6	900	1.0 × 1.0	1	0
				DWI	5300	93		1.15 × 1.15	4	0
3 T	Philips	Ingenia	24							
				T2W	4500	100		0.68 × 0.68	4	1
				Post-contrast T1TFE	8	3.5	950	1.0 × 1.0	1	0
				DWI	4000	60		1.78 × 1.78	4	1
3 T	GE	Discovery MR750	7							
				T2W	5400	107		0.43 × 0.43	4	1
				Post-contrast BRAVO	8.2	3.2	450	1 × 1	1	0
				DWI	6000	65		0.86 × 0.86	4	1
1.5 T	Philips	Intera	6							
				T2W	4000	90		0.41 × 0.41	5	1.5
				Post-contrast T1W	420	11		0.41 x 0.41	5	1.5
				DWI	3200	60		0.82 × 0.82	5	1.5
1.5 T	GE	Optima MR450	8							
				T2W	5300	100		0.45 × 0.45	5	2
				Post-contrast BRAVO	7.8	3.2	450	1 × 1	1	0
				DWI	6000	74		0.86 × 0.86	5	2

DWI performed using 3 diffusion gradients with b values 0 and b = 1000 s/mm^2. T2W, T2-weighted; T1W, T1-weighted; DWI, diffusion-weighted imaging; TR, repetition time; TE, echo time; TI, inversion time; MPRAGE, magnetization-prepared rapid acquisition with gradient echo; TFE, turbo field echo; BRAVO, brain volume imaging.

Morphologic Assessment

Blinded to final pathology results, 3 board-certified neuroradiologists with 6, 17, and 20 years of experience independently assessed the contrast enhancement patterns. Contrast enhancement patterns were categorized into solid (>70% area of the whole tumor on transverse image), scattered, or rim enhancing.

Statistical Analysis

Intra-class correlation coefficient (ICC) analysis, with a two-way random-effects model, was used to assess agreement between observers for measurements of ADC, whole tumor size, and contrast enhancement size. For each ROI of these measurements, the mean of the observers' measurements was adopted as the final value. Fleiss's kappa testing was used to evaluate observer agreement for contrast enhancement patterns and the majority's opinion was designated as the final pattern.

To validate our model for the prediction of MT in LGGs, patients were split into training and validation groups. According to the time of histopathologic diagnosis, instances diagnosed between 2004 and 2018 were included in the training group and those diagnosed between 2018 and 2020 in the validation group.

Data of the training group were used to develop the study model. Univariate logistic regression was applied to test if the following variables could predict MT: sex, age, KPS, histologic subtype, IDH1 mutation, disease duration, presence of baseline residual tumor, radiotherapy (RT), post-RT duration, chemotherapy, whole tumor size, contrast enhancement size, contrast enhancement pattern, and ADC. Selected variables with *P*-values < 0.10 by univariate analysis were subjected to multivariate analysis using logistic regression with a backward selection procedure. Starting from the highest *P*-value, a backward elimination process by using the Wald test was applied to discard variables that did not contribute significantly to the prediction concluding with the most parsimonious model to identify MT (13). Odds ratios and 95% CIs were calculated to demonstrate the relative risk of each significant factor for MT. Using receiver operating characteristic curve analysis, areas under the curve and cutoff values of statistically significant factors and regression models were determined. Cutoff values with the highest sensitivity and lowest false-positive rates were chosen to calculate sensitivity, specificity, and accuracy of each significant factor and model. A commercially available statistical software package (SPSS 23, IBM, Armonk, NY) was used for analysis, and *P*-values < 0.05 were considered to indicate significance.

By inputting the data of the validation group into the study model formula developed by multivariable regression, the MT probabilities for each instance of the validation group were obtained. Using a cut-off probability of 0.5, these MT probabilities were tabulated to calculate the respective sensitivity, specificity, PPV, and NPV for this group to validate the study model.

To further validate the study model developed using multivariate regression, we performed classification and regression trees method (CART) with k-fold cross validation using the 'Tree' command in the SPSS 23 software package (14, 15). All patients were randomly divided into a training set (80%) and a validation set (20%). Using data of the training set, the CART was applied to develop a model with MT as the dependent variable. The independent variables were the parameters included in the most parsimonious model generated using multivariate regression. Five-fold cross validation was performed to validate the model

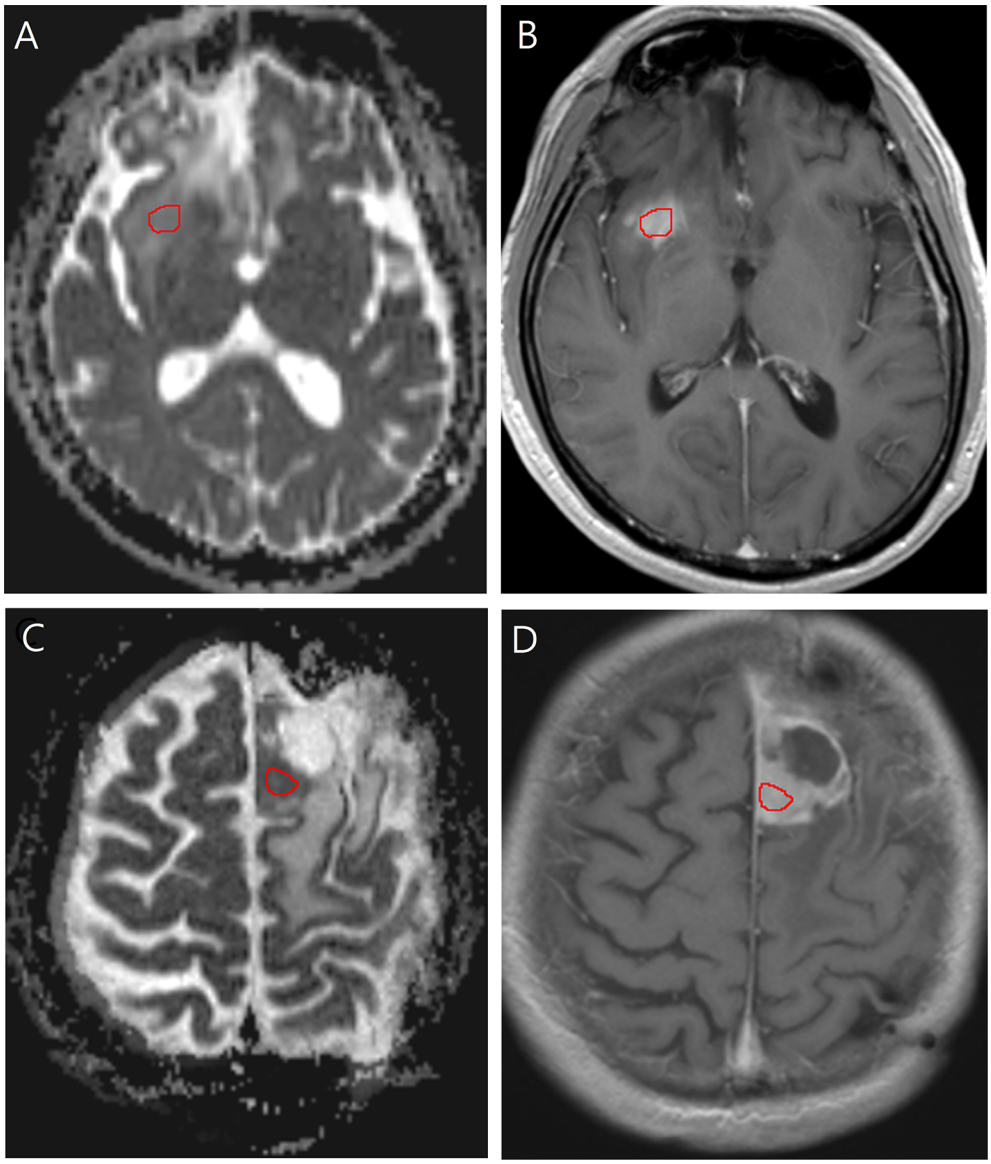

FIGURE 2 | Images in a 40-year-old man with low-grade glioma with increased contrast enhancement but preserved grade II histology. **(A)** Axial apparent diffusion coefficient, and **(B)** Axial post-contrast T1-weighted images show region-of-interest placement in the contrast-enhancing solid portion of the right frontal tumor. Images in a 58-year-old man with low-grade glioma with increased contrast enhancement and malignant transformation. **(C)** Axial apparent diffusion coefficient, and **(D)** Axial post-contrast T1-weighted images show region-of-interest placement in the contrast-enhancing solid portion of the left frontal tumor.

based on the selected parameters. This model was applied to the validation set to assess the performance of the prediction.

RESULTS

Patient Demographics

Table 2 is an overview of clinical and imaging information of 132 instances. One hundred and six instances (median age, 46 years; interquartile range, 27–65 years; 68 male patients) were included in the training group and 26 instances were included in the validation group.

Interobserver Agreement

There were excellent interobserver agreements in the measurement of contrast enhancement size (ICC = 0.958, 95% CI = 0.941–0.970, $P < 0.001$), whole tumor size (ICC = 0.935, 95% CI = 0.903–0.955, $P < 0.001$) and tumor ADC (ICC = 0.924, 95% CI = 0.891–0.947, $P < 0.001$). Interobserver agreement among the 3 readers was substantial-to-perfect for categorization of contrast enhancement

pattern (Fleiss' kappa coefficient = 0.806, 95% CI = 0.801–0.810, $P < 0.001$).

Study Model Development

Table 3 illustrates the results of univariate analysis in which previous radiotherapy ($P = 0.034$), larger whole tumor size ($P = 0.033$), larger contrast enhancement size ($P = 0.006$), and lower ADC ($P < 0.001$) were associated with MT (**Figure 3**). On ROC analysis, the discriminative power of contrast enhancement size measured with AUC was 0.67 (95% CI: 0.57, 0.78). With 3.25 cm^2 as the cutoff value, contrast enhancement size predicted MT with a sensitivity of 48/64 (75%), specificity of 22/42 (52%), and accuracy of 70/106 (66%) (**Figure 4**). The discriminative power of ADC measured with AUC was 0.85 (95% CI: 0.79, 0.93). With the cutoff value of 968.07 $\times 10^{-6}$ mm^2/seconds, using ADC predicted MT with a sensitivity of 55/64 (86%), specificity of 28/42 (67%), and accuracy of 83/106 (78%) (**Figure 4**).

Using multivariate logistic regression analysis with a backward selection procedure, the most parsimonious model for predicting MT was developed and consisted of age in years (P = 0.110), radiotherapy ($P = 0.168$), contrast enhancement size in cm^2 ($P = 0.015$), and ADC in mm^2/s ($P < 0.001$). The model formula was logit (probability) = 8.152 - 0.038*Age -0.853*Radiotherapy + 0.081*Contrast enhancement size - 0.006*ADC. On ROC analysis, the AUC of this model was 0.87 (95% CI: 0.81, 0.94) (**Figure 4**). With 0.5 as the probability cutoff value, the sensitivity, specificity, and accuracy of this model in diagnosing MT were 56/64 (88%), 33/42 (79%), and 89/106 (84%), respectively (**Table 4**).

Study Model Validation

By inputting the data of the validation group (26 instances) into the study model formula, the model correctly classified MT in 22 of 26 instances (85%), with a sensitivity of 17/20 (85%) and specificity of 5/6 (83%) (**Table 4**).

Using the CART with a 5-fold cross validation and incorporating age, radiotherapy, contrast enhancement size, and ADC as the independent variables, the model generated with the training set (106 instances) correctly classified MT in 91 of 106 instances (86%), with a sensitivity of 58/66 (88%) and specificity of 33/40 (83%) (**Table 4**). By applying this model to the validation set (26 instances), MT was correctly classified in 23 of 26 instances (88%), with a sensitivity of 16/18 (89%) and specificity of 7/8 (88%) (**Table 4**).

TABLE 2 | Clinical and imaging data of 132 instances with low-grade gliomas demonstrating increased contrast enhancement.

Clinical and Imaging Information	Training Group (N =106)	Validation Group (N = 26)	All Instances (N = 132)
Sex			
Female	38 (55.9%)	8 (30.8%)	46 (34.8%)
Male	68 (64.2%)	18 (69.2%)	86 (65.2%)
Age range (year)	48 ± 12*	51, 23#	47, 19#
Karnofsky performance status	90, 10#	88.2 ± 9.1*	90, 10#
Histologic subtype			
Diffuse astrocytoma	32 (30.2%)	11 (42.3%)	43 (32.6%)
Oligoastrocytoma	30 (28.3%)	5 (19.2%)	35 (26.5%)
Oligodendroglioma	44 (41.5%)	10 (38.5%)	54 (40.9%)
Isocitrate dehydrogenase 1 mutation			
Wild-type	14 (13.2%)	4 (15.4%)	18 (13.6%)
Mutant	66 (62.3%)	20 (76.9%)	86 (65.2%)
Not available	26 (24.5%)	2 (7.7%)	28 (21.2%)
Baseline residual tumor			
Yes	80 (75.5%)	14 (53.8%)	94 (71.2%)
No	26 (24.5%)	12 (46.2%)	38 (28.8%)
Disease duration (year)	4.6, 6#	4.8, 6.3#	4.7, 5.9#
Adjuvant therapy			
Radiotherapy	80 (56.3%)	22 (100%)	102 (61.4%)
Carmustine implant	49 (34.5%)	0	49 (29.5%)
Temozolomide	13 (9.2%)	0	15 (9.0%)
Post- Radiotherapy duration (month)	42.8, 68.4#	56.7 ± 46.1*	42.8, 60.1#
Whole tumor size (cm^2)	8, 14.6#	9.8, 18.4#	9, 14.3#
Contrast enhancement size (cm^2)	5, 13.5#	10.9 ± 12.8*	5, 13.3#
Contrast enhancement pattern			
Solid	32 (30.2%)	7 (26.9%)	39 (29.5%)
Scattered	44 (41.5%)	11 (42.3%)	55 (41.7%)
Rim	30 (28.3%)	8 (30.8%)	38 (28.8%)
Apparent Diffusion Coefficient (×10-6 mm2/s)			
< 968	56 (52.8%)	16 (61.5%)	72 (54.5%)
> 968	50 (47.2%)	10 (38.5%)	60 (45.5%)
Tumor grade			
II	42 (39.6%)	6 (23.1%)	48 (36.4%)
III	30 (28.3%)	10 (38.5%)	40 (30.3%)
IV	34 (32.1%)	10 (38.5%)	44 (33.3%)

**Data are mean ± SD; #data are median, interquartile range.*

TABLE 3 | Univariate analysis of factors associated with malignant transformation in the study group (106 instances).

Factors	Malignant Transformation		*P* Value	OR	95% CI
	No	Yes			
Sex			.70	1.18	0.52-2.64
Male	26	42			
Female	16	22			
Age (year)	50 ± 12	47 ± 13	.09	0.97	0.94-1.00
Karnofsky performance status	90, 12.6	90, 15	.52	1.01	0.98-1.05
Histologic subtype			.29	NA	NA
Diffuse astrocytoma	13	19			
Oligoastrocytoma	15	15			
Oligodendroglioma	14	30			
Isocitrate dehydrogenase 1 mutation			.38	NA	NA
Yes	25	41			
No	13	13			
Disease duration (year)	4.2, 4.0	4.9, 4.2	.59	1.00	1.00-1.00
Baseline residual tumor			.13	0.47	0.18-1.25
Yes	35	45			
No	7	19			
Radiotherapy			.03	9.46	1.18-75.78
Yes	36	44			
No	6	20			
Post-radiotherapy duration (month)	42.5, 48.4	46, 49.1	.99	0.99	0.99-1.01
Chemotherapy			.12	1.94	0.85-4.47
None	30	36			
Carmustine implant	16	33			
Temozolomide	1	12			
Whole-tumor size (cm^2)	3.8, 9.7	12.0, 9.1	.03	1.05	1.00-1.09
Contrast enhancement size (cm^2)	2.0, 7.0	6.8, 10.2	.01	1.09	1.02-1.15
Contrast enhancement pattern (cm^2)			.64	0.89	0.53-1.48
Solid	11	21			
Scattered	19	25			
Rim	12	18			
Apparent Diffusion coefficient ($\times 10^{-6}$ mm^2/s)	1137.0 ± 287.8	880.3 ± 257.2	< 0.001	0.99	0.99-1.00

Data are mean ± SD for age; data are median, interquartile range for Karnofsky performance status, disease duration, post-radiotherapy duration, whole-tumor size, contrast enhancement size, and apparent diffusion coefficient.

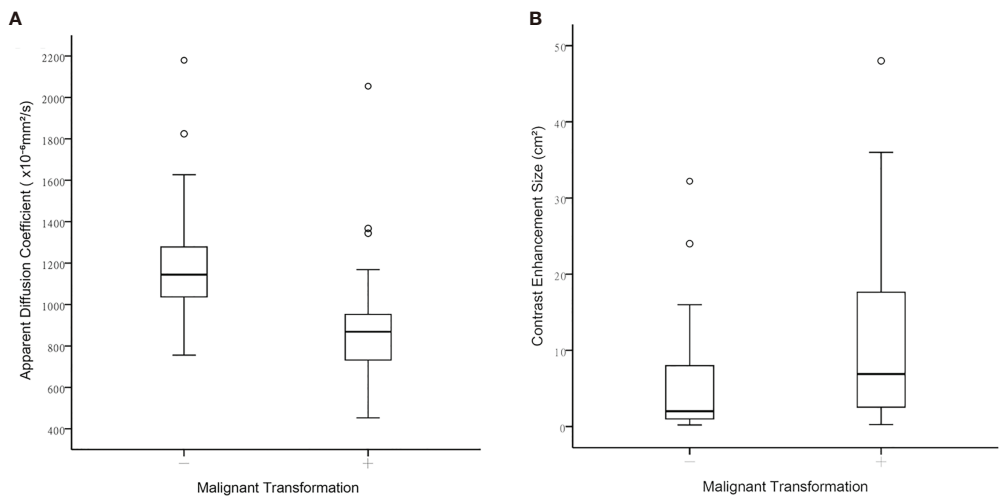

FIGURE 3 | Boxplots between contrast-enhanced tumor portions with malignant transformation and those that remained WHO grade II regarding **(A)** Apparent diffusion coefficient, and **(B)** Contrast-enhancement size.

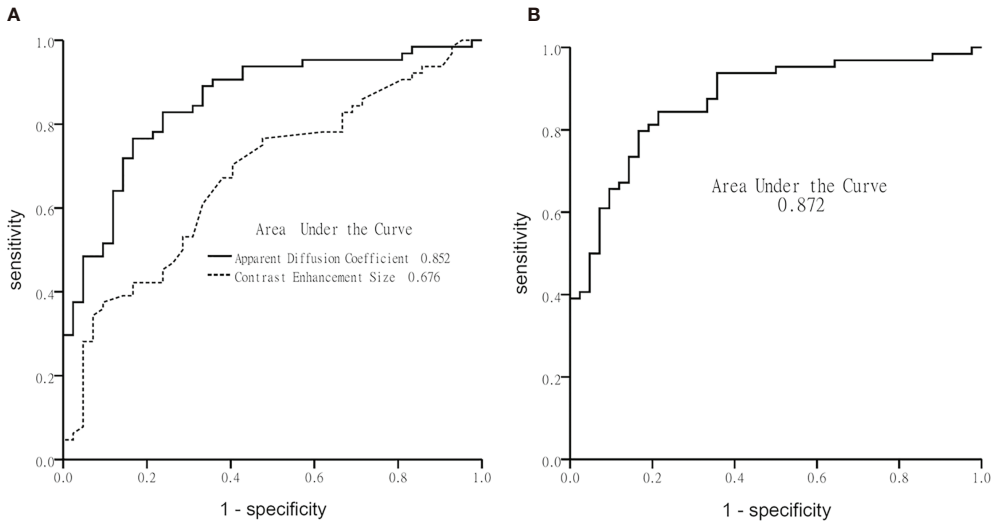

FIGURE 4 | Graphs show receiver operating characteristic curve plotted using calculated sensitivity against 1-specificity to assess test performance (area-under-the-curve) in diagnosing malignant transformation. **(A)** Apparent diffusion coefficient and contrast-enhancement size, and **(B)** the multivariate logistic regression model.

DISCUSSION

Our results show that if we used increasing contrast enhancement as an indication of MT in LGGs, one-third (48/132) of them would remain grade II. A multivariate logistic regression model, including age, presence of radiotherapy, ADC and contrast enhancement size, was established to predict MT (accuracy: 84%, sensitivity: 86%, specificity: 79%). This model was further validated by using data of 26 recently recruited instances (accuracy: 85%, sensitivity: 85%, specificity: 83%). By inputting clinical information and common MRI parameters into the model formula the probability of MT was predicted with high accuracy.

In high-grade gliomas, decreased ADC (16, 17) is associated with increased tumor cellularity. MT is expected to show decreased ADC due to increased cellularity. Previous reports using ADC for differentiation among glioma grades show variable results. Differentiation between LGGs and high-grade gliomas can be achieved using DWI in which ADC values of LGGs are significantly higher than those of high-grade tumors (18, 19). A recent report revealed significant ADC differences between grades II and III, grades II and IV, and between grades II and III-IV gliomas (9). Conversely, a study of non-enhancing gliomas found no significant ADC differences between LGGs and high-grade gliomas (20), Moreover, a considerable overlap of ADC values have been found between grade II and grade IV gliomas (21) and between grade III and grade IV gliomas (19). These inconsistencies may be partly explained by tissue heterogeneity in glial tumors (22). Because tumor grading depends on the location of biopsies or surgical resection, such heterogeneity may cause sampling errors and thus inaccurate grading. In these previous studies, the location of contrast enhancement was not cross-referenced to that of the ROI (8, 9, 18, 19). ADC values have been used to detect early MT in LGG. In a study of 18 patients undergoing MT (10), low intensity on DWI was used to target possible MT. Similarly, because of heterogeneity of high-grade glioma (23) and MT (11), portions of tumors with varying ADC values may coexist making it difficult to locate those with the lowest diffusion further reducing reproducibility. Of note is that in one series contrast enhancement occurred simultaneously with restricted diffusion in 12/18 (66%) patients and appeared about eight months later in the remaining 6/18 (33%) patients with restricted diffusion (10). Contrast enhancement was also found in the location of restricted diffusion about 3 months later in 23/27 (85%) patients with glioblastoma (10). These results suggest that contrast enhancement is likely to appear within months after restricted diffusion in high-grade gliomas. In our study, ADC was only measured in tumor portions with increasing contrast enhancement. Given that our model accurately diagnosed MT in a subset of patients with contrast-enhancing tumors, the combined use

TABLE 4 | Diagnostic accuracy of malignant transformation for study model and model validation.

Statistical Algorithm		Sensitivity	Specificity	PPV	NPV	Accuracy
Multivariate regression	Study model (106 instances)	0.88	0.79	0.86	0.80	0.84
	Model validation (26 instances)	0.85	0.83	0.94	0.63	0.85
Classification and regression trees with 5-fold cross validation	Study model (106 instances)	0.88	0.83	0.89	0.80	0.86
	Model validation (26 instances)	0.89	0.88	0.94	0.78	0.88

of ADC measurements and increasing contrast enhancement improved the specificity by limiting the ADC measurement to the contrast-enhancing tumor portions thus counteracting the effect of tumor heterogeneity.

Recently, an MRS study diagnosing MT of LGGs with increased contrast enhancement showed an accuracy of 89.6% (4). In that study, using single-voxel proton MRS, the NAA/Cho ratio was the only significant factor diagnostic of MT. Unlike that study, ours used DWI and contrast-enhanced imaging which are included in routine MRI protocols. Moreover, pre-localization of lesion as needed for MRS was not required and imaging data can be retrospectively processed to evaluate different tumor components, for example, non-enhancing components. However, when the results of imaging are uncertain using conventional MRI techniques, MRS can be obtained to improve one's interpretation.

In our study, the median time to MT was 5 years and thus comparable to previously reported times to MT that range from 2.7 to 5.4 years (24, 25). However, in our study, none of the previously identified factors (24–26), including old age, male sex, multiple tumor locations, tumor size > 5 cm, adjuvant temozolomide, presence of residual tumor, astrocytoma histology, and IDH wild-type, were significant predictors of MT. This discrepancy may be attributed to different criteria used for MT, such as the fact that in our study MT was confirmed with histology but in others, this confirmation was imaging-based in some patients. While most of the previously mentioned factors were analyzed in our study, ADC was not assessed or analyzed in those other studies. In our study, the combined effect of ADC and contrast enhancement size on MT was stronger than the effect of other factors thus diluting the effect of those factors in the multivariate regression model. More importantly, in other studies, the factors were assessed for associations with MT, but in ours, various factors were used to develop a model to predict MT.

Deep learning has recently become a dominant form of supervised machine learning method that uses a network architecture for a specific application (27). For classification in neuroimaging, imaging features are extracted and act as inputs to enter a neural network, like the convolutional neural network (CNN), which outputs a probability of the image belonging to each class. Deep learning methods have been applied in multiple aspects of gliomas, using MRI metrics to predict long-term outcome, treatment response like pseudopregression, and tumor genetics including 1p19q codeletion, O-6-methylguanine DNA-methyltransferase promoter, and IDH mutations (28). A deep learning approach would be able to model more complex and non-linear relationships between dependent and independent variables. In contrast, the model presented in our study is a simple linear relationship of limited clinicoradiologic features. Our model may not be as robust as one built with deep learning in the prediction of MT, but it allows assessments of the individual associations between MT and clinicoradiologic parameters. This information could be clinically important and is not available with deep learning method. However, if a larger sample size was available, applying a radiomic approach with deep learning to predict MT of gliomas would be a focus of further investigation.

Only LGGs having increasing contrast enhancement were included in our study. The exclusion of non-enhancing tumors was a limitation of our study. Further study of MT in non-enhancing tumors is necessary and should be performed using an alternative approach instead of manual ROI placement, such as whole-tumor histogram analysis. Second, ADC measurements may be affected by heterogeneity in MRI units and protocols. Unfortunately, these heterogeneities are inevitable in a study of patients imaged over 17 years although it has been reported that variability of ADC values across platforms is small (29). Thirdly, the use of 2-dimensional measurements was a limitation of our study. A recent study comparing volumetric segmentation and bidimensional products in the assessment of glioblastoma progression revealed that using the bidimensional measurement was approximately 30% less accurate and tended to underestimate tumor progression (30). Lastly, the inclusion of patients from a single institution may limit the generalizability of our findings, which can be improved by performing a more comprehensive multicenter study using different MRI scanners and MRI protocols.

In conclusion, a model incorporating ADC and contrast enhancement size was established to predict MT in low-grade gliomas with increased contrast enhancement. Compared with using contrast enhancement size alone, taking into consideration ADC more accurately diagnoses MT of low-grade gliomas.

DATA AVAILABILITY STATEMENT

The raw data supporting the conclusions of this article will be made available by the authors, without undue reservation.

ETHICS STATEMENT

The studies involving human participants were reviewed and approved by Chang Gung Medical Foundation Institutional Review Board. Written informed consent for participation was not provided by the participants' legal guardians/next of kin because: This retrospective study was performed after institutional review board approval. The need to obtain patient informed consent was waived by our review board (202100387B0).

AUTHOR CONTRIBUTIONS

AW and CT primarily designed the study. TS, K-CW, P-YC, and MC provided suggestions for improvements from technical and medical perspective. AW, CT, and TS collected and analyzed data. All co-authors provided feedback and were involved in manuscript revision. All authors contributed to the article and approved the submitted version.

FUNDING

This work was funded by grants from the Ministry of Science and Technology, Taiwan (MOST 108-2314-B-182A-015, MOST 108-2314-B-182A-016, MOST 108-2314-B-182A-044).

ACKNOWLEDGMENTS

The authors thank Mr. Morris MF Wu for providing advice on statistical analysis.

REFERENCES

1. Ostrom QT, Cioffi G, Gittleman H, Patil N, Waite K, Kruchko C, et al. CBTRUS Statistical Report: Primary Brain and Other Central Nervous System Tumors Diagnosed in the United States in 2012-2016. *Neuro Oncol* (2019) 21 (Suppl 5):v1–100. doi: 10.1093/neuonc/noz150
2. van den Bent MJ, Wefel JS, Schiff D, Taphoorn MJ, Jaeckle K, Junck L, et al. Response Assessment in Neuro-Oncology (a Report of the RANO Group): Assessment of Outcome in Trials of Diffuse Low-Grade Gliomas. *Lancet Oncol* (2011) 12(6):583–93. doi: 10.1016/S1470-2045(11)70057-2
3. Narang AK, Chaichana KL, Weingart JD, Redmond KJ, Lim M, Olivi A, et al. Progressive Low-Grade Glioma: Assessment of Prognostic Importance of Histologic Reassessment and MRI Findings. *World Neurosurg* (2017) 99:751–7. doi: 10.1016/j.wneu.2016.04.030
4. Toh CH, Castillo M, Wei KC, Chen PY. MRS as an Aid to Diagnose Malignant Transformation in Low-Grade Gliomas With Increasing Contrast Enhancement. *AJNR Am J Neuroradiol* (2020) 41(9):1592–8. doi: 10.3174/ajnr.A6688
5. Fink JR, Carr RB, Matsusue E, Iyer RS, Rockhill JK, Haynor DR, et al. Comparison of 3 Tesla Proton MR Spectroscopy, MR Perfusion and MR Diffusion for Distinguishing Glioma Recurrence From Posttreatment Effects. *J Magn Reson Imaging* (2012) 35(1):56–63. doi: 10.1002/jmri.22801
6. Matsusue E, Fink JR, Rockhill JK, Ogawa T, Maravilla KR. Distinction Between Glioma Progression and Post-Radiation Change by Combined Physiologic MR Imaging. *Neuroradiology* (2010) 52(4):297–306. doi: 10.1007/s00234-009-0613-9
7. Schiff D, Van den Bent M, Vogelbaum MA, Wick W, Miller CR, Taphoorn M, et al. Recent Developments and Future Directions in Adult Lower-Grade Gliomas: Society for Neuro-Oncology (SNO) and European Association of Neuro-Oncology (EANO) Consensus. *Neuro Oncol* (2019) 21(7):837–53. doi: 10.1093/neuonc/noz033
8. Arevalo-Perez J, Peck KK, Young RJ, Holodny AI, Karimi S, Lyo JK. Dynamic Contrast-Enhanced Perfusion MRI and Diffusion-Weighted Imaging in Grading of Gliomas. *J Neuroimaging* (2015) 25(5):792–8. doi: 10.1111/jon.12239
9. Server A, Graff BA, Josefsen R, Orheim TE, Schellhorn T, Nordhoy W, et al. Analysis of Diffusion Tensor Imaging Metrics for Gliomas Grading at 3 T. *Eur J Radiol* (2014) 83(3):e156–65. doi: 10.1016/j.ejrad.2013.12.023
10. Freitag MT, Maier-Hein KH, Binczyk F, Laun FB, Weber C, Bonekamp D, et al. Early Detection of Malignant Transformation in Resected WHO II Low-Grade Glioma Using Diffusion Tensor-Derived Quantitative Measures. *PloS One* (2016) 11(10):e0164679. doi: 10.1371/journal.pone.0164679
11. Jalbert LE, Neill E, Phillips JJ, Lupo JM, Olson MP, Molinaro AM, et al. Magnetic Resonance Analysis of Malignant Transformation in Recurrent Glioma. *Neuro Oncol* (2016) 18(8):1169–79. doi: 10.1093/neuonc/now008
12. Kim YH, Nobusawa S, Mittelbronn M, Paulus W, Brokinkel B, Keyvani K, et al. Molecular Classification of Low-Grade Diffuse Gliomas. *Am J Pathol* (2010) 177(6):2708–14. doi: 10.2353/ajpath.2010.100680
13. Bursac Z, Gauss CH, Williams DK, Hosmer DW. Purposeful Selection of Variables in Logistic Regression. *Source Code Biol Med* (2008) 3:17. doi: 10.1186/1751-0473-3-17
14. Krzywinski M, Altman N. Classification and Regression Trees. *Nat Methods* (2017) 14(8):757–8. doi: 10.1038/nmeth.4370
15. Song YY, Lu Y. Decision Tree Methods: Applications for Classification and Prediction. *Shanghai Arch Psychiatry* (2015) 27(2):130–5. doi: 10.11919/j.issn.1002-0829.215044
16. Chen L, Liu M, Bao J, Xia Y, Zhang J, Zhang L, et al. The Correlation Between Apparent Diffusion Coefficient and Tumor Cellularity in Patients: A Meta-Analysis. *PloS One* (2013) 8(11):e79008. doi: 10.1371/journal.pone.0079008
17. Sadeghi N, D'Haene N, Decaestecker C, Levivier M, Metens T, Maris C, et al. Apparent Diffusion Coefficient and Cerebral Blood Volume in Brain Gliomas: Relation to Tumor Cell Density and Tumor Microvessel Density Based on Stereotactic Biopsies. *AJNR Am J Neuroradiol* (2008) 29(3):476–82. doi: 10.3174/ajnr.A0851
18. Sugahara T, Korogi Y, Kochi M, Ikushima I, Shigematu Y, Hirai T, et al. Usefulness of Diffusion-Weighted MRI With Echo-Planar Technique in the Evaluation of Cellularity in Gliomas. *J Magn Reson Imaging* (1999) 9(1):53–60. doi: 10.1002/(sici)1522-2586(199901)9:1<53::aid-jmri7>3.0.co;2-2
19. Kitis O, Altay H, Calli C, Yunten N, Akalin T, Yurtseven T. Minimum Apparent Diffusion Coefficients in the Evaluation of Brain Tumors. *Eur J Radiol* (2005) 55(3):393–400. doi: 10.1016/j.ejrad.2005.02.004
20. Liu X, Tian W, Kolar B, Yeaney GA, Qiu X, Johnson MD, et al. MR Diffusion Tensor and Perfusion-Weighted Imaging in Preoperative Grading of Supratentorial Nonenhancing Gliomas. *Neuro Oncol* (2011) 13(4):447–55. doi: 10.1093/neuonc/noq197
21. Kono K, Inoue Y, Nakayama K, Shakudo M, Morino M, Ohata K, et al. The Role of Diffusion-Weighted Imaging in Patients With Brain Tumors. *AJNR Am J Neuroradiol* (2001) 22(6):1081–8.
22. Provenzale JM, Mukundan S, Barboriak DP. Diffusion-Weighted and Perfusion MR Imaging for Brain Tumor Characterization and Assessment of Treatment Response. *Radiology* (2006) 239(3):632–49. doi: 10.1148/radiol.2393042031
23. Lee S, Choi SH, Ryoo I, Yoon TJ, Kim TM, Lee SH, et al. Evaluation of the Microenvironmental Heterogeneity in High-Grade Gliomas With IDH1/2 Gene Mutation Using Histogram Analysis of Diffusion-Weighted Imaging and Dynamic-Susceptibility Contrast Perfusion Imaging. *J Neurooncol* (2015) 121(1):141–50. doi: 10.1007/s11060-014-1614-z
24. Murphy ES, Leyrer CM, Parsons M, Suh JH, Chao ST, Yu JS, et al. Risk Factors for Malignant Transformation of Low-Grade Glioma. *Int J Radiat Oncol Biol Phys* (2018) 100(4):965–71. doi: 10.1016/j.ijrobp.2017.12.258
25. Tom MC, Park DYJ, Yang K, Leyrer CM, Wei W, Jia X, et al. Malignant Transformation of Molecularly Classified Adult Low-Grade Glioma. *Int J Radiat Oncol Biol Phys* (2019) 105(5):1106–12. doi: 10.1016/j.ijrobp.2019.08.025
26. Chaichana KL, McGirt MJ, Laterra J, Olivi A, Quinones-Hinojosa A. Recurrence and Malignant Degeneration After Resection of Adult Hemispheric Low-Grade Gliomas. *J Neurosurg* (2010) 112(1):10–7. doi: 10.3171/2008.10.JNS08608
27. Zaharchuk G, Gong E, Wintermark M, Rubin D, Langlotz CP. Deep Learning in Neuroradiology. *AJNR Am J Neuroradiol* (2018) 39(10):1776–84. doi: 10.3174/ajnr.A5543
28. Chow DS, Khatri D, Chang PD, Zlochower A, Boockvar JA, Filippi CG. Updates on Deep Learning and Glioma: Use of Convolutional Neural Networks to Image Glioma Heterogeneity. *Neuroimaging Clin N Am* (2020) 30(4):493–503. doi: 10.1016/j.nic.2020.07.002
29. Newitt DC, Zhang Z, Gibbs JE, Partridge SC, Chenevert TL, Rosen MA, et al. Test-Retest Repeatability and Reproducibility of ADC Measures by Breast DWI: Results From the ACRIN 6698 Trial. *J Magn Reson Imaging* (2019) 49 (6):1617–28. doi: 10.1002/jmri.26539
30. Berntsen EM, Stensjoen AL, Langlo MS, Simonsen SQ, Christensen P, Moholdt VA, et al. Volumetric Segmentation of Glioblastoma Progression Compared to Bidimensional Products and Clinical Radiological Reports. *Acta Neurochir (Wien)* (2020) 162(2):379–87. doi: 10.1007/s00701-019-04110-0

Conflict of Interest: The authors declare that the research was conducted in the absence of any commercial or financial relationships that could be construed as a potential conflict of interest.

frontiers in Neurology

REVIEW
published: 10 November 2021
doi: 10.3389/fneur.2021.733323

Advanced Magnetic Resonance Imaging in Pediatric Glioblastomas

Fabrício Guimarães Gonçalves[1]*, *Angela N. Viaene*[2,3] and *Arastoo Vossough*[1,4]

[1] Division of Neuroradiology, Department of Radiology, Children's Hospital of Philadelphia, Philadelphia, PA, United States, [2] Department of Pathology and Laboratory Medicine, Children's Hospital of Philadelphia, Philadelphia, PA, United States, [3] Department of Pathology and Laboratory Medicine, Perelman School of Medicine, University of Pennsylvania, Philadelphia, PA, United States, [4] Department of Radiology, Perelman School of Medicine, University of Pennsylvania, Philadelphia, PA, United States

The shortly upcoming 5th edition of the World Health Organization Classification of Tumors of the Central Nervous System is bringing extensive changes in the terminology of diffuse high-grade gliomas (DHGGs). Previously "glioblastoma," as a descriptive entity, could have been applied to classify some tumors from the family of pediatric or adult DHGGs. However, now the term "glioblastoma" has been divested and is no longer applied to tumors in the family of pediatric types of DHGGs. As an entity, glioblastoma remains, however, in the family of adult types of diffuse gliomas under the insignia of "glioblastoma, IDH-wildtype." Of note, glioblastomas still can be detected in children when glioblastoma, IDH-wildtype is found in this population, despite being much more common in adults. Despite the separation from the family of pediatric types of DHGGs, what was previously labeled as "pediatric glioblastomas" still remains with novel labels and as new entities. As a result of advances in molecular biology, most of the previously called "pediatric glioblastomas" are now classified in one of the four family members of pediatric types of DHGGs. In this review, the term glioblastoma is still apocryphally employed mainly due to its historical relevance and the paucity of recent literature dealing with the recently described new entities. Therefore, "glioblastoma" is used here as an umbrella term in the attempt to encompass multiple entities such as astrocytoma, IDH-mutant (grade 4); glioblastoma, IDH-wildtype; diffuse hemispheric glioma, H3 G34-mutant; diffuse pediatric-type high-grade glioma, H3-wildtype and IDH-wildtype; and high grade infant-type hemispheric glioma. Glioblastomas are highly aggressive neoplasms. They may arise anywhere in the developing central nervous system, including the spinal cord. Signs and symptoms are non-specific, typically of short duration, and usually derived from increased intracranial pressure or seizure. Localized symptoms may also occur. The standard of care of "pediatric glioblastomas" is not well-established, typically composed of surgery with maximal safe tumor resection. Subsequent chemoradiation is recommended if the patient is older than 3 years. If younger than 3 years, surgery is followed by chemotherapy. In general, "pediatric glioblastomas" also have a poor prognosis despite surgery and adjuvant therapy. Magnetic resonance imaging (MRI) is the imaging modality of choice for the evaluation of glioblastomas. In addition to the typical conventional MRI features, i.e., highly heterogeneous invasive masses with indistinct borders, mass effect on surrounding

OPEN ACCESS

Edited by:
Manoj Kumar, National Institute of Mental Health and Neurosciences (NIMHANS), India

Reviewed by:
Santosh Kumar Yadav, Sidra Medicine, Qatar
Hans-Georg Wirsching, University Hospital Zürich, Switzerland
Manabu Natsumeda, Niigata University, Japan
Timothy Richardson, The University of Texas Health Science Center at San Antonio, United States

***Correspondence:**
Fabrício Guimarães Gonçalves
goncalves.neuroradio@gmail.com

Specialty section:
This article was submitted to Applied Neuroimaging, a section of the journal Frontiers in Neurology

Received: *30 June 2021*
Accepted: *12 October 2021*
Published: *10 November 2021*

Citation:
Gonçalves FG, Viaene AN and Vossough A (2021) Advanced Magnetic Resonance Imaging in Pediatric Glioblastomas. Front. Neurol. 12:733323. doi: 10.3389/fneur.2021.733323

structures, and a variable degree of enhancement, the lesions may show restricted diffusion in the solid components, hemorrhage, and increased perfusion, reflecting increased vascularity and angiogenesis. In addition, magnetic resonance spectroscopy has proven helpful in pre- and postsurgical evaluation. Lastly, we will refer to new MRI techniques, which have already been applied in evaluating adult glioblastomas, with promising results, yet not widely utilized in children.

Keywords: advanced MRI, children, conventional MRI, diffusion-weighted imaging, glioblastoma, magnetic resonance spectroscopy, perfusion weighted imaging

INTRODUCTION

This review was conceived and developed during a watershed moment, in which major changes are occurring in how brain tumors are classified. During the last few years, new concepts and entities have emerged, and well-known diagnoses and terminology have been abandoned. According to the shortly upcoming 5th edition of the World Health Organization Classification of Tumors of the Central Nervous System (CNS) (WHO/CNS/5), the term "glioblastoma" is no longer applicable for tumors in the family of pediatric types of diffuse high-grade gliomas (DHGGs) (1). Glioblastoma only remains, as an entity, in the family of adult types of diffuse gliomas (1).

As stated in the WHO/CNS/5, there are three components in the family of adult types of diffuse gliomas and four in the family of pediatric types of DHGG. The three adult types of diffuse gliomas are represented by the (1) astrocytoma, IDH-mutant (grades 2, 3, and 4); (2) oligodendroglioma, IDH-mutant, and 1p/19q-codeleted (grades 2 and 3) and (3) glioblastoma, IDH-wildtype (grade 4) (1). The four pediatric types of DHGGs (all grade 4 tumors) are represented by the (1) diffuse midline glioma, H3 K27-altered; (2) diffuse hemispheric glioma, H3 G34-mutant; (3) diffuse pediatric-type high-grade glioma, H3-wildtype and IDH-wildtype; and (4) infant-type hemispheric glioma (1). This review will focus on the pediatric types of DHGGs (except the diffuse midline glioma, H3 K27-altered) and the two grade 4 adult types of diffuse gliomas, namely the astrocytoma, IDH-mutant grade 4 (formerly known as glioblastoma, IDH-mutant), and the glioblastoma, IDH-wildtype (1). These two latter diffuse gliomas are typically found in adults, but can also occasionally occur in older children, particularly teenagers.

Despite the separation and removal of the term "glioblastoma" from the family of pediatric type DHGGs, as per the WHO/CNS/5 (1), this paper will still apocryphally employ the term due to a number reasons, including: (1) its preeminent historical relevance, (2) the bulk of the available neuro-oncology literature refers to it as glioblastoma, (3) the paucity of recent literature explicitly dealing with the most current classification (WHO/CNS/5), and (4) a convenient way to refer to grade 4 DHGGs that can occur in children, beyond the diffuse midline glioma, H3 K27-altered, and glioblastoma, IDH-wildtype, which may still be sometimes seen in the pediatric population.

Studies on glioblastomas in children are more limited in number than their adult counterparts, despite this tumor's clinical relevance and the substantial patient burden that accompanies this diagnosis. Even though "glioblastomas in children" share similar morphological characteristics to adult glioblastomas, they are much less common and present distinct gene expression and molecular profiles, explaining observed differences in adjuvant treatment response. Given their relative rarity, most of the available literature relies on studies involving small numbers of patients in the form of case reports and small case series. Fundamental concepts of pathology, clinical features, management, structural imaging, and advanced imaging techniques (some not widely available such as metabolic and physiologic magnetic resonance imaging) to study "glioblastomas in children" will be reviewed.

BACKGROUND

Glioblastomas are highly aggressive tumors whose cell of origin is not fully clarified. They are the most lethal and most common primary CNS neoplasm in adults, with incidence peak in the sixth and seventh decades (2). They are relatively rare in children, representing 0.6–7.9% of all "glioblastomas" (3), and accounting for 3–15% of all primary pediatric CNS tumors (4). They can occur at any age, more frequently around the second decade of life (4–6).

"Glioblastomas" may arise anywhere in the developing CNS. Their most common location is in the supratentorial compartment (7), occurring in 30–50% of the patients in the cerebral hemispheres (8). Involvement of deeper structures such as the thalamus, corpus callosum, and hypothalamus is less common (9). Spinal cord involvement is rare, representing only 3% of all cases (8). Very rarely "pediatric glioblastomas" may occur in the cerebellum (1–2% of all patients) (10).

Signs and Symptoms

Signs and symptoms are often non-specific, typically of short duration, and usually result from increased intracranial pressure (headache, behavior changes, early morning nausea/emesis, diplopia, papilledema, and altered sensorium) (4, 5, 11). In addition, localizing symptoms may occur, namely focal motor deficits, hemiplegia, pyramidal tract findings, dysmetria, and chorea (12). Infants and young children may also manifest ambiguously with failure to thrive, lethargy, and macrocephaly. Finally, precipitous neurological deterioration may also occur,

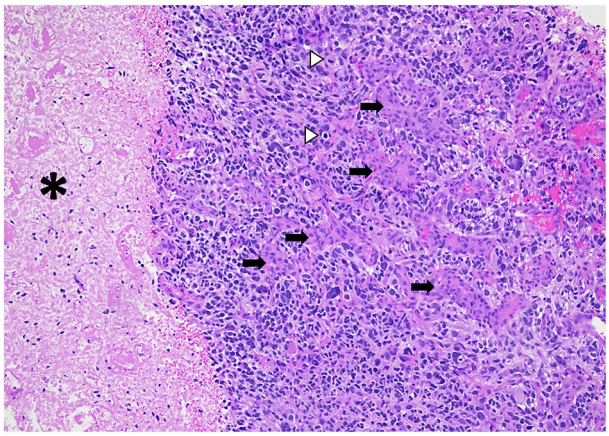

FIGURE 1 | Diffuse hemispheric glioblastoma, H3 G34 mutant (histologic "glioblastoma") demonstrating high cellularity, nuclear pleomorphism, microvascular proliferation (arrows), necrosis (asterisks), and mitotic figures (arrowheads). HandE stain, 100x magnification.

commonly from intratumoral hemorrhage or seizures (9). Seizures may be present in around 30% of affected children, more commonly when lesions are superficially located in the frontal or temporal lobes (5, 11, 13).

Pathology and Molecular Diagnosis

"Glioblastomas" are typically large, highly vascularized, heterogeneous, and infiltrative masses, and often have irregular margins. On gross pathology, the peripheral rims are pink-gray and solid and may contain a yellow, soft necrotic center, and often contain hemorrhagic foci (14). Microscopically, they typically show increased cellularity, high mitotic activity, pleomorphic cells, microvascular proliferation, and necrosis (**Figure 1**). There are no gross or microscopic histologic differences between "glioblastomas" affecting adults or children (15–17); however, certain histologic subtypes may be more frequently encountered in specific age groups.

Their diffusely infiltrative behavior is characteristic, typically showing hypercellularity, nuclear atypia, necrosis (which may be pseudopalisading), and vascular endothelial cell proliferation. Glioblastomas are friable and highly vascularized masses in which thrombosed vessels, bleeding, and necrosis can be identified (18). Calcification is atypical but can be seen in radiation-associated "secondary glioblastomas." Radiation-associated "secondary glioblastomas" may be observed many years following CNS radiation treatment for childhood malignancies, including leukemia and other brain tumors such as medulloblastomas and ependymomas (**Figure 2**) (18). However, radiation-associated "secondary glioblastomas" are uncommon, with an average time to develop around 9 years (18). Contrary to adult patients, the progression of low-grade gliomas into "secondary glioblastoma" is very rare in children.

Traditionally, glioblastomas have been histologically classified as giant-cell glioblastoma, gliosarcoma, and epithelioid glioblastoma (19). Epithelioid "glioblastomas" are known to be more common in children and are characterized by large

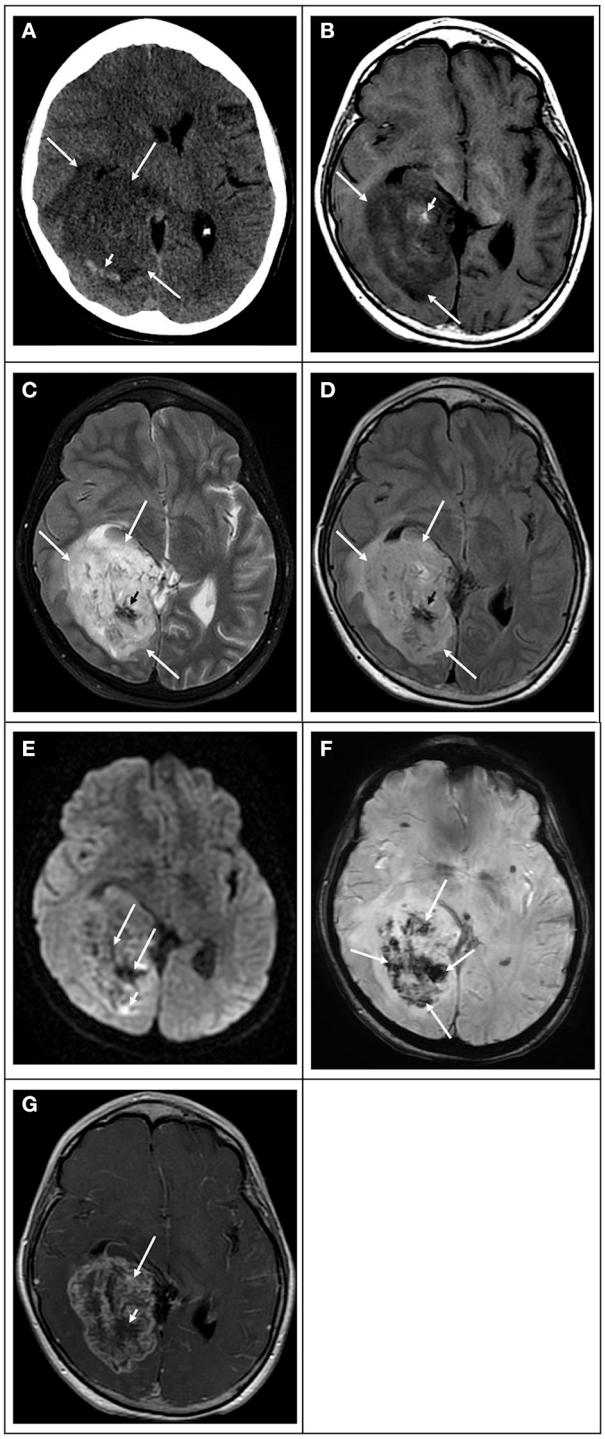

FIGURE 2 | Radiation-induced secondary "glioblastoma" in a 17-year-old girl who had a previous posterior fossa ependymoma at age 5. **(A)** Computed tomography image in the axial plane shows a large ill-defined tumor in the right temporal and occipital lobes (white arrows), causing mass effect, compression of the right lateral ventricle, and midline deviation. The lesion is associated with vasogenic edema and hemorrhage (white arrowhead). **(B)** T1 weighted image in the axial plane shows that the bulk of the lesion is hypointense (white arrows) with scattered hyperintensity foci due to intratumoral hemorrhage

(Continued)

FIGURE 2 | (white arrowhead). **(C)** T2 weighted image and **(D)** FLAIR image in the axial plane show that the bulk of the lesion is hyperintense with scattered hypointense foci due to intratumoral hemorrhage. **(E)** Diffusion-weighted image in the axial plane shows that the lesion is heterogeneous in signal. The bulk of the lesion is isointense to the normal brain parenchyma with scattered hyperintense foci due to intratumoral hemorrhage and small peripheral hyperintense foci (white arrowhead), which had lower values on the ADC maps (not shown) in keeping with restricted diffusion. **(F)** Susceptibility weighted image in the axial plane shows extensive signal drop within the tumoral bed (white arrows) in keeping with diffuse hemorrhage. **(G)** T1-weighted contrast-enhanced image in the axial plane shows that the tumor enhances heterogeneously. The mass has avid enhancement with central non-enhancing areas in keeping with necrotic tissue.

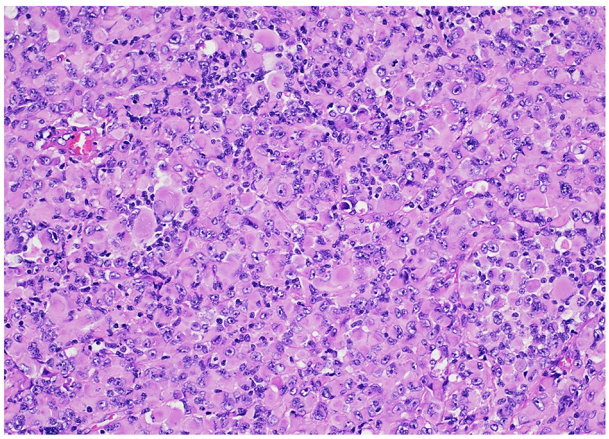

FIGURE 3 | Diffuse pediatric-type high-grade glioma, H3-wildtype and IDH-wildtype ("histologic epithelioid glioblastoma") characterized by sheets of tumor cells with distinct nuclear borders, a moderate to large amount of eosinophilic cytoplasm, eccentrically-located nuclei, and prominent nucleoli. HandE stain, 200x magnification.

eosinophilic cells, prominent melanoma-like nuclei, and often rhabdoid cells (**Figure 3**) (9). However, in the WHO/CNS/5, subtypes are not listed in the classification, but are further discussed in their respective chapters (1).

Many high-grade gliomas (HGGs) have also more recently been classified and diagnosed by methylation profiling, and entities once thought to comprise "pediatric glioblastomas" have been reclassified as other entities and vice versa. In addition, molecular features may vary by location. For example, what was thought to be a uniform group of glioblastomas occurring in the posterior fossa, now comprises distinct molecular entities (based on methylation profiles), namely anaplastic astrocytoma with piloid features; glioblastoma, IDH wildtype; diffuse midline glioma H3 K27M mutant; and astrocytoma, IDH mutant (20).

Previously, CNS tumor grading fundamentally relied on histological features with rare exceptions (i.e., diffuse midline glioma, H3K27M-mutant). Currently, specific molecular markers also play a major role in diagnosis and prognosis and even in assignment of tumor grade. The WHO/CNS/5 has combined histological and molecular grading, meaning that molecular parameters have now been added as biomarkers of grading and can sometimes upgrade a lesion, despite its conventional histology characteristics (1).

Formerly, glioblastomas have been classified, based on the isocitrate dehydrogenase (IDH) gene mutation status, into three major subgroups: IDH-wildtype (the majority of the patients), IDH-mutant, and not otherwise specified (19, 21). "IDH-mutant glioblastomas" were often considered secondary neoplasms (i.e., progressed from lower-grade IDH-mutant astrocytomas), while IDH-wildtype glioblastomas typically represented *de novo* neoplasms, mainly in older adults (9).

According to WHO/CNS/5, glioblastomas, as valid entities, are, by definition, only represented by the IDH-wildtype. They may also incorporate three genetic parameters, namely TERT promoter mutation, EGFR gene amplification, the combined gain of entire chromosome 7, and loss of entire chromosome 10 [+7/−10] (1). Therefore, the presence of one or more of the latter three in a patient with IDH-wildtype diffuse astrocytic tumor suffices to assign the highest WHO grade (1). In the family of adult diffuse gliomas, the tumors that do not show microvascular proliferation or necrosis, but show either TERT promoter mutation, EGFR mutation, or +7/-10 chromosome copy number changes will still be classified as glioblastoma when considering the integrated diagnosis (1). In other words, even though there may not be full histologic features of "glioblastoma" in these diffuse gliomas, the addition of specific molecular information may still classify them as glioblastoma. Note that occasionally, adult type glioblastoma, IDH-wild type may be seen in older children.

At present, the WHO/CNS/5 (1) recognizes three adult types of diffuse gliomas, namely:

1) Astrocytoma, IDH-mutant
2) Oligodendroglioma, IDH-mutant, and 1p/19q-codeleted and the
3) Glioblastoma, IDH-wildtype.

Astrocytomas, IDH-mutant, can be classified in grades 2, 3, or 4 (formerly IDH-mutant glioblastoma) (1). Notably, the term "glioblastoma" is no longer valid in the setting of a pediatric type diffuse glioma (1). In addition, the WHO/CNS/5 (1) endorses four pediatric types of DHHGs, namely:

1) Diffuse midline glioma, H3 K27-altered
2) Diffuse hemispheric glioma, H3 G34-mutant
3) Diffuse pediatric-type high-grade glioma, H3-wildtype and IDH-wildtype
4) Infant-type hemispheric glioma.

The characteristically altered genes and molecular profiles in each of the four pediatric types of DHHGs are (1):

1) Diffuse midline glioma, H3 K27-altered: H3 K27, TP53, ACVR1, PDGFRA, EGFR, EZHIP
2) Diffuse hemispheric glioma, H3 G34-mutant: H3 G34, TP53 (**Figure 4**), ATRX
3) Diffuse pediatric-type high-grade glioma, H3-wildtype, and IDH-wildtype: IDH-wildtype, H3-wildtype, PDGFRA, MYCN, EGFR (methylome)

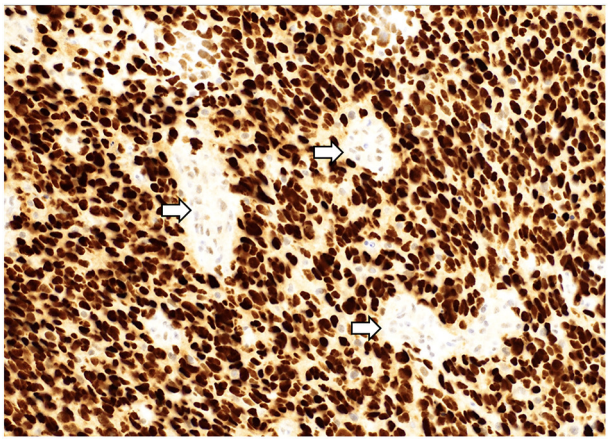

FIGURE 4 | A "glioblastoma" with a mutation in TP53 demonstrating strong, diffuse nuclear staining for p53 with wildtype staining present in vessels (arrows). p53 immunostain, 200x magnification.

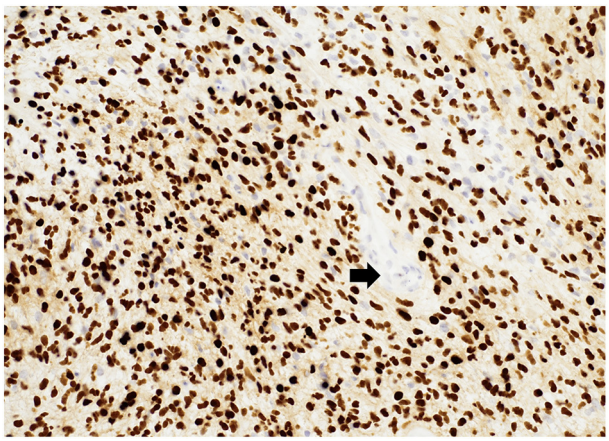

FIGURE 5 | Diffuse midline glioma, H3K27M-altered demonstrating diffuse nuclear staining for H3K27M with negative endothelial cells serving as an internal control (arrow). H3K27M immunostain, 200x magnification.

4) Infant-type hemispheric glioma: NTRK family, ALK, ROS, MET.

Lack of IDH mutation is known to impact therapy outcomes negatively in adult patients. "Glioblastomas in children" and other HGG typically demonstrate a low incidence of IDH mutation (seen in ∼6% of all pediatric HGGs), and such alterations are infrequent in younger children (22). Therefore, the majority of true glioblastomas in children are thought to be IDH-wildtype. The incidence of IDH-mutant or "secondary glioblastomas" may be higher in older adolescents and younger adults (23).

Mutations in histone genes are the most common molecular findings in pediatric HGGs with H3 K27M mutations associated with midline tumors (**Figures 5**, **6**) and H3 p.G34R/V mutations occurring in hemispheric tumors. The majority of these tumors are histologically high-grade; however, it should be noted that infiltrative, astrocytic tumors of the midline with H3 K27M mutations are classified as "diffuse midline gliomas," and regardless of histologic grade, correspond to WHO grade 4 (19). In addition, co-occurring mutations in TP53 (**Figure 4**) and ATRX (**Figure 7**) may be seen in tumors with H3 mutations, whereas IDH mutations are not observed (24, 25). Of note, circumscribed/non-diffuse gliomas of the midline are not considered grade 4, according to the (WHO/CNS/5) (26). Diffuse midline gliomas are not the primary focus of this paper.

Diffuse midline gliomas are one of the most severe pediatric brain tumors, with dismal prognosis despite developments in diagnosis and therapeutics. According to Castel et al. (27) there are two subgroups of diffuse midline gliomas, H3-K27M-mutant, namely H3.1-K27M and H3.3-K27M with differences in prognosis and phenotypes. According to them, the differences between H3.1/H3.3 subgroups may be a result of distinct cells of origin or due to the type of histone mutated. In their study they found that the type of histone H3 mutated could also predict the outcome of DIPG patients more efficiently than

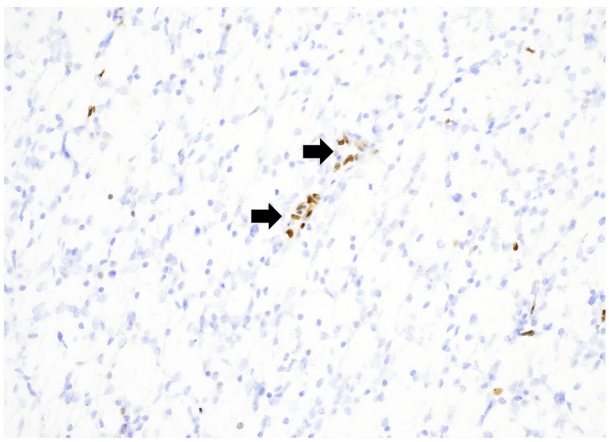

FIGURE 6 | Diffuse midline glioma, H3K27-altered demonstrating a loss of nuclear staining for H3K27me3 with positive endothelial cells serving as an internal control (arrows). H3K27me3 immunostain, 200x magnification.

clinical and radiological characteristics of the tumors (27). An in depth discussion about diffuse midline gliomas was not included here because of their complexity and specificities and due to space limitations, being necessary a specific paper to discuss them accordingly.

"Pediatric glioblastomas" commonly have a higher incidence of p53 mutation/overexpression (particularly in children <3 years) than mutation of epithelial growth factor receptor (EGFR) or deletion of phosphatase and tensin homolog (PTEN), which are common features of "adult glioblastomas" (9). In addition, ATRX mutations (**Figure 7**) have been reported in a fraction of "pediatric glioblastomas," usually associated with other mutations (28). Vascular endothelial growth factor (VEGF) is commonly expressed by "adult glioblastomas" and is responsible for increased vascularity, tumor progression, and infiltration. Therefore, anti-VEGF (bevacizumab) therapy is frequently

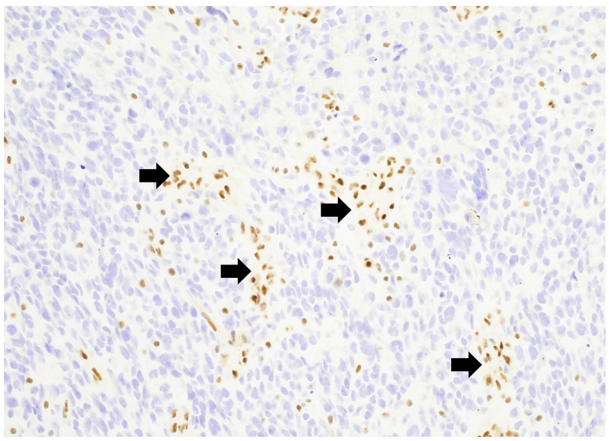

FIGURE 7 | A "glioblastoma" with an ATRX mutation demonstrating a loss of nuclear staining for ATRX with positive endothelial cells serving as an internal control (arrows). ATRX immunostain, 200x magnification.

employed in "adult glioblastomas." However, VEGF expression is relatively infrequent in "pediatric glioblastomas," which may explain the comparative ineffectiveness of anti-VEGF therapy in children (29).

The mechanism of action of temozolomide (TMZ), one of the chemotherapy agents to treat glioblastomas, is by promoting DNA methylation. On the other hand, O^6-Methylguanine-DNA Methyltransferase (MGMT) is a DNA repair enzyme, rescuing neoplastic cells from alkylating agent-induced damage. Therefore, MGMT activation leads to increased resistance to chemotherapy with alkylating agents. MGMT promoter methylation status has crucial prognostic importance in glioblastomas. Inactivation of MGMT generally correlates with chemotherapy responsiveness (30) and increased median event-free survival (31). Studies on MGMT expression in "pediatric glioblastomas" have demonstrated little alteration in the methylation promoter status in children, which may explain the reduced efficacy of TMZ in children compared to adults (32). Regarding the diffuse midline gliomas, H3 K27M mutant, MGMT promoter is unmethylated in almost all cases, which explains the failure of clinical trials administrating TMZ to patients with this diagnosis (33, 34). Whenever present, the prognostic significance of inactivating hypermethylation of MGMT confers a survival benefit to affected children.

NEUROIMAGING

Computed Tomography

Computed tomography (CT) may be the first imaging modality in children to detect an intracranial neoplasm. On CT, "pediatric glioblastomas" typically present as poorly marginated heterogeneous lesions with mass effect and variable areas of hyperattenuation, which may be partially due to hemorrhage (**Figure 8**). Areas of hypoattenuation may correspond to necrosis or surrounding edema. Contrast-enhanced CT features are variable, ranging from minor to marked enhancement and from solid to heterogeneous enhancement. Necrotic lesions may show rim enhancement, typically with irregular borders (35). Typical

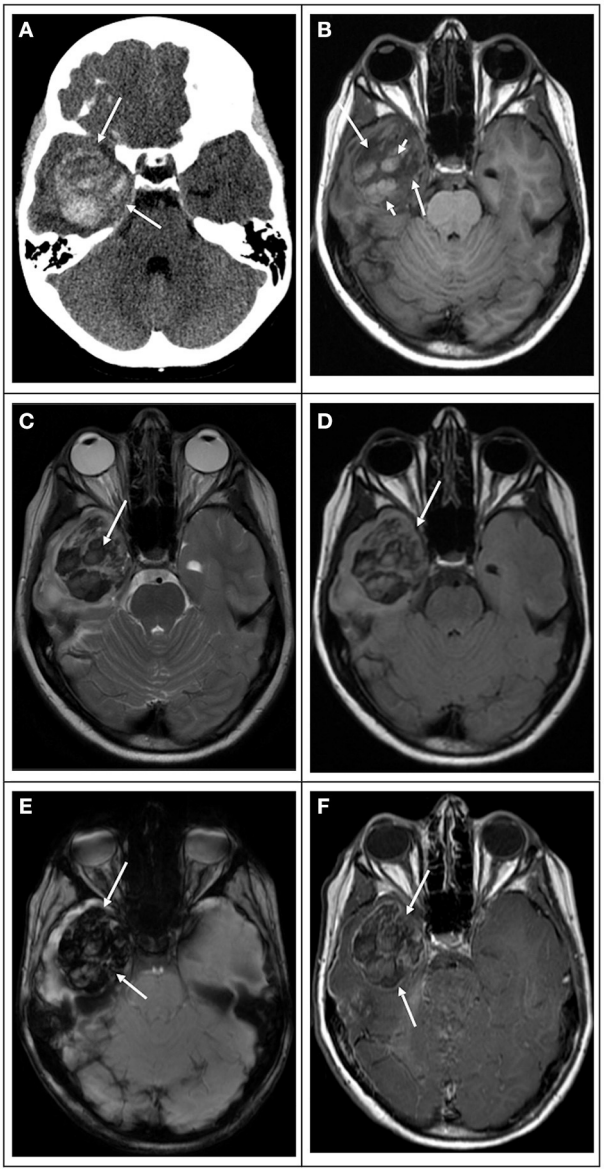

FIGURE 8 | 10-year-old male with worsening headaches and papilledema due to a right temporal lobe "glioblastoma". **(A)** Computed tomography image in the axial plane shows a heterogeneously hyperdense area in the right temporal lobe in keeping with a diffusely hemorrhagic lesion. At this point, the differential includes vascular lesions or tumors. **(B)** T1 weighted image in the axial plane shows that the lesion is heterogeneous with mixed signals. The tumoral bed is hypointense (white arrows) with scattered hyperintensity components due to intratumoral hemorrhage (white arrowheads). **(C)** T2 weighted image and **(D)** FLAIR images in the axial plane show that the bulk of the lesion is hypointense due to diffuse intratumoral hemorrhage. **(E)** Susceptibility weighted image in the axial plane shows extensive signal drop within the tumoral bed (white arrows) in keeping with diffuse hemorrhage. **(F)** T1-weighted contrast-enhanced image in the axial plane shows that the tumor enhances heterogeneously. The mass has thin peripheral enhancement (arrowhead) with internal variable minimal enhancement due to hemorrhage and necrosis.

TABLE 1 | Typical computed tomography and magnetic resonance imaging features of pediatric glioblastomas.

Imaging features	
Generalities	- Variable size (typically large) - Poorly marginated - Heterogeneous - Mass effect - Variable hemorrhage - Variable vasogenic edema
Location	- Cerebral hemispheres (most common) - Brainstem - Cerebellum - Spinal cord
Computed tomography	
Non-enhanced	- Variable areas of hyperattenuation (hemorrhage/hypercellularity) - Hypoattenuation → necrosis or surrounding edema
Contrast enhanced	- Variable enhancement - Minor to marked - Solid to heterogeneous - Necrotic lesions may present ring enhancement
Magnetic resonance imaging	
T1WI	- Iso- to hypointense (relative to gray matter) - Edema and necrosis → Hypointense
T2WI	- Hyperintense (relative to gray matter) - Variable vasogenic edema → hyperintense
FLAIR	- Hyperintense (relative to gray matter) - Variable vasogenic edema → hyperintense
Contrast enhanced T1WI	- Variable - Complex - Thick irregular rim (typical) - No enhancement (rare)
Susceptibility weighted imaging and T2* weighted imaging	- When neoplasms are complicated by hemorrhage → low signal
Diffusion weighted imaging	- Variable restricted diffusion - Restricted diffusion (typical in solid areas)
Dynamic susceptibility contrast	- ↑ CBV
Dynamic contrast-enhanced	- ↑ K^{trans} - ↑ K^{ep} - ↑ Ve - ↑ CBV - ↑ CBF
Arterial spin labeling	- ↑ CBF
Proton 1/H Magnetic resonance spectroscopy	- ↑ Choline - ↓ NAA - ↑ Lactate

T1WI, T1 Weighted imaging/T2WI, T2 Weighted Imaging. ↑, high; ↓, low; →, resulting in.

CT findings of "pediatric glioblastomas" can be seen in the **Table 1**.

Magnetic Resonance Imaging

Magnetic Resonance Imaging (MRI) is the imaging modality of choice in the evaluation of "pediatric glioblastomas." It delivers superior spatial and contrast resolution, allowing improved non-invasive assessment of the tumor and surrounding brain, and helps with neurosurgical and radiation planning (36). MRI findings of "pediatric glioblastomas" are not specific. Masses are typically heterogeneous with indistinct margins, mass effect on surrounding structures, and a variable degree of enhancement (complex, variable, or rarely absent). Relative to gray matter, "pediatric glioblastomas" may demonstrate iso- to hypointense T1 signal and heterogeneously hyperintense T2 signal with surrounding edema, which is readily evident on fluid attenuation inversion recovery (FLAIR) images (35, 37). When the neoplasms are complicated by hemorrhage, different signal characteristics can be seen, such as T1 hyperintense, T2 hypointense, low signal on T2*, and susceptibility-weighted imaging. Typical conventional MRI features of "pediatric glioblastomas" can be seen in the **Table 1**.

A distinction must be made between contrast enhancement and increased perfusion. The degree and extent of contrast enhancement reflect pathologic changes of the blood-brain barrier and extravascular leakage of contrast (38, 39). The blood-brain barrier breakdown can result from the destruction of normal capillaries by a neoplastic process or from the pathologic structure of the vascular walls of newly formed abnormal capillaries. The degree of perfusion reflects tumor vascularity, which may or may not be associated with blood-brain barrier breakdown (38, 39).

"Pediatric glioblastomas" are known to be less common than adult glioblastomas. As stated previously, there are no gross and microscopic pathology differences between adult and pediatric glioblastomas. However, there are major molecular and genetic differences between, which is unequivocally demonstrated and established by the WHO/CNS/5. In addition, these tumors also differ in terms of cause-specific survival and overall survival (9).

Literature comparing imaging differences between adult and pediatric glioblastomas is very scarce. Both tumors are typically heterogeneous and may demonstrate mass effect, vasogenic edema, restricted diffusion, and contrast enhancement. "Pediatric glioblastomas" may present as masses with more solid enhancement, whereas adult glioblastomas have a higher tendency to be necrotic, and therefore more commonly present as rim enhancing lesions.

Advanced MRI Neuroimaging

The number of studies and evidence supporting the utility of advanced MRI neuroimaging techniques in children is much more limited than in adult glioblastomas, but the general principles similarly apply. Most of the literature on advanced MRI neuroimaging techniques in children is with limited affirmed clinical validation if analyzed in isolation. Thus, these techniques should be applied in conjunction with conventional imaging, under a multiparametric approach, for the imaging evaluation of brain tumor diagnosis and follow-up.

Diffusion-Weighted Imaging

Diffusion-weighted imaging (DWI) is a well-known clinical imaging technique applied in the study of brain tumors. However, there are very few studies dedicated specifically to using diffusion-weighted imaging (DWI) and apparent diffusion coefficient (ADC) measurements in assessing "pediatric

glioblastomas." DWI is a superb technique that measures the degree of movement of water molecules and probes their relation to the surrounding environment in both the normal and diseased states. Quantitative DWI information on the extent of the movement of water molecules can be obtained by the apparent ADC calculation (40, 41).

DWI is a mainstay in routine brain tumor MRI, typically acquired with two b-values for ADC calculation (b = 0 and b = 1,000 s/mm^2). DWI is very helpful in pointing toward the diagnosis, providing information regarding tumor grade and type, and monitoring treatment response (42). In addition, several authors have shown that the different components of the tumors, surrounding edema, and normal surrounding white matter may have distinct ADC values (40, 43–45).

Several authors have demonstrated the utility of DWI in the differential diagnosis of cystic masses (46–49). Cystic and necrotic components of a tumor have higher ADC values, reflecting the increased water movement characterizing these components. Enhancing components of HGGs typically show lower ADC values than non-enhancing tumor and peritumoral edema (40). DWI often demonstrates restricted (reduced) diffusion (low ADC values) in solid portions of HGGs, in keeping with high cellular density and/or high nuclear-to-cytoplasm ratios (50). Restricted diffusion can be observed in some gliomas, notably higher grade tumors such as anaplastic astrocytomas, glioblastomas, diffuse midline gliomas, and anaplastic ependymomas.

DWI has been used to distinguish areas of peritumoral neoplastic cell infiltration from peritumoral edema, a critical distinction when dealing with HGGs (40). In addition, ADC values can be used to distinguish normal white matter from necrotic or cystic areas, edema, and solid-enhancing tumors (51). However, the distinction between infiltrating tumors from edema or nearby normal-appearing brain is sometimes inaccurate in glioblastoma, as small amounts of infiltrating tumor cells may be present in these areas, but not in enough quantities to significantly alter the diffusion parameters. DWI may also aid in the differentiation of abscesses from necrotic or cystic brain tumors such as HGGs (52, 53).

ADC is negatively correlated with cell proliferation indices such as Ki-67 (54). The signal characteristics on DWI and ADC maps can be strongly correlated to grade in pediatric brain tumors, and they may assist with preoperative diagnostic predictions (55). In addition, ADC measurements can be used to differentiate between HGGs from low-grade gliomas. Wang et al. (56), in a recent meta-analysis including 1,172 patients, found an area under the curve (AUC) for *b* values of 1,000 and 3,000 s/mm^2 to be of 0.91 and 0.92, respectively. Their results demonstrated that ADC measurements had high diagnostic performance in discriminating HGGs from low-grade gliomas.

A study by Chang et al. (35) involving 11 patients with glioblastomas found that the DWI signal intensity in the solid portion of the tumor was hyperintense compared to the white matter. The ADC values for the solid tumor component ranged from 0.53 to 1.30 $\times$ 10^{-3} mm^2/s (mean, 1.011 $\pm$ 0.29 $\times$ 10^{-3} mm^2/s) and for white matter from 0.60 to 0.98 $\times$ 10^{-3} mm^2/s (mean, 0.824 $\pm$ 0.130 $\times$ 10^{-3} mm^2/s). In one of the patients, a recurrent glioblastoma demonstrated increased DWI signal in the tumoral bed months after total gross removal of the tumor (35). Tumor recurrence has been reported to have significantly lower ADC values than radiation necrosis (57, 58). DWI and ADC calculation may be utilized as a surrogate marker for monitoring the response of tumor therapy (59, 60). For example, Chenevert et al. (59) found a rapid increase in the mean ADC values shortly after treatment initiation, and the magnitude of the diffusion changes corresponded with clinical outcome.

Most published experience in applying DWI in pediatric tumors has focused mainly on posterior fossa tumors. Higher ADC values at the baseline have been reported to have a more favorable outcome in patients of diffuse midline glioma (61–63). In addition, baseline ADC values can be used as an outcome predictor in these tumors, although diffusion-derived metrics showed no significant association with overall survival (64).

Diffusion Tensor Imaging

Literature specifically dealing with diffusion-tensor imaging (DTI) in assessing "pediatric glioblastomas" is quite scarce. DTI is a more sophisticated quantitative analysis of diffusion-based imaging. In DTI, water movement is measured in several directions within the tissue from which tensors can be fit with directionality information. When these measurements are combined and analyzed, in addition to an averaged measure of water diffusion for each voxel (ADC), individual and summary measures of how water diffusion varies along different axes (fraction anisotropy—FA) can be calculated. Both ADC and FA reflect the microstructure of the tissue in which they are measured (65). For example, FA estimates the amount and the direction of diffusion restriction of water molecules along myelinated white matter tracts, which is in turn partly influenced by the degree of preserved and destroyed white matter tracts within the tumoral area (66–68).

DTI can demonstrate white matter tracts and their structural changes related to different brain pathologies. DTI describes the three-dimensional diffusion phenomenon of water molecules about their microenvironmental properties allowing a unique description of the space where this molecular movement occurs. This model provides an *in-vivo* demonstration of the complex ultrastructural organization of the white matter and structural changes due to tumor invasion. Current DTI and magnetic resonance tractography applications allow accurate graphic delineation of the eloquent white matter tracts and their relation with tumoral tissue, which may be essential in surgical treatment planning and useful in assessing post-therapeutic changes (69). Furthermore, DTI in mapping white matter tracts may sometimes enable resection of tumors previously deemed unresectable, such as well-defined pilocytic astrocytomas in the thalamus (**Figure 9**) (70).

Several authors demonstrated that the evaluation of the peritumoral area and the differentiation between tumoral infiltration and pure vasogenic edema might be enhanced by DTI analysis (68, 71–76). Other authors quantified tumoral and peritumoral FA in low- and high-grade gliomas with low-grade gliomas showing higher FA values than HGGs (76–80). The more conspicuous FA reduction in high-grade compared to low-grade

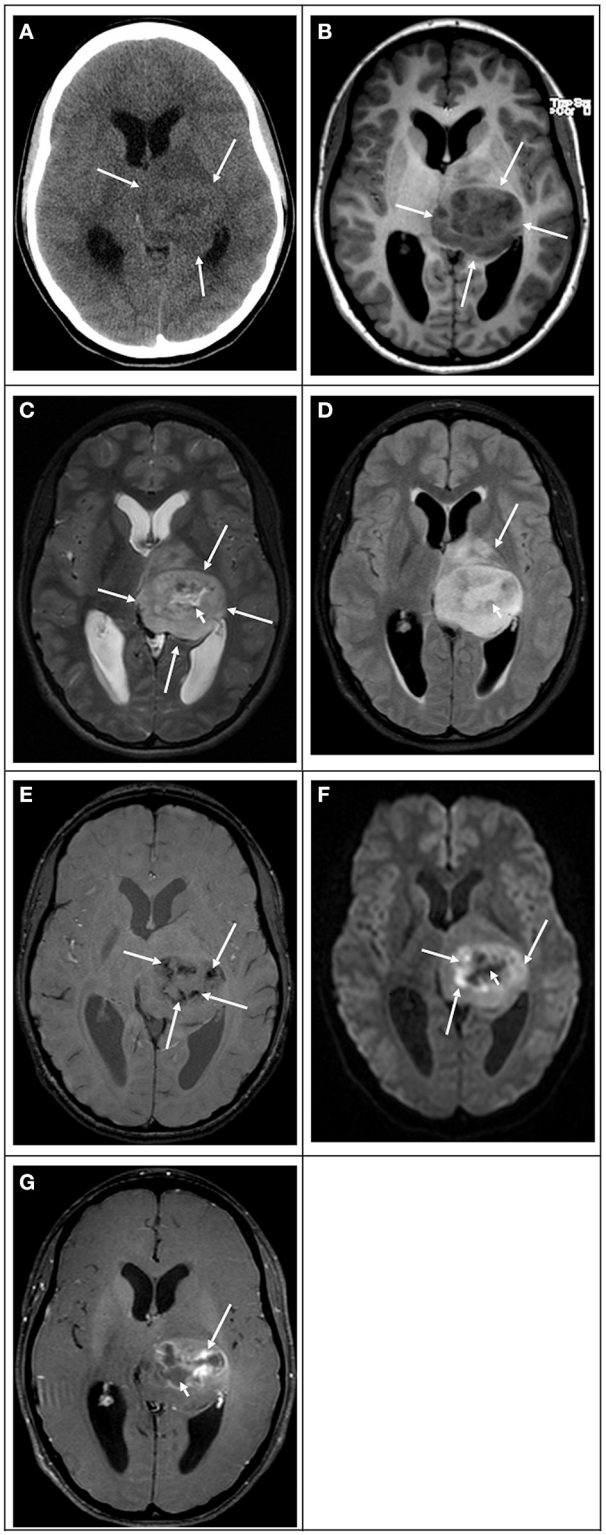

FIGURE 9 | 13-year-old female with blurry vision, facial weakness, and right-sided paresthesias due to a left thalamic glioblastoma. **(A)** Computed tomography image in the axial plane shows an ill-defined slightly hyperdense mass in the left thalamus. **(B)** T1 weighted image in the axial plane shows that *(Continued)*

FIGURE 9 | the lesion is well-demarcated with heterogeneous mixed-signal, predominantly hypointense (white arrows). **(C)** T2 weighted image and **(D)** FLAIR images in the axial plane show that the bulk of the lesion is hyperintense (white arrows) with a central component showing even higher signal. **(E)** Susceptibility weighted image in the axial plane shows irregular signal drop foci within the tumoral bed (white arrows) in keeping with hemorrhage. **(F)** Diffusion-weighted image in the axial plane shows that the lesion is heterogeneous in signal. The periphery of the mass is isointense to the normal brain parenchyma. The center of the mass shows a hypointense signal (white arrow). Surrounding the center, there is an irregular hyperintense thick rim with low values in the ADC map (not shown) in keeping with restricted diffusion. **(G)** T1-weighted contrast-enhanced image in the axial plane shows that the tumor enhances heterogeneously. The thick irregular area that shows restricted diffusion enhances avidly (white arrows) with no enhancement centrally due to necrosis.

tumors is likely due to the higher incidence of cystic and necrotic changes leading to loss of white matter tract organization and integrity. Besides, some researchers also suggest that FA is more sensitive than ADC in the early detection of white matter tumoral involvement (67, 68, 78). White matter tract changes can occur due to fiber destruction (reduced absolute number), fiber edema (reduced density and higher water content), or fiber degradation (abnormal fibers with a normal number and density) (81, 82). In addition, qualitative assessment of DTI maps can suggest the different types of tumoral involvement such as displacement, edema, infiltration, destruction, or a combination of two or more, but one has to be careful of the technical limitations that may lead to false-negative tract visualization (68, 83–85).

Gauvain et al. (65) demonstrated the utility of ADC obtained via DTI assessing pediatric brain tumors. ADC correlated significantly with tumor cellularity and the calculated total nuclear area (nuclear area of each tumor cell type multiplied by the number of cells per high-power field). Brunberg et al. (51) found differences between ADC and FA from normal white matter and solid-enhancing tumor, cystic and necrotic areas, and regions of edema. However, they did not find differences in ADC values between various glioma subtypes.

DTI is also valuable in the assessment of postoperative changes. For example, DTI can compare the status of eloquent cortical pathways before and after the surgery delivering information to the neurosurgeon about the damaged and preserved tracts postoperatively (86–88). DTI also allows detecting and monitoring treatment-induced neurotoxicity in cerebral white matter (87, 89–92). Several studies investigating the effect of cranial irradiation and chemotherapy indicate a prominent decrease in mean FA values that are more severe in the frontal lobes compared with the parietal lobes despite the same radiation dose, suggesting regional susceptibility in the frontal lobe (89–94). Mabbott et al. (93) demonstrated that medulloblastomas treated with cranial-spinal radiation therapy show abnormal FA and ADC in the normal-appearing white matter. Their study observed damaged white matter microstructure and/or fiber integrity as demonstrated by FA and ADC for multiple regions within the cerebral hemispheres. Further, decreased FA and increased ADC were related to lower intellectual outcomes in patients relative to age-matched

controls. A significant advantage of DTI is that it provides measures sensitive to underlying tissue properties, and hence potential damage may be evident even within the normal-appearing white matter.

Perfusion Weighted Imaging

Perfusion weighted imaging (PWI) describes a group of valuable techniques that can non-invasively evaluate the cerebral hemodynamic status and, in many patients, can predict tumor grade and behavior (35, 51). The main clinically utilized PWI techniques include dynamic contrast-enhanced (DCE), dynamic susceptibility contrast (DSC), and arterial spin labeling (ASL). The main parameters derived from these techniques include cerebral blood volume (CBV), cerebral blood flow (CBF), and mean transit time (MTT), among others. Derivation of absolute perfusion parameters may be challenging at times, and therefore, relative CBV (rCBV) or relative CBF (rCBF) may be used when involved regions are normalized to other normal-appearing brain structures.

In general terms, most HGGs typically show higher perfusion (increased CBV and/or CBF) than low-grade gliomas (**Figure 10**). Nevertheless, compared to adults, the higher prevalence in children of malignant non-glioma neoplasms and contrast-enhancing low-grade tumors may confound the accuracy of grading of brain neoplasms using PWI measures in certain types of neoplasms.

Dynamic Susceptibility Contrast (DSC) Perfusion

DSC perfusion is the most widely used PWI technique and requires high-flow contrast injection, often using power injectors, and large-bore intravenous access, which may pose challenges in young children and infants (95). Other drawbacks of the DSC perfusion method are calcification and hemorrhage-induced susceptibility within the tumor and blood-brain barrier breakdown-related contrast leakage (96). Despite this, DSC is feasible and has been performed even in young children (97).

There is an overall significant difference in rCBV and CBF between pediatric low-grade gliomas and HGGs (98). In addition, in the study by Chang et al. (35), rCBV maps helped detect highly vascular areas correlated with areas of enhancement in three of their patients. rCBV maps may also demonstrate increased microvascularity even in the absence of enhancement in some patients with "glioblastoma" (35).

Dynamic Contrast Enhancement (DCE)

DCE may be used as a potential alternative or complementary technique to DSC. It has been mainly used in adult brain tumors, with few studies performed in children (99, 100). DCE provides signal intensity–time curve reflecting a combination of tissue perfusion, microvessel permeability, and extravascular-extracellular space characteristics (101, 102) thus allowing for a multiparametric characterization of tumor microvasculature and leakage quantitation.

The advantages of DCE over DSC are fewer susceptibility artifacts and the quantification of blood-brain barrier (BBB) integrity; indeed, the leading interest for DCE-derived metrics was initially focused on the volume transfer constant (Ktrans),

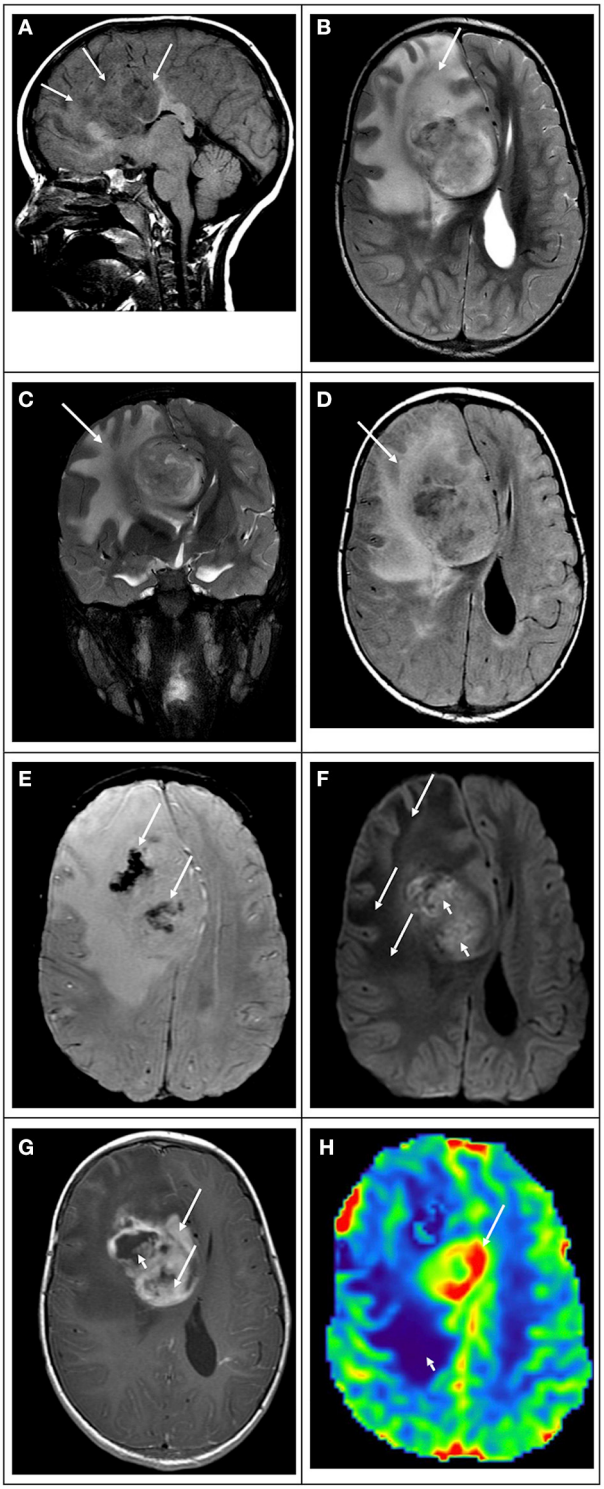

FIGURE 10 | 5-year-old male with headaches and confusion due to a right frontal "glioblastoma." **(A)** T1 weighted image in the sagittal plane shows that the lesion is heterogeneous, ill-defined with mixed-signal, predominantly hypointense, and infiltrates the corpus callosum (white arrows). **(B)** T2 weighted image in the axial plane, **(C)** T2 weighted image in the coronal plane, and **(D)** FLAIR image in the axial plane show that the bulk of the lesion is

(Continued)

FIGURE 10 | hyperintense, with marked mass effect and vasogenic edema (white arrows). **(E)** Susceptibility weighted image in the axial plane shows irregular areas of signal drop within the tumoral bed (white arrows) in keeping with hemorrhage. **(F)** Diffusion-weighted image in the axial plane shows that the lesion is heterogeneous in signal. The extensive area of vasogenic edema shows low signals (white arrows). The midline component shows areas of hyperintense signal with low values in the ADC map (not shown) in keeping with restricted diffusion. **(G)** T1-weighted contrast-enhanced image in the axial plane shows that the tumor enhances heterogeneously. The midline component of the mass shows thick and irregular enhancement (white arrows) with no foci of enhancement in areas of necrosis (white arrowhead). **(H)** Arterial spin labeling perfusion image in the axial plane shows that the midline component has marked increased perfusion (white arrow). Note that the area of vasogenic edema is not associated with increased perfusion (white arrowhead).

a permeability marker correlating with BBB disruption (102) and malignancy (103). Conversely, DSC typically offers better temporal resolution than DCE, allowing potentially better blood volume estimation (104).

A small study demonstrated that DCE could be used to assess tumor grade in pediatric brain tumors, although not all were gliomas (100). Transfer constants from and into blood plasma (K_{trans} and K_{ep}) and extracellular extravascular volume fraction (V_e) showed a sensitivity of 71–76% and a specificity of 82–100% in separating low-grade from high-grade tumors. In another study, fractional plasma volume (V_p) was significantly different between high and low-grade tumors, but K_{trans}, K_{ep}, and V_e were not statistically different.

In a study of 64 pediatric brain tumor patients, Gupta et al. (105) demonstrated that DSC and DCE helped differentiate low-grade tumors, high-grade tumors, and amongst major posterior fossa tumors. rCBV and fractional plasma volume measures differed significantly between high-grade and low-grade tumors. High-grade tumors could be differentiated from low-grade tumors with an rCBV cutoff value of 2.41 and 88.6% sensitivity and 65% specificity. There was no significant difference in Ktrans, Kep, or Ve between these two groups of tumors (105).

Arterial Spin Labeling (ASL) Perfusion

ASL, a PWI technique that uses magnetically labeled water as endogenous contrast, has been used to study pediatric brain tumors (106). However, ASL is limited by a low signal-to-noise ratio, often the need for greater magnetic field strength, and the presence of susceptibility (105).

ASL is considered a reliable PWI technique in evaluating tumor perfusion and predicting glioma grade in adults (107). ASL is advantageous for children since it lacks contrast injection, the need for high flow injections, and has easier potential for CBF quantification. Also, ASL can be repeated if patients move (95). Moreover, younger children's immature paranasal sinuses also result in better ASL image quality, with potentially lesser degrees of distortion artifacts in the frontal and inferior brain regions (108).

In a study of ASL in pediatric brain tumors by Yeom et al. (95), the authors demonstrated that the technique could reasonably distinguish high-grade from low-grade tumors. Their results in "glioblastoma" patients indicated that CBF in the tumoral bed might have a wide range, which suggests vascular heterogeneity similar to what is seen in patients with adult glioblastomas. According to these authors, ASL maps can depict tumor vascular heterogeneity and indicate higher tumor blood flow regions offering a valuable parameter to potentially direct biopsy of higher vascular density or more malignant regions (95). Dangouloff-Ros et al. (106) have confirmed that pediatric high-grade brain tumors generally display higher CBF than low-grade tumors on ASL. Low-grade gliomas had a significantly lower absolute CBF and rCBF than high-grade tumors (CBF: median, 29 mL/min/100g vs. median, 116 mL/min/100 g; $P < 0.001$) (rCBF: median, 0.50 mL/min/100 g vs. median, 2.21 mL/min/100 g; $p < 0.001$). There was no significant difference between the various high-grade neoplasms (grade 3 gangliogliomas, glioblastomas, atypical teratoid rhabdoid tumor, and grade 3 ependymomas) (106). Morana et al. (109) compared ASL and DSC in 37 children with low-grade and HGGs obtained on a 1.5T scanner. Normalized CBV values in the most perfused area of each neoplasm were compared with normalized CBF from DSC and normalized CBF from ASL data and designated with a WHO tumor grade. According to the authors, normalized ASL provides comparable results to DSC and may help distinguish between low-grade and HGGs (109).

A meta-analysis of eight studies assessing pediatric glioma grading using ASL showed many bias and applicability issues. For low and high-grade tumor differentiation, the pooled sensitivity ranged from 0.69 to 0.92, and specificity ranged from 0.63 to 0.93 (110). Relative CBF demonstrated less variability than absolute CBF, as would be expected given the variability of acquisition techniques. In another meta-analysis, although not only composed of gliomas, normalized cerebral blood flow derived from ASL perfusion had 83% accuracy in separating low and high-grade pediatric brain tumors (111). Other authors have also confirmed that ASL can be a potentially valuable tool to differentiate low from high-grade tumors (106, 111–114) and that the technique has comparable results with DSC in the differentiation between low and HGGs (115).

Proton ^{1}H Magnetic Resonance Spectroscopy

Proton ^{1}H MRS is a non-invasive technique that has been used to evaluate tissue metabolism in a wide variety of diffuse and focal CNS diseases, including brain tumors (116). Several brain metabolites such as choline (Cho), N-acetylaspartate (NAA), creatine (Cr), myoinositol (mI), and lactate can show abnormalities in the context of brain neoplasms. For example, in gliomas, as tumor grade increases, there is an increase in the Cho/NAA ratio, reflecting increased metabolic activity. High Cho reflects rapid membrane turnover with glial proliferation, whereas low NAA reflects decreased normal neurons as they are replaced by neoplastic cells in the MRS voxel (35).

Multiple studies have demonstrated that a common feature of many rapidly growing tumors is a decreased NAA/Cr ratio and an increased lactate level (**Figure 11**) (37, 117–122). Cr concentration is supposedly rather stable over time,

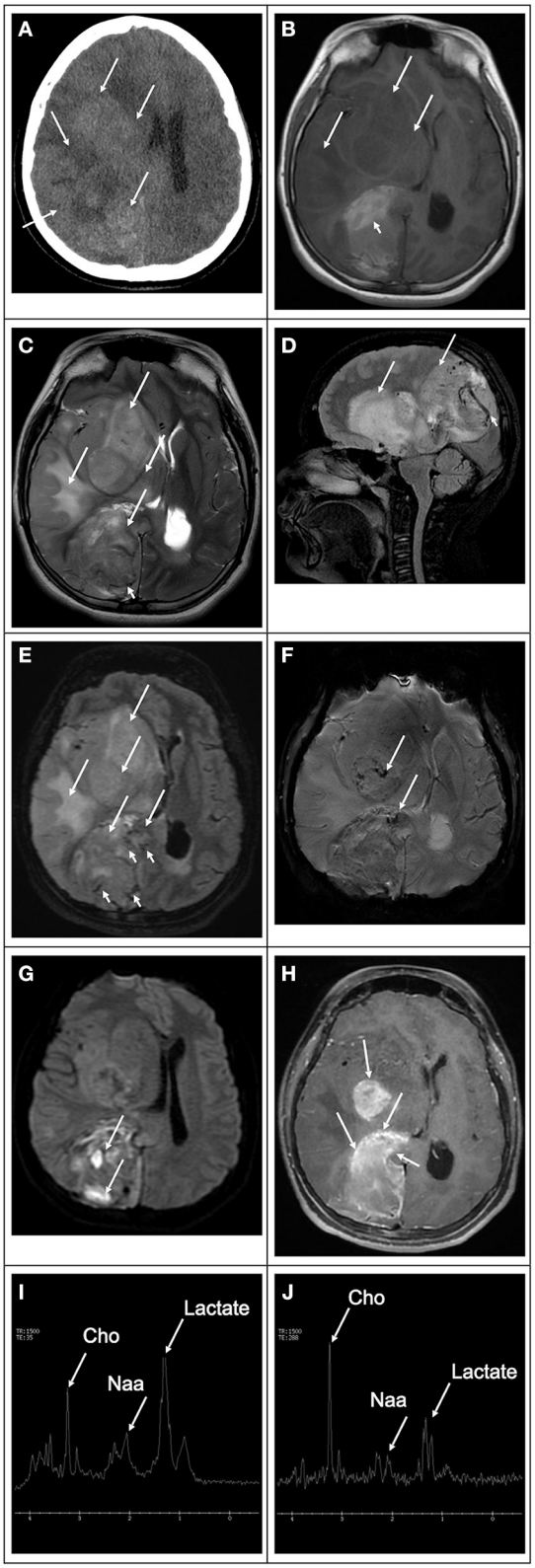

FIGURE 11 | 8-year-old- female with a hemispheric glioblastoma. **(A)** Computed tomography image in the axial plane shows an extensive mass in *(Continued)*

FIGURE 11 | the right hemisphere (white arrows), causing mass effect, compression of the right lateral ventricle, and midline deviation. The lesion is heterogeneous with areas of hyper and hypodensity compatible with hemorrhage and edema, respectively. **(B)** T1 weighted image in the axial plane shows that the bulk of the lesion is hypointense (white arrows). There is a component of the mass that is high in signal intratumoral hemorrhage (white arrowhead). **(C)** T2 weighted image in the axial plane. **(D)** T2 weighted image in the sagittal plane, and **(E)** FLAIR image in the axial plane show that the lesion's bulk is hyperintense with marked mass effect vasogenic edema (white arrows). In addition, there is marked increased vascularity in the component located in the occipital region (white arrowheads). **(F)** Susceptibility weighted image in the axial plane shows scattered signal drop foci within the tumoral bed (white arrows) in keeping with hemorrhage. **(G)** Diffusion-weighted image in the axial plane shows that the lesion is heterogeneous in signal. The bulk of the lesion is isointense to the normal brain parenchyma with scattered hyperintense foci due to intratumoral hemorrhage (white arrows). **(H)** T1-weighted contrast-enhanced image in the axial plane shows that the tumor has multiple enhancing components heterogeneously. The mass has avid peripheral enhancement with internal no enhancing elements in keeping with necrotic tissue. **(I,J)** Magnetic resonance spectroscopy obtained with short and long echo times showing marked decreased N-acetylaspartate peak, which corresponds to neuronal loss, increased choline peak, which corresponds to increase cell membrane turnover in an environment of rapid growing neoplastic tissue, and increased lactate peaks due to anaerobiosis and necrotic changes.

so it is used as a denominator to report the metabolite ratios in most studies. Elevated lipid-lactate peaks are more frequently found in HGGs, particularly in those undergoing central necrotic changes. Mixed MRI spectral patterns can reflect the known heterogeneity seen in many tumors (123). Importantly, patients with diffuse midline gliomas showing high levels of lactate on MRS are associated with poor prognosis (124).

Proton ^{1}H MRS may be used as an adjunct tool in the evaluation of "pediatric glioblastomas." This technique has been applied for the initial diagnosis of brain masses, biopsy guidance, tumor grading, treatment response assessment, recurrence vs. treatment effects detection, and a prognostic marker in brain tumor patients. Higher Cho/Cr and Cho/NAA ratios are typically observed in HGGs compared to low-grade tumors and non-neoplastic masses in broad terms, although exceptions do occur (125). mI is often elevated in low-grade diffuse gliomas, unlike HGGs (123). Previous studies have shown that higher Cho/Cr and Cho/NAA ratios portray a poorer prognosis in pediatric brain tumors (126, 127). Other studies have looked at lactate/NAA ratios and normalized indices combining choline and lipid+lactate levels, demonstrating strong correlations with predictors of outcome (128, 129).

Pathogenic variants in the IDH1 and IDH2 can lead to the accumulation of abnormally high D-2-hydroxyglutarate (2-HG) levels in certain brain tumors. This increased 2-HG level may be detected *in-vivo* by specialized advanced spectral-edited MRS and used to characterize glial neoplasms. IDH1/2 pathogenic variants are considered prognostic biomarkers in subjects with glioma and are associated with more prolonged overall survival (24, 130). A meta-analysis demonstrated excellent sensitivity and specificity of 2-HG MRS to predict *IDH* mutant gliomas (131).

Chemical Exchange Saturation Transfer

Chemical exchange saturation transfer (CEST) is a recently developed technique that can identify very low concentrations of molecules by the presence of groups with exchangeable protons, such as hydroxyls, amides, and amines (132). The vast majority of studies on CEST and "glioblastomas" have been performed in adults. Future studies on "pediatric glioblastomas" are needed to confirm its utility in this age group. CEST signal is affected by endogenous proteins and metabolites such as glutamate, lactate, mI, and glucose that play crucial roles in tumor development, growth, and progression. Hence, studying these macromolecules and metabolites may help understand the brain tumor microenvironment and evaluate response to targeted therapies. Studies have demonstrated that CEST imaging can reasonably differentiate malignant neoplastic infiltration from peritumoral vasogenic edema, differentiate histopathological grades, and discriminate HGGs from the brain lymphomas (133). In addition, CEST can also reliably distinguish recurrent tumors from radiation necrosis (133). Moreover, the intensity of the CEST signal was shown to decrease in irradiated tumors at 3 days and 6 days post-treatment periods relative to baseline, suggesting that CEST may potentially help evaluate treatment response in brain tumors. CEST signal may potentially be an imaging biomarker for distinguishing true progression from pseudoprogression in "glioblastoma" patients (134).

Amide proton transfer (APT) imaging is a CEST technique that measures a decrease in bulk water intensity due to chemical exchange with magnetically labeled amide protons of endogenous proteins and peptides in tissues (135). Studies have shown the potential of APT-weighted imaging in delineating malignant neoplastic infiltration. In addition, the APT signal may also potentially be a valuable imaging biomarker for distinguishing true progression from pseudoprogression in glioblastoma patients (133). Studies have documented significantly higher APT signals in true progression cases than those with pseudoprogression (136). It is widely believed that active tumor cells express more protein species and higher concentrations of protein components, as shown by proteomics (136, 137) and proton MRS studies (138). In contrast to true progression, there are fewer mobile cytosolic proteins and peptides in regions of brain injury associated with pseudoprogression due to lower cellular density and disrupted cytoplasm. Collectively, these studies have indicated that APT based on CEST is fast emerging as a novel molecular MRI technique in neuro-oncology.

Multiparametric Analysis

Multiparametric analysis is an evolving method in which multiple quantitative MRI techniques are analyzed in combination to overcome the intrinsic limitations of conventional MRI and potentiate the individual value of each advanced MRI technique in isolation. For example, quantitative data obtained from metabolic and physiologic techniques such as DWI, DTI, DSC, DCE, ASL, or proton MRS can be variously combined and analyzed with multivariate logistic regression, analysis of variance, or artificial intelligence tools to determine the optimal parameter(s) and thresholds for addressing a specific question prediction.

Multiparametric MRI has been widely used to predict treatment response in glioblastoma patients, to differentiate glioblastoma from solitary brain metastasis (139), to differentiate radiation necrosis from a recurrent tumor (140), to assess tumor invasiveness (141), and to predict tumoral survival (142).

POSITRON EMISSION TOMOGRAPHY (PET)

Positron emission tomography (PET) is a nuclear medicine imaging modality that plays a vital role in evaluating brain tumors, including glioblastomas. PET, as a functional imaging technique, is typically used to complement anatomical imaging, capturing non-invasively functional and biochemical information about the tumor and its surroundings. This information is beneficial for tumor grading, differential diagnosis, tumor delineation, surgery planning, radiotherapy, and post-treatment monitoring follow-up (143). PET can probe the physiological milieu of neoplastic cells, such as glucose metabolism, protein synthesis, and DNA replication. There are multiple groups of PET radionuclide tracers typically used to evaluate tumor metabolism, including glucose metabolism tracers, amino acid tracers, and other miscellaneous tracers that can target various receptors or functions of the cells. These PET tracers are useful in demonstrating cellular proliferation, hypoxia sensing, and inflammation (144).

A typical and widely used glucose metabolism tracer is 18F-2-fluoro-2-deoxy-D-glucose ([18F]FDG). [18F]FDG is taken up by the glucose transporter, engaging in phosphorylation (the first step of glucose metabolism), and subsequently becomes trapped in the cell (145). [18F]FDG demonstrates avid uptake in the brain, which may limit the interpretation of tumors near or involving the gray matter (144). On the other hand, amino acid transport tracers exhibit lower uptake in normal tissue, being more sensitive than 18F-FDG in primary and recurrent tumors, and are helpful in differentiating recurrent tumors from treatment-induced changes (146). Typical amino acid analogs include [11C]11C-methyl-methionine ([11C]MET), 3,4-dihydroxy-6-[18F]-fluoro-L-phenylalanine ([18F]FDOPA), O-(2-[18F]-fluoroethyl)-L-tyrosine ([18F]FET), and deoxynucleoside bases such as [18F]fluoro-thymidine and [18F]clofarabine (143, 145).

[11C]MET is the most studied and validated amino acid tracer. It is an essential amino acid for protein synthesis and is considered more sensitive than [18F]FDG in delineation of tumors. [11C]MET is avidly taken up by glioma cells, with only a low uptake in normal cerebral tissue. Several studies have suggested that tumor uptake of [11C]MET mainly reflects increased amino acid transport (147). Its most important limitation is its very short life (144). 18F-labeled amino acids have been created to increase amino acid tracer half-life and utilization, namely [18F]FET and [18F]FDOPA. [18F]FET is a tracer for both HGGs as well as low-grade gliomas due to an efficient nucleophilic reaction, elevated uptake by tumor tissues, low uptake by inflammatory tissues, and high stability (148). [18F]FDOPA is incorporated into cells through amino

acid transporters that are overexpressed in gliomas, and its transport and uptake are independent of the blood-brain barrier (149). [18F]FDOPA has shown a significant correlation between WHO grade and the volume of MRI contrast enhancement and volume of T2 hyperintensity (150). Another radiotracer, [18F]fluorothymidine ([18F]FLT), is a thymidine analog uptaken in tissues after phosphorylation by the thymidine kinase (151). Thymidine kinase is considered a critical enzyme in the DNA salvage pathway. Nucleotide salvage pathways recover bases and nucleosides that are formed during the degradation of RNA and DNA (152). Since [18F]FLT has lower uptake in the normal brain, it correlates well with proliferative tissue markers (153). The radiotracer has been used in diagnosis and assessment of glioma grading, in differentiating tumor recurrence from radionecrosis, in assessing response to treatment, and in predicting overall survival (154).

PET tracers such as the [18F]Fluoromisonidazole, which sense oxygen levels in cells, can be used to visualize hypoxia. Hypoxia is an essential feature of most solid tumors (153, 155). For example, in a hypoxic tumor microenvironment, radiation therapy could be more effective at a higher dose (143). Inflammation, a component of the immune response, is well-known to occur in glioblastomas. Translocator protein (TSPO) is a component of the mitochondrial membrane protein responsible for cholesterol transport and responds to cell stress. Broadly, TSPO is treated as a biomarker sensitive to pro-inflammatory stimuli (143). Moreover, TSPO PET imaging was found to be correlated with outcome (156).

As neuro-oncology treatment advances and therapies centered on tumor biomarkers are discovered, the development of selective PET tracers can dramatically enhance the efforts toward personalized medicine (143).

TREATMENT

The standard of care for adult glioblastomas involves surgery with maximal safe tumor resection followed by chemoradiation as adjuvant treatment (157). There is not such a well-defined standard of care for "pediatric glioblastomas." Regarding surgery, substantial evidence recommends the adoption of maximal safe surgical resection of the visible tumor, since prognosis correlates positively with the amount of tumor resected (5, 6, 16, 158, 159). However, the choice of adjuvant treatment is debated due to the potentially deleterious effects of radiation treatment in the early developing brain and inconsistent results of various chemotherapy regimens (9). Radiation therapy has become the standard of treatment, particularly for those children older than 3 years with a newly diagnosed "glioblastoma" (36). Younger children, however, are more susceptible to the adverse effects associated with radiation therapy and are typically treated with chemotherapy alone and radiation-sparing approaches (160–162).

Novel classes of treatments such as molecular-targeted therapy and immunotherapy have been recently incorporated as new weapons in the arsenal of treatment of oncology patients (163). Immunotherapy agents include typically chimeric antigen receptor (CAR) T-cell therapy, immune checkpoint inhibitors, virotherapy, cancer vaccines, and dendritic cell therapy. Molecular-targeted therapy consists of drugs or other substances that target specific molecules involved in the growth and spread of cancer cells (164). The most common targets for molecular-targeted therapy in pediatric brain tumors, in particular, HGGs and other high-grade tumors, are the tyrosine kinase (165), tumor-specific surface proteins (monoclonal antibodies) (166), vascular endothelial growth factor (167), platelet-derived growth factor and epidermal growth factor, PI3K-mTOR pathway (mostly animal model studies) (168), ERK-RAS-RAF mitogen-activated protein kinase pathway (BRAF mutation) (169), e PI3K/AKT pathway, gene fusions (170), Sonic Hedgehog pathway (171), and epigenetic targets (DNA methylation, chromatin modeling, and histone modifications signaling) (172). Despite multiple clinical trials in pediatric brain tumors, molecular-targeted therapy, with some exceptions, has not yet made a major impact on survival or, for that matter, quality-of-life for children with brain tumors (164). However, there remains great promise for the future as more agents are developed and included in clinical trials.

CARs are synthetic receptors composed of three major components (an extracellular tumor-specific antibody, an intracellular signaling structure, and a transmembrane domain serving as a bridge), which are typically added to a T cell, augmenting its function (173–175). These receptors allow T cells to recognize and destroy specific cancer cells without the major histocompatibility complex (MHC) presentation (176). In normal conditions, T cells require costimulation by the antigen-presenting cell to exert their cytolytic activity (177). This method has had tremendous success in treating leukemias. CAR T cell administration can be made hematogenously, or via the cerebral spinal fluid, or locally in the tumor cavity. Brain tumors are currently one of the most common solid tumor types undergoing clinical trial testing for CAR T cell efficacy and have shown early promise in treating "glioblastomas" (178, 179). Multiple clinical trials are evaluating the efficacy of CAR T cell therapy in solid tumors. However, none are FDA approved yet.

Checkpoint inhibitors are a group of drugs that target signaling pathways involved in the modulation of host immune responses as part of the normal regulation of immunity and establishment of tolerance. However, neoplastic cells are known to block these checkpoints and suppress the host's immune response, bypassing immune recognition and destruction (180). Exhaustion is a phenomenon that occurs during cancer progression, which refers to immune cell desensitization. At exhaustion, T cells are unable to kill malignant cells (181, 182), which can occur when neoplastic cells upregulate inhibitory receptors such as programmed cell death receptor-1 ligand (PD-L1) and cytotoxic T lymphocyte antigen-4 (CTLA-4) (183). Checkpoint inhibitors seek to reverse this inhibition so that an immune response can be mounted against the malignant cells (180). Researchers have shown that 75–100% of gliomas in a sample of patients exhibited PD-L1 expression, which correlated with the severity of the disease (184, 185).

There are several studies describing the efficacy and side effect profile of checkpoint inhibitors in pediatric patients.

A clinical trial conducted by Gorsi et al. (186) in recurrent or refractory pediatric brain tumors treated with the immune checkpoint inhibitor nivolumab demonstrated transient partial responses in patients with positive PD-L1 expression and higher tumor mutation burden. Nivolumab was well-tolerated with some transient partial responses in patients with positive PD-L1 expression and a higher tumor mutation burden. Median survival for PD-L1 positive patients was 13.7 weeks vs. 4.2 weeks for PD-L1 negative patients ($\rho = 0.08$). These findings suggest that only tumors with elevated PD-L1 expression and tumor mutation burden may benefit from immune checkpoint inhibitors (186). A clinical trial by Cacciotti et al. (187) involving PD-1 and CTLA-4 blockade has shown relatively well tolerability in a group of pediatric patients with DIPG, HGG, ependymoma, craniopharyngioma, high-grade neuroepithelial tumor, and non-germinomatous germ cell tumor. The majority of the patients, during the time of the study, showed stable disease or partial response. Checkpoint inhibition has proved to be a promising new form of immunotherapy, demonstrating efficacy in adult malignancies such as melanoma, renal cell carcinoma, and small cell lung cancer; however, it has failed to produce durable responses in pediatric brain cancer (188).

Virotherapy is an emerging technique that uses viruses as therapeutic agents. Oncolytic viruses combine tumor cell destruction and immune system stimulation, which are the most critical components of virotherapy (189). In addition, viruses can also be used as vectors for gene therapy, inducing the expression of a transgene that modifies the immune environment to promote an anti-tumor response (189). Several oncolytic viruses have been evaluated clinically in pediatric brain tumors, such as myxoma virus (190, 191), recombinant poliovirus (192, 193), adenovirus (194), Seneca Valley-001 (195), reovirus (196), herpesvirus (197), and Newcastle disease virus (198). The administration of oncolytic viruses can be either intravenous or intratumoral. Once the virus reaches the tumor, it can infect both normal and neoplastic cells; however, it only replicates and destroys the tumor cells (198). Cancer vaccines are typically well-tolerated and contain tumor antigens, such as peptides, tumor lysate, nucleic acids, and autologous dendritic cells (196, 199). Mutations such as the H3 K27M in DIPG have been explored as a target for peptide vaccines (199). A number of clinical trials are evaluating the efficacy of virotherapy in pediatric brain tumors. However, none are FDA approved yet.

Dendritic cells are an essential link between the innate and adaptive immune systems. Upon finding foreign antigens, dendritic cells release inflammatory cytokines that activate the immune system. These cells also process and present antigens to T cells and B cells, thereby activating naïve, effector, and memory immune cells or maintaining tolerance against self-antigens (200). For active immunotherapy, dendritic cells are typically generated by isolating monocytes from cancer patients that are expanded and activated *ex vivo*. These cells are loaded with either tumor lysate, peptides, nucleic acids, or viral epitopes that are expressed by the tumor. Dendritic cells are usually matured with GM-CSF, a critical cytokine, then administered as a vaccine. Adjuvants such as tetanus toxoid are important to improve inflammation and immunogenicity in the host (200). Dendritic cell vaccines have demonstrated modest but encouraging results in patients with advanced cancers (201). It is thought that these vaccines can induce tumor-specific T cell responses and immunological memory, constituting a promising platform for pediatric brain tumors (201). There are several trials using dendritic cell vaccines and tumor RNA (201) or tumor lysate for pediatric brain tumors (202, 203). Dendritic cell vaccines are reliably manufactured and extremely well-tolerated; however, for efficacy improvement, enhanced techniques for targeting, antigen loading, and migration *in vivo* are needed (196). There are a number of dendritic cell vaccines in clinical trials; none are available for widespread clinical use.

Immunotherapy has shown efficacy against lymphoid tumors and some solid neoplasms, with less efficacy in the treatment of pediatric brain tumors. Reasons for this limited response include tumor heterogeneity, a suppressive immune microenvironment, and the blood-brain barrier (163). In addition, most pediatric brain tumors are immunologically quiescent, with a low mutational burden. Therefore, immunotherapy strategies should be tailored based on the type of tumor being targeted and its associated microenvironment (163). According to the National Cancer Institute at the National Institutes of Health, there are only six FDA-approved immunotherapy options for brain and nervous system tumors, namely dostarlimab, a checkpoint inhibitor that targets the PD-1/PD-L1 pathway for patients with advanced cases associated with DNA mismatch repair deficiency; granulocyte-macrophage colony-stimulating factor, an immunomodulatory cytokine combined with naxitamab-gqgk, for advanced cases of neuroblastoma; pembrolizumab, a checkpoint inhibitor that targets the PD-1/PD-L1 pathway for patients with advanced cases associated with high microsatellite instability, DNA mismatch repair deficiency, or high tumor mutational burden; bevacizumab, a monoclonal antibody that targets the VEGF/VEGFR pathway and inhibits tumor blood vessel growth for advanced "glioblastoma"; dinutuximab, a monoclonal antibody that targets the GD2 pathway for first-line treatment of high-risk pediatric neuroblastoma; naxitamab-gqgk, a monoclonal antibody that targets the GD2 pathway and approved in combination with GM-CSF for a subset of patients with advanced neuroblastoma.

Regardless of the treatment selected, "pediatric glioblastoma" remains a devastating disease, with median survival ranging from 13 to 73 months, with a 5 year survival of <20% (4–6, 204). Nevertheless, several studies have demonstrated a relatively better prognosis and long-term survival among pediatric patients compared to adults (5–7).

FINAL REMARKS

Glioblastomas are highly aggressive neoplasms that represent a small subset of pediatric brain tumors. "Pediatric glioblastomas" are grossly and microscopically identical to their adult counterparts, but molecularly and genetically distinct. These differences may explain why "pediatric glioblastomas" may have a different prognosis or occasionally be less responsive to current adjuvant therapy regimens.

MRI is the imaging modality of choice in evaluating "pediatric glioblastomas," not only because it is safer due to the absence of radiation exposure but also for its superior spatial and contrast resolution and for delivering physiologic information about the tumor and adjacent brain parenchyma. MRI is also vital for surgical and radiation therapy planning and postsurgical evaluation. Conventional MRI sequences provide precise anatomic detail and detection of blood-brain barrier integrity and leakage. Advanced MRI techniques such as DWI, PWI, and proton ^{1}H MRS may help differentiate non-enhancing tumors from other causes of changes in the signal. It is expected that continued research increases the availability of advanced MRI techniques. This increment, coupled with emerging MRI techniques and advances in personalized medical care, perhaps powered by artificial intelligence techniques, would hopefully result in a better quality of life and overall improvement in survival rates.

AUTHOR CONTRIBUTIONS

All authors listed have made a substantial, direct and intellectual contribution to the work, and approved it for publication.

ACKNOWLEDGMENTS

The authors thank Lydia Sheldon for proofreading and edits.

REFERENCES

1. Louis DN, Perry A, Wesseling P, Brat DJ, Cree IA, Figarella-Branger D, et al. The 2021 WHO classification of tumors of the central nervous system: a summary. *Neuro Oncol.* (2021) 23:1231–51. doi: 10.1093/neuonc/noab106
2. Adamson C, Kanu OO, Mehta AI, Di C, Lin N, Mattox AK, et al. Glioblastoma multiforme: a review of where we have been and where we are going. *Expert Opin Investig Drugs.* (2009) 18:1061–83. doi: 10.1517/13543780903052764
3. Artico M, Cervoni L, Celli P, Salvati M, Palma L. Supratentorial glioblastoma in children: a series of 27 surgically treated cases. *Childs Nerv Syst.* (1993) 9:7–9. doi: 10.1007/BF00301926
4. Perkins SM, Rubin JB, Leonard JR, Smyth MD, El Naqa I, Michalski JM, et al. Glioblastoma in children: a single-institution experience. *Int J Radiat Oncol Biol Phys.* (2011) 80:1117–21. doi: 10.1016/j.ijrobp.2010.03.013
5. Das KK, Mehrotra A, Nair AP, Kumar S, Srivastava AK, Sahu RN, et al. Pediatric glioblastoma: clinico-radiological profile and factors affecting the outcome. *Child's Nerv Syst.* (2012) 28:2055–62. doi: 10.1007/s00381-012-1890-x
6. Nikitović M, Stanić D, Pekmezović T, Gazibara MS, Bokun J, Paripović L, et al. Pediatric glioblastoma: a single institution experience. *Child's Nerv Syst.* (2016) 32:97–103. doi: 10.1007/s00381-015-2945-6
7. Broniscer A, Gajjar A. Supratentorial high-grade astrocytoma and diffuse brainstem glioma: two challenges for the pediatric oncologist. *Oncologist.* (2004) 9:197–206. doi: 10.1634/theoncologist.9-2-197
8. Wolff B, Ng A, Roth D, Parthey K, Warmuth-Metz M, Eyrich M, et al. Pediatric high grade glioma of the spinal cord: results of the HIT-GBM database. *J Neurooncol.* (2012) 107:139–46. doi: 10.1007/s11060-011-0718-y
9. Das KK, Kumar R. Pediatric glioblastoma. In: De Vleeschouwer S, editor. *Glioblastoma*. Brisbane, AU: Codon Publications (2017).
10. Epstein F, Wisoff J. Intra-axial tumors of the cervicomedullary junction. *J Neurosurg.* (1987) 67:483–7. doi: 10.3171/jns.1987.67.4.0483
11. Milano GM, Cerri C, Ferruzzi V, Capolsini I, Mastrodicasa E, Genitori L, et al. Congenital glioblastoma. *Pediatr Blood Cancer.* (2009) 53:124–6. doi: 10.1002/pbc.22008
12. Fangusaro J. Pediatric high-grade gliomas and diffuse intrinsic pontine gliomas. *J Child Neurol.* (2009) 24:1409–17. doi: 10.1177/0883073809338960
13. Chaichana K, Parker S, Olivi A, Quiñones-Hinojosa A. A proposed classification system that projects outcomes based on preoperative variables for adult patients with glioblastoma multiforme. *J Neurosurg.* (2010) 112:997–1004. doi: 10.3171/2009.9.JNS09805
14. Moini J, Piran P, editors. Histophysiology. In: *Functional and Clinical Neuroanatomy.* London: Elsevier (2020). p. 1–49.
15. Suri V, Das P, Pathak P, Jain A, Sharma MC, Borkar SA, et al. Pediatric glioblastomas: a histopathological and molecular genetic study. *Neuro Oncol.* (2009) 11:274–80. doi: 10.1215/15228517-2008-092
16. Mahvash M, Hugo H-H, Maslehaty H, Mehdorn HM, Stark AM. Glioblastoma multiforme in children: report of 13 cases and review of the literature. *Pediatr Neurol.* (2011) 45:178–80. doi: 10.1016/j.pediatrneurol.2011.05.004
17. Urbańska K, Sokołowska J, Szmidt M, Sysa P. Glioblastoma multiforme - an overview. *Contemp Oncol.* (2014) 18:307–12. doi: 10.5114/wo.2014.40559
18. Paulino AC, Mai WY, Chintagumpala M, Taher A, Teh BS. Radiation-induced malignant gliomas: is there a role for reirradiation? *Int J Radiat Oncol Biol Phys.* (2008) 71:1381–7. doi: 10.1016/j.ijrobp.2007.12.018
19. Louis DN, Perry A, Reifenberger G, von Deimling A, Figarella-Branger D, Cavenee WK, et al. The 2016 World Health Organization classification of tumors of the central nervous system: a summary. *Acta Neuropathol.* (2016) 131:803–20. doi: 10.1007/s00401-016-1545-1
20. Reinhardt A, Stichel D, Schrimpf D, Koelsche C, Wefers AK, Ebrahimi A, et al. Tumors diagnosed as cerebellar glioblastoma comprise distinct molecular entities. *Acta Neuropathol Commun.* (2019) 7:163. doi: 10.1186/s40478-019-0801-8
21. International Agency for Research on Cancer, Wiestler OD. *WHO Classification of Tumours of the Central Nervous System*. International Agency for Research on Cancer (2016).
22. Pollack IF, Hamilton RL, Sobol RW, Nikiforova MN, Lyons-Weiler MA, LaFramboise WA, et al. IDH1 mutations are common in malignant gliomas arising in adolescents: a report from the Children's Oncology Group. *Child's Nerv Syst.* (2011) 27:87–94. doi: 10.1007/s00381-010-1264-1
23. Pollack IF, Finkelstein SD, Woods J, Burnham J, Holmes EJ, Hamilton RL, et al. Expression of p53 and prognosis in children with malignant gliomas. *N Engl J Med.* (2002) 346:420–7. doi: 10.1056/NEJMoa012224
24. Mackay A, Burford A, Carvalho D, Izquierdo E, Fazal-Salom J, Taylor KR, et al. Integrated molecular meta-analysis of 1,000 pediatric high-grade and diffuse intrinsic pontine glioma. *Cancer Cell.* (2017) 32:520–37.e5. doi: 10.1016/j.ccell.2017.08.017
25. Sturm D, Witt H, Hovestadt V, Khuong-Quang DA, Jones DT, Konermann C, et al. Hotspot mutations in H3F3A and IDH1 define distinct epigenetic and biological subgroups of glioblastoma. *Cancer Cell.* (2012) 224:425–37. doi: 10.1016/j.ccr.2012.08.024
26. Pratt D, Natarajan SK, Banda A, Giannini C, Vats P, Koschmann C, et al. Circumscribed/non-diffuse histology confers a better prognosis in H3K27M-mutant gliomas. *Acta Neuropathol.* (2018) 135:299–301. doi: 10.1007/s00401-018-1805-3
27. Castel D, Philippe C, Calmon R, Le Dret L, Truffaux N, Boddaert N, et al. Histone H3F3A and HIST1H3B K27M mutations define two subgroups of diffuse intrinsic pontine gliomas with different prognosis and phenotypes. *Acta Neuropathol.* (2015) 130:815–27. doi: 10.1007/s00401-015-1478-0
28. Brat DJ, Aldape K, Colman H, Holland EC, Louis DN, Jenkins RB, et al. cIMPACT-NOW update 3: recommended diagnostic criteria for "Diffuse astrocytic glioma. IDH-wildtype, with molecular features of glioblastoma, WHO grade IV". *Acta Neuropathol.* (2018) 136:805–10. doi: 10.1007/s00401-018-1913-0
29. Paugh BS, Zhu X, Qu C, Endersby R, Diaz AK, Zhang J, et al. Novel oncogenic PDGFRA mutations in pediatric high-grade gliomas. *Cancer Res.* (2013) 73:6219–29. doi: 10.1158/0008-5472.CAN-13-1491
30. Hegi ME, Diserens A-C, Gorlia T, Hamou M-F, de Tribolet N, Weller M, et al. MGMT gene silencing and benefit from temozolomide in glioblastoma. *N Engl J Med.* (2005) 352:997–1003. doi: 10.1056/NEJMoa043331

31. Lee JY, Park C-K, Park S-H, Wang K-C, Cho B-K, Kim S-K. MGMT promoter gene methylation in pediatric glioblastoma: analysis using MS-MLPA. *Childs Nerv Syst.* (2011) 27:1877–83. doi: 10.1007/s00381-011-1525-7
32. Donson AM, Addo-Yobo SO, Handler MH, Gore L, Foreman NK. MGMT promoter methylation correlates with survival benefit and sensitivity to temozolomide in pediatric glioblastoma. *Pediatr Blood Cancer.* (2007) 48:403–7. doi: 10.1002/pbc.20803
33. Korshunov A, Ryzhova M, Hovestadt V, Bender S, Sturm D, Capper D, et al. Integrated analysis of pediatric glioblastoma reveals a subset of biologically favorable tumors with associated molecular prognostic markers. *Acta Neuropathol.* (2015) 129:669–78. doi: 10.1007/s00401-015-1405-4
34. Banan R, Christians A, Bartels S, Lehmann U, Hartmann C. Absence of MGMT promoter methylation in diffuse midline glioma, H3 K27M-mutant. *Acta Neuropathol Commun.* (2017) 5:98. doi: 10.1186/s40478-017-0500-2
35. Chang Y-W, Yoon H-K, Shin H-J, Roh HG, Cho JM. MR imaging of glioblastoma in children: usefulness of diffusion/perfusion-weighted MRI and MR spectroscopy. *Pediatr Radiol.* (2003) 33:836–42. doi: 10.1007/s00247-003-0968-8
36. Fangusaro J. Pediatric high grade glioma: a review and update on tumor clinical characteristics and biology. *Front Oncol.* (2012) 2:105. doi: 10.3389/fonc.2012.00105
37. Panigrahy A, Blüml S. Neuroimaging of pediatric brain tumors: from basic to advanced magnetic resonance imaging (MRI). *J Child Neurol.* (2009) 24:1343–65. doi: 10.1177/0883073809342129
38. Knopp EA, Cha S, Johnson G, Mazumdar A, Golfinos JG, Zagzag D, et al. Glial neoplasms: dynamic contrast-enhanced T2*-weighted MR imaging. *Radiology.* (1999) 211:791–8. doi: 10.1148/radiology.211.3.r99jn46791
39. Shin JH, Lee HK, Kwun BD, Kim J-S, Kang W, Choi CG, et al. Using relative cerebral blood flow and volume to evaluate the histopathologic grade of cerebral gliomas: preliminary results. *AJR Am J Roentgenol.* (2002) 179:783–9. doi: 10.2214/ajr.179.3.1790783
40. Tien RD, Felsberg GJ, Friedman H, Brown M, MacFall J. MR imaging of high-grade cerebral gliomas: value of diffusion-weighted echoplanar pulse sequences. *AJR Am J Roentgenol.* (1994) 162:671–7. doi: 10.2214/ajr.162.3.8109520
41. Le Bihan D, Iima M, Federau C, Sigmund EE. *Intravoxel Incoherent Motion (IVIM) MRI: Principles and Applications*. Singapore: CRC Press (2018).
42. Svolos P, Kousi E, Kapsalaki E, Theodorou K, Fezoulidis I, Kappas C, et al. The role of diffusion and perfusion weighted imaging in the differential diagnosis of cerebral tumors: a review and future perspectives. *Cancer Imaging.* (2014) 14:20. doi: 10.1186/1470-7330-14-20
43. Le Bihan D, Turner R, Douek P, Patronas N. Diffusion MR imaging: clinical applications. *AJR Am J Roentgenol.* (1992) 159:591–9. doi: 10.2214/ajr.159.3.1503032
44. Eis M, Els T, Hoehn-Berlage M, Hossmann KA. Quantitative diffusion MR imaging of cerebral tumor and edema. *Acta Neurochir Suppl.* (1994) 60:344–6. doi: 10.1007/978-3-7091-9334-1_92
45. Krabbe K, Gideon P, Wagn P, Hansen U, Thomsen C, Madsen F. MR diffusion imaging of human intracranial tumours. *Neuroradiology.* (1997) 39:483–9. doi: 10.1007/s002340050450
46. Ebisu T, Tanaka C, Umeda M, Kitamura M, Naruse S, Higuchi T, et al. Discrimination of brain abscess from necrotic or cystic tumors by diffusion-weighted echo planar imaging. *Magn Reson Imaging.* (1996) 14:1113–6. doi: 10.1016/S0730-725X(96)00237-8
47. Okamoto K, Ito J, Ishikawa K, Sakai K, Tokiguchi S. Diffusion-weighted echo-planar MR imaging in differential diagnosis of brain tumors and tumor-like conditions. *Eur Radiol.* (2000) 10:1342–50. doi: 10.1007/s003309900310
48. Dutt SN, Mirza S, Chavda SV, Irving RM. Radiologic differentiation of intracranial epidermoids from arachnoid cysts. *Otol Neurotol.* (2002) 23:84–92. doi: 10.1097/00129492-200201000-00019
49. Camacho DLA, Smith JK, Castillo M. Differentiation of toxoplasmosis and lymphoma in AIDS patients by using apparent diffusion coefficients. *AJNR Am J Neuroradiol.* (2003) 24:633–7.
50. Messina C, Bignone R, Bruno A, Bruno A, Bruno F, Calandri M, et al. Diffusion-weighted imaging in oncology: an update. *Cancers.* (2020) 12:1493. doi: 10.3390/cancers12061493
51. Brunberg JA, Chenevert TL, McKeever PE, Ross DA, Junck LR, Muraszko KM, et al. *In vivo* MR determination of water diffusion coefficients and diffusion anisotropy: correlation with structural alteration in gliomas of the cerebral hemispheres. *AJNR Am J Neuroradiol.* (1995) 16:361–71.
52. Nadal Desbarats L, Herlidou S, de Marco G, Gondry-Jouet C, Le Gars D, Deramond H, et al. Differential MRI diagnosis between brain abscesses and necrotic or cystic brain tumors using the apparent diffusion coefficient and normalized diffusion-weighted images. *Magn Reson Imaging.* (2003) 21:645–50. doi: 10.1016/S0730-725X(03)00084-5
53. Muccio CF, Caranci F, D'Arco F, Cerase A, De Lipsis L, Esposito G, et al. Magnetic resonance features of pyogenic brain abscesses and differential diagnosis using morphological and functional imaging studies: a pictorial essay. *J Neuroradiol.* (2014) 41:153–67. doi: 10.1016/j.neurad.2014.05.004
54. Higano S, Yun X, Kumabe T, Watanabe M, Mugikura S, Umetsu A, et al. Malignant astrocytic tumors: clinical importance of apparent diffusion coefficient in prediction of grade and prognosis. *Radiology.* (2006) 241:839–46. doi: 10.1148/radiol.2413051276
55. Kan P, Liu JK, Hedlund G, Brockmeyer DL, Walker ML, Kestle JRW. The role of diffusion-weighted magnetic resonance imaging in pediatric brain tumors. *Childs Nerv Syst.* (2006) 22:1435–9. doi: 10.1007/s00381-006-0229-x
56. Wang Q-P, Lei D-Q, Yuan Y, Xiong N-X. Accuracy of ADC derived from DWI for differentiating high-grade from low-grade gliomas: systematic review and meta-analysis. *Medicine.* (2020) 99:e19254. doi: 10.1097/MD.0000000000019254
57. Asao C, Korogi Y, Hotta A, Shimomura O, Kitajima M, Negi A, et al. Orbital pseudotumors: value of short inversion time inversion-recovery MR imaging. *Radiology.* (1997) 202:55–9. doi: 10.1148/radiology.202.1.8988192
58. Hein PA, Eskey CJ, Dunn JF, Hug EB. Diffusion-weighted imaging in the follow-up of treated high-grade gliomas: tumor recurrence versus radiation injury. *AJNR Am J Neuroradiol.* (2004) 25:201–9.
59. Chenevert TL, Stegman LD, Taylor JM, Robertson PL, Greenberg HS, Rehemtulla A, et al. Diffusion magnetic resonance imaging: an early surrogate marker of therapeutic efficacy in brain tumors. *J Natl Cancer Inst.* (2000) 92:2029–36. doi: 10.1093/jnci/92.24.2029
60. Evelhoch JL. Magnetic resonance measurement of tumor perfusion and vascularity. In: Shields AF, Price P, editors. *In Vivo Imaging of Cancer Therapy. Cancer Drug Discovery and Development*. Totowa, NJ: Humana Press. doi: 10.1007/978-1-59745-341-7_5
61. Poussaint TY, Kocak M, Vajapeyam S, Packer RI, Robertson RL, Geyer R, et al. MRI as a central component of clinical trials analysis in brainstem glioma: a report from the Pediatric Brain Tumor Consortium (PBTC). *Neuro Oncol.* (2011) 13:417–27. doi: 10.1093/neuonc/noq200
62. Lober RM, Cho Y-J, Tang Y, Barnes PD, Edwards MS, Vogel H, et al. Diffusion-weighted MRI derived apparent diffusion coefficient identifies prognostically distinct subgroups of pediatric diffuse intrinsic pontine glioma. *J Neurooncol.* (2014) 117:175–82. doi: 10.1007/s11060-014-1375-8
63. Aboian MS, Tong E, Solomon DA, Kline C, Gautam A, Vardapetyan A, et al. Diffusion characteristics of pediatric diffuse midline gliomas with histone H3-K27M mutation using apparent diffusion coefficient histogram analysis. *AJNR Am J Neuroradiol.* (2019) 40:1804–10. doi: 10.3174/ajnr.A6302
64. Ceschin R, Kocak M, Vajapeyam S, Pollack IF, Onar-Thomas A, Dunkel IJ, et al. Quantifying radiation therapy response using apparent diffusion coefficient (ADC) parametric mapping of pediatric diffuse intrinsic pontine glioma: a report from the pediatric brain tumor consortium. *J Neurooncol.* (2019) 143:79–86. doi: 10.1007/s11060-019-03133-y
65. Gauvain KM, McKinstry RC, Mukherjee P, Perry A, Neil JJ, Kaufman BA, et al. Evaluating pediatric brain tumor cellularity with diffusion-tensor imaging. *AJR Am J Roentgenol.* (2001) 177:449–54. doi: 10.2214/ajr.177.2.1770449
66. Basser PJ. Inferring microstructural features and the physiological state of tissues from diffusion-weighted images. *NMR Biomed.* (1995) 8:333–44. doi: 10.1002/nbm.1940080707
67. Lori NF, Akbudak E, Shimony JS, Cull TS, Snyder AZ, Guillory RK, et al. Diffusion tensor fiber tracking of human brain connectivity: aquisition methods, reliability analysis and biological results. *NMR Biomed.* (2002) 15:494–515. doi: 10.1002/nbm.779
68. Field AS, Alexander AL, Wu Y-C, Hasan KM, Witwer B, Badie B. Diffusion tensor eigenvector directional color imaging patterns in the evaluation of

cerebral white matter tracts altered by tumor. *J Magn Reson Imaging.* (2004) 20:555–62. doi: 10.1002/jmri.20169
69. Bulakbaşi N. Diffusion-tensor imaging in brain tumors. *Imaging Med.* (2009) 1:155–71. doi: 10.2217/iim.09.20
70. Moshel YA, Elliott RE, Monoky DJ, Wisoff JH. Role of diffusion tensor imaging in resection of thalamic juvenile pilocytic astrocytoma. *J Neurosurg Pediatr.* (2009) 4:495–505. doi: 10.3171/2009.7.PEDS09128
71. Lu S, Ahn D, Johnson G, Law M, Zagzag D, Grossman RI. Diffusion-tensor MR imaging of intracranial neoplasia and associated peritumoral edema: introduction of the tumor infiltration index. *Radiology.* (2004) 232:221–8. doi: 10.1148/radiol.2321030653
72. Provenzale JM, McGraw P, Mhatre P, Guo AC, Delong D. Peritumoral brain regions in gliomas and meningiomas: investigation with isotropic diffusion-weighted MR imaging and diffusion-tensor MR imaging. *Radiology.* (2004) 232:451–60. doi: 10.1148/radiol.2322030959
73. Morita K-I, Matsuzawa H, Fujii Y, Tanaka R, Kwee IL, Nakada T. Diffusion tensor analysis of peritumoral edema using lambda chart analysis indicative of the heterogeneity of the microstructure within edema. *J Neurosurg.* (2005) 102:336–41. doi: 10.3171/jns.2005.102.2.0336
74. Tsuchiya K, Fujikawa A, Nakajima M, Honya K. Differentiation between solitary brain metastasis and high-grade glioma by diffusion tensor imaging. *Br J Radiol.* (2005) 78:533–7. doi: 10.1259/bjr/68749637
75. Price SJ, Jena R, Burnet NG, Hutchinson PJ, Dean AF, Peña A, et al. Improved delineation of glioma margins and regions of infiltration with the use of diffusion tensor imaging: an image-guided biopsy study. *AJNR Am J Neuroradiol.* (2006) 27:1969–74.
76. Stadlbauer A, Ganslandt O, Buslei R, Hammen T, Gruber S, Moser E, et al. Gliomas: histopathologic evaluation of changes in directionality and magnitude of water diffusion at diffusion-tensor MR imaging. *Radiology.* (2006) 240:803–10. doi: 10.1148/radiol.2403050937
77. Tropine A, Vucurevic G, Delani P, Boor S, Hopf N, Bohl J, et al. Contribution of diffusion tensor imaging to delineation of gliomas and glioblastomas. *J Magn Reson Imaging.* (2004) 20:905–12. doi: 10.1002/jmri.20217
78. Goebell E, Paustenbach S, Vaeterlein O, Ding X-Q, Heese O, Fiehler J, et al. Low-grade and anaplastic gliomas: differences in architecture evaluated with diffusion-tensor MR imaging. *Radiology.* (2006) 239:217–22. doi: 10.1148/radiol.2383050059
79. Nilsson D, Rutka JT, Snead OC III, Raybaud CR, Widjaja E. Preserved structural integrity of white matter adjacent to low-grade tumors. *Childs Nerv Syst.* (2008) 24:313–20. doi: 10.1007/s00381-007-0466-7
80. Yuan W, Holland SK, Jones BV, Crone K, Mangano FT. Characterization of abnormal diffusion properties of supratentorial brain tumors: a preliminary diffusion tensor imaging study. *J Neurosurg Pediatr.* (2008) 1:263–9. doi: 10.3171/PED/2008/1/4/263
81. Field AS. Diffusion tensor imaging at the crossroads: fiber tracking meets tissue characterization in brain tumors. *AJNR Am J Neuroradiol.* (2005) 26:2168–9.
82. Roberts TPL, Liu F, Kassner A, Mori S, Guha A. Fiber density index correlates with reduced fractional anisotropy in white matter of patients with glioblastoma. *AJNR Am J Neuroradiol.* (2005) 26:2183–6.
83. Jellison BJ, Field AS, Medow J, Lazar M, Salamat MS, Alexander AL. Diffusion tensor imaging of cerebral white matter: a pictorial review of physics, fiber tract anatomy, and tumor imaging patterns. *AJNR Am J Neuroradiol.* (2004) 25:356–69.
84. Helton KJ, Phillips NS, Khan RB, Boop FA, Sanford RA, Zou P, et al. Diffusion tensor imaging of tract involvement in children with pontine tumors. *AJNR Am J Neuroradiol.* (2006) 27:786–93.
85. Yen PS, Teo BT, Chiu CH, Chen SC, Chiu TL, Su CF. White Matter tract involvement in brain tumors: a diffusion tensor imaging analysis. *Surg Neurol.* (2009) 72:464–9; discussion 469. doi: 10.1016/j.surneu.2009.05.008
86. Laundre BJ, Jellison BJ, Badie B, Alexander AL, Field AS. Diffusion tensor imaging of the corticospinal tract before and after mass resection as correlated with clinical motor findings: preliminary data. *AJNR Am J Neuroradiol.* (2005) 26:791–6.
87. Yu CS, Li KC, Xuan Y, Ji XM, Qin W. Diffusion tensor tractography in patients with cerebral tumors: a helpful technique for neurosurgical planning and postoperative assessment. *Eur J Radiol.* (2005) 56:197–204. doi: 10.1016/j.ejrad.2005.04.010
88. Lui YW, Law M, Chacko-Mathew J, Babb JS, Tuvia K, Allen JC, et al. Brainstem corticospinal tract diffusion tensor imaging in patients with primary posterior fossa neoplasms stratified by tumor type. *Neurosurgery.* (2007) 61:1199–208. doi: 10.1227/01.neu.0000306098.38141.81
89. Khong PL, Kwong DL, Chan GC, Sham JS, Chan FL, Ooi GC. Diffusion-tensor imaging for the detection and quantification of treatment-induced white matter injury in children with medulloblastoma: a pilot study. *AJNR Am J Neuroradiol.* (2003) 24:734–40.
90. Leung LHT, Ooi GC, Kwong DLW, Chan GCF, Cao G, Khong PL. White-matter diffusion anisotropy after chemo-irradiation: a statistical parametric mapping study and histogram analysis. *Neuroimage.* (2004) 21:261–8. doi: 10.1016/j.neuroimage.2003.09.020
91. Qiu D, Leung LHT, Kwong DLW, Chan GCF, Khong P-L. Mapping radiation dose distribution on the fractional anisotropy map: applications in the assessment of treatment-induced white matter injury. *Neuroimage.* (2006) 31:109–15. doi: 10.1016/j.neuroimage.2005.12.007
92. Qiu D, Kwong DLW, Chan GCF, Leung LHT, Khong P-L. Diffusion tensor magnetic resonance imaging finding of discrepant fractional anisotropy between the frontal and parietal lobes after whole-brain irradiation in childhood medulloblastoma survivors: reflection of regional white matter radiosensitivity? *Int. J Radiat Oncol Biol Phys.* (2007) 69:846–51. doi: 10.1016/j.ijrobp.2007.04.041
93. Mabbott DJ, Noseworthy MD, Bouffet E, Rockel C, Laughlin S. Diffusion tensor imaging of white matter after cranial radiation in children for medulloblastoma: correlation with IQ. *Neuro Oncol.* (2006) 8:244–52. doi: 10.1215/15228517-2006-002
94. Welzel T, Niethammer A, Mende U, Heiland S, Wenz F, Debus J, et al. Diffusion tensor imaging screening of radiation-induced changes in the white matter after prophylactic cranial irradiation of patients with small cell lung cancer: first results of a prospective study. *AJNR Am J Neuroradiol.* (2008) 29:379–83. doi: 10.3174/ajnr.A0797
95. Yeom KW, Mitchell LA, Lober RM, Barnes PD, Vogel H, Fisher PG, et al. Arterial Spin-Labeled Perfusion of Pediatric Brain Tumors. *AJNR Am J Neuroradiol.* (2014) 35:395–401. doi: 10.3174/ajnr.A3670
96. Lacerda S, Law M. Magnetic resonance perfusion and permeability imaging in brain tumors. *Neuroimaging Clin N Am.* (2009) 19:527–57. doi: 10.1016/j.nic.2009.08.007
97. Gaudino S, Martucci M, Botto A, Ruberto E, Leone E, Infante A, et al. Brain DSC MR perfusion in children: a clinical feasibility study using different technical standards of contrast administration. *AJNR Am J Neuroradiol.* (2019) 40:359–65. doi: 10.3174/ajnr.A5954
98. Dallery F, Bouzerar R, Michel D, Attencourt C, Promelle V, Peltier J, et al. Perfusion magnetic resonance imaging in pediatric brain tumors. *Neuroradiology.* (2017) 59:1143–53. doi: 10.1007/s00234-017-1917-9
99. Miyazaki K, Jerome NP, Collins DJ, Orton MR, d'Arcy JA, Wallace T, et al. Demonstration of the reproducibility of free-breathing diffusion-weighted MRI and dynamic contrast enhanced MRI in children with solid tumours: a pilot study. *Eur Radiol.* (2015) 25:2641–50. doi: 10.1007/s00330-015-3666-7
100. Vajapeyam S, Stamoulis C, Ricci K, Kieran M, Poussaint TY. Automated processing of dynamic contrast-enhanced MRI: correlation of advanced pharmacokinetic metrics with tumor grade in pediatric brain tumors. *AJNR Am J Neuroradiol.* (2017) 38:170–5. doi: 10.3174/ajnr.A4949
101. Essig M, Nguyen TB, Shiroishi MS, Saake M, Provenzale JM, Enterline DS, et al. Perfusion MRI: the five most frequently asked clinical questions. *AJR Am J Roentgenol.* (2013) 201:W495–510. doi: 10.2214/AJR.12.9543
102. Heye AK, Culling RD, Valdés Hernández MDC, Thrippleton MJ, Wardlaw JM. Assessment of blood-brain barrier disruption using dynamic contrast-enhanced MRI. A systematic review. *Neuroimage Clin.* (2014) 6:262–74. doi: 10.1016/j.nicl.2014.09.002
103. Li X, Zhu Y, Kang H, Zhang Y, Liang H, Wang S, et al. Glioma grading by microvascular permeability parameters derived from dynamic contrast-enhanced MRI and intratumoral susceptibility signal on susceptibility weighted imaging. *Cancer Imaging.* (2015) 15:4. doi: 10.1186/s40644-015-0039-z
104. Anzalone N, Castellano A, Cadioli M, Conte GM, Cuccarini V, Bizzi A, et al. Brain gliomas: multicenter standardized assessment of dynamic contrast-enhanced and dynamic susceptibility contrast MR images. *Radiology.* (2018) 287:933–43. doi: 10.1148/radiol.2017170362

105. Gupta PK, Saini J, Sahoo P, Patir R, Ahlawat S, Beniwal M, et al. Role of dynamic contrast-enhanced perfusion magnetic resonance imaging in grading of pediatric brain tumors on 3T. *Pediatr Neurosurg.* (2017) 52:298–305. doi: 10.1159/000479283
106. Dangouloff-Ros V, Deroulers C, Foissac F, Badoual M, Shotar E, Grévent D, et al. Arterial spin labeling to predict brain tumor grading in children: correlations between histopathologic vascular density and perfusion MR imaging. *Radiology.* (2016) 281:553–66. doi: 10.1148/radiol.2016152228
107. Warmuth C, Gunther M, Zimmer C. Quantification of blood flow in brain tumors: comparison of arterial spin labeling and dynamic susceptibility-weighted contrast-enhanced MR imaging. *Radiology.* (2003) 228:523–32. doi: 10.1148/radiol.2282020409
108. Deibler AR, Pollock JM, Kraft RA, Tan H, Burdette JH, Maldjian JA. Arterial spin-labeling in routine clinical practice, part 1: technique and artifacts. *AJNR Am J Neuroradiol.* (2008) 29:1228–34. doi: 10.3174/ajnr.A1030
109. Morana G, Tortora D, Staglianò S, Nozza P, Mascelli S, Severino M, et al. Pediatric astrocytic tumor grading: comparison between arterial spin labeling and dynamic susceptibility contrast MRI perfusion. *Neuroradiology.* (2018) 60:437–46. doi: 10.1007/s00234-018-1992-6
110. Delgado AF, De Luca F, van Westen D, Delgado AF. Arterial spin labeling MR imaging for differentiation between high- and low-grade glioma—a meta-analysis. *Neuro Oncol.* (2018) 20:1450–61. doi: 10.1093/neuonc/noy095
111. Hales PW, d'Arco F, Cooper J, Pfeuffer J, Hargrave D, Mankad K, et al. Arterial spin labelling and diffusion-weighted imaging in paediatric brain tumours. *Neuroimage Clin.* (2019) 22:101696. doi: 10.1016/j.nicl.2019.101696
112. Hales PW, Phipps KP, Kaur R, Clark CA. A two-stage model for *in vivo* assessment of brain tumor perfusion and abnormal vascular structure using arterial spin labeling. *PLoS ONE.* (2013) 8:e75717. doi: 10.1371/journal.pone.0075717
113. Dangouloff-Ros V, Grevent D, Pagès M, Blauwblomme T, Calmon R, Elie C, et al. Choroid plexus neoplasms: toward a distinction between carcinoma and papilloma using arterial spin-labeling. *AJNR Am J Neuroradiol.* (2015) 36:1786–90. doi: 10.3174/ajnr.A4332
114. Kikuchi K, Hiwatashi A, Togao O, Yamashita K, Yoshimoto K, Mizoguchi M, et al. Correlation between arterial spin-labeling perfusion and histopathological vascular density of pediatric intracranial tumors. *J Neurooncol.* (2017) 135:561–9. doi: 10.1007/s11060-017-2604-8
115. ElBeheiry AA, Emara DM, Abdel-Latif AA-B, Abbas M, Ismail AS. Arterial spin labeling in the grading of brain gliomas: could it help? *Egyptian J Radiol Nucl Med.* (2020) 51:1–11. doi: 10.1186/s43055-020-00352-6
116. Brandão LA, Poussaint TY. Pediatric brain tumors. *Neuroimaging Clin N Am.* (2013) 233:499–525. doi: 10.1016/j.nic.2013.03.003
117. Sutton LN, Wang Z, Gusnard D, Lange B, Perilongo G, Bogdan AR, et al. Proton magnetic resonance spectroscopy of pediatric brain tumors. *Neurosurgery.* (1992) 31:195–202. doi: 10.1227/00006123-199208000-00004
118. Ott D, Hennig J, Ernst T. Human brain tumors: assessment with *in vivo* proton MR spectroscopy. *Radiology.* (1993) 186:745–52. doi: 10.1148/radiology.186.3.8430183
119. Shimizu H, Kumabe T, Tominaga T, Kayama T, Hara K, Ono Y, et al. Noninvasive evaluation of malignancy of brain tumors with proton MR spectroscopy. *AJNR Am J Neuroradiol.* (1996) 17:737–47.
120. Tien RD, Lai PH, Smith JS, Lazeyras F. Single-voxel proton brain spectroscopy exam (PROBE/SV) in patients with primary brain tumors. *AJR Am J Roentgenol.* (1996) 167:201–9. doi: 10.2214/ajr.167.1.8659372
121. Meyerand ME, Pipas JM, Mamourian A, Tosteson TD, Dunn JF. Classification of biopsy-confirmed brain tumors using single-voxel MR spectroscopy. *AJNR Am J Neuroradiol.* (1999) 20:117–23.
122. Lemort M, Canizares-Perez AC, Van der Stappen A, Kampouridis S. Progress in magnetic resonance imaging of brain tumours. *Curr Opin Oncol.* (2007) 19:616–22. doi: 10.1097/CCO.0b013e3282f076b2
123. Zarifi M, Tzika AA. Proton MRS imaging in pediatric brain tumors. *Pediatr Radiol.* (2016) 46:952–62. doi: 10.1007/s00247-016-3547-5
124. Yamasaki F, Kurisu K, Kajiwara Y, Watanabe Y, Takayasu T, Akiyama Y, et al. Magnetic resonance spectroscopic detection of lactate is predictive of a poor prognosis in patients with diffuse intrinsic pontine glioma. *Neuro Oncol.* (2011) 13:791–801. doi: 10.1093/neuonc/nor038
125. Chawla S, Lee S-C, Mohan S, Wang S, Nasrallah M, Vossough A, et al. Lack of choline elevation on proton magnetic resonance spectroscopy in grade I-III gliomas. *Neuroradiol J.* (2019) 32:250–8. doi: 10.1177/1971400919846509
126. Girard N, Wang ZJ, Erbetta A, Sutton LN, Phillips PC, Rorke LB, et al. Prognostic value of proton MR spectroscopy of cerebral hemisphere tumors in children. *Neuroradiology.* (1998) 40:121–5. doi: 10.1007/s002340050551
127. Warren KE, Frank JA, Black JL, Hill RS, Duyn JH, Aikin AA, et al. Proton magnetic resonance spectroscopic imaging in children with recurrent primary brain tumors. *J Clin Oncol.* (2000) 18:1020.doi: 10.1200/JCO.2000.18.5.1020
128. Tarnawski R, Sokol M, Pieniazek P, Maciejewski B, Walecki J, Miszczyk L, et al. 1H-MRS *in vivo* predicts the early treatment outcome of postoperative radiotherapy for malignant gliomas. *Int J Radiat Oncol Biol Phys.* (2002) 52:1271–6. doi: 10.1016/S0360-3016(01)02769-9
129. Marcus K, Astrakas L, Zurakowski D, Zarifi M, Mintzopoulos D, Poussaint T, et al. Predicting survival of children with CNS tumors using proton magnetic resonance spectroscopic imaging biomarkers. *Int J Oncol.* (2007) 30:651–7. doi: 10.3892/ijo.30.3.651
130. Sanson M, Marie Y, Paris S, Idbaih A, Laffaire J, Ducray F, et al. Isocitrate dehydrogenase 1 codon 132 mutation is an important prognostic biomarker in gliomas. *J Clin Oncol.* (2009) 27:4150–4. doi: 10.1200/JCO.2009.21.9832
131. Suh CH, Kim HS, Jung SC, Choi CG, Kim SJ. 2-Hydroxyglutarate MR spectroscopy for prediction of isocitrate dehydrogenase mutant glioma: a systemic review and meta-analysis using individual patient data. *Neuro Oncol.* (2018) 20:1573–83. doi: 10.1093/neuonc/noy113
132. Jones KM, Pollard AC, Pagel MD. Clinical applications of chemical exchange saturation transfer (CEST) MRI. *J Magn Reson Imaging.* (2018) 47:11–27. doi: 10.1002/jmri.25838
133. Zhou J, Heo H-Y, Knutsson L, van Zijl PCM, Jiang S. APT-weighted MRI: Techniques, current neuro applications, and challenging issues. *J Magn Reson Imaging.* (2019) 50:347–64. doi: 10.1002/jmri.26645
134. Regnery S, Adeberg S, Dreher C, Oberhollenzer J, Meissner J-E, Goerke S, et al. Chemical exchange saturation transfer MRI serves as predictor of early progression in glioblastoma patients. *Oncotarget.* (2018) 9:28772–83. doi: 10.18632/oncotarget.25594
135. Zhou J, Payen J-F, Wilson DA, Traystman RJ, van Zijl PCM. Using the amide proton signals of intracellular proteins and peptides to detect pH effects in MRI. *Nat Med.* (2003) 9:1085–90. doi: 10.1038/nm907
136. Ma B, Blakeley JO, Hong X, Zhang H, Jiang S, Blair L, et al. Applying amide proton transfer-weighted MRI to distinguish pseudoprogression from true progression in malignant gliomas. *J Magn Reson Imaging.* (2016) 44:456–62. doi: 10.1002/jmri.25159
137. Hobbs SK, Shi G, Homer R, Harsh G, Scott W, Atlas, et al. Magnetic resonance image-guided proteomics of human glioblastoma multiforme. *J Magn Reson Imaging.* (2003) 18:530–6. doi: 10.1002/jmri.10395
138. Isobe T, Matsumura A, Anno I, Yoshizawa T, Nagatomo Y, Itai Y, et al. Quantification of cerebral metabolites in glioma patients with proton MR spectroscopy using T2 relaxation time correction. *Magn Reson Imaging.* (2002) 20:343–9. doi: 10.1016/S0730-725X(02)00500-3
139. Chen XZ, Yin XM, Ai L, Chen Q, Li SW, Dai JP. Differentiation between brain glioblastoma multiforme and solitary metastasis: qualitative and quantitative analysis based on routine MR imaging. *AJNR Am J Neuroradiol.* (2012) 33:1907–12. doi: 10.3174/ajnr.A3106
140. Nael K, Bauer AH, Hormigo A, Lemole M, Germano IM, Puig J, et al. Multiparametric MRI for differentiation of radiation necrosis from recurrent tumor in patients with treated glioblastoma. *AJR Am J Roentgenol.* (2018) 210:18–23. doi: 10.2214/AJR.17.18003
141. Li C, Wang S, Yan J-L, Torheim T, Boonzaier NR, Sinha R, et al. Characterizing tumor invasiveness of glioblastoma using multiparametric magnetic resonance imaging. *J Neurosurg.* (2019) 132:1465–72. doi: 10.3171/2018.12.JNS182926
142. Stringfield O, Arrington JA, Johnston SK, Rognin NG, Peeri NC, Balagurunathan Y, et al. Multiparameter MRI predictors of long-term survival in glioblastoma multiforme. *Tomography.* (2019) 5:135–44. doi: 10.18383/j.tom.2018.00052
143. Drake LR, Hillmer AT, Cai Z. Approaches to PET imaging of glioblastoma. *Molecules.* (2020) 25:568. doi: 10.3390/molecules25030568

144. Verger A, Langen KJ. PET imaging in glioblastoma: use in clinical practice. In: *Glioblastoma*. Codon Publications (2017). Available online at: https://www.ncbi.nlm.nih.gov/books/NBK469986/
145. Som P, Atkins HL, Bandoypadhyay D, Fowler JS, MacGregor RR, Matsui K, et al. A fluorinated glucose analog, 2-fluoro-2-deoxy-D-glucose (F-18): nontoxic tracer for rapid tumor detection. *J Nucl Med*. (1980) 21:670–5.
146. von Neubeck C, Seidlitz A, Kitzler HH, Beuthien-Baumann B, Krause M. Glioblastoma multiforme: emerging treatments and stratification markers beyond new drugs. *Br J Radiol*. (2015) 88:20150354. doi: 10.1259/bjr.20150354
147. Grosu A-L, Weber WA, Riedel E, Jeremic B, Nieder C, Franz M, et al. L-(methyl-11C) methionine positron emission tomography for target delineation in resected high-grade gliomas before radiotherapy. *Int J Radiat Oncol Biol Phys*. (2005) 63:64–74. doi: 10.1016/j.ijrobp.2005.01.045
148. Wang L, Lieberman BP, Ploessl K, Kung HF. Synthesis and evaluation of ^{18}F labeled FET prodrugs for tumor imaging. *Nucl Med Biol*. (2014) 41:58–67. doi: 10.1016/j.nucmedbio.2013.09.011
149. Janvier L, Olivier P, Blonski M, Morel O, Vignaud J-M, Karcher G, et al. Correlation of SUV-derived indices with tumoral aggressiveness of gliomas in static 18F-FDOPA pet: use in clinical practice. *Clin Nucl Med*. (2015) 40:e429–35. doi: 10.1097/RLU.0000000000000897
150. Patel CB, Fazzari E, Chakhoyan A, Yao J, Raymond C, Nguyen H, et al. F-FDOPA PET and MRI characteristics correlate with degree of malignancy and predict survival in treatment-naïve gliomas: a cross-sectional study. *J Neurooncol*. (2018) 139:399–409. doi: 10.1007/s11060-018-2877-6
151. Toyohara J, Waki A, Takamatsu S, Yonekura Y, Magata Y, Fujibayashi Y. Basis of FLT as a cell proliferation marker: comparative uptake studies with [3H]thymidine and [3H]arabinothymidine, and cell-analysis in 22 asynchronously growing tumor cell lines. *Nucl Med Biol*. (2002) 29:281–7. doi: 10.1016/S0969-8051(02)00286-X
152. Been LB, Suurmeijer AJH, Cobben DCP, Jager PL, Hoekstra HJ, Elsinga PH. [18F]FLT-PET in oncology: current status and opportunities. *Eur J Nucl Med Mol Imaging*. (2004) 31:1659–72. doi: 10.1007/s00259-004-1687-6
153. Yamamoto Y, Ono Y, Aga F, Kawai N, Kudomi N, Nishiyama Y. Correlation of 18F-FLT uptake with tumor grade and Ki-67 immunohistochemistry in patients with newly diagnosed and recurrent gliomas. *J Nucl Med*. (2012) 53:1911–5. doi: 10.2967/jnumed.112.104729
154. Zhao F, Cui Y, Li M, Fu Z, Chen Z, Kong L, et al. Prognostic value of 3'-deoxy-3'-18F-fluorothymidine ([(18)F] FLT PET) in patients with recurrent malignant gliomas. *Nucl Med Biol*. (2014) 41:710–5. doi: 10.1016/j.nucmedbio.2014.04.134
155. Horsman MR, Mortensen LS, Petersen JB, Busk M, Overgaard J. Imaging hypoxia to improve radiotherapy outcome. *Nat Rev Clin Oncol*. (2012) 9:674–87. doi: 10.1038/nrclinonc.2012.171
156. Vlodavsky E, Soustiel JF. Immunohistochemical expression of peripheral benzodiazepine receptors in human astrocytomas and its correlation with grade of malignancy, proliferation, apoptosis and survival. *J Neurooncol*. (2007) 81:1–7. doi: 10.1007/s11060-006-9199-9
157. Stupp R, Mason WP, van den Bent MJ, Weller M, Fisher B, Taphoorn MJB, et al. Radiotherapy plus concomitant and adjuvant temozolomide for glioblastoma. *N Engl J Med*. (2005) 352:987–96. doi: 10.1056/NEJMoa043330
158. Packer RJ. Diagnosis and treatment of pediatric brain tumors. *Curr Opin Neurol*. (1994) 7:484–91. doi: 10.1097/00019052-199412000-00003
159. Finlay JL, Boyett JM, Yates AJ, Wisoff JH, Milstein JM, Geyer JR, et al. Randomized phase III trial in childhood high-grade astrocytoma comparing vincristine, lomustine, and prednisone with the eight-drugs-in-1-day regimen. *Childrens Cancer Group J Clin Oncol*. (1995) 13:112–23. doi: 10.1200/JCO.1995.13.1.112
160. Geyer JR, Finlay JL, Boyett JM, Wisoff J, Yates A, Mao L, et al. Survival of infants with malignant astrocytomas. A Report from the Childrens Cancer Group. *Cancer*. (1995) 75:1045–50.
161. Dufour C, Grill J, Lellouch-Tubiana A, Puget S, Chastagner P, Frappaz D, et al. High-grade glioma in children under 5 years of age: a chemotherapy only approach with the BBSFOP protocol. *Eur J Cancer*. (2006) 42:2939–45. doi: 10.1016/j.ejca.2006.06.021
162. Sanders RP, Kocak M, Burger PC, Merchant TE, Gajjar A, Broniscer A. High-grade astrocytoma in very young children. *Pediatr Blood Cancer*. (2007) 49:888–93. doi: 10.1002/pbc.21272
163. Foster JB, Madsen PJ, Hegde M, Ahmed N, Cole KA, Maris JM, et al. Immunotherapy for pediatric brain tumors: past and present. *Neuro Oncol*. (2019) 21:1226–38. doi: 10.1093/neuonc/noz077
164. Packer RJ, Kilburn L. Molecular-targeted therapy for childhood brain tumors: a moving target. *J Child Neurol*. (2020) 35:791–8. doi: 10.1177/0883073820931635
165. Wetmore C, Daryani VM, Billups CA, Boyett JM, Leary S, Tanos R, et al. Phase II evaluation of sunitinib in the treatment of recurrent or refractory high-grade glioma or ependymoma in children: a children's Oncology Group Study ACNS1021. *Cancer Med*. (2016) 5:1416–24. doi: 10.1002/cam4.713
166. Chatwin HV, Cruz Cruz J, Green AL. Pediatric high-grade glioma: moving toward subtype-specific multimodal therapy. *FEBS J*. (2021) doi: 10.1111/febs.15739. [Epub ahead of print].
167. Narayana A, Kunnakkat S, Chacko-Mathew J, Gardner S, Karajannis M, Raza S, et al. Bevacizumab in recurrent high-grade pediatric gliomas. *Neuro Oncol*. (2010) 12:985–90. doi: 10.1093/neuonc/noq033
168. Lin F, de Gooijer MC, Hanekamp D, Chandrasekaran G, Buil LCM, Thota N, et al. PI3K-mTOR pathway inhibition exhibits efficacy against high-grade glioma in clinically relevant mouse models. *Clin Cancer Res*. (2017) 23:1286–98. doi: 10.1158/1078-0432.CCR-16-1276
169. Robinson GW, Orr BA, Gajjar A. Complete clinical regression of a BRAF V600E-mutant pediatric glioblastoma multiforme after BRAF inhibitor therapy. *BMC Cancer*. (2014) 14:258. doi: 10.1186/1471-2407-14-258
170. Zhao X, Kotch C, Fox E, Surrey LF, Wertheim GB, Baloch ZW, et al. NTRK fusions identified in pediatric tumors: the frequency, fusion partners, and clinical outcome. *JCO Precis Oncol*. (2021) 1:PO.20.00250. doi: 10.1200/PO.20.00250
171. Huang SY, Yang J-Y. Targeting the hedgehog pathway in pediatric medulloblastoma. *Cancers*. (2015) 7:2110–23. doi: 10.3390/cancers7040880
172. Long W, Yi Y, Chen S, Cao Q, Zhao W, Liu Q. Potential new therapies for pediatric diffuse intrinsic pontine glioma. *Front Pharmacol*. (2017) 8:495. doi: 10.3389/fphar.2017.00495
173. Sadelain M, Brentjens R, Rivière I. The basic principles of chimeric antigen receptor design. *Cancer Discov*. (2013) 3:388–98. doi: 10.1158/2159-8290.CD-12-0548
174. van der Stegen SJC, Hamieh M, Sadelain M. The pharmacology of second-generation chimeric antigen receptors. *Nat Rev Drug Discov*. (2015) 14:499–509. doi: 10.1038/nrd4597
175. June CH, Sadelain M. Chimeric antigen receptor therapy. *N Engl J Med*. (2018) 379:64–73. doi: 10.1056/NEJMra1706169
176. Patterson JD, Henson JC, Breese RO, Bielamowicz KJ, Rodriguez A. CAR T Cell therapy for pediatric brain tumors. *Front Oncol*. (2020) 10:1582. doi: 10.3389/fonc.2020.01582
177. Gaudino SJ, Kumar P. Cross-talk between antigen presenting cells and T cells impacts intestinal homeostasis, bacterial infections, and tumorigenesis. *Front Immunol*. (2019) 10:360. doi: 10.3389/fimmu.2019.00360
178. Akhavan D, Alizadeh D, Wang D, Weist MR, Shepphird JK, Brown CE. CAR T cells for brain tumors: lessons learned and road ahead. *Immunol Rev*. (2019) 290:60–84. doi: 10.1111/imr.12773
179. Vitanza NA, Johnson AJ, Wilson AL, Brown C, Yokoyama JK, Künkele A, et al. Locoregional infusion of HER2-specific CAR T cells in children and young adults with recurrent or refractory CNS tumors: an interim analysis. *Nat Med*. (2021) 27:1544–52. doi: 10.1038/s41591-021-01404-8
180. Kabir TF, Chauhan A, Anthony L, Hildebrandt GC. Immune checkpoint inhibitors in pediatric solid tumors: status in 2018. *Ochsner J*. (2018) 18:370–6. doi: 10.31486/toj.18.0055
181. Peggs KS, Quezada SA, Allison JP. Cell intrinsic mechanisms of T-cell inhibition and application to cancer therapy. *Immunol Rev*. (2008) 224:141–65. doi: 10.1111/j.1600-065X.2008.00649.x
182. Park JA, Cheung N-KV. Limitations and opportunities for immune checkpoint inhibitors in pediatric malignancies. *Cancer Treat Rev*. (2017) 58:22–33. doi: 10.1016/j.ctrv.2017.05.006
183. Wherry EJ, Kurachi M. Molecular and cellular insights into T cell exhaustion. *Nat Rev Immunol*. (2015) 15:486–99. doi: 10.1038/nri3862

184. Wintterle S, Schreiner B, Mitsdoerffer M, Schneider D, Chen L, Meyermann R, et al. Expression of the B7-related molecule B7-H1 by glioma cells. *Cancer Res.* (2003) 63:7462–7.
185. Yao Y, Tao R, Wang X, Wang Y, Mao Y, Zhou LF. B7-H1 is correlated with malignancy-grade gliomas but is not expressed exclusively on tumor stem-like cells. *Neuro Oncol.* (2009) 11:757–66. doi: 10.1215/15228517-2009-014
186. Gorsi HS, Malicki DM, Barsan V, Tumblin M, Yeh-Nayre L, Milburn M, et al. Nivolumab in the treatment of recurrent or refractory pediatric brain tumors: a single institutional experience. *J Pediatr Hematol Oncol.* (2019) 41:e235–41. doi: 10.1097/MPH.0000000000001339
187. Cacciotti C, Choi J, Alexandrescu S, Zimmerman MA, Cooney TM, Chordas C, et al. Immune checkpoint inhibition for pediatric patients with recurrent/refractory CNS tumors: a single institution experience. *J Neurooncol.* (2020) 149:113–22. doi: 10.1007/s11060-020-03578-6
188. Wang SS, Bandopadhayay P, Jenkins MR. Towards immunotherapy for pediatric brain tumors. *Trends Immunol.* (2019) 40:748–61. doi: 10.1016/j.it.2019.05.009
189. Soldozy S, Skaff A, Soldozy K, Sokolowski JD, Norat P, Yagmurlu K, et al. From bench to bedside, the current state of oncolytic virotherapy in pediatric glioma. *Neurosurgery*. (2020) 87:1091–7. doi: 10.1093/neuros/nyaa247
190. Lun XQ, Zhou H, Alain T, Sun B, Wang L, Barrett JW, et al. Targeting human medulloblastoma: oncolytic virotherapy with myxoma virus is enhanced by rapamycin. *Cancer Res.* (2007) 67:8818–27. doi: 10.1158/0008-5472.CAN-07-1214
191. Wu Y, Lun X, Zhou H, Wang L, Sun B, Bell JC, et al. Oncolytic efficacy of recombinant vesicular stomatitis virus and myxoma virus in experimental models of rhabdoid tumors. *Clin Cancer Res.* (2008) 14:1218–27. doi: 10.1158/1078-0432.CCR-07-1330
192. Ashley DM, Thompson EM, Landi D, Desjardins A, Friedman AH, Threatt S, et al. HGG-22. phase 1b study polio vaccine sabin-rhinovirus poliovirus (PVSRIPO) for recurrent malignant glioma in children. *Neuro Oncol.* (2018) 20:i93. doi: 10.1093/neuonc/noy059.294
193. Gromeier M, Nair SK. Recombinant poliovirus for cancer immunotherapy. *Annu Rev Med.* (2018) 69:289–99. doi: 10.1146/annurev-med-050715-104655
194. Tejada S, Alonso M, Patiño A, Fueyo J, Gomez-Manzano C, Diez-Valle R. Phase I trial of DNX-2401 for diffuse intrinsic pontine glioma newly diagnosed in pediatric patients. *Neurosurgery.* (2018) 83:1050–6. doi: 10.1093/neuros/nyx507
195. Liu Z, Zhao X, Mao H, Baxter PA, Huang Y, Yu L, et al. Intravenous injection of oncolytic picornavirus SVV-001 prolongs animal survival in a panel of primary tumor-based orthotopic xenograft mouse models of pediatric glioma. *Neuro Oncol.* (2013) 15:1173–85. doi: 10.1093/neuonc/not065
196. Landi DB, Thompson EM, Ashley DM. Immunotherapy for pediatric brain tumors. *Neuroimmunol Neuroinflamm.* (2018) 5:29. doi: 10.20517/2347-8659.2018.35
197. Friedman GK, Johnston JM, Bag AK, Bernstock JD, Li R, Aban I, et al. Oncolytic HSV-1 G207 immunovirotherapy for pediatric high-grade gliomas. *N Engl J Med.* (2021) 384:1613–22. doi: 10.1056/NEJMoa2024947
198. Varela-Guruceaga M, Tejada-Solís S, García-Moure M, Fueyo J, Gomez-Manzano C, Patiño-García A, et al. Oncolytic viruses as therapeutic tools for pediatric brain tumors. *Cancers.* (2018) 10:226. doi: 10.3390/cancers10070226
199. Ochs K, Ott M, Bunse T, Sahm F, Bunse L, Deumelandt K, et al. K27M-mutant histone-3 as a novel target for glioma immunotherapy. *Oncoimmunology.* (2017) 6:e1328340. doi: 10.1080/2162402X.2017.1328340
200. Schaller TH, Sampson JH. Advances and challenges: dendritic cell vaccination strategies for glioblastoma. *Expert Rev Vaccines.* (2017) 16:27–36. doi: 10.1080/14760584.2016.1218762
201. Banchereau J, Palucka K. Immunotherapy: cancer vaccines on the move. *Nat Rev Clin Oncol.* (2018) 15:9–10. doi: 10.1038/nrclinonc.2017.149
202. Rutkowski S, De Vleeschouwer S, Kaempgen E, Wolff JEA, Kühl J, Demaerel P, et al. Surgery and adjuvant dendritic cell-based tumour vaccination for patients with relapsed malignant glioma, a feasibility study. *Br J Cancer.* (2004) 91:1656–62. doi: 10.1038/sj.bjc.6602195
203. De Vleeschouwer S, Fieuws S, Rutkowski S, Van Calenbergh F, Van Loon J, Goffin J, et al. Postoperative adjuvant dendritic cell-based immunotherapy in patients with relapsed glioblastoma multiforme. *Clin Cancer Res.* (2008) 14:3098–104. doi: 10.1158/1078-0432.CCR-07-4875
204. Faury D, Nantel A, Dunn SE, Guiot M-C, Haque T, Hauser P, et al. Molecular profiling identifies prognostic subgroups of pediatric glioblastoma and shows increased YB-1 expression in tumors. *J Clin Oncol.* (2007) 25:1196–208. doi: 10.1200/JCO.2006.07.8626

Conflict of Interest: The authors declare that the research was conducted in the absence of any commercial or financial relationships that could be construed as a potential conflict of interest.

Publisher's Note: All claims expressed in this article are solely those of the authors and do not necessarily represent those of their affiliated organizations, or those of the publisher, the editors and the reviewers. Any product that may be evaluated in this article, or claim that may be made by its manufacturer, is not guaranteed or endorsed by the publisher.

frontiers in Neurology

MINI REVIEW
published: 16 March 2022
doi: 10.3389/fneur.2022.789355

Emerging MR Imaging and Spectroscopic Methods to Study Brain Tumor Metabolism

Manoj Kumar[1], *Ravi Prakash Reddy Nanga*[2], *Gaurav Verma*[3], *Neil Wilson*[2], *Jean Christophe Brisset*[4], *Kavindra Nath*[2] *and Sanjeev Chawla*[2]*

[1] Department of Neuroimaging and Interventional Radiology, National Institute of Mental Health and Neurosciences, Bengaluru, India, [2] Department of Radiology, Perelman School of Medicine at the University of Pennsylvania, Philadelphia, PA, United States, [3] Department of Radiology, Icahn School of Medicine at Mount Sinai, New York, NY, United States, [4] Median Technologies, Valbonne, France

Proton magnetic resonance spectroscopy (^{1}H-MRS) provides a non-invasive biochemical profile of brain tumors. The conventional ^{1}H-MRS methods present a few challenges mainly related to limited spatial coverage and low spatial and spectral resolutions. In the recent past, the advent and development of more sophisticated metabolic imaging and spectroscopic sequences have revolutionized the field of neuro-oncologic metabolomics. In this review article, we will briefly describe the scientific premises of three-dimensional echoplanar spectroscopic imaging (3D-EPSI), two-dimensional correlation spectroscopy (2D-COSY), and chemical exchange saturation technique (CEST) MRI techniques. Several published studies have shown how these emerging techniques can significantly impact the management of patients with glioma by determining histologic grades, molecular profiles, planning treatment strategies, and assessing the therapeutic responses. The purpose of this review article is to summarize the potential clinical applications of these techniques in studying brain tumor metabolism.

Keywords: brain tumor, chemical exchange saturation transfer (CEST), MRI and MRS, glioblastomas (GBMs), neurometabolites, two-dimensional correlation spectroscopy (2D-COSY), three-dimensional echo-planar spectroscopic imaging (3D-EPSI)

OPEN ACCESS

Edited by:
Itamar Ronen, Brighton and Sussex Medical School, United Kingdom

Reviewed by:
Chloe Najac, Leiden University Medical Center, Netherlands
Jana Ivanidze, Cornell University, United States

***Correspondence:**
Sanjeev Chawla
Sanjeev.Chawla@pennmedicine.upenn.edu

Specialty section:
This article was submitted to Applied Neuroimaging, a section of the journal Frontiers in Neurology

Received: *04 October 2021*
Accepted: *31 January 2022*
Published: *16 March 2022*

Citation:
Kumar M, Nanga RPR, Verma G, Wilson N, Brisset JC, Nath K and Chawla S (2022) Emerging MR Imaging and Spectroscopic Methods to Study Brain Tumor Metabolism. Front. Neurol. 13:789355. doi: 10.3389/fneur.2022.789355

INTRODUCTION

Gliomas are the most common primary brain tumors of the central nervous system (CNS) in adults and carry a grim prognosis (1–3). Proton magnetic resonance spectroscopy (^{1}H-MRS) is a valuable tool for the non-invasive assessment of metabolic alterations present within brain tumors (4). Several prior studies have reported potential utilities of ^{1}H-MRS in evaluating histological grades, molecular profiles, determination of prognosis, and assessment of treatment response to established novel therapies in patients with gliomas (5–10).

Despite presenting promising findings in clinical practice, the widely used single-voxel or single-slice two-dimensional ^{1}H-MRS methods suffer from some limitations. First, the conventional ^{1}H-MRS methods are constrained by the incomplete sampling of gliomas due to limited coverage of a region of interest. Consequently, it may not always be possible to interrogate the entire tumor volume, and as such, metabolic alterations from the essential regions of glioma may not be sampled. Conversely, the sampled large voxels from solid/contrast-enhancing regions of gliomas might include the edges of necrotic regions, peritumoral edematous regions, normal brain tissues,

or a combination of these tissue compartments. In such circumstances, metabolite levels in a particular tissue region of a tumor might be influenced by contributions from adjacent tissue compartments, thereby lowering the diagnostic accuracy of ^{1}H-MRS by falsely including features that do not actually exist in that particular tumor region. Second, the neoplastic cells in high-grade gliomas have a propensity to infiltrate beyond contrast-enhancing regions in the normal brain parenchyma, often along the myelinated axons and blood vessels (11–13). However, standard ^{1}H-MRS sequences do not often map the widespread metabolite abnormalities and suffer from the incomplete sampling of a glioma. Third, it is challenging to resolve several overlapping resonances existing over a small chemical shift range using conventional ^{1}H-MRS techniques, hampering the reliable separation of several metabolites, which are of critical importance in understanding the metabolic processes occurring within these gliomas. Over the last several years, alternative MR-based techniques have been developed and successfully implemented in research and clinical settings to unravel the metabolic profiling of gliomas.

In this review article, we will provide an overview of emerging metabolic MRI techniques that have revolutionized the field of neuro-oncology in the recent past. These techniques include three-dimensional echoplanar spectroscopic imaging (3D-EPSI), two-dimensional correlation spectroscopy (2D-COSY), and chemical exchange saturation technique (CEST) MRI methods. Recently, ^{13}C hyperpolarized and deuterium-based techniques have also gained momentum for studying metabolic pathways in brain tumors. While it is not in the scope of the current review for presenting a discussion on these novel multinuclear spectroscopic techniques, readers are referred to excellent articles available in the literature for a detailed overview on basic concepts and potential applications in neuro-oncology (14–20).

THREE-DIMENSIONAL ECHOPLANAR SPECTROSCOPIC IMAGING

Three-dimensional echo planar spectroscopic imaging (3D-EPSI) is an elegant method that provides high-resolution (nominal voxel size = 0.1 cm^3) volumetric metabolite maps covering supratentorial and infratentorial brain regions in a clinically acceptable acquisition window (21, 22). These volumetric maps can be spatially co-registered with anatomical images to facilitate mapping of metabolite alterations from normal brain parenchyma and from different tumor regions (central core, solid/contrast-enhancing, and peritumoral regions) with minimal partial volume averaging, thus projecting a more comprehensive representation of a tumor true spatial extent (23). Moreover, the whole-brain data acquisition scheme obviates the subjectivity and user bias for placing voxels in a tissue of interest (24, 25).

On routine clinical MR systems (1.5 or 3 T), the whole brain 3D-EPSI data is acquired using a spin-echo sequence with parallel imaging scheme using generalized autocalibrating partially parallel acquisition (GRAPPA) (26). This sequence requires strong, fast switching gradients with excellent eddy current performance. It takes ∼17–18 min to acquire a 3D-EPSI sequence that involves interleaved metabolite and water reference scans. The water scan is employed to improve the reconstruction and analysis of metabolite maps in the presence of magnetic field inhomogeneity and drift, besides using it as a reference signal for metabolite concentration scaling. To reduce lipid signal contamination from the skull and scalp, an inversion recovery prepared lipid inversion nulling is generally used in addition to employing an outer volume saturation band covering the skull base.

In neuro-oncology, multiple studies have shown the potential clinical utility of 3D-EPSI in studying brain tumor metabolism (23, 27–32). Glioblastomas (GBMs) are well known for their infiltrative nature with finger-like tentacles extending into the normal brain parenchyma like "mixing black and white sand" together, making differentiation of tumor cells from normal brain cells challenging on postcontrast T1-weighted images (33, 34). It is well established that cellular and metabolic alternations initiate much earlier than the appearance of actual lesions or anatomical changes in any pathological conditions, including brain tumors. By using 3D-EPSI, metabolite profile can be assessed both from the supratentorial and infratentorial brain regions simultaneously. Any deviation in the normal metabolite profile from normal-appearing brain tissues may be indicative of tumor infiltration. More importantly, these infiltrative tumor regions are generally associated with tumor recurrence and treatment failure (35, 36). Hence, it is crucial to develop a roadmap for precise delineation of tumor margins that will eventually aid in appropriate individualized therapeutic planning, including maximal safe tumor resection and delivery of accurate radiation therapy in these patients. To this end, 3D-EPSI derived total choline (tCho)/total N-acetyl aspartate (tNAA) maps were used in a study to detect regions of microscopic occult tumor infiltration beyond the areas of contrast enhancement in patients with GBM (26, 28, 37). The strong positive correlations were observed between tCho/tNAA ratios and quantitative measures of tumor infiltration (Sox2-positive cell density and *ex-vivo* fluorescence signals), supporting the notion that whole-brain metabolic maps can be used for reliable detection of infiltrative tumor regions (23).

Moreover, the investigators found that metabolically active disease does not always receive appropriate dose coverage in conventional radiation therapy planning in a routine clinical setting. The authors suggested using whole-brain tCho/tNAA maps in defining a target volume for delivering a maximum dose of radiation to active tumor regions for improved clinical outcomes in patients with GBM.

Surgical resection followed by concurrent chemoradiotherapy (CCRT) along with adjuvant temozolomide (TMZ) is the current standard of care treatment for patients with GBM (38). However, within 6 months after completing CCRT, a contrast-enhancing lesion within the radiation field at the site of original tumor or resection margins appears (39). While this lesion may represent true progression (TP) of a neoplasm, it may also reflect either a predominant treatment effect/pseudoprogression (PsP) that is mediated by TMZ-induced increased vascular permeability and inflammatory response. Specifically, PsP is a subacute and

posttreatment reaction that subsequently regresses or remains stable (40). Patients with TP are considered for repeat surgery or for alternative treatment strategies (41). On the other hand, patients with PsP are associated with a favorable prognosis and these patients are usually continued on adjuvant TMZ therapy (42, 43). Therefore, it is essential to differentiate TP from PsP for making informed decisions on future therapeutic interventions and for prognostication of disease in these patients. Using 3D-EPSI, our group demonstrated the clinical utility of tCho/tNAA and tCho/total creatine (tCr) maps in distinguishing TP from PsP with a discriminatory accuracy of over 90% (27). We observed significantly higher tCho/tNAA from contrast-enhancing, immediate, and distal peritumoral regions of GBMs in TP than those in patients with PsP. In addition, significantly elevated tCho/tCr levels from the contrast-enhancing areas were observed in TP compared with PsP. When these parameters were incorporated into multivariate logistic regression analyses, a discriminatory model with a sensitivity of 94% and a specificity of 87% was observed in distinguishing TP from PsP (27). Representative 3D-EPSI derived volumes of tCho/tNAA, and T_2-FLAIR abnormalities from patients with TP and PsP are demonstrated in **Figure 1A**. In addition, summed ^{1}H-MRS spectra encompassing the entire volumes of contrast-enhancing regions of neoplasms from these two patients are given in **Figure 1B**.

In another study, our group documented the clinical utility of 3D-EPSI in assessing the deleterious effects of whole-brain radiation therapy on normal brain parenchyma in patients with metastases (32). This study reported a significant increase in tCho/tCr levels in the hippocampus and genu of the corpus callosum at a 1-month postirradiation period relative to the baseline MRI study. These alterations in tCho levels support the idea that radiation therapy disrupts the metabolism of the normal brain tissues secondary to the breakdown of the myelin sheath and cell membranes following radiation-induced damage to oligodendrocytes. In addition, trends toward decrease in tNAA/tCr ratio were observed from the hippocampus (32).

Numerous other studies have also reported the immense clinical potential of 3D-EPSI in characterizing histological grades of gliomas, mapping distribution of glycine in gliomas, defining target volumes for radiation therapy in GBMs, and evaluating treatment response to immunotherapy and electric field therapy in patients with GBM (23, 28–31). Collectively these studies have reported that volumetric EPSI sequence can evaluate the spatial extent of metabolic alterations with high accuracy, which is essential for assessing disease burden in patients with glioma.

Mutation in isocitrate dehydrogenase (IDH) 1 and 2 families of enzymes in the TCA cycle causes NADPH-dependent reduction of α-ketoglutarate to 2-hydroxyglutarate (2HG), resulting in a two-to-three order of magnitude increase in the cellular 2HG concentration, which otherwise is present in vanishingly small quantities in the normal human brain regions. This mutation occurs at a single amino acid residue of the IDH active site resulting in loss of the enzyme's ability to catalyze the conversion of isocitrate to α-ketoglutarate. Several studies have reported that patients with glioma harboring IDH mutation demonstrate a better response to chemoradiation therapy and prolonged overall survival outcomes than those harboring IDH wild-type alleles (44, 45), thus emphasizing the importance of non-invasive identification of IDH mutant gliomas. An alteration

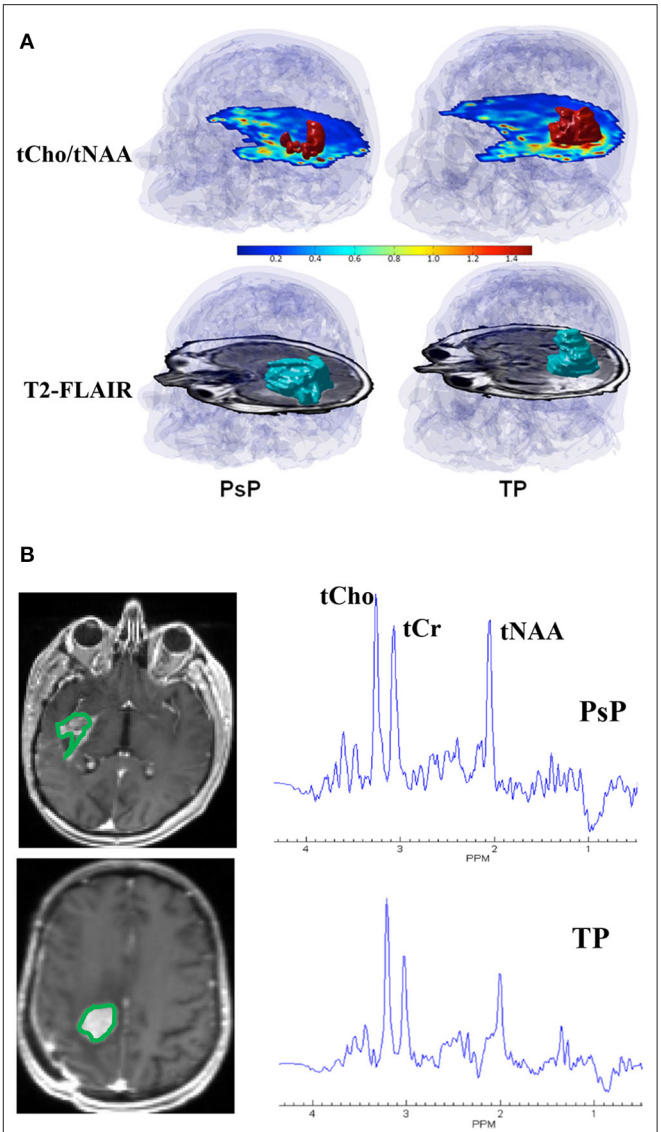

FIGURE 1 | (A) Top Row: tCho/tNAA maps from patients with representative PsP (left) and TP (right) showing red color 3D volumes corresponding to voxels that exceed a threshold value of 0.85 for tCho/tNAA overlaid on the inferior most slices of tCho/tNAA maps encompassing the neoplasm. A transparent blue shows an outline of the brain and skull derived from a coregistered T_1-weighted MPRAGE image. Bottom Row: T_2-FLAIR image from these two patients showing blue color 3D volumes corresponding to FLAIR abnormality that is approximately similar in size (227 voxels, 24.4 cm^3 for PsP and 219 voxels, and 23.6 cm^3 for TP). Please note that the red 3D volume of tCho/tNAA is smaller in patients with PsP than patients with TP despite the presence of approximately comparable volumes of FLAIR abnormality, emphasizing the importance of 3D-EPSI in ascertaining the true extent of metabolic abnormalities in patients with TP and PsP. **(B)** Summed ^{1}H-MRS spectra encompassing the entire volumes of contrast-enhancing regions of neoplasms from patients with TP and PsP are shown. Please note, higher tCho/tNAA ratio in TP than in PsP.

in tumor metabolism results in the aberrant accumulation of an oncometabolite 2HG, which has been considered as a putative marker for identifying IDH mutant gliomas (10, 45). Structurally, the oncometabolite 2HG consists of a 5-spin system and the scalar (J) coupling pattern of 2HG leads to several multiplets with spectral peaks centered around 4.02 (H2), 1.9 (H3 and H3′), and 2.25 ppm (H4 and H4′) spectral locations. The noninvasive detection of 2HG on conventional ^{1}H-MRS is challenging due to the extensive overlap of its resonances with those from metabolites, namely, NAA, glutamate (Glu), glutamine (Gln), gamma-aminobutyric acid (GABA), and lipids. Some previous ^{1}H-MRS studies have employed sophisticated acquisition and postprocessing strategies for reliable *in-vivo* detection and quantification of 2HG (46–48). It is well known that improved spectral resolution and reduced overlap can be achieved by applying a longer echo time (TE) to a standard point resolved spectroscopy (PRESS) sequence in order to take advantage of the differences in J-evolution observed in the coupled spin system (49). In a study, Choi et al. conducted several quantum mechanical simulations and finally used an optimal TE of 97 ms for the detection of 2HG signals from gliomas scanned on a 3 T MR system. The authors reported 100% sensitivity and specificity for detecting 2HG in gliomas (47). In a related study, the investigators used a triple refocusing sequence with a TE of 137 ms for improved detection of 2HG by successfully suppressing the confounding signals from Glu, Gln, and GABA (48). Using an innovative approach in a recent study, new lipid basis sets were used for detecting 2HG signals especially in those brain tumors, which exhibited high lipid resonances. Despite presenting encouraging findings, all these studies employed single voxel and/or single slice multivoxel ^{1}H-MRS methods. Lately, a high-resolution whole-brain ^{1}H-MRS technique has been proposed to map the oncometabolite 2HG from the entire volume of IDH mutant gliomas (50). Another recent study has demonstrated significantly higher tCho/tCr and tCho/tNAA ratios in IDH mutant than in IDH wild-type gliomas using whole-brain ^{1}H-MRS (51). Taken together, this wide range of clinical applications provide a strong impetus to use the 3D-EPSI sequence for the non-invasive quantification and assessment of metabolite alterations in gliomas.

The volumetric EPSI sequence is also associated with some limitations that include the effects of magnetic field inhomogeneity, especially from frontal and brain stem regions that may limit the spectroscopic characterization of tumors located in those particular regions. To avoid the inclusion of low-quality spectroscopic data, an automatic quality assurance procedure is used for each voxel using several metrics such as Cramer-Rao lower bounds (CRLB), line shapes, CSF partial volume contribution, and degree of residual water and lipid signals. The voxels that do not meet these predefined criteria are excluded from the final data analysis (21). Given that the volumetric EPSI sequence provides reliable metabolic information from different regions of gliomas and multiple normal brain regions simultaneously, we expect this sequence to be used widely in neuro-oncological applications in the near future. Moreover, the implementation of the whole-brain 3D-EPSI sequence on 7 T MRI scanners will open more avenues for studying brain tumor metabolism.

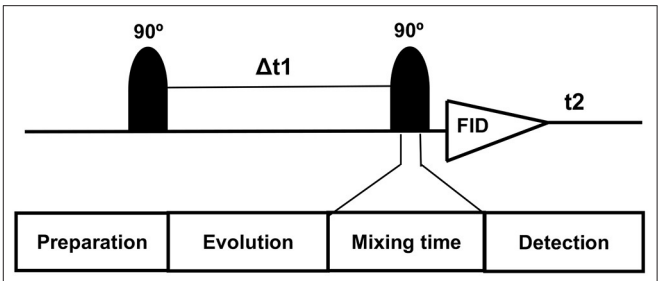

FIGURE 2 | Basic pulse diagram of a 2D-NMR experiment preparation time allows the nuclei in the sample to reach equilibrium with the static external magnetic field environment and solvent suppression is performed. During the evolution period, the magnetization of spins evolves. This time domain is incremented during the 2D-NMR experiment. During mixing time, coherence transfer takes place between J-coupled spins. During the detection period, transverse magnetization is recorded.

TWO-DIMENSIONAL-CORRELATION SPECTROSCOPY

On conventional one-dimensional (1D) ^{1}H-MRS, spectral peaks due to methyl, methylene, and methane protons from the number of metabolites, namely, NAA, N-acetyl aspartyl glutamate (NAAG), Glu, Gln, GABA, and 2HG neurometabolic peaks severely overlap in the spectral region of 2–4 ppm, often confounding the detection and quantification of metabolite concentrations. In contrast, the 2D-COSY method offers the ability to identify potentially overlapping resonances of metabolites by dispersing the multiplet structure of scalar (J)-coupled spin systems into a second spectral dimension and by exploiting the unlikely possibility that two metabolites would share identical chemical shifts in two dimensions (52–55). A basic pulse sequence of a 2D-COSY consists of preparation time that allows the nuclei in the sample to reach equilibrium with the static external magnetic field environment and during which water suppression is performed. During the evolution period, the magnetization of spins evolves. This time domain is incremented during a pulse sequence. During mixing time, coherence transfer occurs between scalar (J)-coupled spins, and finally, transverse magnetization is recorded during the detection period (**Figure 2**). In a 2D-COSY experiment, the MR signal is recorded as a function of two-time variables, t_1 (incremented time delay) and t_2 (fixed time delay) (**Figure 3**). The series of 1D-free induction decays are Fourier transformed along the first dimension in t_2 followed by another Fourier transformation in t_1. The signals of each transformation may differ in amplitude and/or phase. Higher resolution in t_2 (direct dimension) costs little time, but the higher resolution in t_1 (indirect dimension) adds directly to the acquisition time of the experiment.

As shown in **Figure 4**, a typical 2D-COSY spectrum comprises of two types of peaks (a) diagonal peak, which indicates that protons are not J-coupled with neighboring protons and

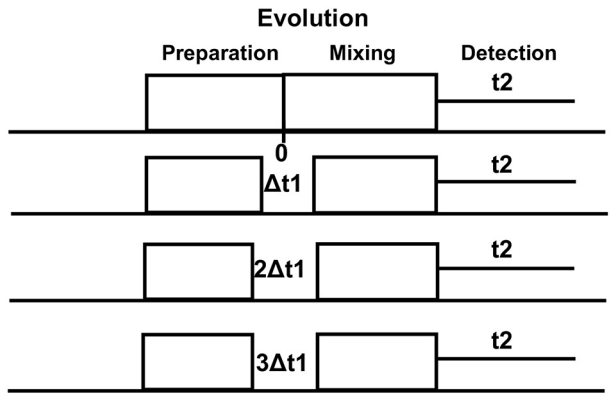

FIGURE 3 | Multiple (~64) evolutionary periods (Δt1 increments) are collected in a typical 2D-NMR experiment which is a simple series of 1D-NMR experiments acquired with different timings. Higher resolution in t2 (direct dimension) costs little time, but the higher resolution in t1 (indirect dimension) adds directly to the acquisition time of the experiment.

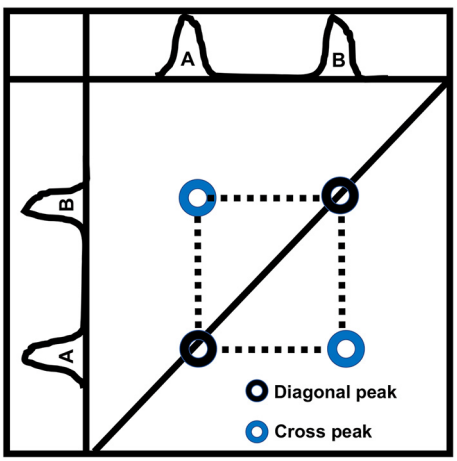

FIGURE 4 | A schematic diagram showing a typical 2D-COSY spectrum. Two types of peaks are observed. Auto peak/diagonal peak indicates that protons from a chemical moiety are not J-coupled with protons of a neighboring moiety. Cross-peak/off-diagonal peak indicates spin-spin couplings between two protons up to three bonds apart (vicinal coupling).

(b) cross-peak or off-diagonal peak, which indicates spin-spin couplings between two protons up to three bonds apart (vicinal coupling). Though well-separated, the cross-peaks show lower signal intensity than primary resonances because they originate only from the small fraction of spins undergoing coherence transfer during t_1 evolution.

Several earlier studies have reported the feasibility and clinical importance of *in-vivo* 2D-COSY sequence with human brains scanned at routine clinical scanners, mainly at 1.5 and 3 T MR systems (56–58). However, the introduction of ultra-high field (7T) MR systems has improved the sensitivity of 2D-COSY technique in detecting metabolites, particularly with overlapping resonance peaks. Previously, our group has implemented a 2D-COSY pulse sequence on a 7 T MR system and demonstrated enhanced signal-to-noise ratio (SNR) and increased chemical shift dispersion compared to a similar 2D-COSY scheme and voxel size acquired at a lower field strength of 3 T (59). In this reproducibility study, test-retest experiments of brain phantom using 2D-COSY sequence on 7 T revealed coefficients of variation (CVs) of 3–20% for most metabolites, suggesting high diagnostic accuracy of this method. A direct comparison of SNR indicated that most metabolite peaks were 2–3 times more intense at 7 T than at 3 T.

Furthermore, *in vivo* 2D-COSY spectra allowed the detection of several metabolite resonances from multiple brain regions of normal volunteers, and intersubject experiments revealed CVs of 4–26% for most metabolites (59). Collectively, these results demonstrate the feasibility, reliability, and clinical potential of the 2D-COSY sequence in unambiguously detecting additional metabolites in the human brain than what can be generally ascertained either by 1D studies at 7 T or analogous 2D-COSY studies at lower field strengths (1.5 or 3 T). Moving forward, our group implemented a non-uniformly weighted sampling (NUWS) scheme for faster acquisition of 2D-COSY data on a 7T MR system. The NUWS 2D-COSY facilitated a 25% shorter acquisition time while maintaining almost similar SNR in humans (+0.3%) and phantom experiments (+6.0%) to that of the uniform averaging method (60). This new approach could make the clinical applications of 2D-COSY sequences faster, easier, and more versatile.

In brain tumors, an elevated resonance of tCho at 3.2 ppm is generally observed on conventional ^{1}H-MRS, indicating increased cellular proliferation (4, 7, 8, 61). This prominent resonance of tCho is composed of signals from free Cho, phosphocholine (PC), and glycerophosphocholine (GPC) (62). To fully understand the dysregulated phospholipid metabolism in brain tumors, it is essential to detect and quantify relative levels of PC and GPC (4). In a previous *in-vitro* ^{1}H-MRS study from tumor extracts, it was found that PC was a predominant contributor to the tCho peak in high-grade gliomas (61). At the same time, GPC dominated in low-grade gliomas suggesting the potential role of relative amounts of PC and GPC in predicting tumor grades. The higher PC observed in high-grade gliomas has been attributed to elevated expression of choline transporters and/or enzymatic activities of choline kinase, and phospholipase-C (63). Furthermore, alterations in the PC/GPC ratio have been proposed as a marker of malignant transformation and treatment response (61). On conventional ^{1}H-MRS, the individual peak components of tCho (free Cho, PC, and GPC) cannot be reliably resolved (4, 61, 64).

There has been an increasing interest in investigating the crucial roles of neurotransmitters in dynamic remodeling and regulation of metabolic pathways in brain tumors. Hence, it is imperative to understand the alterations in Glu, Gln, and GABA cycle as Glu is involved in the cellular anabolic pathways and is also associated with facilitating tumor invasion (65–67). Consequently, reliable detection of these metabolites is valuable for studying tumor metabolism. Detection of elevated lactate (Lac) in brain tumors may reflect elevated tumor glycolysis

and/or poor tissue perfusion (68). However, reliable detection of Lac on 1D ^{1}H-MRS is problematic due to intense co-resonant lipids signals that are also known to be present at elevated levels, especially in high-grade gliomas.

In a study, we published our initial experience of using 2D-COSY sequence on a 7 T MRI scanner for successfully identifying IDH mutant gliomas by unambiguously detecting resonances of 2HG besides reporting other clinically relevant metabolites (69).

Representative 2D-COSY spectrum from a patient with grade-III astrocytoma harboring IDH wild-type genotype is shown in **Figure 5**. In another study, Ramadan et al. reported several characteristic metabolites from GBMs using 2D-COSY (70). Collectively, these studies suggest the potential utility of 2D-COSY in the characterization of brain tumors. However, future studies with larger patient populations are required to validate these encouraging findings.

We recognize the limitations of the 2D-COSY technique in terms of its relatively longer acquisition time (∼17 min). However, future modifications of this pulse sequence would benefit from implementing acceleration techniques like matched accumulation or sparse sampling to reduce overall scan time. Quantification of metabolic resonances detected on 2D-COSY could also be improved by implementing a prior-knowledge-based fitting approach analogous to linear combination (LC)-model fitting on 1D-MRS rather than using a peak integration method that is generally used. ProFit is one such 2D prior-knowledge-based fitting algorithm, and adopting this program could improve the reliable quantification of brain tumor metabolites (52, 71, 72). Future developments also include designing multivoxel-based 2D-COSY sequences using concentric circular echoplanar encoding or spiral encoding schemes for facilitating faster data with greater anatomical coverage and higher spatial resolution.

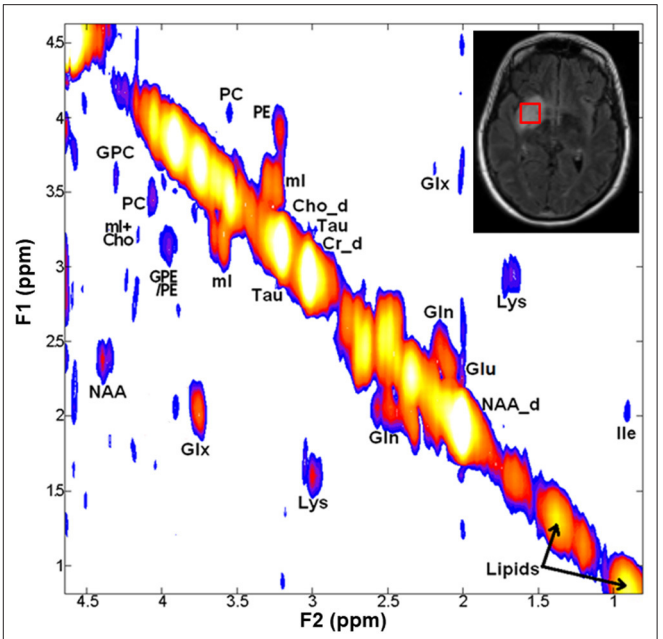

FIGURE 5 | A 2D-COSY spectrum (from a voxel placed on hyperintense signal abnormality as visible on T2-FLAIR image, right inset) from a patient with grade-III astrocytoma harboring IDH wild-type genotype showing various metabolites. Abbreviations: choline (Cho); ethanolamine (Eth); glutamate (Glu); glutamine (Gln); glutamate + glutamine (Glx); glycerophosphocholine (GPC); isoleucine (Ile); lysine (Lys); Myo-inositol (mI); N-acetyl aspartate (NAA); phosphocholine (PC); phosphoethanolamine (PE); and taurine (Tau).

CHEMICAL EXCHANGE SATURATION TRANSFER

Chemical exchange saturation transfer (CEST) is a relatively novel metabolic imaging modality that allows the detection of specific exogenous and endogenous metabolites/molecules present at very low concentrations (73–75). In CEST imaging, exchangeable solute protons present on the chemical functional groups such as hydroxyls (–OH), amides (–CONH), and amines (–NH_2) resonate at a frequency different from the bulk water protons (off-resonance frequencies for -OH, –CONH, and –NH_2 protons are ∼ 0.5–1.5, ∼3.5, and 1.8–3.0 ppm, respectively). These labile protons are selectively saturated using radiofrequency (RF) irradiation centered at the resonance frequencies of these protons. This saturation is subsequently transferred to bulk water pool when solute protons exchange with water protons leading to a decrease in the water signal proportional to the concentration of solute molecules and exchange rate of labile protons. While the saturation pulse is being applied, this process continues to decrease the water magnetization. Simultaneously, longitudinal relaxation processes return the saturated proton spins to their thermal equilibrium state until the system reaches a steady-state condition or the saturation pulse is turned off. This reduction in the water signal can be imaged by modifying fast imaging pulse sequences. For the exchangeable solute protons of interest, two factors that play a critical role in obtaining the optimal contrast are (i) the applied power and (ii) the duration of the RF pulse.

The CEST imaging provides a powerful contrast for detecting endogenous mobile proteins/peptides and neurometabolites such as Glu and Cr, which play a crucial role in tumor development, tumor growth, and disease progression (76–79). Therefore, studying these macromolecules and metabolites using CEST imaging techniques may provide valuable insights for understanding the brain tumor microenvironment.

Amide Proton Transfer

Amide proton transfer imaging is a CEST technique developed to detect and quantitatively visualize endogenous mobile peptides and proteins present within the biological tissues (76, 80). Amide protons resonate at around 8.2 ppm on the MR spectrum and hence have a chemical shift of 3.5 ppm downfield from the water signal. Due to the prolonged exchange rate (∼30 s^{-1}) of amide protons, it is possible to obtain nearly complete saturation using a low-power, long-duration saturation RF pulse (81). APT imaging can also be performed on 3 T clinical MRI scanners mainly due to the slow exchange rate of amide protons. As an APT signal is dependent on the variations in tissue pH values, APT imaging

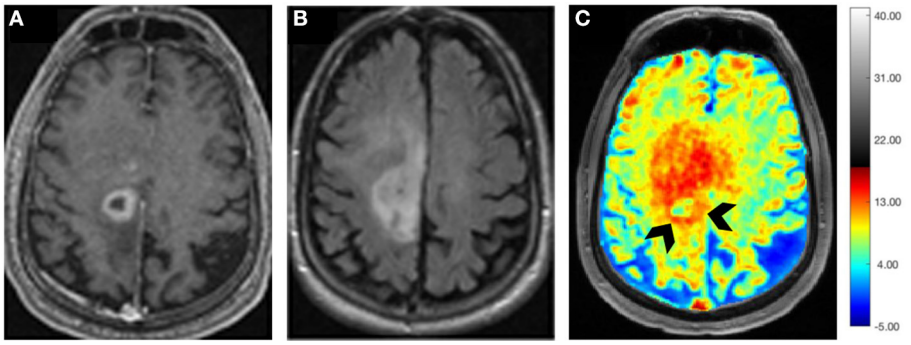

FIGURE 6 | Axial postcontrast T_1 weighted image **(A)** demonstrating a ring-enhancing GBM with hypointense vasogenic edema in the left frontal lobe, which is visible as a hyperintense mass on the corresponding T_2-FLAIR image **(B)**. B_0 and B_1 field in-homogeneity corrected Glu-CEST map **(C)** showing high glutamate signals from contrast-enhancing ring (arrowheads) and the surrounding brain regions beyond the contrast enhancement, suggesting infiltrative nature of this neoplasm.

may be helpful in determining the tumor pH after performing appropriate calibration of the signals (82).

It is widely believed that active tumor cells express higher concentrations of mobile protein and peptide components (83, 84). Also, metabolically active tumors produce a higher amount of lactic acid in the extracellular tumor microenvironment (85). This decrease in tumor pH should generate lower APT contrast due to the slower exchange rate of amide protons because the chemical exchange of protons from the amide group to water is base-catalyzed. On the contrary, higher APT contrast is generally observed from tumors than from normal tissues. The plausible reason for this observation could be that higher peptides/protein contents present within the tumors might offset the pH-dependent lower APT signals (80).

Using orthotropic glioma models in rats, a preclinical study reported the potential utility of APT imaging in differentiating viable tumors from radiation necrosis. While actively growing tumor regions exhibited hyperintensities on APT images, necrotic regions showed hypointense to isointense signal intensities (86). In addition, the intensity of the APT signal was shown to decrease in irradiated tumors at 3-day and 6-day of posttreatment periods relative to baseline suggesting APT imaging may aid in evaluating treatment response to radiation therapy in brain tumors. Several clinical studies have also demonstrated the great potential of APT-weighted imaging in delineating malignant neoplastic infiltration from peritumoral vasogenic edema, differentiating histopathological grades, and discriminating high-grade gliomas from primary cerebral lymphomas (87–89). In addition, some studies have documented significantly higher APT signals in TP than those with PsP in patients with GBM. This difference may be attributed to the presence of lower concentrations of mobile cytosolic proteins and peptides in PsP secondary to reduced cellular density and disrupted cytoplasm than those present in TP (84, 87).

Amide proton transfer-weighted imaging has also been used to identify IDH mutation status in gliomas (90–93). Intriguingly, lower APT signal intensities have been observed in IDH-mutant (phenotypically indolent tumors with more favorable prognosis) than in IDH-wildtype (phenotypically aggressive tumors with poor prognosis) gliomas (94–96). APT imaging has also been used for identifying O^6-methylguanine-DNA methyltransferase (MGMT) promoter methylation status in GBMs. In a study, significantly lower APT signal intensities were observed in MGMT methylated (a prognostic marker for more favorable prognosis) than in MGMT unmethylated GBMs (97). In summary, APT imaging is fast emerging as a novel molecular MRI technique in neuro-oncology that can be used for classifying brain tumor types, determining histological grades and molecular profiles of gliomas, and evaluating treatment response in patients with glioma.

Glutamate-CEST

It has been demonstrated that Glutamate (Glu) exhibits a pH and concentration-dependent CEST effect between its amine protons observed at ∼3.0 ppm downfield from bulk water protons. A CEST method for imaging Glu (Glu-CEST) can be utilized to generate high-resolution (in-plane resolution varies between 0.8 × 0.8 and 1.0 × 1.0 mm^2) parametric maps for better understanding the role of this crucial metabolite in studying brain tumor metabolism (98–100). In a pilot study, higher Glu-CEST signals were observed from peritumoral regions of grade II–III gliomas compared to contralateral brain regions. Interestingly, these high Glu-CEST contrast regions were associated with seizure activities in these patients (101). These findings substantiate the notion that the peritumoral regions could be potential epileptogenic zones in gliomas. In an ongoing study at our institution, we are currently investigating the potential role of Glu-CEST imaging on a 7 T MR scanner for detecting occult neoplastic infiltration into the normal brain parenchyma and evaluating the extent of glutamatergic excitatory activity in patients with GBM (**Figure 6**). We believe that improved delineation of tumor margins (*precision diagnostics*) will aid in appropriate individualized therapeutic planning, including maximal safe tumor resection and enhanced delivery of radiation dose to actively proliferating regions of a GBM (*personalized therapeutics*), thus improving the quality of life and survival outcomes in these patients.

TABLE 1 | Head-to-head comparison of three metabolic techniques (3D-EPSI, 2D-COSY, and CEST imaging).

Type of characteristics	3D-EPSI	2D-COSY	CEST imaging
General features	Simultaneous spatial-spectral encoding technique and potentially valuable tool for mapping metabolite profiles from multiple brain regions	Identify potentially overlapping resonances of metabolites by spreading out the multiplet structure of scalar (J)-coupled spin systems into a second spectral dimension and by exploiting the unlikely possibility that two metabolites would share identical chemical shifts in two-dimensions	Generates unique image contrast between tissues by targeting labile protons present within the endogenous molecules or exogenous compounds
Potential strengths	Offers advantages of greater spatial coverage and higher spatial resolution compared to multivoxel spectroscopic imaging techniques	Provides better dispersion of J-coupled peaks and unambiguously disentangles peaks present at similar chemical shift positions	Provides higher spatial resolution images for detecting metabolites with higher sensitivity compared to routine spectroscopy methods
Potential challenges	Longer shimming and acquisition times, the trade-off between spatial resolution and spectral bandwidth, prone to artifacts due to B_0 inhomogeneity and magnetic field susceptibility	Long acquisition times to adequately sample t1 dimension, limited spatial coverage (typical single voxel size of 4–8cm^3), and limited availability of post-processing tools	High RF power deposition, the requirement of ultrahigh magnetic field strength ($\geq$7 T) for observing some fast-exchanging metabolites, e.g., glutamate, sensitivity to B_0 and B_1 field inhomogeneities
Future directions	Implementation of robust, whole-brain 3D-EPSI sequence on 7T MRI scanners	Development of sequences for allowing faster data acquisition with greater anatomical coverage and higher spatial resolution	Development of reliable multi-slice CEST imaging sequences
Potential clinical applications in brain tumors	Characterization of multiple brain tumor lesions, intratumoral heterogeneity, tumor infiltration, harmful effects of radiation therapy from multiple normal brain regions	Detection and quantification of metabolites whose resonances severely overlap with those of other metabolites. For example, separation of lactate from lipids, phosphocholine from glycerophosphocholine, identification of glutamate, glutathione, and 2-hydroxyglutarate, etc	Quantitative mapping of proteins/peptides and metabolites present within the brain tumors with high sensitivity and spatial resolution

Creatine-CEST

Creatine-CEST (Cr-CEST) provides an imaging method to evaluate free Cr non-invasively with much improved spatial and temporal resolution than standard ^{1}H-MRS methods (102). Under normal physiological conditions, Cr-CEST contrast is observed predominantly from Cr with negligible contributions from phosphorylcreatine centered at +1.8 ppm downfield from water resonance. It has been shown that Cr-CEST imaging has over 1,000 times higher detection sensitivity compared to single-voxel ^{1}H-MRS enabling high-resolution mapping of Cr signal within a biological tissue (103).

Using the 9L gliosarcoma rat brain tumor model, a previous study demonstrated lower Cr-CEST peak integral from tumor regions than from contralateral normal brain regions. Moreover, the Cr-CEST peak integral decreased further with tumor progression (79). Furthermore, significantly lower Cr-CEST peak integrals were found in F98 (more aggressive) rat brain tumor model than in the 9L tumors (less aggressive) (79). It is well known that F98 gliomas share the essential characteristics of human GBMs (Grade-IV gliomas, the most malignant brain tumors), such as invasiveness and formation of hypoxia and necrosis. On the other hand, 9L gliosarcoma grows slowly and homogeneously and these tumors rarely exhibit regions of necrosis (104–106). Taken together, the findings of Cr-CEST studies on rodent tumor models indicate that levels of Cr diminish as the tumor progresses and the degree of aggressiveness increases. These findings are in good agreement with previously published studies that have shown a decreased level of Cr and/or creatine kinase activity in several different types of cancers (107, 108).

Over the last decade, several encouraging findings have been obtained by using CEST imaging; however, these are mostly restricted to animal models or pilot clinical studies. To translate these promising results of CEST imaging into a routine clinical setting, some critical issues, including B_1 inhomogeneities effects, especially in the temporal brain regions, the requirements for lower power deposition, longer scan time, and correct interpretation of CEST data need to be addressed. Sequences with radial or spiral k-space-filling strategies are being explored for CEST imaging to achieve a shorter acquisition time. Some developments such as parallel transmission, RF shimming, and post-B_1 correction strategies are also currently in progress to address some of the shortcomings associated with CEST imaging.

SUMMARY

New advances in metabolic MRI and spectroscopic techniques have been evolving rapidly over the last few years. A comparative analysis of three metabolic techniques (3D-EPSI, 2D-COSY, and CEST imaging) is given in **Table 1**. These techniques will have significant roles in reshaping our understanding of brain tumor biology and metabolism for accurate tumor diagnosis, prognosis, and identification of new molecular targets for fostering the discovery of new treatments. However, it is critical to standardize

and harmonize the acquisition parameters of these metabolic techniques for fast-tracking the translation and implementation into routine clinical workflows. Further progress in this field also requires data sharing and large multicentric, collaborative validation studies.

AUTHOR CONTRIBUTIONS

All authors listed have made a substantial, direct, and intellectual contribution to the work and approved it for publication.

FUNDING

This work was supported by funding obtained from University Research Foundation (URF), Perelman School of Medicine at the University of Pennsylvania, Philadelphia, USA (PI: SC, PhD, DABMP), extramural research grants [(BT/RLF/Re-entry/16/2015), and (CRG/2021/000668)] from Department of Biotechnology (DBT) and Science & Technology (DST), Govt. of India, respectively (PI: MK).

REFERENCES

1. Hanif F, Muzaffar K, Perveen kahkashan, Malhi S, Simjee S. Glioblastoma multiforme: a review of its epidemiology and pathogenesis through clinical presentation and treatment. *APJCP.* (2017) 18:3. doi: 10.22034/APJCP.2017.18.1.3
2. Ostrom QT, Patil N, Cioffi G, Waite K, Kruchko C, Barnholtz-Sloan JS, et al. Statistical report: primary brain and other central nervous system tumors diagnosed in the United States in 2013-2017. *Neuro Oncol.* (2020) 22:iv1–iv96. doi: 10.1093/neuonc/noaa200
3. Davis M. Glioblastoma: overview of disease and treatment. *CJON.* (2016) 20:S2–8. doi: 10.1188/16.CJON.S1.2-8
4. Kauppinen RA, Peet AC. Using magnetic resonance imaging and spectroscopy in cancer diagnostics and monitoring: preclinical and clinical approaches. *Cancer Biol Ther.* (2011) 12:665–79. doi: 10.4161/cbt.12.8.18137
5. Delikatny EJ, Chawla S, Leung D-J, Poptani H. MR-visible lipids and the tumor microenvironment. *NMR Biomed.* (2011) 24:592–611. doi: 10.1002/nbm.1661
6. Chawla S, Krejza J, Vossough A, Zhang Y, Kapoor GS, Wang S, et al. Differentiation between oligodendroglioma genotypes using dynamic susceptibility contrast perfusion-weighted imaging and proton MR spectroscopy. *AJNR Am J Neuroradiol.* (2013) 34:1542–9. doi: 10.3174/ajnr.A3384
7. Chawla S, Oleaga L, Wang S, Krejza J, Wolf RL, Woo JH, et al. Role of proton magnetic resonance spectroscopy in differentiating oligodendrogliomas from astrocytomas. *J Neuroimag.* (2010) 20:3–8. doi: 10.1111/j.1552-6569.2008.00307.x
8. Chawla S, Wang S, Wolf RL, Woo JH, Wang J, O'Rourke DM, et al. Arterial spin-labeling and MR spectroscopy in the differentiation of gliomas. *Am J Neuroradiol.* (2007) 28:1683–9. doi: 10.3174/ajnr.A0673
9. Yang D, Korogi Y, Sugahara T, Kitajima M, Shigematsu Y, Liang L, et al. Cerebral gliomas: prospective comparison of multivoxel 2D chemical-shift imaging proton MR spectroscopy, echoplanar perfusion and diffusion-weighted MRI. *Neuroradiology.* (2002) 44:656–66. doi: 10.1007/s00234-002-0816-9
10. Pope WB, Prins RM, Albert Thomas M, Nagarajan R, Yen KE, Bittinger MA, et al. Non-invasive detection of 2-hydroxyglutarate and other metabolites in IDH1 mutant glioma patients using magnetic resonance spectroscopy. *J Neurooncol.* (2012) 107:197–205. doi: 10.1007/s11060-011-0737-8
11. Yamahara T, Numa Y, Oishi T, Kawaguchi T, Seno T, Asai A, et al. Morphological and flow cytometric analysis of cell infiltration in glioblastoma: a comparison of autopsy brain and neuroimaging. *Brain Tumor Pathol.* (2010) 27:81–7. doi: 10.1007/s10014-010-0275-7
12. Chawla S, Zhang Y, Wang S, Chaudhary S, Chou C, O'Rourke DM, et al. Proton magnetic resonance spectroscopy in differentiating glioblastomas from primary cerebral lymphomas and brain metastases. *J Comput Assist Tomogr.* (2010) 34:836–41. doi: 10.1097/RCT.0b013e3181ec554e
13. Mohan S, Wang S, Coban G, Kural F, Chawla S, O'Rourke DM, et al. Detection of occult neoplastic infiltration in the corpus callosum and prediction of overall survival in patients with glioblastoma using diffusion tensor imaging. *Eur J Radiol.* (2019) 112:106–11. doi: 10.1016/j.ejrad.2019.01.015
14. Kurhanewicz J, Bok R, Nelson SJ, Vigneron DB. Current and potential applications of clinical 13C MR spectroscopy. *J Nucl Med.* (2008) 49:341–4. doi: 10.2967/jnumed.107.045112
15. Subramani E, Radoul M, Najac C, Batsios G, Molloy AR, Hong D, et al. Glutamate is a noninvasive metabolic biomarker of IDH1-mutant glioma response to temozolomide treatment. *Cancer Res.* (2020) 80:5098–108. doi: 10.1158/0008-5472.CAN-20-1314
16. Molloy AR, Najac C, Viswanath P, Lakhani A, Subramani E, Batsios G, et al. MR-detectable metabolic biomarkers of response to mutant IDH inhibition in low-grade glioma. *Theranostics.* (2020) 10:8757–70. doi: 10.7150/thno.47317
17. Viswanath P, Batsios G, Ayyappan V, Taglang C, Gillespie AM, Larson PEZ, et al. Metabolic imaging detects elevated glucose flux through the pentose phosphate pathway associated with TERT expression in low-grade gliomas. *Neuro Oncol.* (2021) 23:1509–22. doi: 10.1093/neuonc/noab093
18. Rich LJ, Bagga P, Wilson NE, Schnall MD, Detre JA, Haris M, et al. 1H magnetic resonance spectroscopy of 2H-to-1H exchange quantifies the dynamics of cellular metabolism in vivo. *Nat Biomed Eng.* (2020) 4:335–42. doi: 10.1038/s41551-019-0499-8
19. Kreis F, Wright AJ, Hesse F, Fala M, Hu D-E, Brindle KM. Measuring tumor glycolytic flux in vivo by using fast deuterium MRI. *Radiology.* (2020) 294:289–96. doi: 10.1148/radiol.2019191242
20. Straathof M, Meerwaldt AE, De Feyter HM, de Graaf RA, Dijkhuizen RM. Deuterium metabolic imaging of the healthy and diseased brain. *Neuroscience.* (2021) 474:94–9. doi: 10.1016/j.neuroscience.2021.01.023
21. Maudsley AA, Darkazanli A, Alger JR, Hall LO, Schuff N, Studholme C, et al. Comprehensive processing, display and analysis for *in vivo* MR spectroscopic imaging. *NMR Biomed.* (2006) 19:492–503. doi: 10.1002/nbm.1025
22. Ebel A, Soher BJ, Maudsley AA. Assessment of 3D proton MR echo-planar spectroscopic imaging using automated spectral analysis. *Magn Reson Med.* (2001) 46:1072–8. doi: 10.1002/mrm.1301
23. Cordova JS, Shu H-KG, Liang Z, Gurbani SS, Cooper LAD, Holder CA, et al. Whole-brain spectroscopic MRI biomarkers identify infiltrating margins in glioblastoma patients. *Neuro Oncol.* (2016) 18:1180–9. doi: 10.1093/neuonc/now036
24. Parra NA, Maudsley AA, Gupta RK, Ishkanian F, Huang K, Walker GR, et al. Volumetric spectroscopic imaging of glioblastoma multiforme radiation treatment volumes. *Int J Radiat Oncol Biol Phys.* (2014) 90:376–84. doi: 10.1016/j.ijrobp.2014.03.049
25. Donadieu M, Le Fur Y, Lecocq A, Maudsley AA, Gherib S, Soulier E, et al. Metabolic voxel-based analysis of the complete human brain using fast 3D-MRSI: proof of concept in multiple sclerosis. *J Magn Reson Imaging.* (2016) 44:411–9. doi: 10.1002/jmri.25139
26. Sabati M, Zhan J, Govind V, Arheart KL, Maudsley AA. Impact of reduced k-space acquisition on pathologic detectability for volumetric MR spectroscopic imaging. *J Magn Reson Imaging.* (2014) 39:224–34. doi: 10.1002/jmri.24130
27. Verma G, Chawla S, Mohan S, Wang S, Nasrallah M, Sheriff S, et al. Three-dimensional echo planar spectroscopic imaging for differentiation of true progression from pseudoprogression in patients with glioblastoma. *NMR Biomed.* (2019) 32:e4042. doi: 10.1002/nbm.4042

28. Roy B, Gupta RK, Maudsley AA, Awasthi R, Sheriff S, Gu M, et al. Utility of multiparametric 3-T MRI for glioma characterization. *Neuroradiology.* (2013) 55:603–13. doi: 10.1007/s00234-013-1145-x
29. Maudsley AA, Gupta RK, Stoyanova R, Parra NA, Roy B, Sheriff S, et al. Mapping of glycine distributions in gliomas. *AJNR Am J Neuroradiol.* (2014) 35:S31–36. doi: 10.3174/ajnr.A3845
30. Mohan S, Chawla S, Wang S, Verma G, Skolnik A, Brem S, et al. Assessment of early response to tumor-treating fields in newly diagnosed glioblastoma using physiologic and metabolic MRI: initial experience. *CNS Oncol.* (2016) 5:137–44. doi: 10.2217/cns-2016-0003
31. Wang S, O'Rourke DM, Chawla S, Verma G, Nasrallah MP, Morrissette JJD, et al. Multiparametric magnetic resonance imaging in the assessment of anti-EGFRvIII chimeric antigen receptor T cell therapy in patients with recurrent glioblastoma. *Br J Cancer.* (2019) 120:54–6. doi: 10.1038/s41416-018-0342-0
32. Chawla S, Wang S, Kim S, Sheriff S, Lee P, Rengan R, et al. Radiation injury to the normal brain measured by 3D-echo-planar spectroscopic imaging and diffusion tensor imaging: initial experience: assessment of radiation injury to normal brain. *J Neuroimaging.* (2015) 25:97–104. doi: 10.1111/jon.12070
33. Hambardzumyan D, Bergers G. Glioblastoma: defining tumor niches. *Trends in Cancer.* (2015) 1:252–65. doi: 10.1016/j.trecan.2015.10.009
34. D'Alessio A, Proietti G, Sica G, Scicchitano BM. Pathological and molecular features of glioblastoma and its peritumoral tissue. *Cancers.* (2019) 11:469. doi: 10.3390/cancers11040469
35. Tan AC, Ashley DM, López GY, Malinzak M, Friedman HS, Khasraw M. Management of glioblastoma: state of the art and future directions. *CA A Cancer J Clin.* (2020) 70:299–312. doi: 10.3322/caac.21613
36. Barker HE, Paget JTE, Khan AA, Harrington KJ. The tumour microenvironment after radiotherapy: mechanisms of resistance and recurrence. *Nat Rev Cancer.* (2015) 15:409–25. doi: 10.1038/nrc3958
37. Lin DDM, Lin Y, Link K, Marsman A, Zessler A, Usama SM, et al. Echoplanar magnetic resonance spectroscopic imaging before and following radiation therapy in patients with high-grade glioma. *Int J Radiat Oncol Biol Phys.* (2016) 96:E133–4. doi: 10.1016/j.ijrobp.2016.06.926
38. Johnson DR, Chang SM. Recent medical management of glioblastoma. *Adv Exp Med Biol.* (2012) 746:26–40. doi: 10.1007/978-1-4614-3146-6_3
39. Topkan E, Topuk S, Oymak E, Parlak C, Pehlivan B. Pseudoprogression in patients with glioblastoma multiforme after concurrent radiotherapy and temozolomide. *Am J Clin Oncol.* (2012) 35:284–9. doi: 10.1097/COC.0b013e318210f54a
40. Thust SC, van den Bent MJ, Smits M. Pseudoprogression of brain tumors: pseudoprogression of brain tumors. *J Magn Reson Imaging.* (2018) 48:571–89. doi: 10.1002/jmri.26171
41. Gerstner ER, McNamara MB, Norden AD, Lafrankie D, Wen PY. Effect of adding temozolomide to radiation therapy on the incidence of pseudo-progression. *J Neurooncol.* (2009) 94:97–101. doi: 10.1007/s11060-009-9809-4
42. Chawla S, Shehu V, Gupta PK, Nath K, Poptani H. Physiological imaging methods for evaluating response to immunotherapies in glioblastomas. *IJMS.* (2021) 22:3867. doi: 10.3390/ijms22083867
43. Roldán GB, Scott JN, McIntyre JB, Dharmawardene M, de Robles PA, Magliocco AM, et al. Population-based study of pseudoprogression after chemoradiotherapy in GBM. *Can J Neurol Sci.* (2009) 36:617–22. doi: 10.1017/s0317167100008131
44. Zhang C-B, Bao Z-S, Wang H-J, Yan W, Liu Y-W, Li M-Y, et al. Correlation of IDH1/2 mutation with clinicopathologic factors and prognosis in anaplastic gliomas: a report of 203 patients from China. *J Cancer Res Clin Oncol.* (2014) 140:45–51. doi: 10.1007/s00432-013-1519-9
45. Dang L, White DW, Gross S, Bennett BD, Bittinger MA, Driggers EM, et al. Cancer-associated IDH1 mutations produce 2-hydroxyglutarate. *Nature.* (2009) 462:739–44. doi: 10.1038/nature08617
46. Askari P, Dimitrov IE, Ganji SK, Tiwari V, Levy M, Patel TR, et al. Spectral fitting strategy to overcome the overlap between 2-hydroxyglutarate and lipid resonances at 225 ppm. *Magn Reson Med.* (2021) 86:1818–28. doi: 10.1002/mrm.28829
47. Choi C, Raisanen JM, Ganji SK, Zhang S, McNeil SS, An Z, et al. Prospective longitudinal analysis of 2-hydroxyglutarate magnetic resonance spectroscopy identifies broad clinical utility for the management of patients with IDH-mutant glioma. *J Clin Oncol.* (2016) 34:4030–9. doi: 10.1200/JCO.2016.67.1222
48. An Z, Ganji SK, Tiwari V, Pinho MC, Patel T, Barnett S, et al. Detection of 2-hydroxyglutarate in brain tumors by triple-refocusing MR spectroscopy at 3T *in vivo*. *Magn Reson Med.* (2017) 78:40–8. doi: 10.1002/mrm.26347
49. Allen PS, Thompson RB, Wilman AH. Metabolite-specific NMR spectroscopy in vivo. *NMR Biomed.* (1997) 10:435–44. doi: 10.1002/(sici)1099-1492(199712)10:8<435::aid-nbm480>3.0.co;2-d
50. Li X, Strasser B, Jafari-Khouzani K, Thapa B, Small J, Cahill DP, et al. Super-resolution whole-brain 3D MR spectroscopic imaging for mapping D-2-hydroxyglutarate and tumor metabolism in isocitrate dehydrogenase 1-mutated human gliomas. *Radiology.* (2020) 294:589–97. doi: 10.1148/radiol.2020191529
51. Goryawala M, Saraf-Lavi E, Nagornaya N, Heros D, Komotar R, Maudsley AA. The association between whole-brain MR spectroscopy and IDH mutation status in gliomas. *J Neuroimaging.* (2020) 30:58–64. doi: 10.1111/jon.12685
52. Iqbal Z, Nguyen D, Thomas MA, Jiang S. Deep learning can accelerate and quantify simulated localized correlated spectroscopy. *Sci Rep.* (2021) 11:8727. doi: 10.1038/s41598-021-88158-y
53. Kreis R, Boesch C. Spatially localized, one- and two-dimensional NMR spectroscopy and in vivo application to human muscle. *J Magn Reson B.* (1996) 113:103–18. doi: 10.1006/jmrb.1996.0163
54. Aue WP, Bartholdi E, Ernst RR. Two-dimensional spectroscopy. Application to nuclear magnetic resonance. *J Chem Phys.* (1976) 64:2229–46. doi: 10.1063/1.432450
55. Ryner LN, Sorenson JA, Thomas MA. Localized 2D J-resolved 1H MR spectroscopy: strong coupling effects in vitro and in vivo. *Magn Reson Imaging.* (1995) 13:853–69. doi: 10.1016/0730-725x(95)00031-b
56. Ziegler A, Gillet B, Beloeil J-C, Macher J-P, Décorps M, Nédelec J-F. Localized 2D correlation spectroscopy in human brain at 3 T. *MAGMA.* (2002) 14:45–9. doi: 10.1007/BF02668186
57. Thomas MA, Hattori N, Umeda M, Sawada T, Naruse S. Evaluation of two-dimensional L-COSY and JPRESS using a 3?T MRI scanner: from phantoms to human brain *in vivo*. *NMR Biomed.* (2003) 16:245–51. doi: 10.1002/nbm.825
58. Thomas MA, Yue K, Binesh N, Davanzo P, Kumar A, Siegel B, et al. Localized two-dimensional shift correlated MR spectroscopy of human brain. *Magn Reson Med.* (2001) 46:58–67. doi: 10.1002/mrm.1160
59. Verma G, Hariharan H, Nagarajan R, Nanga RPR, Delikatny EJ, Albert Thomas M, et al. Implementation of two-dimensional L-COSY at 7 tesla: an investigation of reproducibility in human brain: Implementation of 2D L-COSY at 7T. *J Magn Reson Imaging.* (2014) 40:1319–27. doi: 10.1002/jmri.24510
60. Verma G, Chawla S, Nagarajan R, Iqbal Z, Albert Thomas M, Poptani H. Non-uniformly weighted sampling for faster localized two-dimensional correlated spectroscopy of the brain in vivo. *J Magn Reson.* (2017) 277:104–12. doi: 10.1016/j.jmr.2017.02.012
61. Kumar M, Arlauckas SP, Saksena S, Verma G, Ittyerah R, Pickup S, et al. Magnetic resonance spectroscopy for detection of choline kinase inhibition in the treatment of brain tumors. *Mol Cancer Ther.* (2015) 14:899–908. doi: 10.1158/1535-7163.MCT-14-0775
62. Sonkar K, Ayyappan V, Tressler CM, Adelaja O, Cai R, Cheng M, Glunde K. Focus on the glycerophosphocholine pathway in choline phospholipid metabolism of cancer. *NMR Biomed.* (2019) 32:e4112. doi: 10.1002/nbm.4112
63. Ackerstaff E, Glunde K, Bhujwalla ZM. Choline phospholipid metabolism: a target in cancer cells? *J Cell Biochem.* (2003) 90:525–33. doi: 10.1002/jcb.10659
64. McKnight TR, Smith KJ, Chu PW, Chiu KS, Cloyd CP, Chang SM, et al. Choline metabolism, proliferation, and angiogenesis in nonenhancing grades 2 and 3 astrocytoma. *J Magn Reson Imaging.* (2011) 33:808–16. doi: 10.1002/jmri.22517
65. Pavlova NN, Thompson CB. The emerging hallmarks of cancer metabolism. *Cell Metab.* (2016) 23:27–47. doi: 10.1016/j.cmet.2015.12.006

66. Bak LK, Schousboe A, Waagepetersen HS. The glutamate/GABA-glutamine cycle: aspects of transport, neurotransmitter homeostasis and ammonia transfer. *J Neurochem.* (2006) 98:641–53. doi: 10.1111/j.1471-4159.2006.03913.x
67. Natarajan SK, Venneti S. Glutamine metabolism in brain tumors. *Cancers.* (2019) 11:1628. doi: 10.3390/cancers11111628
68. Sijens PE, Levendag PC, Vecht CJ, van Dijk P, Oudkerk M. 1H MR spectroscopy detection of lipids and lactate in metastatic brain tumors. *NMR Biomed.* (1996) 9:65–71. doi: 10.1002/(SICI)1099-1492(199604)9:2<65::AID-NBM397>3.0.CO;2-N
69. Verma G, Mohan S, Nasrallah MP, Brem S, Lee JYK, Chawla S, et al. Non-invasive detection of 2-hydroxyglutarate in IDH-mutated gliomas using two-dimensional localized correlation spectroscopy (2D L-COSY) at 7 tesla. *J Transl Med.* (2016) 14:274. doi: 10.1186/s12967-016-1035-1
70. Ramadan S, Andronesi OC, Stanwell P, Lin AP, Sorensen AG, Mountford CE. Use of in vivo two-dimensional MR spectroscopy to compare the biochemistry of the human brain to that of glioblastoma. *Radiology.* (2011) 259:540–9. doi: 10.1148/radiol.11101123
71. Kazimierczuk K, Orekhov VYu. Accelerated NMR spectroscopy by using compressed sensing. *Angew Chem Int Ed.* (2011) 50:5556–9. doi: 10.1002/anie.201100370
72. Schulte RF, Boesiger P. ProFit: two-dimensional prior-knowledge fitting of J-resolved spectra. *NMR Biomed.* (2006) 19:255–63. doi: 10.1002/nbm.1026
73. Vinogradov E, Sherry AD, Lenkinski RE, CEST. From basic principles to applications, challenges and opportunities. *J Magn Reson.* (2013) 229:155–72. doi: 10.1016/j.jmr.2012.11.024
74. van Zijl PCM, Yadav NN. Chemical exchange saturation transfer (CEST): What is in a name and what isn't? CEST: What is in a Name and What Isn't? *Magn Reson Med.* (2011) 65:927–48. doi: 10.1002/mrm.22761
75. Knutsson L, Xu J, Ahlgren A, van Zijl PCM. CEST, ASL, and magnetization transfer contrast: How similar pulse sequences detect different phenomena. *Magn Reson Med.* (2018) 80:1320–40. doi: 10.1002/mrm.27341
76. Dou W, Lin C-YE, Ding H, Shen Y, Dou C, Qian L, et al. Chemical exchange saturation transfer magnetic resonance imaging and its main and potential applications in pre-clinical and clinical studies. *Quant Imaging Med Surg.* (2019) 9:1747–66. doi: 10.21037/qims.2019.10.03
77. Consolino L, Anemone A, Capozza M, Carella A, Irrera P, Corrado A, et al. Non-invasive investigation of tumor metabolism and acidosis by MRI-CEST imaging. *Front Oncol.* (2020) 10:161. doi: 10.3389/fonc.2020.00161
78. Haris M, Yadav SK, Rizwan A, Singh A, Wang E, Hariharan H, et al. Molecular magnetic resonance imaging in cancer. *J Transl Med.* (2015) 13:313. doi: 10.1186/s12967-015-0659-x
79. Cai K, Tain R-W, Zhou XJ, Damen FC, Scotti AM, Hariharan H, et al. Creatine CEST MRI for differentiating gliomas with different degrees of aggressiveness. *Mol Imaging Biol.* (2017) 19:225–32. doi: 10.1007/s11307-016-0995-0
80. Sagiyama K, Mashimo T, Togao O, Vemireddy V, Hatanpaa KJ, Maher EA, et al. In vivo chemical exchange saturation transfer imaging allows early detection of a therapeutic response in glioblastoma. *Proc Nat Acad Sci.* (2014) 111:4542–7. doi: 10.1073/pnas.1323855111
81. Zhang XY, Wang F, Xu J, Gochberg DF, Gore JC, Zu Z. Increased CEST specificity for amide and fast-exchanging amine protons using exchange-dependent relaxation rate. *NMR Biomed*. (2018) 31:10.1002/nbm.3863. doi: 10.1002/nbm.3863
82. Ladd ME, Bachert P, Meyerspeer M, Moser E, Nagel AM, Norris DG, et al. Pros and cons of ultra-high-field MRI/MRS for human application. *Prog Nucl Magn Reson Spectrosc.* (2018) 109:1–50. doi: 10.1016/j.pnmrs.2018.06.001
83. Marqus S, Pirogova E, Piva TJ. Evaluation of the use of therapeutic peptides for cancer treatment. *J Biomed Sci.* (2017) 24:21. doi: 10.1186/s12929-017-0328-x
84. Ma B, Blakeley JO, Hong X, Zhang H, Jiang S, Blair L, et al. Applying amide proton transfer-weighted MRI to distinguish pseudoprogression from true progression in malignant gliomas: APT-MRI of Pseudo- vs. true progression. *J Magn Reson Imaging.* (2016) 44:456–62. doi: 10.1002/jmri.25159
85. de la Cruz-López KG, Castro-Muñoz LJ, Reyes-Hernández DO, García-Carrancá A, Manzo-Merino J. Lactate in the regulation of tumor microenvironment and therapeutic approaches. *Front Oncol.* (2019) 9:1143. doi: 10.3389/fonc.2019.01143
86. Zhou J, Tryggestad E, Wen Z, Lal B, Zhou T, Grossman R, et al. Differentiation between glioma and radiation necrosis using molecular magnetic resonance imaging of endogenous proteins and peptides. *Nat Med.* (2011) 17:130–4. doi: 10.1038/nm.2268
87. Gonçalves FG, Chawla S, Mohan S. Emerging MRI techniques to redefine treatment response in patients with glioblastoma. *J Magn Reson Imaging.* (2020) 52:978–97. doi: 10.1002/jmri.27105
88. Zhou J, Heo H-Y, Knutsson L, van Zijl PCM, Jiang S. APT-weighted MRI: techniques, current neuro applications, and challenging issues: APTw MRI for neuro applications. *J Magn Reson Imaging.* (2019) 50:347–64. doi: 10.1002/jmri.26645
89. Kessler AT, Bhatt AA. Brain tumour post-treatment imaging and treatment-related complications. *Insights Imaging.* (2018) 9:1057–75. doi: 10.1007/s13244-018-0661-y
90. Jiang S, Zou T, Eberhart CG, Villalobos MAV, Heo H-Y, Zhang Y, et al. Predicting IDH mutation status in grade II gliomas using amide proton transfer-weighted (APTw) MRI: predicting IDH Status With APTw MRI. *Magn Reson Med.* (2017) 78:1100–9. doi: 10.1002/mrm.26820
91. Han Y, Wang W, Yang Y, Sun Y-Z, Xiao G, Tian Q, et al. Amide proton transfer imaging in predicting isocitrate dehydrogenase 1 mutation status of grade II/III gliomas based on support vector machine. *Front Neurosci.* (2020) 14:144. doi: 10.3389/fnins.2020.00144
92. Sartoretti E, Sartoretti T, Wyss M, Reischauer C, van Smoorenburg L, Binkert CA, et al. Amide proton transfer weighted (APTw) imaging based radiomics allows for the differentiation of gliomas from metastases. *Sci Rep.* (2021) 11:5506. doi: 10.1038/s41598-021-85168-8
93. Nakajo M, Bohara M, Kamimura K, Higa N, Yoshiura T. Correlation between amide proton transfer-related signal intensity and diffusion and perfusion magnetic resonance imaging parameters in high-grade glioma. *Sci Rep.* (2021) 11:11223. doi: 10.1038/s41598-021-90841-z
94. Aibaidula A, Chan AK-Y, Shi Z, Li Y, Zhang R, Yang R, et al. Adult IDH wild-type lower-grade gliomas should be further stratified. *Neuro Oncol.* (2017) 19:1327–37. doi: 10.1093/neuonc/nox078
95. Shen G, Wang R, Gao B, Zhang Z, Wu G, Pope W. The MRI features and prognosis of gliomas associated with IDH1 mutation: a single center study in Southwest China. *Front Oncol.* (2020) 10:852. doi: 10.3389/fonc.2020.00852
96. Liu S, Liu Y, Li G, Feng J, Chen L, Qiu X. High-dose radiation associated with improved survival in IDH-wildtype low-grade glioma. *Chin Neurosurg J.* (2021) 7:22. doi: 10.1186/s41016-021-00239-z
97. Jiang S, Rui Q, Wang Y, Heo H-Y, Zou T, Yu H, et al. Discriminating MGMT promoter methylation status in patients with glioblastoma employing amide proton transfer-weighted MRI metrics. *Eur Radiol.* (2018) 28:2115–23. doi: 10.1007/s00330-017-5182-4
98. Crescenzi R, DeBrosse C, Nanga RPR, Byrne MD, Krishnamoorthy G, D'Aquilla K, et al. Longitudinal imaging reveals subhippocampal dynamics in glutamate levels associated with histopathologic events in a mouse model of tauopathy and healthy mice: subhippocampal dynamics in glutamate levels. *Hippocampus.* (2017) 27:285–302. doi: 10.1002/hipo.22693
99. Cai K, Haris M, Singh A, Kogan F, Greenberg JH, Hariharan H, et al. Magnetic resonance imaging of glutamate. *Nat Med.* (2012) 18:302–6. doi: 10.1038/nm.2615
100. Nanga RPR, DeBrosse C, Kumar D, Roalf D, McGeehan B, D'Aquilla K, et al. Reproducibility of 2D GluCEST in healthy human volunteers at 7 T. *Magn Reson Med.* (2018) 80:2033–9. doi: 10.1002/mrm.27362
101. Neal A, Moffat BA, Stein JM, Nanga RPR, Desmond P, Shinohara RT, et al. Glutamate weighted imaging contrast in gliomas with 7 Tesla magnetic resonance imaging. *NeuroImage Clin.* (2019) 22:101694. doi: 10.1016/j.nicl.2019.101694
102. Singh A, Debnath A, Cai K, Bagga P, Haris M, Hariharan H, Reddy R. Evaluating the feasibility of creatine-weighted CEST MRI in human brain at 7 T using a Z-spectral fitting approach. *NMR Biomed.* (2019) 32:e4176. doi: 10.1002/nbm.4176
103. Haris M, Nanga RPR, Singh A, Cai K, Kogan F, Hariharan H, et al. Exchange rates of creatine kinase metabolites: feasibility of imaging creatine by chemical exchange saturation transfer MRI: feasibility of imaging creatine by chemical exchange saturation transfer MRI. *NMR Biomed.* (2012) 25:1305–9. doi: 10.1002/nbm.2792

104. Doblas S, He T, Saunders D, Pearson J, Hoyle J, Smith N, et al. Glioma morphology and tumor-induced vascular alterations revealed in seven rodent glioma models by in vivo magnetic resonance imaging and angiography. *J Magn Reson Imaging.* (2010) 32:267–75. doi: 10.1002/jmri.22263
105. Vonarbourg A, Sapin A, Lemaire L, Franconi F, Menei P, Jallet P, et al. Characterization and detection of experimental rat gliomas using magnetic resonance imaging. *MAGMA.* (2004) 17:133–9. doi: 10.1007/s10334-004-0049-5
106. Barth RF, Kaur B. Rat brain tumor models in experimental neuro-oncology: the C6, 9L, T9, RG2, F98, BT4C, RT-2 and CNS-1 gliomas. *J Neurooncol.* (2009) 94:299–312. doi: 10.1007/s11060-009-9875-7
107. Pretlow TG, Whitehurst GB, Pretlow TP, Hunt RS, Jacobs JM, McKenzie DR, et al. Decrease in creatine kinase in human prostatic carcinoma compared to benign prostatic hyperplasia. *Cancer Res.* (1982) 42:4842–8.
108. Joseph J, Cardesa A, Carreras J. Creatine kinase activity and isoenzymes in lung, colon and liver carcinomas. *Br J Cancer.* (1997) 76:600–5. doi: 10.1038/bjc.1997.43

Conflict of Interest: JB was employed by Median Technologies.

The remaining authors declare that the research was conducted in the absence of any commercial or financial relationships that could be construed as a potential conflict of interest.

Publisher's Note: All claims expressed in this article are solely those of the authors and do not necessarily represent those of their affiliated organizations, or those of the publisher, the editors and the reviewers. Any product that may be evaluated in this article, or claim that may be made by its manufacturer, is not guaranteed or endorsed by the publisher.

Advantages of publishing in Frontiers

OPEN ACCESS
Articles are free to read for greatest visibility and readership

FAST PUBLICATION
Around 90 days from submission to decision

HIGH QUALITY PEER-REVIEW
Rigorous, collaborative, and constructive peer-review

TRANSPARENT PEER-REVIEW
Editors and reviewers acknowledged by name on published articles

Frontiers
Avenue du Tribunal-Fédéral 34
1005 Lausanne | Switzerland

Visit us: www.frontiersin.org
Contact us: frontiersin.org/about/contact

REPRODUCIBILITY OF RESEARCH
Support open data and methods to enhance research reproducibility

DIGITAL PUBLISHING
Articles designed for optimal readership across devices

FOLLOW US
@frontiersin

IMPACT METRICS
Advanced article metrics track visibility across digital media

EXTENSIVE PROMOTION
Marketing and promotion of impactful research

LOOP RESEARCH NETWORK
Our network increases your article's readership